PhD-FSTM-2020-123

The Faculty of Science, Technology and Medicine

DISSERTATION

Defence held on 09/09/2022 in Esch-sur-Alzette

to obtain the degree of

DOCTEUR DE L'UNIVERSITÉ DU LUXEMBOURG
EN PHYSIQUE

by

Youri Dilan NOUCHOKGWE KAMGUE

Born on 03 July 1996 in Douala (Cameroon)

SCALE LAW ON MATERIALS EFFICIENCY OF ELECTROCALORIC MATERIALS

Dissertation defence committee

Prof. Dr. Alex Redinger, Chairman

Professor, University of Luxembourg

Assoc. Prof. Dr. Christian Bahl, Vice Chairman

Senior Researcher, Technical University of Denmark

Prof. Dr. Hana Uršič Nemevšek

Senior Researcher, Jožef Stefan Institute

Assoc. Prof. Dr. Pol Lloveras

Associate Professor, Universitat Politècnica de Catalunya

Dr. Emmanuel Defay, Dissertation Supervisor

Head of Unit, Luxembourg Institute of Science and Technology

Affidavit

I hereby confirm that the PhD thesis entitled “*Scale law on energy efficiency of electrocaloric materials*” has been written independently and without any other sources than cited.

Luxembourg, 12/10/2022

Youri Nouchokgwe

Name

Acknowledgements

I would like to thank the Fonds National de la Recherche (FNR) for funding my Ph.D. project under the project CAMELHEAT C17/MS/11703691/Defay. My appreciation goes as well to the University of Luxembourg for offering through the Doctoral School, relevant transferable and scientific courses that have participated in my personal and scientific development.

To my supervisor, Merci beaucoup Manu, merci de m’avoir fait confiance et choisi pour ce projet de thèse. Tu as été et es un vériable leader. Merci d’avoir toujours été à l’écoute. Que ce soit sur le plan professionnel et personnel tu as été un mentor, une source d’inspiration et parfois voir un ”papa” . Ces quatre années de thèse ont été les plus belles années de ma vie académique, et ceci en partie grâce à toi. Je me rappellerai toujours de tous les coups de fous rires, de tes encouragements, de ton soutien constant dans les moments difficiles et de ta disponibilité. J’ai énormément appris de toi, je sors de cette thèse très bien formé et meilleur qu’il y a quatre années. Merci de tout coeur Manu.

I am very thankful to Dr. Christian Bahl for kindly inviting me to the DTU where I spent almost a month as visiting Ph.D. student. Thank you for sharing with me your expertise in calorimetry. You as a magnetocaloric material and I as an electrocaloric guy, we could have very fruitful discussions and learn from each other field. Finally, I would like to thank you as well for following my work during these four years, your feedback and recommendations have helped improve my understanding of the field. I would like to thank Dr. Alex Redinger for following my work. My appreciation goes to the jury members for accepting to be part of my committee defense and for revising my dissertation manuscript.

Thanks to Dr. Alvar Torello, my EC buddy. Thank you for filling me in on the topic when

I started my Ph.D. Your passion for research and your great sense of humor have made my Ph.D. journey a very fun and exciting time. You have become with time for me a best friend in and out of work. Thanks for the great tennis matches we played, thanks for the mocktails at Coyote after long working days, and thanks for being there in the bad moments.

I am grateful to all the former and present colleagues from the EC team. Thanks to Pierre for helping with the coding and for our interesting and challenging discussions on thermodynamics. “Merci” to Romain for transferring its knowledge on EC after leaving LIST. My thoughts go to Veronika, Uros, Ashwath, and Junning. I would like to thank you guys for your feedback during our EC regular meetings and all the fun and laughs we had out of work.

I would like to thank my colleagues from the FMT group. Jorge thanks for your feedback during group talks, your high expectations always help us improve ourselves and our work. Muchas gracias Hugo, I had the opportunity to work with you and it was instructive and enjoyable. Thanks to Torsten for sharing with me your expertise on ferroelectrics and for our interesting conversations on related topics. To Sebastian thanks for your advice and the fun discussions. To Constance, Nathalia, Monica, Carlos, and Robert thank you for the nice memories. Naveen, Christina, Sangitta, Alfredo, Longfei, and Poorani thank you guys for being amazing friends and for making the workplace a living and enjoyable area.

Many thanks to my friends for making my stay in Luxembourg so lovely: Niels (for kicking my arse at tennis and being an amazing friend), Marino (muchas gracias hermano, mi caballero de la salsa, gracias para todo.), Emma (my sister, thanks for being my eldest sister, putting me back on track sometimes when I needed and thanks for being there for me). Merci à toi Alicia, tu as été une très bonne amie durant ces quatre dernières années, merci pour tes conseils et ton soutien que je n’oublierai jamais.

To all my teachers and professors thank you. A special thank you goes to Dr. C. Pinettes and Dr. P. Frébourg - You triggered in me the envy of doing research. You believed in me

and motivated me. You have also been an inspiration and example for me. Thank you for always being there for me when I needed advice, thanks for your support, and thanks for showing me the way. This work is also yours.

Maman, Papa, vous avez réussi, nous avons réussi. Je vous dois tout ce que je suis et ce dont je suis devenu. Merci d'avoir toujours été présents, merci pour votre constant soutien, merci d'avoir toujours cru en moi. Merci d'avoir été rigoureux, patient et à l'écoute. Depuis mon départ de Douala à 15 ans pour les études supérieures, vous avez toujours été là. Vous étiez présents dans toutes les nouvelles adventures que j'ai entreprises. Je ne serai pas devenu l'homme que je suis sans vous. À Tristan et Killian, mes deux petits frangins, durant ces quatre dernières années vous avez été mes meilleurs amis. Merci de m'avoir supporté dans les bons et mauvais moments, merci d'avoir souvent joué le rôle de grand frère aussi, votre soutien inconditionnel a été d'un grand aide. Merci beaucoup !

La famille ce n'est pas toujours les liens de sang, tu m'as tenu la main depuis mon arrivée en Europe. Tu m'as ouvert tes portes, ton coeur et tu ne m'as jamais abandonné. Du fond de mon coeur, merci pour tout *Mamie* (Annie Granier). Cet accomplissement est aussi le tien. Merci ma poule !

Merci à vous, mes autres parents, Maman Thérèse et Papa Benoît, merci pour le soutien durant ces quatre années. Merci à toi Dr. C. Tayou, pour tes constants mots d'encouragements.

Une belle pensée à toi Joelle, tu m'as offert mon cartable quand je commençais cette adventure. Merci beaucoup pour tes conseils chère grande sœur merci pour ton soutien et d'avoir été présente pour moi. Je tiens à te remercier Maman Cecile, tes appels réguliers pour savoir comment je vais et comment mon projet de thèse évoluait. Cela me réconfortait et me motivait. Mon projet de thèse étant très éloigné de ton champ d'expertise, tu t'es toujours intéressée à ce que je faisais. Merci pour ton soutien chère maman.

Merci à mes tantes, Tata Flora Kiki, Tata Mamou, Tata Josée, Tata Sylvie, Tata Marceline. À toi tata Mimi, tu es ma deuxième maman, tu m'as élevé, éduqué, ta rigueur m'a rendu l'homme que je suis aujourd'hui. Je te remercie de tout mon coeur, merci pour ton soutien pendant ces quatre années. Ceci est un fruit de tous tes efforts. Merci ma mère.

Merci à mes tontons ! Tonton Hubert Nembot, Tonton Ghislain Kengne, Tonton Sylvain, Tonton Emmanuel Tefouet et Tonton Blaise. Une pensée pour toi tonton Philippe. Tu m'as pris avec toi, m'a fait connaitre l'industrie, m'a guidé dans mes premiers stages industriels et m'a donné la motivation de poursuivre des études. Tu as été un mentor et modèle pour moi. Merci beaucoup a toi tonton.

Mes dernières pensées sont pour toi ma chère et tendre épouse. Ces quatre années ont été marquées par ta présence, ce projet de thèse n'a jamais été seulement le mien, il était le nôtre. Merci pour ton soutien inconditionnel, merci d'avoir été toujours présente surtout dans mes moments de stress. Tu m'as constamment valorisé, réconforté, supporté: "tu es le meilleur", "on va réussir", "tu aimes trop stressé tout ira bien", "la thèse si ne peux pas nous dépasser" tu me disais. Nous avons réussi Madame *Docteur*. Merci JMB - Merci Olivia.

Abbreviations and Notations

ΔP_0	Polarization entropy jump
ΔS	Isothermal entropy change
ΔS_0	Transition entropy change
ΔS_t	Transition entropy change
ΔT_{adiab}	Adiabatic temperature change
ΔT_{span}	Temperature span
η	Scaled efficiency, second-law efficiency
η_{mat}	Materials efficiency
λ	Wavelength
μ_0	permeability of free space
Ω	B-site cation order, long-range order parameter
ρ	Density
σ	Uniaxial stress
ε	Strain, emissivity, dielectric constant
A	Area

C	Capacitance
C_p	Specific heat capacity
COP_{mat}	COP materials efficiency
D	Electrical displacement
DE	Displacement versus electric field
E	Electric field
F	Free energy
G	Gibbs energy
H	Magnetic field
I	Current
M	Magnetization
P	Polarization
p	pressure
PE	Polarization versus electric field
PT	Polarization versus temperature
Q	EC heat, isothermal heat
Q_0	Latent heat
R	Resistance
S	Entropy
T	Temperature
T_c	Curie temperature

T_s	Starting temperature
TE	Temperature-Electric field
TE	Temperature-Electric field
U	Internal energy, Voltage
W	work
W_e	Electrical work energy
AFE	Antiferroelectric
BC	Barocaloric
BCE	Barocaloric effect
CFC	Chlorofluorocarbons
COP	Coefficient Of Performance
DMA	Dynamic Mechanical Analysis
DSC	Differential Scanning Calorimeter, Differential Scanning Calorimetry
EC	Electroaloric
eC	elastocaloric
ECE	Electrocaloric effect
FE	Ferroelectric
FEM	Finite Element Method
HF	Heat Flow
HFC	Hydrochlorofluorocarbons
IPCC	Intergovernmental Panel on Climate Change

IR	Infrared
MC	Magnetocaloric
MCE	Magnetocaloric effect
MLC	Multilayer capacitor
NECE	Negative electrocaloric effect
SEM	Scanning Electron Microscope
XRD	X-Ray Diffraction

Abstract

Caloric materials are suggested as energy-efficient refrigerants for future cooling devices. They could replace the greenhouse gases used for decades in our air conditioners, fridges, and heat pumps. Among the four types of caloric materials (electro, baro, elasto, magneto caloric), electrocaloric materials are more promising as applying large electric fields is much simpler and cheaper than the other fields. The research in the last years has been focused on looking for electrocaloric materials with high thermal responses. However, the energy efficiency crucial for future replacement of the vapor compression technology has been overlooked. The intrinsic efficiency of electrocaloric has been barely studied. In the present dissertation, we will study the efficiency of EC materials defined as materials efficiency. It is the ratio of the reversible electrocaloric heat to the reversible electrical work required to drive this heat. In this work, we will study the materials efficiency of the benchmark lead scandium tantalate in different shapes (bulk ceramic and multilayer capacitors). A comparison to other caloric materials is presented in this dissertation. Our work gives more insights on the figure merit of materials efficiency to further improve the efficiency of our devices.

Contents

Affidavit ii
Acknowledgements iii
Abbreviations and Notations vii
Abstract xi
List of Figures xvi
List of Tables xxviii

1 Introduction **1**

2 Background **8**
- 2.1 A brief history of electrocaloric effect 8
- 2.2 Electrocaloric materials 9
- 2.3 Electrocaloric devices 12
- 2.4 Thermodynamic of electrocaloric effect 14
- 2.5 Materials Efficiency 19

3 Experimental Methods **26**
- 3.1 EC setup 27
  - 3.1.1 InfraRed (IR) imaging 30
  - 3.1.2 Electrical Work extraction 34
- 3.2 Calorimetric measurements 35
  - 3.2.1 Differential Scanning Calorimetry 36
  - 3.2.2 Our DSC setup 41

3.2.3 Latent heat and entropy change calculation 44
3.2.4 Specific heat capacity measurements 45
3.2.5 DSC under electric field 50
3.3 X-Ray Diffraction (XRD) 54
3.4 Scanning Electron Microscopy (SEM) 55
3.5 Electrical characterization 57
3.5.1 Dielectric permittivity 57
3.5.2 Polarization – Electric field 59

4 Giant electrocaloric efficiency of highly ordered lead scandium tantalate 62
4.1 Motivation 62
4.2 Lead Scandium Tantalate - PST 64
4.3 Results 68
4.3.1 Experimental details 68
4.3.2 Characterization of PST bulk ceramic 72
4.3.3 Electrocaloric effect of PST bulk ceramic 76
4.3.4 Electrical work 85
4.3.5 Materials efficiency of PST bulk ceramic 87
4.3.6 Materials Efficiency of Gadolinium 88
4.3.7 Comparison of materials efficiency of PST and Gd 90
4.4 Discussion 92
4.5 Conclusion 100

5 Materials efficiency of lead scandium tantalate multilayer capacitors 101
5.1 Motivation 101
5.2 ECE in Multi-Layer Capacitors 103
5.3 Results 105
5.3.1 Experimental details 105
5.3.2 Scanning Electron Microscopy (SEM) 107
5.3.3 Dedicated setup for work extraction 107

5.3.4 Characterization of PST MLC 108
5.3.5 Materials efficiency of PST MLC 112
5.4 Discussion: Scale law on materials efficiency of PST 117
5.5 Conclusion 120

6 Quantifying the electrocaloric effect in multilayer capacitors using Clausius-Clapeyron equation 121
6.1 Motivation 121
6.2 Results 126
6.2.1 Experimental details 126
6.2.2 Case study: PST MLC 127
6.3 Discussion 132
6.4 Conclusion 134

7 Explaining the negative electrocaloric effect in the antiferroelectric lead zirconate 135
7.1 Motivation 135
7.2 Antiferroelectrics 137
7.2.1 Background 137
7.2.2 Negative electrocaloric effect in AFEs 139
7.3 Results 143
7.3.1 Experimental details 143
7.3.2 Zero-field thermal properties of $PbZrO_3$ 144
7.3.3 Electrocaloric effect in $PbZrO_3$ ceramic 146
7.3.4 Isofield measurements of $PbZrO_3$ 147
7.4 Discussion 149
7.5 Conclusion 152

8 Conclusions and future perspectives 153
PhD Output 155

Bibliography **160**

List of Figures

1.1 **Electrocaloric cooling cycle.** S-T diagram explaining the EC cooling cycle (ABCD). S(E_0) is the entropy at zero- electric field and S(E_1) entropy curve at a non-zero electric field ($E_1 > E_0$). A to B is the polarization of the EC material by applying a voltage (V). This leads to an increase of the materials' temperature from T_s to T_B. ΔT_{adiab} is the difference between T_h and T_B. B-C, the voltage is kept constant, the material relaxes and its temperature decreases from T_B to T_s. C-D, the depolarization of the material by removal of the voltage. It induces cooling of the material from T_s to T_D. Finally D-A, the field is kept off and the material's temperature goes back to its initial temperature T_s, closing the cycle. 4

2.1 **EC publications from 1960 to date.** These data were obtained from Scopus Bibiliography database. An increase in publications is observed since 2006 due to the publication of [28]. 10

2.2 **EC coolers from 1989 to 2021.** This plot was made from the data collected in the 2021 review article [67] on EC coolers. 13

2.3 **Phase order transitions.** Order parameter versus temperature for first (red curve) and second order (green curve) transition materials. 17

2.4 **Temperature-Electric field diagram.** This figure describes the TE of the phase transition of a first-order transition materials from lower temperature phase B to higher temperature phase A diagram B with infinitesimal change in temperature T or electric field E from state 1 to state 2. The full black line is the coexistence line where both phases have the same Gibbs energy G. This figure was adapted from [80]. 19

2.5 **Materials Efficiency of caloric materials.** Comparison of the materials efficiency η_{mat} of different caloric materials for similar heat $|Q|$. The blue bubble are MC materials driven mechanically with permanent magnet at 2 Tesla. The two dark blue bubbles are the MC materials driven electrically with solenoid at 2 Tesla and 5 Tesla. The dark green bubbles refers to the EC materials driven electrically and the light green bubbles are the EC materials using energy recovery. Finally, the grey and red bubbles are respectively the BC and eC materials. This figure was adapted from [35]. 22

2.6 **Materials efficiency in elastoCaloric materials.** This figure shows the Stress-Strain loop of an eC material. Q is the heat absorbed or released. The red area corresponds to the non-recoverable work. This red area is used for the calculation of COP$_{mat}$. However, the work W (red area + green area) is the work considered for the calculation of η_{mat}. 25

3.1 **EC Setup.** This figure describes the EC setup utilized to collect ΔT_{adiab} and W_e. The IR camera, temperature stage, and power supply were used respectively to record temperature changes in the EC material, control the starting temperature T_s of the EC material, and apply/remove an electric field in the EC material. The three devices are connected (dash lines) to a controller for fast data acquisition. Liquid nitrogen was used to reach temperatures down to 253 K. The region of interest (ROI) of the sample visible by the IR camera was black painted to increase its emissivity to 1. 28

3.2 **Example of an EC cycle. a** Temperature change of PST bulk ceramic at 26 ℃ under the application/removal of 22 kV cm^{-1}. This fields corresponds to 1100 V in 0.5 mm thick sample. The black curve is the temperature change and the red curve is the voltage applied/removed to get this temperature change. The blue numbers indicate the different steps of an EC cycle. **b** Example of the charge of the PST capacitor (step 2 in Figure 3.2a) as function of time. It was collected simultaneously with the adiabatic temperature change. The black curve describes the charge to a given maximum voltage and the red curve, the change in current as a function of time. 30

3.3 **Radiations received by an IR Camera.** The IR camera received radiations from the body being observed (W_{obj}), the atmosphere (W_{atmos}) and from the environment (W_{envir}). 33

3.4 **Heat flow rate $\frac{dQ}{dt}$ measured.** This figure describes the heat flow rate of a ceramic sample measured as a function of temperature T. The sample presents a first-order transition described by the peak observed in the DSC measurement. The measurement was taken at a heating rate of 10 K min^{-1} using our DSC setup. 37

3.5 **Different types of Differential Scanning Calorimeters (DSCs).** S and R represent respectively the sample and the reference sample. **a** Power-compensated DSC. **b** Heat-flux DSC. This figure was adapted from [110]. 37

3.6 **Sketch of a calorimeter.** S and R represent respectively the sample and the reference sample. R$_s$ is the resistance between the sample and calorimeter and R$_r$ the resistance between the reference and the calorimeter. 39

3.7 **Sketch of our DSC setup.** 42

3.8 **Our DSC3's furnace.** This figure describes the furnace of our DSC3 from Mettler Toledo. It contains a ceramic DSC sensor FRS5+. 56 thermocouples are embedded on each side (sample side and reference side) of the DSC sensor. 43

3.9 **Latent heat measurement.** An example of heat flow measurement $\frac{dQ}{dT}$ of a material that exhibits a first-order transition material described by sharp peaks on heating (red curve) and cooling (blue curve). A baseline spline was removed from the raw data of $\frac{dQ}{dT}$. The area under the peaks on cooling and heating is respectively the energy released (orange area) and absorbed (yellow area) by the material. T_{h1} and T_{h2} are the temperature chosen respectively before and after the heating peak.T_{c1} and T_{c2} bounds the cooling peak and are chosen after and before the cooling peak. 46
3.10 **Three-step procedure for specific heat capacity.** An example of three-step procedure carried out to determine the specific heat capacity of a sample. Here the measurements were done a first-order transition material. Heat flow measurements of blank curve (**a**), sample (red curve in **b**) and calibration sample (black curve in **b**) as a function of time and temperature. **c** Temperature program used to the three measurements. 48
3.11 **DSC under electric field setup.** 51
3.12 ***S*-*T* diagram.** 53
3.13 **Isothermal heat flow measurements.** 54
3.14 **X-Ray Diffraction mechanism.** d is the spacing between the diffracting planes and θ represents the incident angle. This figure was adapted from [117]. 55
3.15 **Scanning Electron Microscope a** Basic mechanism of a SEM. This image was adapted from [122]. **b** Example of a SEM image showing the structure of a multilayer capacitor of lead scandium tantalate. From this image the different dimensions (length, width, thickness) of the sample were calculated. 56
3.16 **Dielectric constant mechanism a** RC parallel circuit **b** Complex permittivity vector in a complex plane. ε' is the real part, ε'' is the imaginary part and δ is the angle between the sum vector and the real part ε'. The tan δ represents the dielectric losses. 57
3.17 **Sawyer-Tower circuit** 59

4.1 **Perovskite structure of PbSc$_{1/2}$Ta$_{1/2}$O$_3$. a** A simple cubic perovskite unit cell. **b** Perovskite crystallographic structure of ordered PbSc$_{1/2}$Ta$_{1/2}$O$_3$. This image was adapted from [137]. Here, the B-cation is share between two atoms (Sc and Ta) thereby doubling the ABO$_3$ unit cell. Sc and Ta alternate at the corners of the unit cell. 64

4.2 **Structure of bulk PST for IR Camera.** The bulk PST is 0.5 mm thick. The area of the top electrodes seen by the IR Camera is 0.480 cm^2 70

4.3 **X-Rays Diffraction of bulk PST powerdered.** 72

4.4 **Dielectric measurements of bulk PST.** Blue and red curves denote respectively cooling and heating. The top plot shows the relative permittivity ϵ and the lower plot the loss tangent tan(δ), both as a function of temperature T. . . 73

4.5 **Polarisation versus electric field loops of bulk PST.** PE loops of bulk PST before, around, and after T_0 = 300 K. 73

4.6 **Zero field calorimetric measurements of bulk PST.** Blue and red curves denote respectively cooling and heating in the three plots. **a** Heat flow $\frac{dQ}{dT}$ measurement as function of temperature T. **b** Zero-field specific heat C_p (background value) measurement associated with latent heat Q_0 (integral under the first-order phase transition peak at T_0 = 300 K on heating and 296 K on cooling). **c** $S'(T) = S(T) - S(280\,K)$ represents the entropy $S(T)$ referenced to the entropy at 280 K far from T_0 with $S'(280\,K) = 0$. 75

4.7 **Isofield measurements of bulk PST. a** Heat flow measurement as a function of temperature T at constant values of electric fields E on heating and cooling. As the sample was wired with electrodes, we observed a slight difference in the peak at 0 kV cm^{-1} compare to the heat flow measured on pure PST without electrodes and wires (figure 4.6). **b** Transition temperature on heating $T_{0,h}$ and on cooling $T_{0,c}$ as function of electric field E. **c** Latent heat Q_0 (integral under the heat flow peak) as a function of electric field E on heating and cooling. **d** Entropy change at the transition $|\Delta S_0|$ as function of electric field on heating and on cooling. 77

4.8 **Isothermal entropy change of bulk PST. a** Heat capacity measurements at different electric fields. **b** Entropy curves referenced to the entropy at 280 K, i.e S'(280 K) = 0 K as function of temperature T at different electric fields E. **c** Isothermal entropy change ΔS obtained from isofield and heat capacity measurements (see Chapter 3) at different electric fields, on applying (E_{ON}) and removing (E_{OFF}) field. **d** Peak of isothermal entropy change $|\Delta S_{peak}|$ as function of electric field E, on cooling (blue curves) and heating (red curves). 79

4.9 **Adiabatic conditions in bulk PST.** ΔT_{adiab} versus applied current I. The measurements were done on PST sample 1 bulk at 22 kV cm^{-1}. 80

4.10 **IR images of bulk PST sample 1 during a standard EC characterization sequence.** In step 1 the material is at T_s of 299 K, in step 2, 1100 V are applied and the materials temperature increases. Subsequently, in the two following images the material thermalizes and goes back to T_s (no Joule heating). In step 4, the materials temperature decreases as voltage is removed. Finally, in Step 5 the material thermalizes back to T_s 80

4.11 **Reproducibility of EC measurements** This figure shows the ΔT_{adiab} measured after of the first, second and third cycle in function of starting temperature T_s at 11 kV cm^{-1} (**a**) 14 kV cm^{-1} (**b**) 18 kV cm^{-1} (**c**) 22 kV cm^{-1} (**d**). In the legend, 1^{st+}, 2^{nd+},3^{rd+} are the ΔT_{adiab} on-field of respectively the first, second and third cycle and, 1^{st-}, 2^{nd-},3^{rd-} are the ΔT_{adiab} off-field of respectively the first, second and third cycle. 81

4.12 **Reversible ECE. a** Direct measurement of adiabatic temperature change ΔT_{adiab} and EC heat Q upon application (red curves) and removal (blue curves) of 11, 14, 18 and 22 kV cm^{-1}. ΔT_{adiab} and Q are shown as a function of T_s. **b** Temperature range (full width at 80% of the maximum ΔT_{adiab}) as a function of electric field. **c** ΔT_{adiab} as a function of time at the electric field of 40 kV cm^{-1} and T_s = 300 K. **d** Reversibility of EC measurements. Here we show ΔT_{adiab} of PST bulk at 22 kV cm^{-1} versus T_s. Red curves and dark blue curves are respectively ΔT_{adiab} due to the ECE when the field is on and off. These two curves are obtained from experimental measurements with an IR camera. The cyan dash curve is the ΔT_{adiab} due to ECE when the field is off and derived from the equation (4.3). $\Delta T_{adiab,off,exp}$ and $\Delta T_{adiab,off,exp,derived}$ coincide well and thereby validate the reversibility of our EC measurements. . 83

4.13 **ECE in PST bulk ceramics.** The ΔT_{adiab} values of bulk ceramics PST collected from literature [ref] are compared to our PST samples (PST sample 1, Ω = 0.98 and PST sample 2, Ω =0.89). The number displayed in bold close to each symbol is the field applied in kV cm^{-1} and in brackets are the references. Our PST sample 1 shows the highest ECE measured. The results on PST sample 2 are present in Annex. 84

4.14 **Isothermal heat** Here we justify equation (4.2) as a good approximation for EC heat Q. **a** Isothermal application of electric field (14 kV cm^{-1}) during 200 s. The integral under the peak corresponds to the isothermal heat exchanged $Q = -T_s \Delta S_{isothermal}$. **b** Comparison of $C_p\ \Delta T_{adiab}$ to $-T_s \Delta S_{isothermal}$. ΔT_{adiab} was collected with IR camera (Figure 4.12a). There is a good match between $C_p\ \Delta T_{adiab}$ and $-T_s \Delta S_{isothermal}$. 85

4.15 **Electrical work of bulk PST. a.** Example of charge in PST capacitor at a maximum voltage of 1100 V (22 kV cm^{-1}) as a function of time t at selected T_s. **b.** Electrical work W_e needed to charge a PST capacitor as a function of T_s at different electric fields E. W_e is obtained from the data of voltage across PST at constant current. 86

4.16 **Comparison of direct and indirect calculation of electrical work W_e. a** P(E) loops of bulk PST capacitor at different T_s, from 288 K to 313 K. The blue shaded area is the electrical work ($W_e = \int EdD$) per unit volume to charge the PST capacitor at 299 K up to 18 kV cm^{-1}. This area takes into account the FE hysteresis losses. 87

4.17 **Materials Efficiency of bulk PST.** η_{mat} of bulk PST versus T_s at different electric fields E. The dash line shows the temperature at which PST exchanges the most heat Q. η_{mat} is calculated from data of Q in Fig. 4.12a and W_e in Fig. 4.15b. 88

4.18 **Materials Efficiency of Gd.** Heat Capacity (**a**), ΔT_{adiab} (**b**), and magnetisation M (**d**) of Gd taken from Bjork et al. **c.** Heat exchanged Q of Gd. **e** Mechanical work - W_m. **f** $\eta_{mat} = |Q/W_m|$ of Gd calculated from (**c**) and (**e**). . 89

4.19 **Comparison Materials Efficiency of PST to Gd.** The bubble map represents η_{mat} of PST (green bubbles) and Gd (blue bubbles) as a function of maximum caloric heat Q per cm^3. The values of Q are taken at the material transition temperature. The bubbles' colour yields the field applied. The bubbles' diameter shows the temperature range of the material at a given field. 91

4.20 **Comparison Materials Efficiency caloric materials.** This energy efficiency map of caloric materials as a function of the heat Q per volume is adapted from Crossley et al. [ref]. The caloric materials include magnetocaloric (MC) under permanent magnet of 2 T, MC under solenoid, elastocaloric (eC) materials, barocaloric (BC), EC (electrically driven) and EC materials using energy recovery. In this map we added the materials efficiency of PST bulk. PST is shown here as being as efficient as the best caloric materials which are magnetocaloric (MC) under permanent magnet 2 T, barocaloric (BC) and EC materials using energy recovery. 93

4.21 **Potential use of bulk PST in a regenerator.** **a** Regenerator A operating between 300-300.5 K, on a temperature window of 0.5 K. **b** Regenerator B operating on a temperature window of 1.5 K. **c** Adiabatic temperature change of PST bulk at 11 kV cm^{-1}. The orange and black lines represent respectively the regenerators A and B. **d** the table shows for each regenerator, its temperature window, the heat exchanged and the corresponding measured materials efficiency. 95

4.22 **Potential use of bulk PST in a regenerator at higher Q.** The heat exchanged can be increase by increasing the electric field but this will decrease the materials efficiency as shown in **d**. **a** regenerator C at the electric field of 14 kV cm^{-1} **b** regenerator D at 18 kV cm^{-1} **c** regenerator E at field of 22 kV cm^{-1} **d** for each regenerator, the heat exchanged, materials efficiency and adiabatic temperature change. 96

4.23 **Regenerator Modelling** The time evolution of the hot side (red) and cold side (blue) of an active regenerator based on the EC effect from Supplementary Fig. 20c at starting temperatures **a** 297 K, **b** 299 K, **c** 301 K and **d** 303 K. **e** shows the dimensions of the regenerator simulated. This simulation was done by A. Torello. 97

5.1 **Geometry of a Multi-Layer Capacitor (MLC)** The red rectangle represents the active area of the MLC structure where the layers of interdigitated electrodes overlap. The terminals are the outer electrodes. 103

5.2 **Structure of a PST MLC** **a** Geometry of a MLC. The red rectangle is the active area where the electrodes overlap. **b** SEM image of a PST MLC. The white lines are the platinum (Pt) electrodes in between layers of PST. **c** Electronic microscope image of a PST MLC. 108

5.3 **SEM image of the left edge (a), centre (b) and right edge of PST MLC (c).** We measured an average thickness of 0.42 mm. 109

5.4 **The 11 layers of PST and 10 layers of platinum electrodes of a PST MLC.** 109

5.5 **XRD of powdered PST MLCs** X-ray diffraction measurements were carried out on crushed PST MLC. From the intensities of the (111) and (200) peaks (inset image), we calculated the B-site cation ordering Ω of PST MLC using the equation (4.1). 110

5.6 **Dielectric and thermal measurements in PST MLC** The blue and red denote respectively the cooling and heating. **a** Dielectric constant (top panel) and losses (bottom panel) as function of temperature *T*. **b** Heat flow measurements at 0 kV cm^{-1}. **c** Zero-field heat capacity measurements. **d** Entropy $S'(T)$ = $S(T)$ - S(263 K) at 0 kV cm^{-1} referenced to the entropy at 263 K. These entropy curves were constructed as explained in Chapter 3. 111

5.7 **Adiabatic conditions in PST MLC** ΔT_{adiab} versus applied current I. These measurements were done at room temperature on a PST MLC at 118 kV cm^{-1}. 113

5.8 **ECE in PST MLC** Adiabatic temperature change ΔT_{adiab} (left y-axis) and exchangeable EC heat Q (right y-axis) as a function of starting temperature T_s at different electric fields E. The orange to red curves corresponds to the temperature change obtained upon application of an electric field. The light to dark blue curves are data of temperature change which result from the removal of an electric field. Q is calculated using the formula in equation (4.2). 114

5.9 **Reproducibility of ECE in PST MLC a** ECE of PST MLC at 198 kV cm^{-1} and T_s = 20.5 ℃ = 293.65 K after three successive runs. From these data collected at different T_s we draw Figure 5.9b. **b** ΔT_{adiab} obtained from first, second and third cycles upon application (positive values) and removal (negative values) of 198 kV cm^{-1}. ΔT_{adiab} under and off field doesn't change after three EC cycle. 115

5.10 **Supercritical region in PST MLC** This figure describes the peak in ΔT_{adiab} as a function of electric field E below (283 K), at (293 K) and beyond (303, 313, 323 K) the transition temperature. The red area represents the supercritical regime. 116

5.11 **Electrical work of PST MLC. a** Voltage versus time at different starting temperatures Ts. Around the transition temperature (290 K), we observe a difference in slopes in the $U(t)$ curves, showing the change of transition from FE-PE in PST MLC. **b** electrical work as a function of the electric field. . . . 116

5.12 **Materials efficiency of PST MLC** 117

5.13 **Scale law on material efficiency** The bubble chart compares the materials efficiency of PST MLC, PST bulk and Gd for the same EC heat exchanged by volume Q. The data of η_{mat} of PST MLC (five red bubbles) was included into Figure 4.17 which shows η_{mat} of PST bulk ceramic (green bubbles, the smallest one indicated with an arrow) and Gd (three blue bubbles). The bubble area describes the temperature range defined as the full width at 80% of the maximum ΔT_{adiab}. Each colour represents the field applied (electric field E in PST and magnetic field $\mu_0 H$ in Gd) 118

6.1 **Polarization P versus temperature T of first-order transition material.** . . 125

6.2 **Isofield measurements on PST MLC.** Heat flow measurements at different constant electric fields (0, 3.9, 5.5, 10, 13, 26, 39 kV cm^{-1}) against temperature T. The red and blue data were respectively collected on heating and cooling at 5 K min^{-1}. In order to apply an electric field, these measurements were carried out on an entire PST MLC of $\approx$ 300 mg. The y-axis values are not displayed as they are quantitatively incorrect due to the weight of PST MLC too big for DSC measurements. The position of the peaks in temperature are nonetheless correct. 128

6.3 **Inactive peak of PST MLC under electric field.** Zoom in of the inactive peak of PST MLC under different electric fields on cooling (**a**) and on heating (**b**). 129

6.4 **T=f(E) diagram of PST MLC** Temperature versus electric field of PST MLC collected from isofield measurements in Figure 6.2. 130

6.5 **PE loops of PST MLC at different temperatures a** PE loops of PST MLC collected at different temperatures from 266 K to 323 K at the maximum electric field applied of 39 kV cm^{-1}. **b** Remanent polarization as a function of temperature 131

6.6 **Zero-field calorimetric measurement in PST MLC.** Heat flow measurements on 18 mg of PST MLC cut at its centre. The red and blue curves denotes respectively the heating and cooling. 132

7.1 **Ferroelectrics. a** Hysteresis loop of a FE material. P_s is the saturation polarization, E_c the coercive field (value of the electric field at zero polarization), and P_r the remanent (spontaneous) polarization. **b** FE dipoles in domains in the absence ($E = 0$) and presence ($E \neq 0$) of an electric field. 137

7.2 **Antiferroelectrics. a** Double hysteresis loop of an AFE material **b** AFE dipoles in domains in abscence (E = 0) and presence of an electric field (E $\neq$ 0)138

7.3 **Lead Zirconate - PbZrO$_3$.** These images were adapted from [185]. **a** Atomic arrangement showing antiparallel dipoles of PbZrO$_3$ in the AFE phase. The arrows show the shift of the lead (Pb) ions. **b** Dielectric constant versus temperature of PbZrO$_3$ and its anomaly at the AFE-PE transition. **c** Double hysteresis loop of PbZrO$_3$ at 501 K under applied field of 20 kV cm^{-1}. 139

7.4 **Energy storage in dielectric materials. a** linear dielectric **b** relaxor ferroelectric **c** ferroelectric **d** antiferroelectric. The shaded area in orange represents the energy recovered W$_{energy\ recovered}$ by each dielectric material. W$_{energy\ recovered}$ is larger in AFE compared to its counters dielectrics.The energy loss corresponds to half of the area shaded in blue. 140

7.5 **Negative electrocaloric effect** Temperature of a material (y-left axis) as a function of time. The y-right axis in red shows the voltage applied. Here, the material's temperature decreases when the voltage (electric field * thickness) is on and increases when the voltage is off. 141

7.6 **Dipole canting illustration.** This figure was adapted from Liu et al. [75]. It illustrates the NECE of an AFE material based on the dipole canting model. The temperature change ΔT_{adiab} as a function of temperature *T* at increasing electric fields *E*. T_c is the transition temperature. 142

7.7 **Zero-field measurements in PbZrO$_3$** This figure shows the calorimetric measurements as a function of temperature *T*, done on bulk ceramic PbZrO$_3$ on heating (red curves) and cooling (blue curves) at 0 kV cm^{-1}. **a** Heat flow d*Q*/d*T*. **b** Specific heat C_p. **c** *S'*(*T*) the entropy referenced at 482 K far from the transition. *S'*(*T*) = *S*(*T*) -*S*(482 K) with *S*(482 K) = 0. ΔS_0 is the entropy change at the transition driven thermally. 145

7.8 **Adiabatic temperature change of PbZrO$_3$.** Direct measurements of ΔT_{adiab} as a function of different starting temperatures T_s under the application of different electric fields E_{ON} (10, 16, 21, 24, 28, 35 and 42 kV cm^{-1}). These measurements were done by P. Vales-Castro. 147

7.9 **Isofield measurements in PbZrO$_3$ ceramic** Heat flow measurements of bulk ceramic PbZrO$_3$ at different constant electric fields (0, 2.5, 5 and 10 kV cm^{-1}). These measurements were carried out on cooling (**a**) and heating (**b**) using a customized DSC (see experimental details). 148

7.10 **Temperature-Electric field diagram of PbZrO$_3$ ceramic** This *T*-*E* diagram was constructed from DSC measurements on PbZrO$_3$ ceramic. The application of an electric field in the AFE and PE phase, leads respectively to a NECE to the FE phase, and a positive ECE to the FE. 149

7.11 **Entropy curves of PbZrO$_3$ ceramic.** *S'*(*T*) the entropy referenced at 482 K as a function of temperature *T* at 0 kV cm^{-1} (**c**), 2. kV cm^{-1} (**b**), 10 kV cm^{-1} (**a**). T_c is the transition temperature which is shifted towards high temperature with increasing electric field 150

List of Tables

1.1 **Caloric materials** This table shows the different caloric materials with their corresponding field, conjugated order parameter, phase transitions from low temperature (LT) phase to high temperature (HT) phase. Fluidic refrigerants mostly used in our cooling devices nowadays are added at the end of this table for comparison. 3

2.1 **Isothermal heat and Work of caloric materials.** The isothermal heat $|Q|$ is obtained from the Maxwell relations (equation 2.10). W_m and W_e are respectively the mechanical and electrical work. B is the magnetic flux density. E, H, σ and p are respectively the electric field, magnetic field, uniaxial stress and pressure with their respective order parameter P(polarization), M(magnetization), ε(strain) and V(volume). 23

4.1 **Adiabatic temperature change of PST bulk ceramics** This table shows the influence of the B-site ordering on the adiabatic temperature change and temperature range of PST bulk ceramics. ΔT_{adiab} were measured directly and the temperature range is defined as the full width at 80% of the maximum ΔT_{adiab}. Data of our PST sample 2 are presented in Appendix. Due to the high B-site ordering of our material (PST sample 1) we obtained the highest ΔT_{adiab} directly measured. 98

4.2 **Comparison of materials efficiency of PST and Gd** In this table we compare the energy efficiency of PST bulk ceramic sample 1 with Gd for the same EC heat exchanged Q (in bold underline and italic). 99

Chapter 1

Introduction

Around 20% [1] of the electricity generated is used for cooling our buildings, beverages, food, vaccines, and medicines [2–5]. Created more than twenty decades ago, the vapor compression refrigeration cycle remains to date the most used cooling technology in devices such as fridges, air conditioners, and heat pumps. However, this technology is reaching its theoretical efficiency limit (around 40%) [6–8]. Moreover, it utilizes harmful gases: hydrochlorofluorocarbons (HFC) and chlorofluorocarbons (CFC) as refrigerants. These gases have a global warming potential that is a thousand times greater than carbon dioxide and account for 7% of the greenhouse gases emitted [9–11] into the atmosphere. As stated in the latest (sixth) report from the Intergovernmental Panel on Climate Change (IPCC) [12], the temperatures around the world are about to reach +1.5 ℃ by 2030. This is 10 years earlier than the IPCC's former estimations. Hence, the increasing demand for cooling (triple by 2050) and the increase of HFCs emissions (double by 2030) [13]. Consequently, a highly energy-efficient and environmentally friendly cooling alternative is required to replace the traditional vapor compression.

In that regard, different governmental procedures have aimed to reduce these issues. The 1987 Montreal Protocol [14] and the Kigali agreement planned to reduce the world's temperature by banning CFC production and reducing by 80% the HFCs by 2047 [13]. Moreover, companies are setting goals to phase out HFCs and CFCs and rather use alternatives such as CO_2 or natural refrigerants with a zero global warming potential. Scientists have suggested solid-state caloric materials as refrigerants to build future cooling devices. Caloric cooling based on caloric materials has the potential to replace the vapor compression technology [6, 15–18]. It is energy efficient (around 60%), noiseless, compact, and environmentally friendly [6].

Caloric materials are ferroic materials that exhibit reversible thermal responses under the application/removal of an external stimulus. These caloric materials are named according to the stimulus applied/removed. We distinguish: **electro**caloric (electric field), **magneto**caloric (magnetic field) and **mechano**caloric (stress field) materials. Mechanocaloric materials are divided in **elasto**caloric (uniaxial stress) and **baro**caloric (isotropic stress i.e hydrostatic pressure) materials [6, 17]. It is worth it mentioning that a single material could exhibit several caloric effects under sequential or simultaneous application/removal of external fields. This is called multicaloric effect [19–22]. Ferroic materials are interesting because at a specific temperature (transition temperature) their symmetry is being altered. They present a transition from a high-temperature phase (disordered state) to a low-temperature phase (ordered state). Moreover, in the vicinity of the transition temperature, this transition can be driven by an external field, making them interesting for caloric cooling applications. The application/removal of an external field induces large changes in the material's order parameter and therefore, a transition from a high temperature (large order parameter) with no domains (ordered entities) to a low temperature (small or zero-order parameter) forming domains that can be aligned or switched with an external field. In Table 1.1, we present the different caloric materials with their corresponding field, conjugate order parameter, and phase transitions.

Table 1.1: **Caloric materials** This table shows the different caloric materials with their corresponding field, conjugated order parameter, phase transitions from low temperature (LT) phase to high temperature (HT) phase. Fluidic refrigerants mostly used in our cooling devices nowadays are added at the end of this table for comparison.

Calorics	**Field applied/removed**	**Order Parameter**	**LT phase**	**HT phase**
Magnetocalorics	Magnetic field, H	Magnetization, M	Ferromagnetic Antiferromagnetic	Paramagnetic
Electrocalorics	Electric field, E	Polarization, P	Ferroelectric Antiferroelectric	Paraelectric
Elastocalorics	Uniaxial stress, σ	Strain, ε	Martensitic	Austenitic
Barocalorics	Hydrostatic pressure, p	Volume, V	Plastic crystal	Crystal
Fluidic refrigerants	Pressure, p	Density, ρ	Liquid	Gas

Depending on the way the field is being applied one can measure differently the caloric effect in caloric materials. The thermal responses observed in caloric materials are quantified by the three parameters below:

- ΔT_{adiab}: the adiabatic temperature change
- ΔS: the isothermal entropy change
- Q: the isothermal heat

On one hand, if the field is being applied/removed adiabatically i.e in such a way that the application/removal time is smaller than the relaxation time of the material, ΔT_{adiab} is being observed. On the other hand, if the field is isothermally applied, ΔS and Q are measured. In case of conventional caloric effect, $\Delta T_{adiab} > 0$, $\Delta S < 0$ and $Q < 0$ with the increasing field. In an inverse caloric effect, $\Delta T_{adiab} < 0$, $\Delta S > 0$ and $Q > 0$ with the increasing field.

Figure 1.1 describes the working principle of an electrocaloric (EC) cooling device (ABCD in Figure 1.1). Depending on the field applied the same cycle is used for magnetocaloric (MC), elastocaloric (eC), or barocaloric (BC) cooling. The EC cycle is divided into the four following steps.

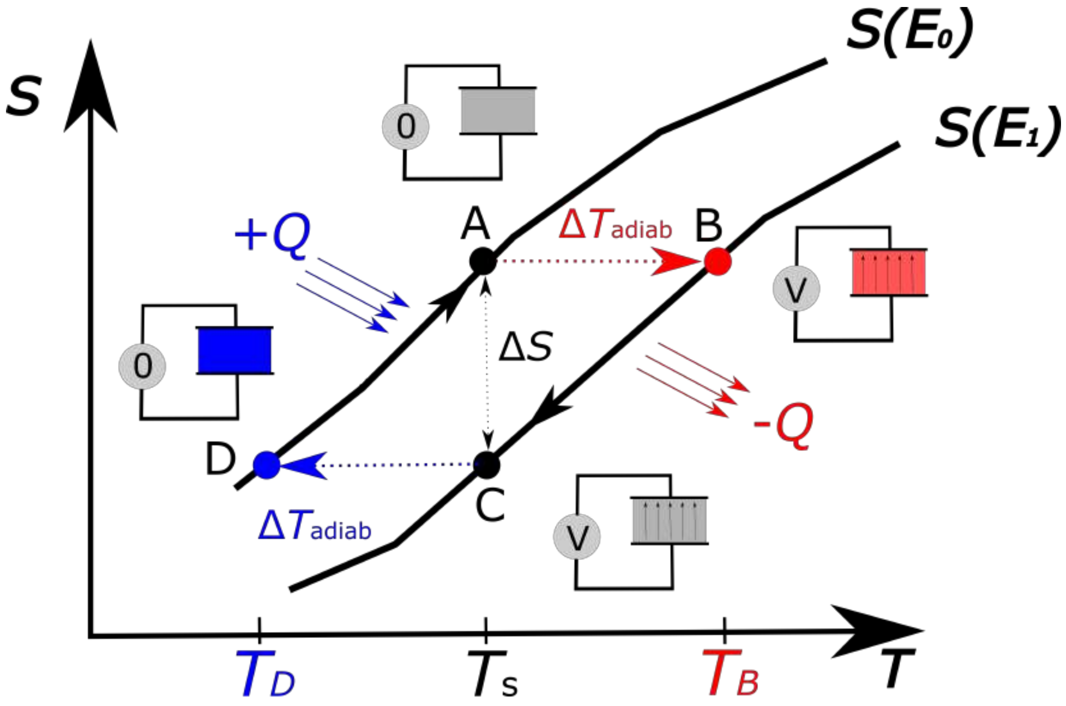

Figure 1.1: **Electrocaloric cooling cycle.** S-T diagram explaining the EC cooling cycle (ABCD). S(E_0) is the entropy at zero- electric field and S(E_1) entropy curve at a non-zero electric field ($E_1 > E_0$). A to B is the polarization of the EC material by applying a voltage (V). This leads to an increase of the materials' temperature from T_s to T_B. ΔT_{adiab} is the difference between T_h and T_B. B-C, the voltage is kept constant, the material relaxes and its temperature decreases from T_B to T_s. C-D, the depolarization of the material by removal of the voltage. It induces cooling of the material from T_s to T_D. Finally D-A, the field is kept off and the material's temperature goes back to its initial temperature T_s, closing the cycle.

- **First step** the material is at a given starting temperature T_s in the vicinity of the materials transition temperature (point A in Figure 1.1). Under the adiabatic application of an external electric field (equal to the voltage divided by the material's thickness) the material undergoes changes in polarization. This induces a phase transition in the material therefore changes in dipolar entropy (orientation of dipoles) by promoting the low-temperature phase and leads to an increase in the material's temperature to T_B (point B in Figure 1.1). The difference between T_B and T_s is ΔT_{adiab}.
- **Second step** From B to C the electric field is kept constant. Due to the electrocaloric effect (ECE) , heat (Q) is released to an external reservoir therefore, the material goes

back to its initial T_s (point C in Figure 1.1).

- **Third step** Under the adiabatic depolarization (EC) of the material, its temperature decreases from T_s to T_D due to changes in dipolar entropy.
- **Fourth step** Finally, from D to A, the material goes back to its initial T_s by absorbing heat (Q) from the cold reservoir and closing the EC cooling cycle.

Discovered respectively for the first time in 1881 and 1859, the MC effect (MCE) and the eC effect (eCE) have been more studied than their counterparts BC effect (BCE) and ECE [6, 17, 23]. However, MC and eC materials present intrinsic drawbacks. MC materials require large magnetic fields that are expensive and difficult to generate. Besides, the MC materials are rare, expensive, and can be toxic therefore, increasing the cost of a MC device. eC materials suffer from fatigue and plastic deformation. Moreover, the stress applied requires costly and complex apparatus. EC materials are more promising as applying large electric fields is much simpler and cheaper than magnetic and stress fields. Lastly, when dealing with electrical charges, it is easy to use electronic systems to recover the charges and thereby enhance efficiency [24]. In this dissertation, we will focus on the efficiency of EC materials.

90% of literature has been focusing on looking for the EC materials with large EC performance i.e large ΔT_{adiab} or ΔS, or Q [6, 17, 25–27]. Since the discovery of “Giant” ECE in PbZr$_{0.95}$T$_3$ thin films [28], a vast number of publications have reported on the ECE in EC materials in different shapes (films, bulk, and multilayer capacitors) as the shape of the materials influences the ECE. Among these EC materials, lead scandium tantalate comes out as the EC benchmark material [29–31]. The discovery of reversible large EC performant materials has led to a few EC prototypes with one of them displaying the highest temperature span of 13 K [32] (difference between the cold and hot side of a device). However, the intrinsic efficiency [33] of the EC modules which plays a role in the performance of EC cooling devices has been overlooked. This intrinsic efficiency also called materials efficiency and symbolized by η_{mat}, is the ratio of the isothermal heat Q exchanged by the material with its surroundings to the electrical work W_e required to drive this heat [34–36]. In other words, W_e the energy used to charge or to discharge an EC material is barely reported. The dimensionless figure of merit η_{mat} is independent of the parameters of a cooling device (sink or load temperatures) and is rather intrinsic to the material. This leads us to our research questions which are: **How energy efficient are our best EC materials? How much electrical work is required to drive EC heat in an EC material? How does the shape of material influences its materials efficiency?** These questions are of importance for future energy-efficient cooling devices and motivate the research work presented in this dissertation.

This dissertation will mainly focus on studying the materials efficiency of EC materials. Our approach consists of choosing one of the best EC materials: lead scandium tantalate in different shapes and studying their materials efficiency. In order to obtain η_{mat}, on one hand, we will characterize the ECE of these materials and extract their isothermal heat exchanged. On the other hand, we will extract the electrical work energy required to charge these materials. The dissertation is organized as follows:

- **Chapter 2** describes a brief history of ECE and a background on materials efficiency. Moreover, we present the fundamentals of ECE and materials efficiency.
- **Chapter 3** reveals the different experimental methods developed and implemented to characterize the EC properties of EC materials and to calculate their materials efficiency. We will describe the calorimetry under applied electric field setup and IR camera used to extract Q. Besides, we will show the electrical setup utilized to extract W_e. Other thermal, electrical, and structural techniques used to determine the material's properties are described in this chapter.
- **Chapter 4** presents a background on the EC benchmark material lead scandium tantalate and shows the results on the giant materials efficiency of lead scandium tantalate in the shape of bulk ceramic. These results are compared to the materials efficiency of the benchmark magnetocaloric material Gd.

- **Chapter 5** provides results on the materials efficiency of PST in the shape of a multilayer capacitor (MLC) and compares the materials efficiency of PST MLC to the results obtained in chapter 4.
- **Chapter 6** shows an approach used to determine the ECE in PST MLC using Clausius-Clapeyron equation and calorimetry under an electric field.
- **Chapter 7** stems from a collaboration with the group of Gustau Catalan in Spain. We were able to bring an explanation to the controversial origin of the negative electrocaloric effect (NECE) in antiferroelectric (AFE) material lead zirconate. In this chapter, I will focus on my main contribution to this work.
- **Chapter 8** gives a general conclusion of this dissertation with perspectives for future studies.

Chapter 2

Background

In this chapter, we will briefly present a history of electrocaloric (EC) materials and prototypes. Important discoveries in the field of EC will be discussed. Subsequently, we will give a background on the figure of merit **materials efficiency** used in this dissertation to quantity the intrinsic efficiency of caloric materials. Moreover, a fundamental approach to the electrocaloric effect (ECE) and materials efficiency will be detailed. We will present a thermodynamic definition of the different EC physical concepts such as heat Q, work W, entropy S, materials efficiency η_{mat}, entropy change ΔS , and adiabatic temperature change ΔT_{adiab} .

2.1 A brief history of electrocaloric effect

ECE was firstly discovered seventy years after the first discovery of caloric effect in Indian rubber. Indeed, in 1805, John Gough discovered elastocaloric effect (eCE) in Indian rubber (shape memory polymer). By stretching adiabatically (quickly) the rubber and putting it on his lips, he could feel an increase in the rubber's temperature [37]. E. Warburg is often attributed to being the first scientist to discover the magnetocaloric (MCE) in his work in 1881 on iron. However, this is argued [38] as Warburg didn't claim MCE in his paper [39]. In 1917, Weiss and Piccard firstly reported on MCE in Nickel [40]. It is more than a decade later (1930) that the first observation of ECE was done in Rochelle salt (sodium potassium tartrate tetrahydrate) by Kobeko and Kurtschatov [41]. In 1963, Wiseman and Kuebler measured a temperature change smaller than 4 mK when driven at 1.4 kV cm^{-1} at 295 K [42]. The low magnitude of ECE observed in these first experiments suggested no interest in studying EC materials for cooling devices.

2.2 Electrocaloric materials

The discovery of several ferroelectric (FE) perovskites oxides [43] and the reports on pyroelectric effect (converse ECE) has led to the finding of more EC materials between 1950 and 1980. In 1960, ECE was measured in perovskites oxides of $SrTiO_3$ and $CdTiO_3$. However, these measurements were done at cryogenic temperatures. A temperature change of 0.3 K was obtained in $SrTiO_3$ single crystal at 7 kV cm^{-1} [44]. ECE of 1.8 K and 1.6 K was measured respectively in bulk ceramics $BaTiO_3$ [45] and $PbZrTiO_3$ compounds [46]. One of the highest ΔT_{adiab} was measured in 1981, in $Pb_{0.99}Nb_{0.02}(Zr_{0.75}Sn_{0.20}Ti_{0.05})_{0.98}O_3$. Tuttle et al.[47] measured directly 2.6 K at the electric field E=30 kV cm^{-1}. Other EC materials such as $Pb(Mg,Nb)O_3$ [48], $Pb(Zr,Sn,Ti)O_3$ (PZST) [49], $Pb(Sc,Nb)O_3$ (PSN)[50], $KaTiO_3$ [51] were reported until the early 2000s along with Shebanov's studies on $PbSc_{1/2}Ta_{1/2}O_3$ (PST) [52–55]. Shebanov and co-workers measured a maximum ΔT_{adiab} of 2.3 K.

Yet, no ECE greater than 3 K was reported in the literature until 2002. This can be explained by the fact that most ECE discoveries were done in bulk ceramics materials. Due to the thickness of the materials, bulk ceramics present a lower breakdown field than thin films. Consequently, in 2006, one of the most important papers in the field, reported on a ”giant” (greater than 10 K) ECE in AFE ceramic thin films of $PbZr_{0.95}Ti_{0.05}O_3$ (PZT) [28]. The authors measured 12 K at a starting temperature of 480 K under the electric field of 480 kV cm^{-1}. It is worth it mentioning that, these measurements were obtained indirectly using Maxwell relations (described in the following Section 2.4) and to date remain unproved by direct measurements. As seen in Figure 2.1, this work has triggered several studies

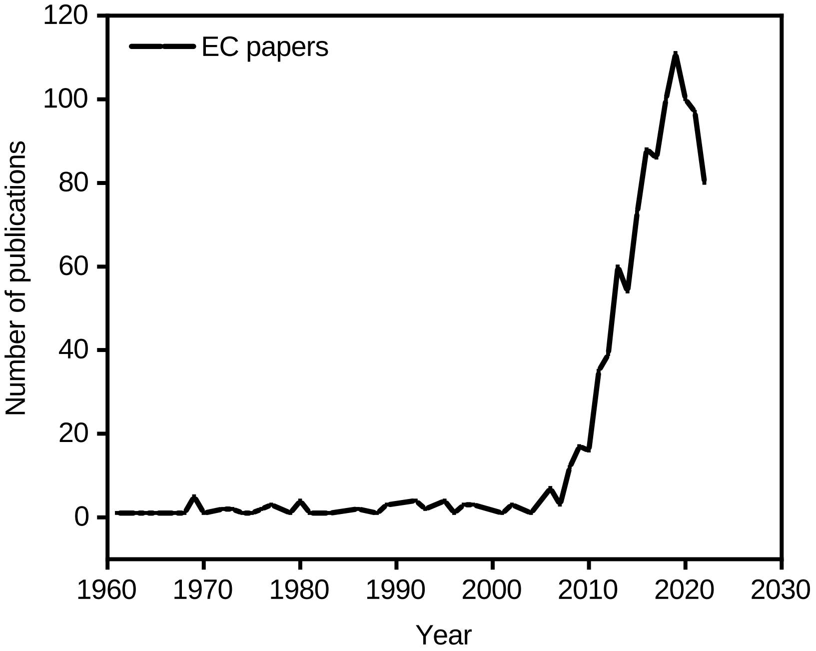

Figure 2.1: **EC publications from 1960 to date.** These data were obtained from Scopus Bibiliography database. An increase in publications is observed since 2006 due to the publication of [28].

on the ECE in perovskite materials (thin films, bulk), polymers, and plastic crystals [15]. Two years later, using the same indirect method, Qiming Zhang's group measured in the ferroelectric poly(vinylidene fluoride-trifluoroethylene) [P(VDF-TrFE)] copolymer, an entropy change of 55 J kg^{-1} K^{-1} [56]. This entropy change corresponds to an indirect ΔT_{adiab} of 12.5 K at E=2090 kV cm^{-1}. ECE was also reported in relaxor materials such as La-doped Pb(Zr,Ti)O$_3$ ceramic thin films [57], PbMg$_{2/3}$Nb$_{1/3}$O$_3$-PbTiO$_3$ thin films [58] and PST thin films [59]. Relaxors FE materials present slim FE loop (small hysteresis losses), high pyroelectric coefficient i.e high ECE, and finally their broad temperature range make them interesting for cooling applications.

As mentioned above, ECE could be realized in a dielectric fluid. In contrast to solid-sate EC materials, dielectric fluids are interesting as they can play the role of the EC medium and heat exchange fluid in an EC cooler. In the liquid crystal 5CB, at its nematic-isotropic transition, the authors [60] reported on an indirectly entropy change of 23.6 J kg^{-1} K^{-1}. Three years later, Kutnjak's group from Josef Stefan Institute in Slovenia, measured in a mixture of 12CB liquid crystal with functionalized CdSSe nanoparticles, a direct ECE of 5.18 K at the modest field of 30 kV cm^{-1} [61].

The EC field has been marked by the discovery of negative electrocaloric effect (NECE) or inverse ECE in relaxors or AFEs. NECE corresponds to the cooling of an EC material under the application of an electric field and the heating of this material upon removal of the field. It was firstly discovered in relaxor FE 0.72 Pb(Mg$_{1/3}$Nb$_{2/3}$) O$_3$ - 0.28 PbTiO$_3$. A negative temperature change of -5 K was measured indirectly in AFE thin films of La-doped Pb(ZrTi)O$_3$ [62]. We recently show that direct measurements of NECE in bulk ceramics PbZrO$_3$. We measured via an infrared camera a negative temperature change of -3.6 K [63]. This work will be covered thoroughly in chapter 7 of this dissertation.

Large to colossal values of ECE are being measured indirectly in thin films thereby, direct measurements of ECE in thin films is required to check the viability of these indirect measurements as they can lead to artifacts in the data [6, 17]. However, direct measurements on thin films remain challenging. The main challenge is the fact that the film lies on a bulk sample that plays the role of a thermal anchor and this reduces the effect observed.

A well-known structure multilayer capacitor (MLC) has been suggested as a good solution to avoid the drawbacks of thin films (small mass) and bulk ceramics (low breakdown field). MLC-based EC materials are bulky materials made of thin layers of EC material with interdigitated electrodes. ECE was reported in MLC-based PST, BaTiO$_3$ (BTO), 0.9PbMg$_{1/3}$Nb$_{2/3}$O$_3$-PbTiO$_3$ (PMN-PT), copolymer PVDF-TrFE. Recently, Neil Mathur's group at the University Cambridge in collaboration with the Japenese company Murata Manufacturing measured directly in MLC PST, a ΔT_{adiab} of 5.5 K at 290 kV cm^{-1} [29]. This is so far the highest ECE measured in a bulk material. Two years later (in 2021), a Nature article from Qiming Zhang's group, showed that by putting double-bonds in an EC polymer they could enhance the EC performance of the polymer by 275% in comparison to the state of art. The EC polymer studied was the relaxor poly(vinylidene fluoride-trifluoroethylene-chlorofluoroethylene) terpolymer. By replacing the bulky chlorofluoroethylene (CFE) groups present in the terpolymer with covalent doubles bonds, they could enhance the number of the polar entities and increase the polar–nonpolar interfacial areas of the terpolymer[64, 65]. The authors measured an EC entropy change of 37.7 J kg^{-1} K^{-1} and adiabatic temperature change of 7.5 K under the electric field of 500 kV cm^{-1}. Besides, the EC performance of the material was maintained after 10^{6} cycles with a 10% reduction in performance.

2.3 Electrocaloric devices

The first EC prototypes date back to the late 1980s. Between 1989 and 1995 researchers from the Moscow Power Engineering Institute used bulk ceramic PST as a working medium to build EC refrigeration prototypes. From a ΔT_{adiab}=1 K in the material, they build an EC prototype of 2.5 K of temperature span ΔT_{span} using pressurized helium as the heat exchanger. ΔT_{span} measures the temperature difference between the hot and the cold side of a prototype. Later on, a liquid pentane EC regenerator based on PST bulk was reported with ΔT_{span}=5 K. A prototype with a higher ΔT_{span} of 12.7 K was reported in 1995 by the same group. However, as mentioned by Nair [66], this value is ”buried in their paper” and subjected to debate.

The resurgence of papers on ECE in EC materials since 2006, has led to more EC prototypes as shown in Figure 2.2. From Torello et al. review article [67] published six months ago, we count around fifteen EC coolers up to date. Most of these prototypes are based on the principle of regeneration [15, 67, 68] used already in the past in MC prototypes [69, 70]. Regeneration permits reaching a temperature span (in the device) greater than the adiabatic temperature change of the material. In 2013, Gu et al.[71] reported on solid-based regenerator of ΔT_{span} = 6.6 K using polymer multilayers capacitors of ΔT_{adiab}=2.2 K. Researchers from the University of Ljubljana showed a fluid (silicone oil) based cooler with

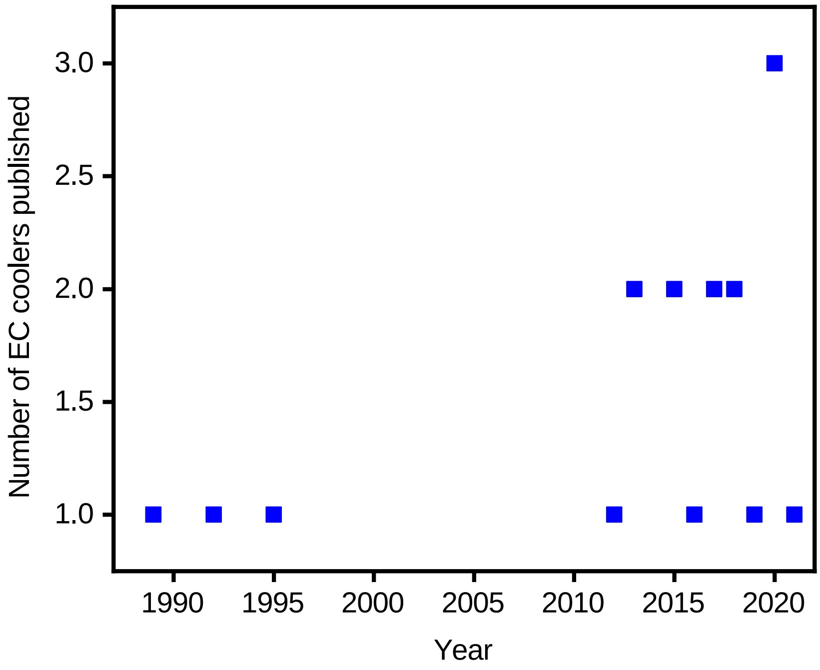

Figure 2.2: **EC coolers from 1989 to 2021.** This plot was made from the data collected in the 2021 review article [67] on EC coolers.

3.3 K of temperature span using PMN bulk ceramics. Defay et al. revealed that the Coefficient Of Performance (COP) of an EC prototype could be enhanced by recovering the work done to drive the EC cycles. In an EC device of 24 $BaTiO_3$ MLCs, by the means of simple circuitry, they could recover 65% of the work done to drive the ECE and therefore enhance by a factor of 2.9 the device's COP [24]. Following the development of PST MLC material, two EC devices were published in Science. Wang et al. [72] reported on a ΔT_{span} of 5.2 K in a solid-based regenerator using PST MLC as the main body. In the same issue, we published a liquid-based EC regenerator using 128 ceramic PST MLCs. Under the electric field of 160 $\mathrm{kV\,cm^{-1}}$ we measured a temperature span of 13 K [32]. This is to date the highest temperature span measured in an EC cooler. During the same year, Qibing Pei et al. [73] reported in Nature Energy, on a solid EC cooler using the cascading system. Their EC cooler used 0.1-mm-thick polymer multilayer to reach a temperature span of 8.2 K. In comparison to the EC device reported in [32], Qibing Pei's cascading cooler opens avenues to small and lightweight EC devices [74].

2.4 Thermodynamic of electrocaloric effect

The ECE and caloric effect in general can be described using well-known thermodynamics concepts. In this section we will define the EC quantities (ΔT_{adiab} or ΔS or Q) and study their influence to temperature and field.

Let's consider a dielectric material under the influence of an electric field E with the conjugate electrical displacement variable D . The Gibbs energy G of the materials can be written as a function of the internal energy U, temperature T, entropy S, electric field E and displacement D:

$$G = U - T\,S - E\,D \tag{2.1}$$

The differential form of G writes:

$$dG = -S\,dT - D\,dE \tag{2.2}$$

Note that in most EC materials the electrical displacement D is proportional to the polarization P ($D \approx P$). Equation (2.2) implies:

$$S = -\Big(\frac{\partial G}{\partial T}\Big)_P \tag{2.3}$$

$$P = -\Big(\frac{\partial G}{\partial E}\Big)_T \tag{2.4}$$

As G is a state function i.e independent of the path, one can write by symmetry of the second derivatives the following expression:

$$\frac{\partial}{\partial E}\Big(\frac{\partial G}{\partial T}\Big)_P = \frac{\partial}{\partial T}\Big(\frac{\partial G}{\partial E}\Big)_T \tag{2.5}$$

Equations (2.3), (2.4) and (2.5) yields one of the Maxwell relations:

$$\left(\frac{\partial S}{\partial E}\right)_T = \left(\frac{\partial P}{\partial T}\right)_E \tag{2.6}$$

Equation (2.6) is one of the most important EC Maxwell relations as it describes the change of entropy of the EC system with respect to the change of electric field as being equal to the change of polarization with respect to changes in temperature.

The total differential entropy change dS of the EC system can be written as a function of specific heat capacity $C_p = T\left(\frac{\partial S}{\partial T}\right)_E$ and $\left(\frac{\partial S}{\partial E}\right)_T$ as follows:

$$dS = \left(\frac{\partial S}{\partial T}\right)_E dT + \left(\frac{\partial S}{\partial E}\right)_T dE$$

$$dS = \frac{C_p}{T} dT + \left(\frac{\partial S}{\partial E}\right)_T dE \tag{2.7}$$

- Under isothermal conditions, $dT = 0$ and equation (2.7) becomes :

$$dS = \left(\frac{\partial S}{\partial E}\right)_T dE \tag{2.8}$$

Therefore, we obtain the isothermal field-driven entropy change ΔS from (2.7) and (2.11).

$$\Delta S = \Delta S\,(0 \to E) = \int_0^E \left(\frac{\partial P}{\partial T}\right)_E dE \tag{2.9}$$

We deduce the isothermal heat Q:

$$Q = T\,\Delta S = T\int_0^E \left(\frac{\partial P}{\partial T}\right)_E dE \tag{2.10}$$

- Under adiabatic conditions i.e $dS = 0$, equation (2.7) becomes :

$$0 = \frac{C_p}{T} dT + \left(\frac{\partial S}{\partial E}\right)_T dE \tag{2.11}$$

Hence, the adiabatic temperature change ΔT_{adiab} induced by the application of an electric field.

$$\Delta T_{adiab} = \Delta T_{adiab}\left(0 \rightarrow E\right) = -\int_{0}^{E} \frac{T}{C_p}\left(\frac{\partial P}{\partial T}\right)_E dE \tag{2.12}$$

The three EC parameters ΔT_{adiab}, ΔS and Q can be interconverted using the traditional interconversion relation (2.13) [17, 25]. In this equation, one has to be careful of the value of C_p which is not often taken as field or temperature dependent. An effective value of C_p is often chosen as the constant baseline value of the C_p measurements as function of temperature.

$$|Q| = |C_p\, \Delta T_{adiab}| = |T\, \Delta S| \tag{2.13}$$

It is clear from equations (2.9), (2.10), (2.12) that the magnitude of the ECE is dependent on the magnitude of $\left(\frac{\partial P}{\partial T}\right)_E$. In other words the ECE is the highest where the change of polarization with respect to changes in temperature at a constant electric field is the highest. However, $\left(\frac{\partial P}{\partial T}\right)_E$ is different from one type of phase transitions to another and varies with temperature. As already mentioned in the introduction chapter, ferroic materials exhibit phase changes (changes in order parameter or symmetry breaking) under the influence of temperature or electric field. The order parameter vanishes to zero after the transition as displayed in Figure 2.3. The phase transitions are categorized in two types: the first-order phase transition and the second-order phase transition. The first-order transition is defined by a discontinuous jump in the order parameter at T_c (red curve in Figure 2.3). Moreover, it is associated with latent heat and sharps peaks in the specific heat capacity measurements [75]. However, in second order transitions materials, the order parameter changes smoothly (in a continuous manner) from one phase to the other (green curve in 2.3).

From Figure 2.3, $\left(\frac{\partial P}{\partial T}\right)_E$ is predominant at T_c and higher in first-order transitions materials. Therefore, the ECE is expected from equation (2.9) to be dominant in materials

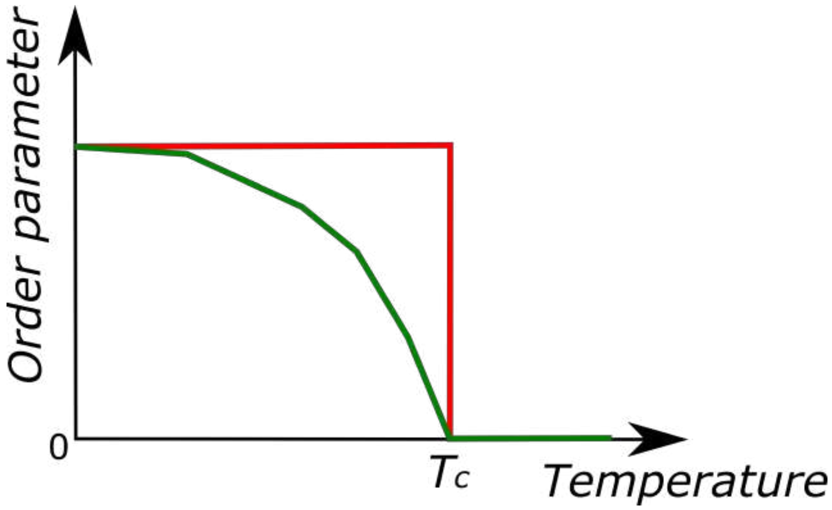

Figure 2.3: **Phase order transitions.** Order parameter versus temperature for first (red curve) and second order (green curve) transition materials.

exhibiting sharp phase transitions. Besides, from (2.12) we can deduce that materials with low specific heat capacity will show high ΔT_{adiab}.

In practice, from PE loops collected experimentally at different temperatures, one will construct the temperature dependence of the polarization (isothermal PT curves) and fit them with a polynomial to deduce the derivative of the polarization with respect to temperature. The EC properties ΔT_{adiab} or ΔS or Q are therefore deduced from integration over electric fields using the equations 2.12, 2.9 and 2.10. This approach is known as the ”indirect method” [15, 17]. The PE loops should be collected in thermodynamic equilibrium as a single valued function of temperature and field. This is achievable in continuous (second-order) phase transitions whilst it is challenging for first-order transitions materials due to the discontinuity in transition. The use of the Maxwell relations for first-order transitions materials is subject to arguments in the community [76–78].

An indirect alternative to estimate the EC performance of first-order transition materials is the Clausius-Clapeyron equation. This approach is only valid for such transitions (discontinuous) and is suggested as a more reliable way to determine the isothermal entropy change due to the phase transition [79].

Let's consider the Gibbs free energy G of a first-order transition material that exhibits transition from a low temperature phase B to a high temperature phase A with a coexistence of the two phases (critical point) at constant temperature and electric field. The differential change of the Gibbs energy dG of each phases can be written as:

$$dG^A = -S^A\, dT - P^A\, dE$$

$$dG^B = -S^B\, dT - P^B\, dE$$

At the coexistence phase, in order to guarantee stability, the Gibbs energy should be the same in both phases i.e $G^A = G^B$ (Figure 2.4). In case of transition from phase A to B by infinitesimal change in temperature T or electric field E from state 1 to state 2 in Figure 2.4, the mixed system moves along the coexistence line in the phase diagram (Figure 2.4).

Therefore,

$$dG^A = dG^B$$

$$-S^A\, dT - P^A\, dE = -S^B\, dT - P^B\, dE$$

The Clausius-Clapeyron equation writes:

$$\frac{dT_0}{dE} = -\frac{\Delta P_0}{\Delta S_0} \tag{2.14}$$

The subscript 0 refers to the transition. Equation (2.14) is nominally equivalent to the Maxwell equations and enables the estimation of the transition entropy change ΔS_0 of first-order transitions materials from the inverse of the electric dependence of the transition temperature $\frac{dE}{dT_0}$ and the polarization jump at the transition ΔP_0.

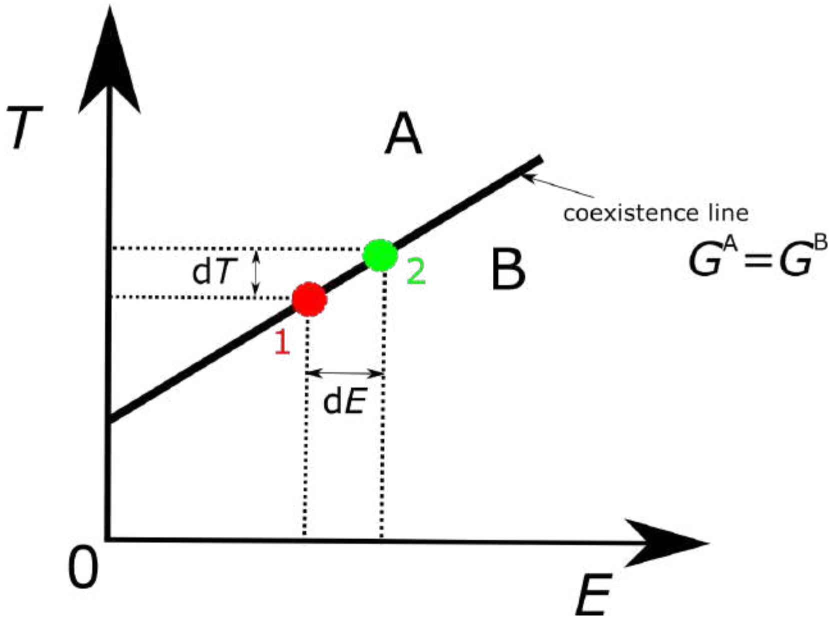

Figure 2.4: **Temperature-Electric field diagram.** This figure describes the TE of the phase transition of a first-order transition materials from lower temperature phase B to higher temperature phase A diagram B with infinitesimal change in temperature T or electric field E from state 1 to state 2. The full black line is the coexistence line where both phases have the same Gibbs energy G. This figure was adapted from [80].

2.5 Materials Efficiency

When it comes to replacing the existing cooling technology, energy efficiency remains one of the key factor. Amongst the EC articles (Figure 2.1) published since 1960, around twenty of them report on EC coolers. The remaining articles are centered on the EC performance of EC materials. Surprisingly, very few articles report on energy efficiency [30, 33–35, 81, 82]. Most of the studies on ECE, have been focused on looking for EC materials with high thermal changes (ΔT_{adiab} or ΔS or Q). However the work done to drive reversible thermal changes in these materials has barely been studied. In 2013, Defay et al. [33] firstly introduced the EC efficiency as a figure of merit to measure the efficiency of the ECE. This figure of merit denoted by η_{mat} or η, is a dimensionless quantity. It is intrinsic to the material and doesn't depend on parameters (temperature span, cooling power, etc) of a cooling device. For simplicity, we are going to refer to the materials efficiency as η_{mat}. It is defined as the absolute value of the ratio of reversible EC heat Q to reversible electrical work W_e under isothermal conditions. η_{mat} writes:

$$\eta_{mat} = |Q/W_e| \tag{2.15}$$

η_{mat} remains positive for an EC material that releases heat ($Q < 0$) when electrically charged ($W_e > 0$) or absorbs heat ($Q > 0$) when electrically discharged ($W_e < 0$) [33]. An energy efficient material will exchange more EC heat than the work required to drive this heat. This is possible around the material's transition temperature where more heat (latent heat for instance in case of first-order transition material) is available than the work energy. Hence, η_{mat} is a value usually greater than unity. The materials efficiency η_{mat} should not be confused with the scaled efficiency or second-law efficiency. The latter will be refer to as η . It is defined as the ratio of the device's COP to the Carnot COP.

$$\eta = |COP/COP_{Carnot}| \tag{2.16}$$

In contrast to η_{mat}, the scaled efficiency η depends on the device parameters and is maximized at 1. η_{mat} was thought as a tool to compare different caloric materials in terms of their intrinsic efficiency for similar values of $|Q|$.

η_{mat} was firstly used in [33] to compare the EC efficiency of the EC films of ceramic PZT and polymer P(VDF-TrFE) (55/45 mol%). Using the integration method i.e from the integration of the isothermal DE (displacement versus electric field) loops of both materials collected respectively from [28] and [56], the authors calculated the volume normalized $|Q|$ and the volume normalized $|W_e|$ at the maximum electric field applied. For nearly similar values of $|Q|$ per volume in both materials (31.4 J cm^{-3} in PZT and 37.6 J cm^{-3} in P(VDF-TrFE)), they obtained η_{mat} of 3.0 and 7.3 in respectively PZT and P(VDF-TrFE). Therefore, showing that EC polymer P(VDF-TrFE) requires 2.4 times less electrical work energy than the ceramic film PZT to exchange the same amount of EC heat per volume at their respective T_c (Curie temperature). Moreover, using a different approach (Landau mathod) that considers the sample interior in contrast to the integration method, the authors showed that the ceramic film (2.8) is nearly as efficient as the polymer film (3.9). In fact the Landau method indicates that the films comprise a strained interior (present in FE thin films [83]) between the non-EC edge layers. The intrinsic efficiency of ceramic BTO MLC and 0.93PbMg$_{2/3}$Nb$_{1/3}$O$_3$-0.07PbTiO$_3$ (PMN-PT) films was also measured indirectly (integration method). The authors revealed an efficiency of 3.0 and 5.6 in respectively BTO MLC and PMN-PT films at their respective T_c.

Two years later, Moya et al. and Crossley et al. generalized the concept of materials efficiency to all the caloric materials. A shown in Figure 2.5, they compared the materials efficiency of MC, eC, EC and BC materials for the same volume normalized heat exchanged $|Q|$. In their work, for the case of MC and EC materials, the authors mentioned the fact that the work done to drive respectively MCE and ECE could be triggered mechanically or electrically. Based on V. Heine formalism's [84], it is demonstrated that is more efficient to drive MCE mechanically (dark blue bubble in Figure 2.5) and ECE electrically (dark green bubble in Figure 2.5).

From isothermal measurements (at T_c) of order-parameter versus field applied curves approximated as a singled value function (with no hysteresis ideally) the volume normalized isothermal heat $|Q|$ and volume normalized isothermal work $|W|$ were calculated using the indirect approach describes in Section 2.4. The expressions of $|Q|$ and $|W|$ are summarized in Table 2.1. We distinguish between $|W_m|$ the work done mechanically and $|W_e|$ the work done electrically.

The MC efficiency analog to the EC efficiency is the ratio of the reversible isothermal heat to the reversible work done to (de)magnetize the material. Work is done mechanically to generate a magnetic field in a MC sample by relative motion of the sample with respect to the permanent magnet [34]. Electrically, this work is generated by running charges in a solenoid attached around a MC sample. From data of magnetization M as a function of

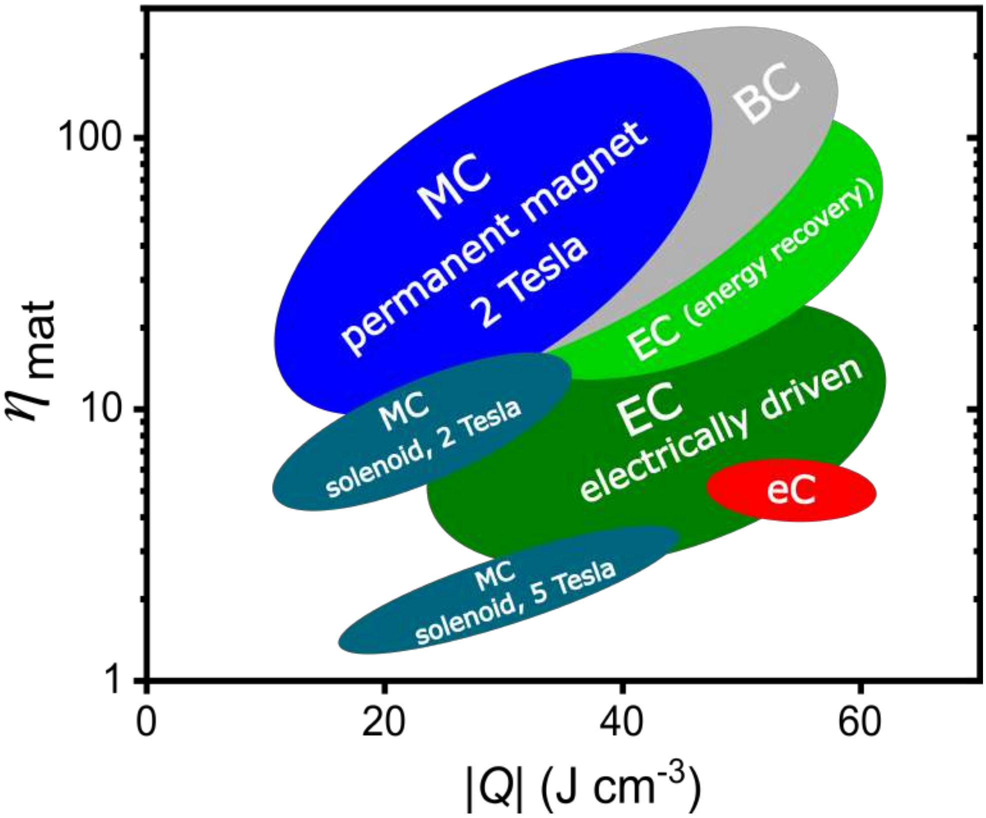

Figure 2.5: **Materials Efficiency of caloric materials.** Comparison of the materials efficiency η_{mat} of different caloric materials for similar heat $|Q|$. The blue bubble are MC materials driven mechanically with permanent magnet at 2 Tesla. The two dark blue bubbles are the MC materials driven electrically with solenoid at 2 Tesla and 5 Tesla. The dark green bubbles refers to the EC materials driven electrically and the light green bubbles are the EC materials using energy recovery. Finally, the grey and red bubbles are respectively the BC and eC materials. This figure was adapted from [35].

magnetic field H at isothermal temperature, Moya et al. calculated the MC efficiency of several MC materials. The MC samples were driven at 2T and 5T. As a result (Figure 2.5), it was shown that MC materials are an order of magnitude more energy efficient when driven mechanically than electrically. This difference is explained by the fact that it costs more energy to create the applied magnetic field in a solenoid that is already present in permanent magnets. Besides, it was observed that the MC efficiency decreases with the increasing

Table 2.1: **Isothermal heat and Work of caloric materials.** The isothermal heat $|Q|$ is obtained from the Maxwell relations (equation 2.10). W_m and W_e are respectively the mechanical and electrical work. B is the magnetic flux density. E, H, σ and p are respectively the electric field, magnetic field, uniaxial stress and pressure with their respective order parameter P(polarization), M(magnetization), ε(strain) and V(volume).

Calorics	**Isothermal heat Q**	**Mechanical work W_m**	**Electrical work W_e**
Magnetocalorics	$\int_0^H T\left(\frac{\partial M}{\partial T}\right)_H dH$	$\int_0^H -\mu_0 M\,dH$	$\int_0^H H\,dB$
Electrocalorics	$\int_0^E T\left(\frac{\partial P}{\partial T}\right)_E dE$	$\int_0^P E\,dP$	$\int_0^P -P\,dE$
Elastocalorics	$\int_0^\sigma T\left(\frac{\partial \varepsilon}{\partial T}\right)_\sigma d\sigma$	$\int_0^\varepsilon \sigma\,d\varepsilon$	
Barocalorics	$\int_0^p T\left(\frac{\partial V}{\partial T}\right)_p dp$	$\int_0^V -p\,dV$	

magnetic field due to the saturation of the MCE. In fact, $|Q|$ saturates very fast especially above the field required to drive completely the material's transition. Prototypical materials such as Gadolinium (Gd) and $Gd_5Si_2Ge_2$ have a materials efficiency of 12.6 and 27.2 respectively at their T_c (294 K for Gd and 276 K for $Gd_5Si_2Ge_2$) when driven mechanically at 2 T.

In terms of energy efficiency, EC materials are interesting as it is much easier to generate electrical field than magnetic field or mechanical stress. The EC efficiency has been characterized so far in thin films materials. The work done to drive work in a polarizable material can be done either electrically by varying the charge on the EC capacitor plates or mechanically by relative motion of the sample using unscreened fixed charges that are on the capacitor plates (in vacuum to avoid breakdown with air). The latter is less energy efficient and induces values of η_{mat} that are smaller than 1 [34]. The electric field created from mechanical work is associated with screening leading to large variations in the electric field, therefore high values of mechanical work. It is worth it noting that, if the work done to drive ECE or MCE is done electrically, more work must be done to generate magnetic or electric field through flow of charges [34]. However this additional work is not taken into account in the materials efficiency calculation. In comparison to MC materials, EC materials driven electrically (dark green bubble in Figure 2.5) are as efficient as MC driven electrically. However, by artificially (via simple circuitry) recovering the electrical energy used to drive EC effects, one can enhance the η_{mat} of EC materials by a factor of five. Thereby, positioning EC materials by means of energy recovery (light green in Figure 2.5) as efficient as the MC driven mechanically with permanent magnets (dark blue in Figure 2.5).

Finally, the materials efficiency of eC and BC materials were carried out respectively from uniaxial stress–strain and pressure-volume data. Crossley et al. [35] showed that BC materials such as $\text{Ni}_{49.26}\text{Mn}_{36.08}\text{In}_{14.66}$ (η_{mat} =211) are as efficient as the most energy efficient materials (MC driven by permanent magnets). However, eC materials (red bubble in Figure 2.5) present a lower efficiency than BC, MC and EC materials. In the prototypical eC material nickel titanium (NiTi), η_{mat} of 5.3 was obtained at the eC heat exchanged of 60.4 J cm^{-3} [34]. Higher values of intrinsic efficiency of NiTi wires are reported in the eC literature [85–87]. In fact, a similar figure of merit called COP$_{mat}$ [16, 88–91] is used in the eC community to quantity the intrinsic efficiency of eC materials. The main difference between COP$_{mat}$ and η_{mat} is the way the work is calculated. As shown in Figure 2.6, in the COP$_{mat}$ calculation, the work corresponds to the interior of the loop (non recoverable work - red area in Figure 2.6) whereas for η_{mat}, the work corresponds to more than the hysteresis loop (green + red area in Figure 2.6).

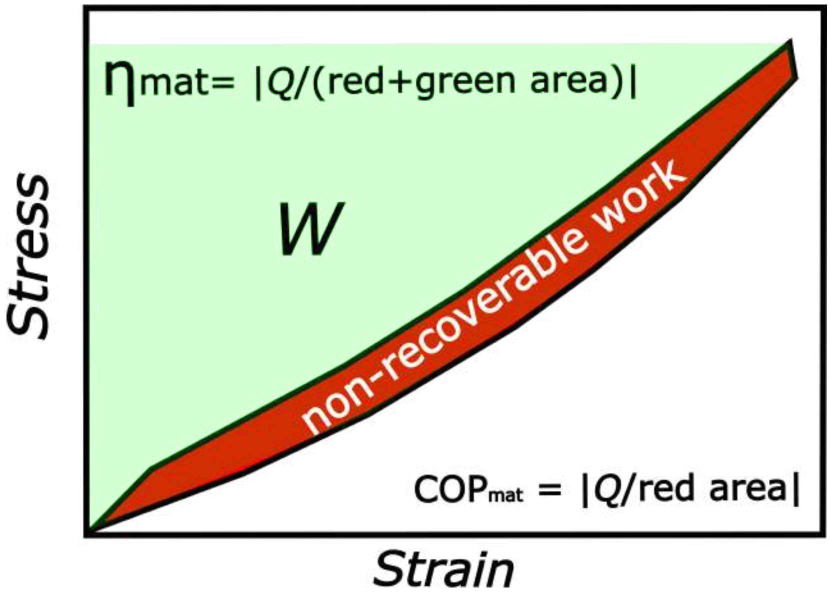

Figure 2.6: **Materials efficiency in elastoCaloric materials.** This figure shows the Stress-Strain loop of an eC material. Q is the heat absorbed or released. The red area corresponds to the non-recoverable work. This red area is used for the calculation of COP$_{mat}$. However, the work W (red area + green area) is the work considered for the calculation of η_{mat}.

In this dissertation, in order to obtain the materials efficiency of EC materials, we will calculate their isothermal heat Q from direct measurements of adiabatic temperature change and specific heat using the equation 2.13. Direct measurements of isothermal heat will be also done for comparison. Voltage (U) versus time (t) data of the charge/discharge of the capacitor at constant current I , will be collected directly to calculate the electric work using the equation (2.17).

$$W_e = I \int_0^t U(t)\, dt \tag{2.17}$$

Chapter 3

Experimental Methods

The purpose of this chapter is to present the various experimental methods and tools used to quantify the materials efficiency η_{mat} of EC materials and, characterize their thermal, structural and electrical properties. η_{mat} is obtained by determining the electrocaloric (EC) heat exchanged Q and the electrical work W_e required to drive this heat. Q defined as $mC_p\Delta T_{adiab}$ was determined by direct characterization of ΔT_{adiab} and C_p. W_e was extracted directly using a dedicated experimental setup. In the following sections, we will describe:

- **the EC setup** used to determine the adiabatic temperature change in EC materials and extract the electrical work. This setup includes mainly an **IR camera** to collect ΔT_{adiab} and a **dedicated setup** to collect W_e.
- **the calorimeter** utilized for direct measurements of the isothermal entropy change ΔS, specific heat C_p, and EC heat Q induced by changes in temperature.
- **the customized calorimeter under electric field** used to quantify directly isothermal Q, isothermal ΔS and quasi-directly C_p, Q and ΔS.
- **the X-Ray Diffraction (XRD)** and **Scanning Electron Microscope (SEM)** methods to determine the material's structure.
- **the impedance spectrometer** used for the characterization of dielectric permittivity
- **the electrical techniques** used to obtain Polarization-Electric (PE) loops

3.1 EC setup

In this section, we will describe the setup and the process followed to extract both ΔT_{adiab} and electrical work W_e needed to drive the ECE in EC materials. In order to calculate the materials efficiency, ΔT_{adiab} and W_e were collected at different starting temperatures T_s and electric field E applied adiabatically.

Figure 3.1 describes the setup utilized for EC characterization. The linkam stage T95 (temperature stage) is used to control the T_s of the EC sample investigated. This stage can heat up to 573 K and cool the sample down to 253 K using liquid nitrogen. The top and bottom surfaces of the sample are electroded with silver paste. The same silver paste is used as a paste to glue one extremity of the thin wires on both surfaces. The other extremity is connected to a power supply Keithley 2410 for the application of the electric field. As shown in Figure 3.1 a very thin layer of Kapton tape is placed on the linkam stage for electrical insulation. The electroded EC sample is placed on thermal grease that lays between the sample and the Kapton tape to facilitate heat transfer. An IR camera described in the following subsection is utilized to collect the temperature values of the EC sample as a function of time.

As displayed in Figure 3.1 three instruments: Linkam stage, IR camera, and Keithley 2410 are controlled by a computer. For fast and multiple acquisitions, a Python code was built to sequentially trigger each instrument and collect simultaneously data of ΔT_{adiab} and W_e. At a given electric field and T_s, three consecutive EC cycles were done to verify the reproducibility of our measurements. For a given electric field, EC measurements were collected at different T_s after moving to the next electric field. Preferentially, the EC measurements are taken from low to high values of electric field to avoid breaking the sample. The sample is first cooled down to 283 K and heated to the desired starting temperature T_s. The EC measurements go as follows:

1. The sample is at a given T_s, step 1 in Figure 3.2a.

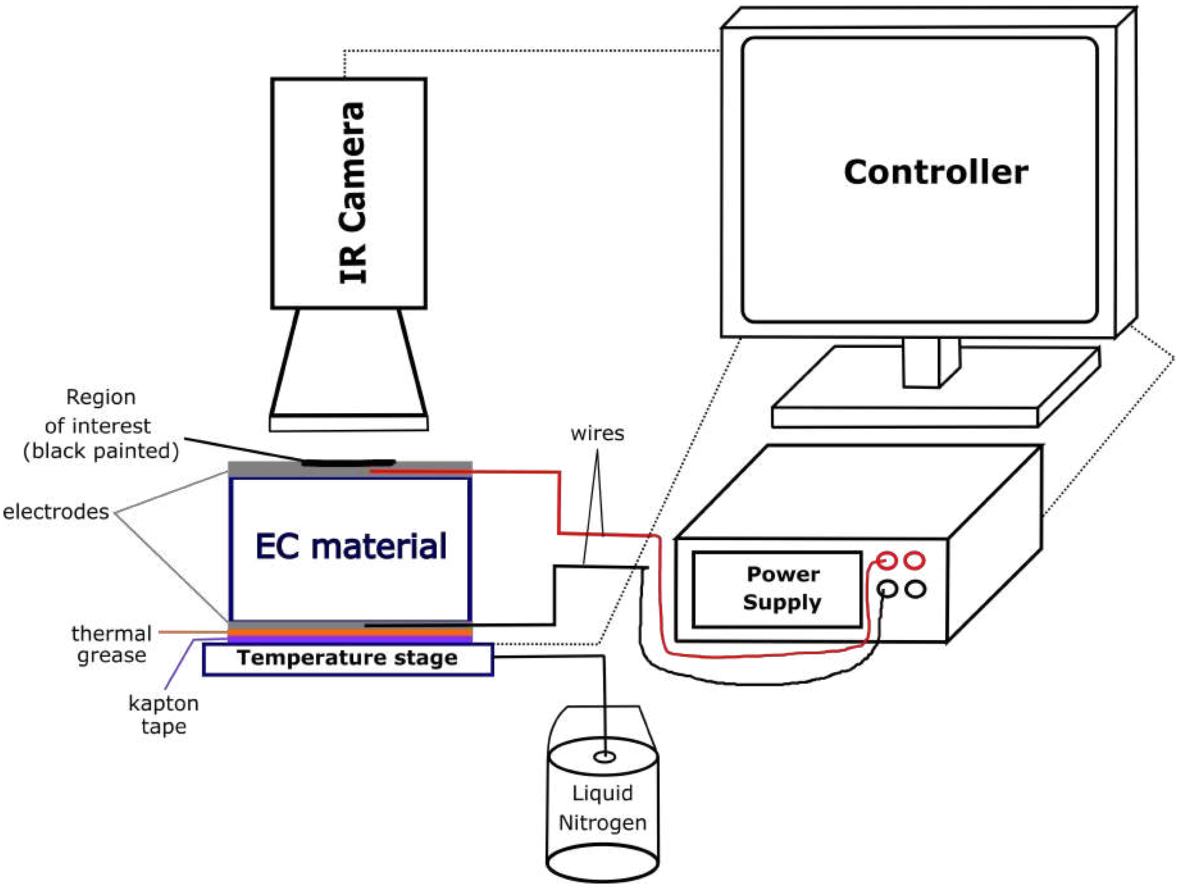

Figure 3.1: **EC Setup.** This figure describes the EC setup utilized to collect ΔT_{adiab} and W_e. The IR camera, temperature stage, and power supply were used respectively to record temperature changes in the EC material, control the starting temperature T_s of the EC material, and apply/remove an electric field in the EC material. The three devices are connected (dash lines) to a controller for fast data acquisition. Liquid nitrogen was used to reach temperatures down to 253 K. The region of interest (ROI) of the sample visible by the IR camera was black painted to increase its emissivity to 1.

2. The IR camera is activated to record a video

3. An electric field is then applied adiabatically at constant current rather than constant voltage because it is more efficient in terms of energy (demonstration in Section 3.1.2). The adiabaticity is controlled by the current applied which depends on the sample studied. For each sample characterized, an adiabatic study is carried out to determine the ideal current. The charging time of the capacitor has to be smaller than its relaxation

time to guarantee adiabatic conditions. In the case of conventional ECE, the application of an electric field leads to a positive jump in the temperature of the material (step 2 in Figure 3.2a). The ΔT_{adiab} on-field corresponds to the difference in temperature between the peak in step 2 and T_s.

4. Subsequently, in step 3, the field is kept on and the material relaxes by exchanging with the surroundings. By doing so, the material exchanges EC heat Q. Ideally, the material decreases to the initial T_s without Joule heating.
5. Afterwards, the electric field is removed adiabatically to 0 kV cm^{-1} thereby a negative temperature jump is observed. The ΔT_{adiab} off-field is the difference in temperature between the peak in step 4 and the T_s.
6. Finally, the material relaxes and gets back to its initial T_s (step 5 in Figure 3.2).
7. From 3 to 6 the process is repeated two more times as shown in Figure 3.2a and the video is stopped.
8. The sample is heated up to the next temperature and the process from 2 to 7 is repeated. The process is repeated at a different electric field.

It is worth it to mention that these measurements can be time-consuming exceptionally when done manually. Some of the measurements shown in this dissertation were done manually and others automatically i.e using a Python code to communicate with the three devices. The automatic system done using Python was done with the help of Pierre Lheritier a postdoc researcher in the our team.

As displayed in Figure 3.2b, simultaneously with the adiabatic temperature change measurements, the data of charge of the capacitor and current were collected to calculate the electric work as described in Section 3.1.2.

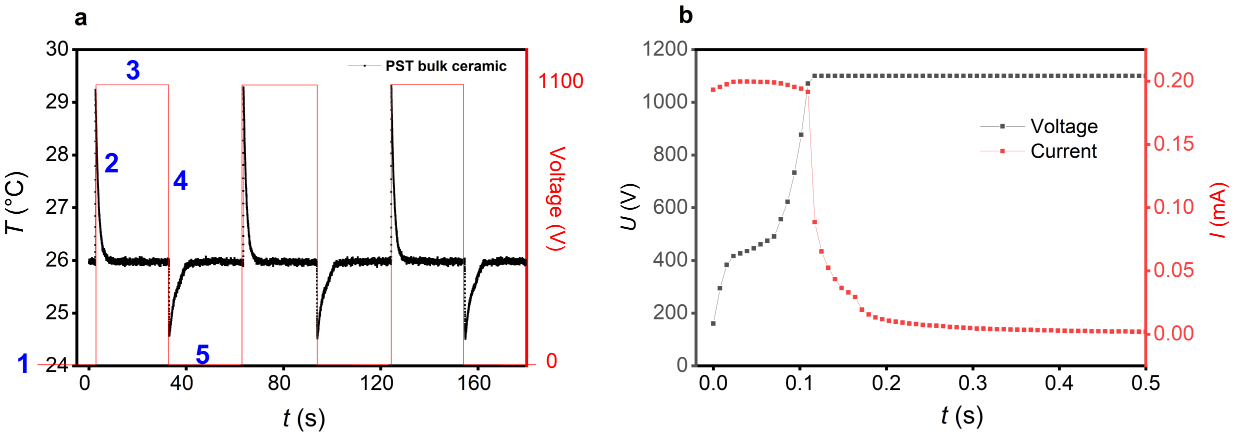

Figure 3.2: **Example of an EC cycle.** **a** Temperature change of PST bulk ceramic at 26 ℃ under the application/removal of 22 kV cm^{-1}. This fields corresponds to 1100 V in 0.5 mm thick sample. The black curve is the temperature change and the red curve is the voltage applied/removed to get this temperature change. The blue numbers indicate the different steps of an EC cycle. **b** Example of the charge of the PST capacitor (step 2 in Figure 3.2a) as function of time. It was collected simultaneously with the adiabatic temperature change. The black curve describes the charge to a given maximum voltage and the red curve, the change in current as a function of time.

3.1.1 InfraRed (IR) imaging

IR imaging or thermometry was used in this dissertation to extract the temperature change of EC materials due to the ECE. It permits accurate and fast measurements of ΔT_{adiab} both temporally and spatially [29, 30, 63, 75, 81, 92–96] as opposed to contact-thermometry [87, 97–101]. Indeed, contact thermometry is a source of errors such as the thermal influence of the sensor (thermocouple for instance) on the temperature of the sample or the heat loss in the environment. A non-contact thermometry technique such as an IR camera detects and measures heat (infrared energy) and subsequently converts it into an image that describes the temperature surface of the object being measured [102]. It is worth it to stress that the main advantage of an IR camera compare to a DSC or thermocouple is the possibility to spatially directly image the EC response of an EC material. An IR camera possesses a lens that directs the infrared radiations towards the sensor (detector) that contains thousands of pixels. The pixels are responsible for the conversion of infrared energy into an electronic signal. From a calibration file, the IR signal is then converted to temperature and one can obtain a colour map images describing the object's temperature. The camera's resolution is given by the configuration of the pixels. The IR radiations are collected at a certain frequency frame rate in a given integration time. This integration time corresponds to the amount of time the camera is open and collects IR radiations. Evidently, the frequency frame rate is limited by the integration time. In the case of long integration time, the sensor saturates due to too many IR radiations and on the contrary, short integration time leads to small IR radiations and less accuracy on the temperature.

The IR camera X6580sc from FLIR [92, 103] was used in this dissertation to measure ΔT_{adiab} by spatially and temporarily recording the temperature change of the EC material. It has a digital InSb detector with a broadband spectral sensitivity of 1.5 to 5.1 μm. has a thermal sensibility of 20 mK. This tool is suitable for adiabatic temperature as it enables fast acquisition of heat at the frequency frame rate that lies between 100 and 2 kHz. For bulk materials the frequency frame rate often used is between 100 and 200 Hz and in the case of thin films where the heat is very fast lost in the substrate, the IR images are collected between 1 and 2 kHz. We used here, the lens MW 50mm without an extension ring. It has a spectral range comprised between 3.5 and 5 μm. The software ResearchIR4 Software from FLIR is used to analyze the data. It enables selecting the region of interest (ROI) in the field of view for temperature acquisition. It averages the temperature values in the ROI given by the pixels. A csv file containing the temperature values as a function of time can be extracted. The thermal images have a thermal sensitivity of 20 mK and a spatial resolution of a few micrometers.

To obtain accurate values of the temperature of EC materials being observed by the IR camera, emissivity calibration has to be done. An IR camera is calibrated to see everything like a black body i.e with an emissivity of 1. The emissivity of a body quantifies how efficiently a body emits heat. Its values range from 0 to 1. In the case of a perfect mirror that reflects all energy the emissivity is 0 and for a black body that absorbs and emits all energy, its emissivity is 1. The emissivity of material can be verified or calculated as follows.

The conservation of energy states:

$$1 = \alpha_{\lambda,T,\theta} + \rho_{\lambda,T,\theta} + \tau_{\lambda,T,\theta} \tag{3.1}$$

For a given wavelength λ, temperature T and angle θ.

- α is the absorption energy
- ρ is the reflected energy
- τ is the transmitted energy

In the case of a black body which is a perfect emitter and absorber, the absorption energy is equal to the emitted energy. Hence, $\alpha_{\lambda,T,\theta} = \varepsilon_{\lambda,T,\theta}$ and equation (3.1) can be written as:

$$1 = \varepsilon_{\lambda,T,\theta} + \rho_{\lambda,T,\theta} + \tau_{\lambda,T,\theta} \tag{3.2}$$

Here we consider an opaque body i.e that $\tau_{\lambda,T,\theta} = 0$. As shown in Figure 3.3, the radiations received by the IR camera include three different contributions:

- the radiation sent by the target object with factor ε, which attenuated when passing through the atmosphere before reaching the IR camera
- the radiation coming from the surroundings and then reflected onto the object's surface towards the camera with a factor $\rho = 1 - \varepsilon$.
- the atmosphere radiation's which emits with the factor $1 - \tau$

Therefore, the total radiation received by the IR camera is defined as:

$$W_{measured} = \tau\,\varepsilon\,W_{object} + \tau\,(1-\varepsilon)W_{envir} + (1-\tau)W_{atmos} \tag{3.3}$$

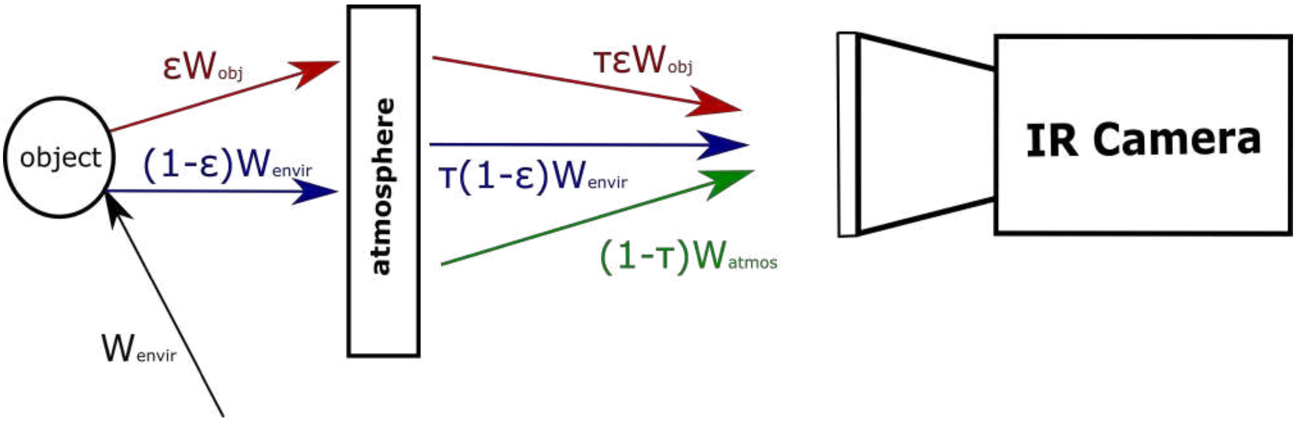

Figure 3.3: **Radiations received by an IR Camera.** The IR camera received radiations from the body being observed (W_{obj}), the atmosphere (W_{atmos}) and from the environment (W_{envir}).

τ can be considered equal to 1 as the distance between the IR camera and the object is smaller than 3 m in our measurements. Hence equation (3.3) becomes:

$$W_{measured} = \tau \, \varepsilon \, W_{object} + (1 - \varepsilon) W_{envir} \tag{3.4}$$

We deduce the emissivity:

$$\varepsilon = \frac{W_{measured} - W_{envir}}{W_{obj} - W_{envir}} \tag{3.5}$$

In the case of a black body, $W_{measured} = W_{obj}$ as all the radiations are emitted to the camera. The emissivity can be calculated by knowing the real temperature or counts of the object, the temperature or counts of the object measured by the IR camera, and finally the temperature or counts of the surroundings. The radiance W is proportional to σT^4 as defined by Stefan-Boltzman [102]. Then equation (3.5) can be written as :

$$\varepsilon = \begin{cases} \dfrac{counts_{measured} - counts_{envir}}{counts_{obj} - counts_{envir}} \\ \\ \qquad or \\ \dfrac{T^4_{measured} - T^4_{envir}}{T^4_{obj} - T^4_{envir}} \end{cases}$$

One way to determine the environment's temperature is to measure with the IR Camera the temperature of a wrinkled aluminum foil which will reflect the surroundings into the camera.

It is worth it to mention that from the material's and environment's temperatures, the emissivity calculation can also be done directly using the ResearchIR4 Software.

In this dissertation, the surface of the EC materials observed with an IR camera was coated in black using *Colorjelt Noir Mat* [104] to improve their emissivity. An emissivity of 0.99 was calculated on this black coating using the equation (3.5). This is very close to the emissivity of a black body required to get accurate values of temperature.

3.1.2 Electrical Work extraction

A dedicated electrical setup was built to determine the electrical work energy W_e used to charge the capacitor. The EC capacitors are charged at a constant current up to a target voltage. A code script written in Python that communicates with the power supply (Keithley 2410) was used to collect the voltage U and current I_0 as a function of time t. W_e is defined as $I_0 \int U(t)dt$. The main challenge here is to choose the current high enough to guarantee the adiabaticity of the measurements and small (not too fast) to acquire voltage and current as a function of time with enough number of points.

3.2 Calorimetric measurements

Invented in the middle of the 18th century, calorimetry is a famous technique used to measure heat. The word ”latent heat” was firstly given by Joseph Black between 1757 and 1764, after carrying measurements on the fusion heat of ice and the vaporization heat of water [105, 106]. However, his work wasn’t published. Thirty years later, the French scientists Laplace and Lavoisier reported on the first calorimeter; an ice calorimeter that could inaccurately measure the heat of fusion. After his work in 1840 on the inter-convertibility of different forms of energy (mechanical, electrical, and heat), James Joule initiated the electric calibration of calorimeters [107, 108]. This was an important discovery in the field of calorimetry as he was one of the first to define latent heat as a form of energy and not of matter. Consequently, the calorimetric unit ”caloric” was changed to ”Joule” which, is still today the international unit of energy. Since then, several modern calorimeters have been created and are widely used to measure heat, specific heat capacity, transition temperatures, and also determine crystallinity and purity of substances.

As part of this work, we will use a Differential Scanning Calorimeter (DSC) to measure the EC heat Q absorbed or released by an EC material. From the calorimetric measurements of heat flux against temperature, time, and electric field, we can deduce different caloric properties such as specific heat capacity, transition temperature, entropy change, latent heat, and can construct the entropy curves of EC materials.

In this section, we describe the DSC principle and the tool utilized. We will explain how the different caloric properties are obtained. Moreover, we will show the customized DSC used for isofield (constant electric field) and isothermal (constant temperature) calorimetric measurements under an electric field.

3.2.1 Differential Scanning Calorimetry

Differential Scanning Calorimetry (DSC) is a technique that uses a Differential Scanning Calorimeter (DSC) as an instrument to measure the change of the difference in heat flow rate to the sample and to a reference sample while subjected to a controlled temperature program. This definition was paraphrased from G.W.H. Hohne's [109] definition of DSC. This difference in heat flow occurs when the sample absorbs or releases heat i.e when the sample undergoes a thermal reaction such as phase transition, melting crystallization, chemical reaction, etc. The direct and primary measurement of a DSC measurement is the temperature difference between the sample and the reference. Heat flows only if there is a difference in temperature between the sample and the reference sample and their surroundings due to a sample transition. Therefore, a change in heat flow rate difference implies a temperature change. This is a mark by the appearance of a peak as shown in the heat flow rate measurement in Figure 3.4.

DSC enables fast and accurate measurements of samples in the mg range. One main feature of this differential technique, is its twin-type design as both the measuring system of the sample and reference sample are built identically. Both samples (preferentially of the same kind) are heated symmetrically. If the system is in steady-state equilibrium the temperature difference between both samples is zero. However, in the case of transition, a differential signal is generated. As shown in Figure 3.5 we distinguish two types of DSC: the power-compensation DSC and the heat-flux DSC [109–111].

In the power-compensation DSC, the sample and the reference sample are placed in two separate and identical furnaces. Separate heating elements are used to control the temperature of each furnace. Both furnaces are heated symmetrically. Separate thermocouples placed underneath the sample holders are used to measure the temperature of both samples. In the case of phase transition, power is supplied or removed from the sample furnace to compensate for the difference in temperature between the sample and reference sample, thereby maintaining thermal equilibrium. The power is proportional to the energy flow to and

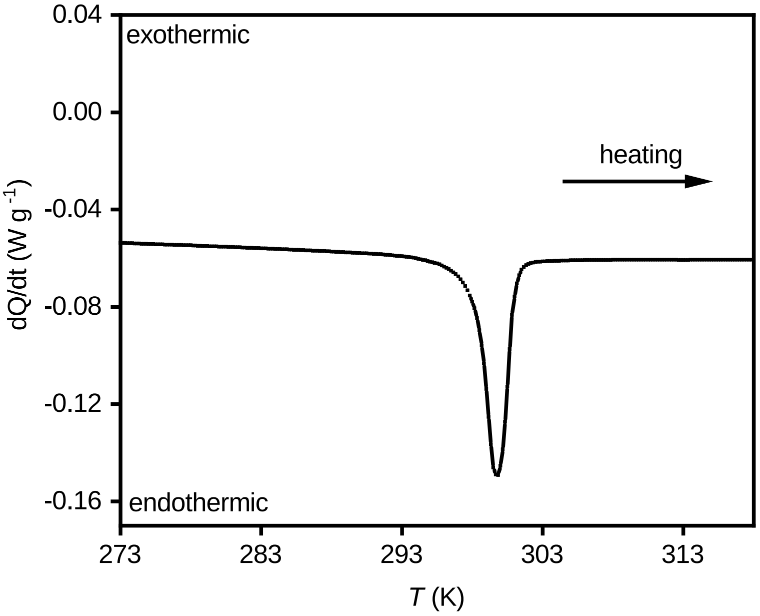

Figure 3.4: **Heat flow rate $\frac{dQ}{dt}$ measured.** This figure describes the heat flow rate of a ceramic sample measured as a function of temperature T. The sample presents a first-order transition described by the peak observed in the DSC measurement. The measurement was taken at a heating rate of $10\,\mathrm{K\,min^{-1}}$ using our DSC setup.

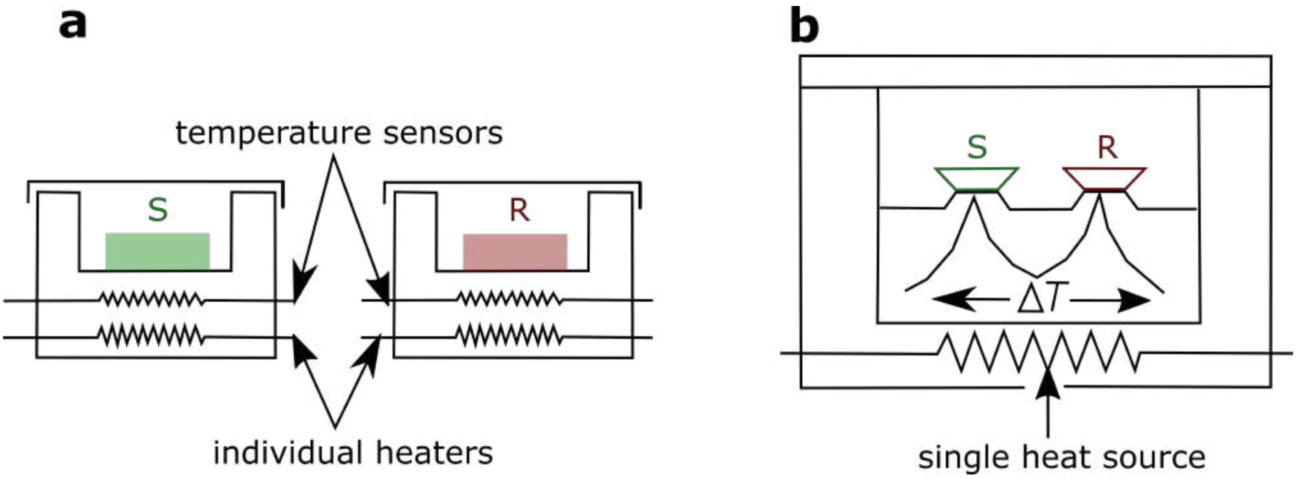

Figure 3.5: **Different types of Differential Scanning Calorimeters (DSCs).** S and R represent respectively the sample and the reference sample. **a** Power-compensated DSC. **b** Heat-flux DSC. This figure was adapted from [110].

from the sample. In the heat-flux DSC, the sample and reference sample are placed in a single furnace and are heated by thermal resistance through a well-defined heat conduction path. Thermocouples placed at the bottom of the sample holders measure the temperature difference. In the case of phase transition, an electric signal is generated. The heat flow is proportional to the temperature difference following thermal Ohm's Law. In this dissertation, we will mainly focus on the heat flux DSC which is the type of DSC we used here.

Let's consider the calorimeter in Figure 3.6. The sample **S** and the reference sample **R** are heated identically by heaters. We consider that there is no temperature gradient inside the sample. Using a control program, the temperature T of the calorimeter is changed. Here, the temperature scanning is done at a constant heating or cooling rate i.e linearly with time. Note that no external stimuli such as electric field are applied here. DSC under electric field will be presented in the following subsections. T can be written as:

$$T(t) = T_i + \alpha t \tag{3.6}$$

with T_i the initial temperature of the furnace, $\alpha = \frac{dT}{dt}$ the heating or cooling rate, and t the time.

The measured heat flow rate $\frac{dQ}{dt}$ is expressed as:

$$\frac{dQ}{dt} = \frac{dQ_i}{dt} + \frac{dQ_{C_p}}{dt} + \frac{dQ_0}{dt} \tag{3.7}$$

- $\frac{dQ_i}{dt}$ represents the heat flow rate from the unavoidable asymmetry of the DSC. This is often minimized. This is included in the baseline of the $\frac{dQ}{dt}$ in Figure 3.4.
- $\frac{dQ_{C_p}}{dt}$ is the heat flow rate caused by the difference in heat capacity between the sample and the reference sample. Similarly to $\frac{dQ_i}{dt}$, this term is included in the baseline of the heat flow rate measured.

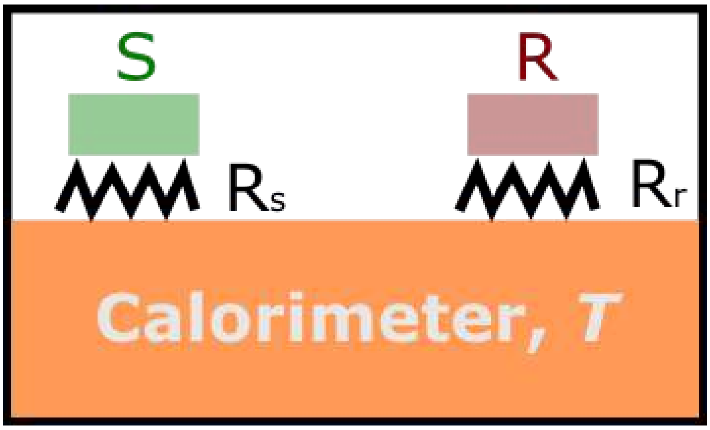

Figure 3.6: **Sketch of a calorimeter.** S and R represent respectively the sample and the reference sample. R$_s$ is the resistance between the sample and calorimeter and R$_r$ the resistance between the reference and the calorimeter.

- $\frac{dQ_0}{dt}$ stems from the transition (latent heat in case of first-order transition material) occurring in the sample. This last term represent the peak of $\frac{dQ}{dt}$ in Figure 3.4.

Following Ohm's Law, the heat flow is defined as:

$$\frac{dQ}{dt} = \frac{\Delta T}{R} \tag{3.8}$$

with the R the thermal resistance and ΔT the temperature difference between the sample and the calorimeter.

Now, let's supposed that the sample undergoes a thermal reaction such as transition therefore, the temperature difference ΔT between sample and reference will be non-zero. This will induce a heat flow of transition $\frac{dQ_0}{dt}$ in the sample. From the equation (3.7), we write the heat flow between the sample and the calorimeter as follows [112, 113]:

$$\frac{dQ_0}{dt} = C_S \frac{dT_S}{dt} + \frac{T_S - T}{R_S} \tag{3.9}$$

And the heat flow between the reference and calorimeter reads:

$$0 = C_R \frac{dT_R}{dt} + \frac{T_R - T}{R_R} \tag{3.10}$$

C_R and C_S are the heat capacities of respectively the reference sample and the sample. R_R and R_S are the thermal resistances of the reference sample and the sample respectively. As both samples are heated identically at the same heating or cooling rate, we consider they have the same resistance $R = R_R = R_S$ and both samples are heated or cooled at the same rate $\frac{dT_R}{dt} = \frac{dT_S}{dt} = \frac{dT}{dt}$. The temperature difference between the sample and the reference sample is then obtained by subtracting equations (3.9) and (3.10). The subtraction yields:

$$\frac{dQ_0}{dt} = (C_S - C_R)\frac{dT}{dt} + \frac{T_S - T_R}{R} \tag{3.11}$$

From equation (3.8) and (3.11), ΔT is then expressed as:

$$\Delta T = T(t)_S - T(t)_R = R\left(\frac{dQ_0}{dt} + (C_S - C_R)\frac{dT}{dt}\right) \tag{3.12}$$

In the case where $T_S > T_R$ the peak observed is endothermic and for $T_S < T_R$ the peak is exothermic.

The electric output Y provided to compensate for the temperature difference is proportional to ΔT. Then Y reads:

$$Y = B\Delta T$$

$$Y = S\left(\frac{dQ_0}{dt} + (C_S - C_R)\frac{dT}{dt}\right) \tag{3.13}$$

With $S = BR$ the sensitivity of the DSC and B is the proportional factor. By calibration, the electric output is converted into heat flow $\frac{dQ}{dt}$, which we measured. Therefore,

$$\frac{dQ}{dt} = \frac{Y}{S} = \frac{dQ_0}{dt} + (C_S - C_R)\,\frac{dT}{dt}$$

The heat flow measurements presented in this dissertation are written as $\frac{dQ}{dT}$. This done by dividing $\frac{dQ}{dt}$ by the heating or cooling rate $\frac{dT}{dt}$. Hence,

$$\frac{dQ}{dT} = \frac{dQ}{dt}\frac{dt}{dT} = \frac{dQ_0}{dT} + (C_S - C_R) \tag{3.14}$$

3.2.2 Our DSC setup

In this section we will describe the DSC setup used in this dissertation for heat flow measurement, heat capacities, latent heat and entropy change of EC materials without an electric field.

Figure 3.7 shows a sketch of our DSC setup utilized for zero-field calorimetric measurements. It includes a commercial DSC (DSC3) from METTLER TOLEDO, a CO_2 intracooler to cool down to -35 °C, and a computer to control the DSC. The DSC is a silver furnace that contains the sample and the reference holders. Each of them lays on a DSC sensor FRS 5+ presented in Figure 3.8. The sample's and reference's DSC sensors are identical. These sensors are made of 56 thermocouples that will measure the temperature of the sample and reference sample. The samples are heated with flat heaters (in red in Figure 3.7) placed on the sample and reference side. A thermocouple PT100 measures the temperature of the furnace. A computer is used to set the DSC parameters and launch heat flow measurements. A software STAR from Mettler Toledo was utilized to build the temperature program and analyze the data generated. Indium was used by the supplier (Mettler Toledo) to calibrate the DSC.

The furnace's temperature is set at the temperature of the intracooler (-35 °C) and can be increased to 500 °C. The temperature is regulated by heating the furnace to the desired temperature. Choosing the appropriate heating/cooling rates is crucial for heat flow measurements. One wants to run fast measurements while being able to observe precisely the material's features. The heating/cooling rate depends on the mass of the sample. The bigger the sample, the slower the heating/cooling rate, and the smaller the sample, the faster the heating/cooling rate. For a certain mass of material, its transition temperature can get

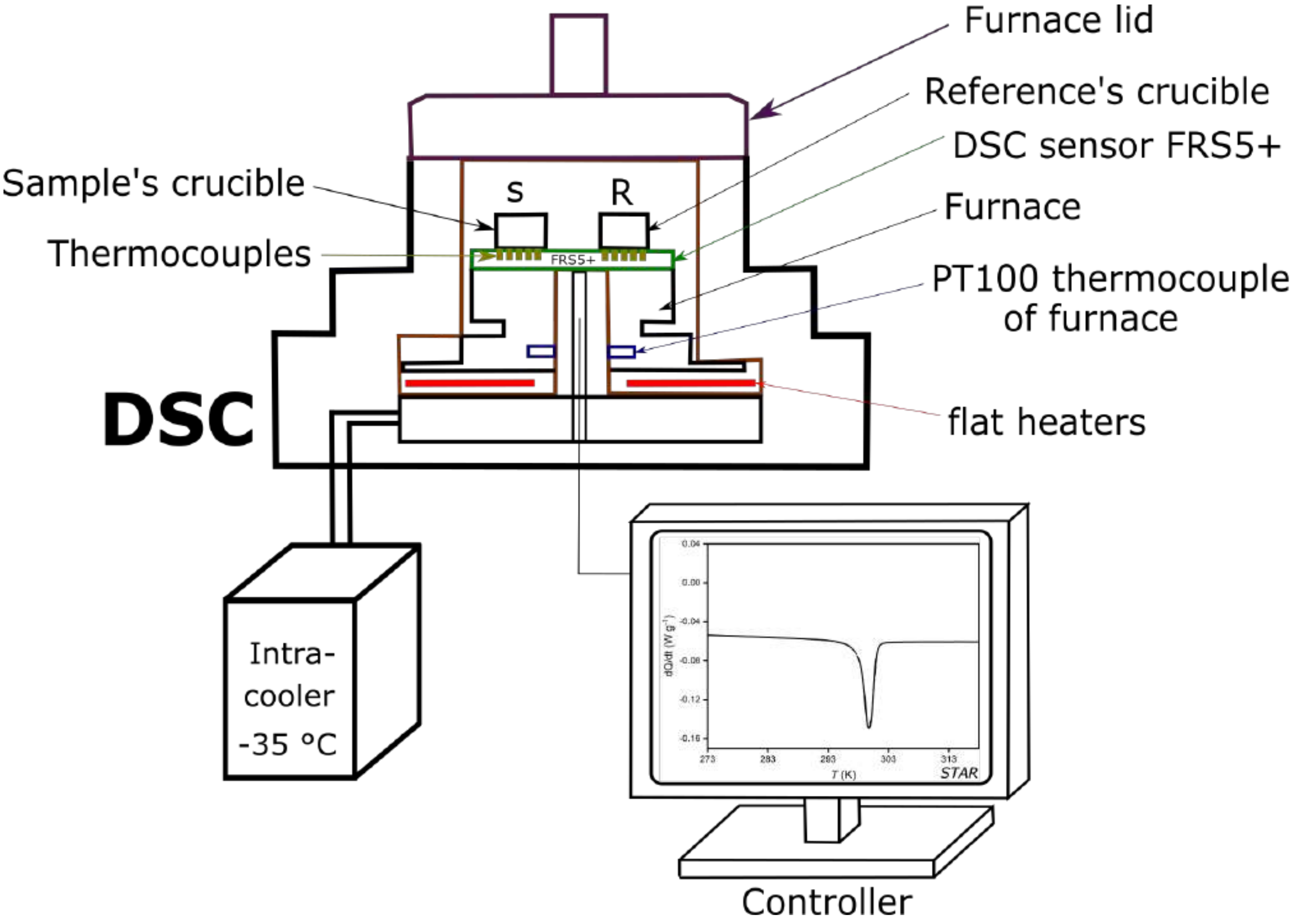

Figure 3.7: **Sketch of our DSC setup.**

shifted depending on the heating/cooling rate chosen. It is worth it mentioning that very slow measurements are good to get precise transitions in a material. However, this comes along with noises in the DSC signal. Heating rates of $5\,\mathrm{K\,min^{-1}}$ and $10\,\mathrm{K\,min^{-1}}$ were used in this dissertation for heat flow measurements.

DSC measurements are limited by the mass of the sample. To be able to measure accurate heat flow values, samples not bigger than 30 mg should be studied. Nevertheless, it is as well important to have some quantity to be able to observe a DSC signal. On our DSC, using the FRS5+ sensor, we were able to measure samples with masses in the range of 0.08 mg to 30 mg. For masses smaller than 0.08 mg one will measure a signal of $2\,\mu\mathrm{W}$

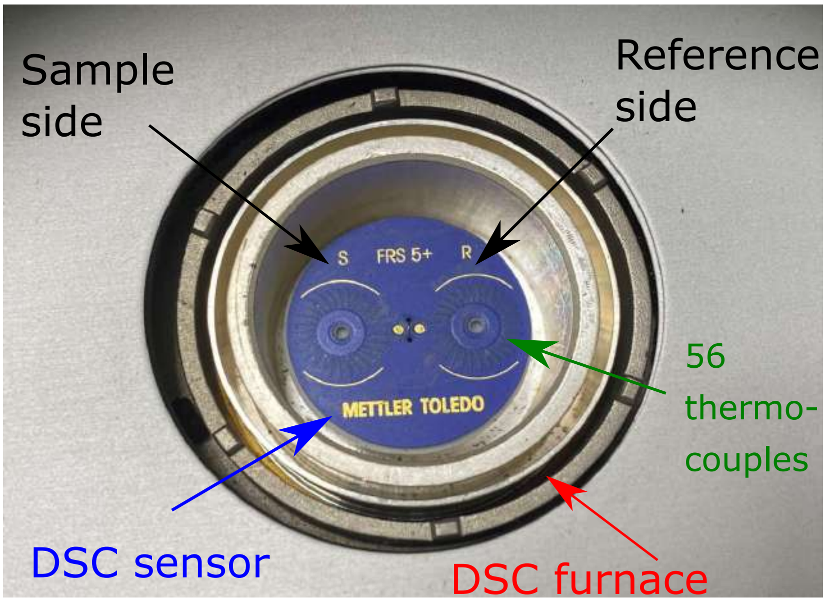

Figure 3.8: **Our DSC3's furnace.** This figure describes the furnace of our DSC3 from Mettler Toledo. It contains a ceramic DSC sensor FRS5+. 56 thermocouples are embedded on each side (sample side and reference side) of the DSC sensor.

which corresponds to the background noise of the FSR5+ sensor used here. For smaller masses, one should use a more sensitive sensor with lower background noise.

As part of this work, heat flow measurements were carried out on powder samples and bulk ceramic samples. The powder was put in 40 μL of Aluminium (Al) crucibles from Mettler Toledo. The Al crucibles facilitate the heat exchange between the calorimeter and the substance. Identical crucibles of the same mass were used for the sample and reference. Air was used as a reference sample for heat flow measurements as the reference's crucible was kept empty. The sample's crucible was filled with the powder sample to study. Bulk ceramic samples (mass smaller than 30 mg) were also characterized in this work. They were placed directly in contact with the DSC sensor. This was possible as the temperature ranges investigated in this dissertation were between -10 ℃ and 250 ℃ therefore, no risk for the ceramic samples to melt and consequently destroy the DSC sensor. The reference side was kept empty

Before any heat flow measurements, a cleaning program followed by a stabilization temperature program must be launched in DSC (furnace empty). The cleaning program heats the furnace from room temperature to 500 ℃ in order to burn any particles present in the DSC. This is important as the particles might affect future heat flow measurements. The stabilization program maintains the furnace's temperature at room temperature for at least 20 min to stabilize the DSC signal. Following these two runs, a temperature program should be created using the software STAR from Mettler Toledo. A temperature program includes linear dynamic and isothermal changes in temperature with time. Note that a sinusoidal or modulated temperature program can also be done. The modulated temperature change will not be studied in this dissertation. It is worth it mentioning that an isothermal of at least 2 min should be done between every dynamic to maintain the material's initial temperature stable. Following the temperature-programmed, heat flow measurements can be now carried out.

3.2.3 Latent heat and entropy change calculation

First-order transition materials are materialized by sharp peaks in the DSC heat flow measurements. The latent heat corresponds to the area of the peak. It is the energy absorbed (endothermic) or released (exothermic) by a first-order transition material to change its phase. From the DSC heat flow measurements against temperature, one can determine this latent heat. It represents the first term in the right part of the equation (3.14). To obtain accurate values of latent heat Q_0, a baseline is subtracted from the heat flow $\frac{dQ}{dT}$ as it is experimentally often displaced from zero. The baseline should follow $\frac{dQ}{dT}$ before and after the peak, where the $\frac{dQ_0}{dT}$ is zero. This enables separating $C_S - C_R$ and asymmetrical contributions of the DSC from the peak (latent heat). By integrating (trapezoid method) the heat flow $\frac{dQ}{dT}$ with the baseline value set at zero, one can determine the latent heat Q_0 of transition from one phase to another phase. Q_0 is expressed in Joules per kilograms.

$$Q_0 = \int_{T_a}^{T_b} \frac{dQ}{dT}\, dT \tag{3.15}$$

T_a and T_b are the temperatures chosen respectively before and after the peak on heating. On cooling, T_a and T_b are chosen respectively after and before the peak.

In Figure 3.9, we show an example of heat flow measurement done on a first-order transition material on heating and cooling. Due to the first-order transition of the material sharp peaks are observed in the heat flow scan. A baseline has been subtracted from the raw data of heat flow. The latent heat represents the area (yellow on heating and orange on cooling in Figure 3.9) under the peaks. The area under the peak is limited by well-defined temperatures before and after the peak.

The entropy change of transition ΔS_0 driven by temperature is determined using the equation below:

$$\Delta S_0 = \int_{T_a}^{T_b} \frac{1}{T} \frac{dQ}{dT} \, dT \tag{3.16}$$

3.2.4 Specific heat capacity measurements

The specific heat capacity (C_p) is one of the most important thermodynamic quantities. Expressed in Joules per Kelvin per kilograms, C_p is defined as the amount of energy needed to increase the temperature of 1 kg of material by 1 K. This quantity is important as it will be used in this dissertation to calculate the EC heat Q $(= m \, C_p \, \Delta T_{adiab})$. The specific heat capacity was experimentally measured using a DSC. Among the different standardized measurements used for the measurements of C_p, the three-step procedure is one of the most accurate techniques [109, 114]. In this section, we describe this classical procedure utilized in this dissertation to measure the specific heat capacity of different EC materials.

Suggested more than 30 years, the main idea of the three-step procedure technique is to compare the heat flow of a material with the heat flow of a calibration sample with a well-known C_p. In order to do so, this technique requires three measurements. Ideally, the sample and calibration sample should have the same mass. Before the three measure-

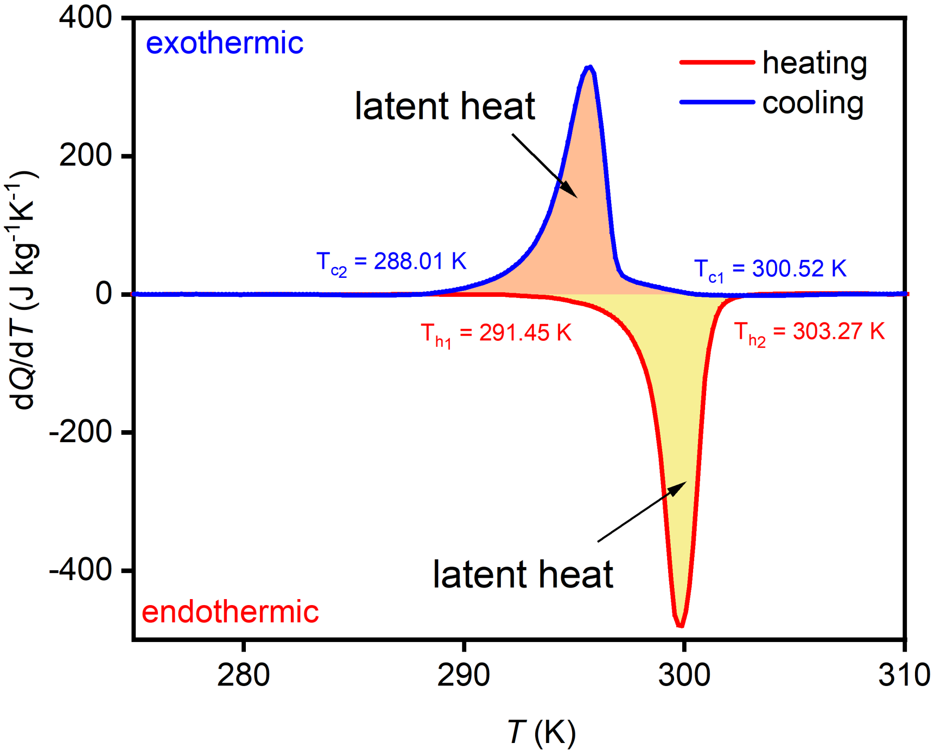

Figure 3.9: **Latent heat measurement.** An example of heat flow measurement $\frac{dQ}{dT}$ of a material that exhibits a first-order transition material described by sharp peaks on heating (red curve) and cooling (blue curve). A baseline spline was removed from the raw data of $\frac{dQ}{dT}$. The area under the peaks on cooling and heating is respectively the energy released (orange area) and absorbed (yellow area) by the material. T_{h1} and T_{h2} are the temperature chosen respectively before and after the heating peak.T_{c1} and T_{c2} bounds the cooling peak and are chosen after and before the cooling peak.

ments, a temperature program that will be used for all three has to be defined. The three measurements are:

1. The blank curve measurement is the heat flow measurement of the zero-line. This corresponds to DSC measurement against the temperature/time of the empty furnace i.e no samples on the sample and reference sides. If crucibles are being used, the blank curve is done with two empty crucibles (one on the sample side and the other on the reference side) of the same mass. It is important to first run the blank curve measurement as it shows the asymmetry of the DSC which, has to be removed from

the following measurements.

2. The heat flow measurement of the calibration sample is done against temperature/time. This sample is placed on the sample side. The reference side stays empty. In the case crucibles are being used, the calibration sample is put in the sample's crucible and the reference's crucible is kept empty. Preferentially, the same crucibles utilized for the blank curve measurement should be used here. The most common calibration samples used for C_p measurements are sapphire or copper. In this dissertation, sapphire purchased from METLLER TOLEDO, was used for C_p measurements.
3. Heat flow measurement of the sample. The calibration sample is replaced by the sample and the DSC measurement is done following the same temperature program as in the two other measurements.

Figure 3.10 shows the three-step procedure carried out to determine the specific heat capacity of a material on heating and cooling. The temperature program described in Figure 3.10c, consists of 5 steps.

1. an isothermal run of 5 min at -10 ℃
2. dynamic heating at a heating rate of 5 K min^{-1} from -10 ℃ to 50 ℃
3. a second isothermal run of 5 min at 50 ℃
4. a dynamic cooling at 5 K min^{-1} from 50 ℃ to -10 ℃
5. finally a last isothermal run of 5 min at -10 ℃

Following this temperature program (3.10c), a blank curve (Figure 3.10a), the heat flow of the sample (red curve in Figure 3.10b), and the heat flow of calibration sample (black curve in Figure 3.10b) were done against temperature/time.

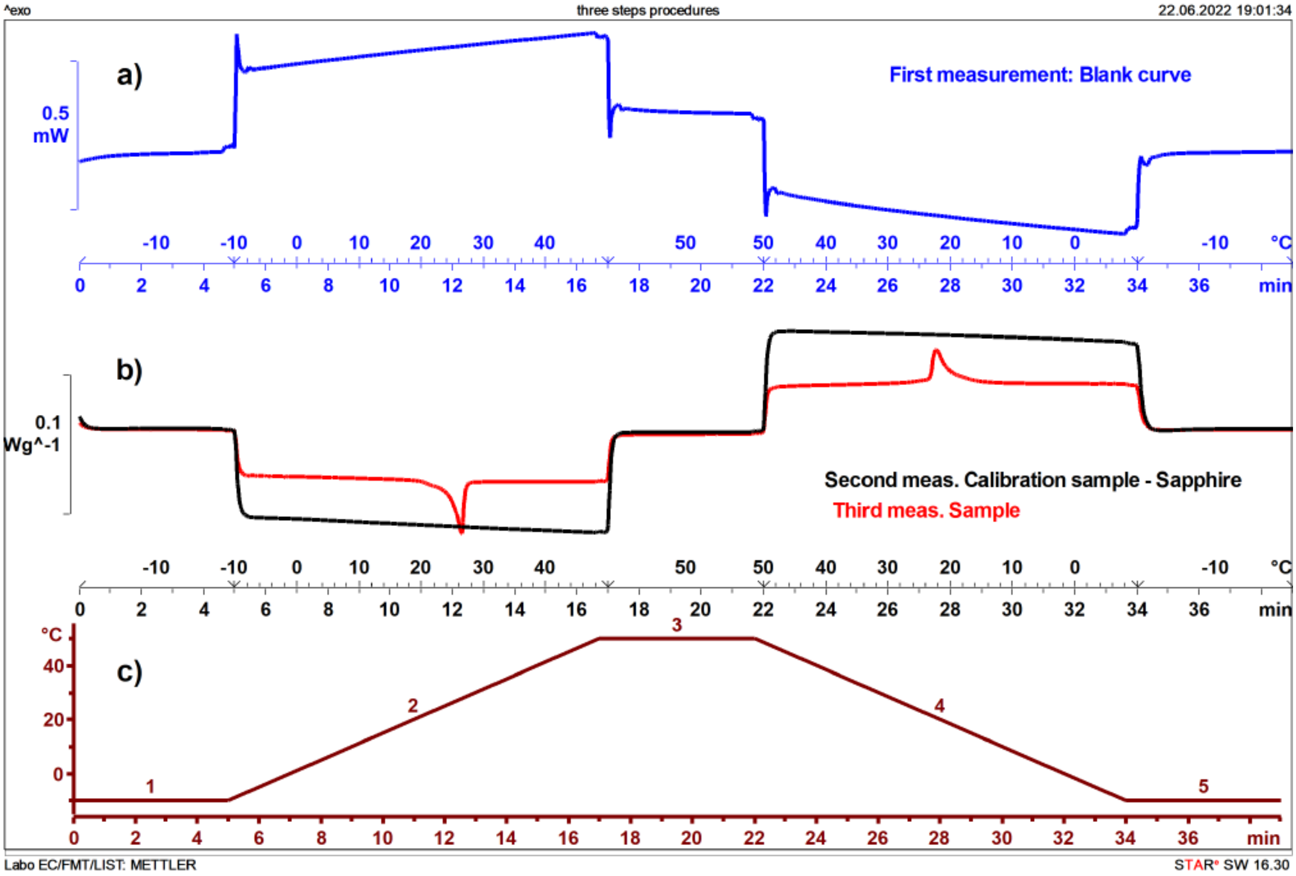

Figure 3.10: **Three-step procedure for specific heat capacity.** An example of three-step procedure carried out to determine the specific heat capacity of a sample. Here the measurements were done a first-order transition material. Heat flow measurements of blank curve (**a**), sample (red curve in **b**) and calibration sample (black curve in **b**) as a function of time and temperature. **c** Temperature program used to the three measurements.

The specific heat capacity C_p is then calculated using the equation below:

$$C_S = \frac{HF_S - HF_{blank}}{HF_{ref} - HF_{blank}} \frac{m_{ref}}{m_S} C_{ref} \tag{3.17}$$

with HF standing for the heat flow ($\frac{dQ}{dT}$),

- HF_S is the sample's heat flow
- HF_{blank} is the heat flow of the zero-line or blank curve
- HF_{ref} is the calibration sample's heat flow
- C_{ref} is the well-known specific heat capacity of the calibration sample.

3.2.5 DSC under electric field

Heat flow measurements were carried out under electric field to determine different properties (latent heat, isothermal entropy change, entropy curves) of EC materials when driven by an electric field. In this section we will describe the setup used to measure heat flow under an electric field and the methods used to calculate these different thermal properties.

The DSC utilized for zero-field measurements in Figure 3.7 was customized for DSC under electric field. As shown in Figure 3.11, a power supply Keithley 2410 was used to control the field applied or removed. A perfectly flat sample should be used to guarantee a good thermal contact between the sample and the DSC sensor. Thin layers of electrodes (silver paste), were deposited on both surfaces of the sample (inset image in Figure 3.11). The same silver paste was used to maintain the thin copper wires (red and black in Figure 3.11) on the top and bottom sides of the sample. It is worth mentioning that only the two ends of the copper wires should be electrically conductive. One end is connected to the sample and the other end to the power supply. The wires should be long enough as they pass through the furnace lid to reach the power supply. Between these two ends the cable should be insulated as the DSC contains several metallic parts. Kapton tape was placed in direct contact with the DSC sensor for two reasons. Firstly, the kapton tape ensures a good thermal contact and electrical insulation. Secondly, it protects the DSC sensor from any contamination (silver paste for instance). Moreover, an empty ceramic crucible can be used to improve further the thermal contact between the sample and the DSC sensor. It is put on top of the sample. For symmetric reasons, the same kapton tape was put on the reference sample side and an identical ceramic crucible was placed on the reference. Air was used here as a reference for our measurements.

Two types of DSC measurements were done under an electric field in this manuscript: isofield and isothermal measurements.

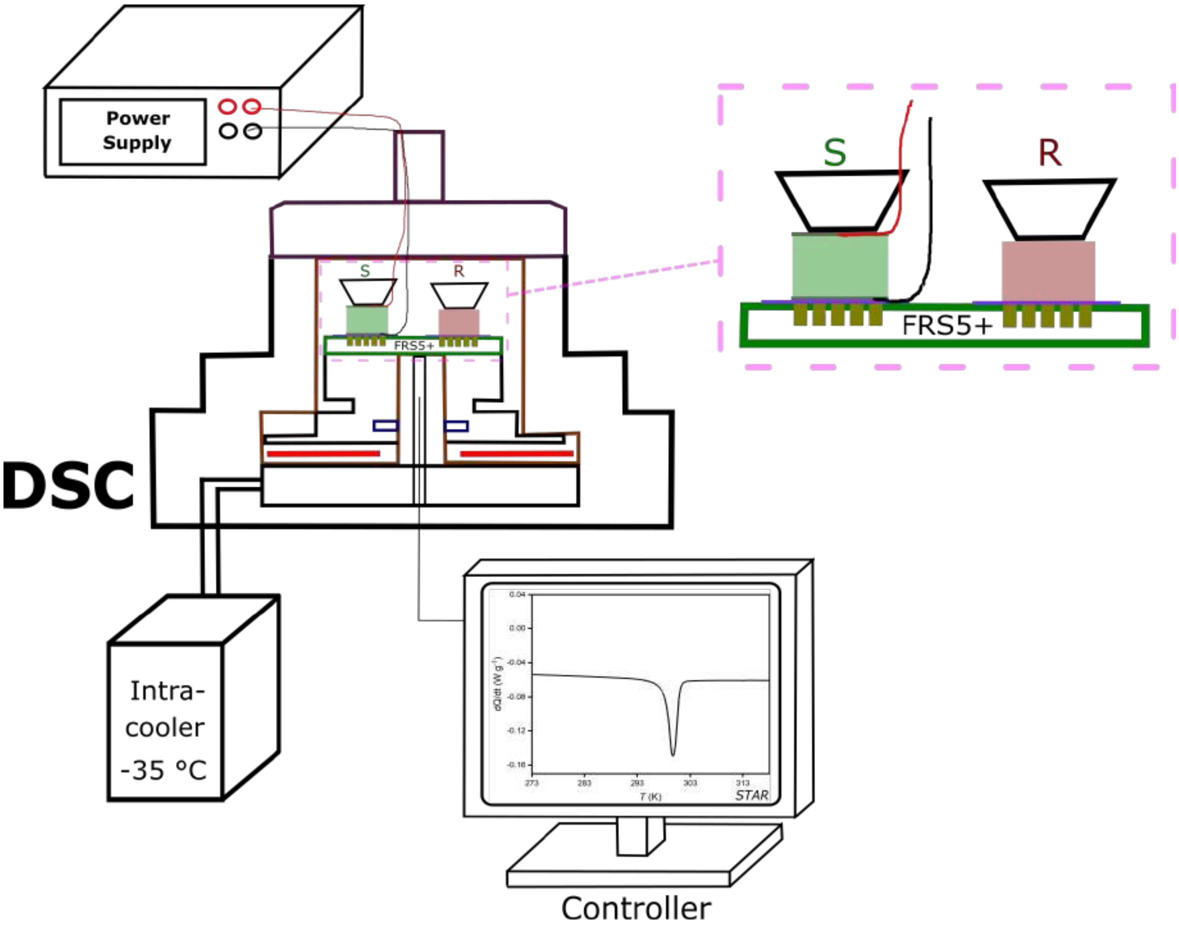

Figure 3.11: **DSC under electric field setup.**

Isofield measurements

Isofield measurements consist of heat flow measurements at constant electric field when sweeping in temperature. In other words, a constant electric field is kept in the sample during the temperature program. These measurements enable quasi-direct measurements of heat Q_0, by integrating with respect to temperature T, the heat flow measurements $\frac{dQ(T,E)}{dT}$ at constant electric field E.

$$Q_0(E) = \int_{T_a}^{T_b} \frac{dQ(T,E)}{dT}\,dT \tag{3.18}$$

T_a and T_b are the temperatures chosen respectively before and after the peak on heating.

On cooling, T_a and T_b are chosen respectively after and before the peak.

From isofield measurements of the sample's specific heat capacity C_p and heat flow measurements $\frac{dQ}{dT}$, one can construct the *S*-*T* diagram of EC materials. This diagram corresponds to the entropy curves $S'(T, E)$ as a function of temperature at different electric field. $S'(T, E)$ is the entropy of the material referenced to the absolute entropy at T_{ref} i.e that $S'(T_{ref}, E) = 0$. T_{ref} is chosen far below the transition temperature. $S'(T, E)$ is expressed as:

$$S'(T,E) = S(T,E) - S(T_{ref},E) =$$

$$\begin{cases} \displaystyle\int_{T_{ref}}^{T} \frac{C_p(T',E)}{T'}\,dT' & \text{for } T \le T_a \\[2em] \displaystyle S(T_a,E) + \int_{T_a}^{T} \frac{C_p(T',E)}{T'}\,dT' + \frac{dQ(T',E)}{T'}\,dT' & \text{for } T_a \le T \le T_b \\[2em] \displaystyle S(T_b,E) + \int_{T_b}^{T} \frac{C_p(T',E)}{T'}\,dT' & \text{for } T \ge T_b \end{cases} \tag{3.19}$$

with T_a and T_b defining the temperatures bounding the transition peak.

As shown in Figure 3.12, the isothermal entropy change $\Delta S_{isothermal}$ is calculated by subtracting the entropy curves S' at a given electric field E with the entropy curve at zero field. ΔS under the application of E writes:

$$\Delta S_{isothermal}(T,E) = S'(T,E) - S'(T,0) \tag{3.20}$$

The adiabatic temperature ΔT_{adiab} can be estimated by following the isentropic contours of the *S*-*T* diagram as shown in Figure 1.1 and 3.12.

In the case of materials presenting large thermal hysteresis, reversible ΔT_{adiab} and $\Delta S_{isothermal}$ should be determined from the heating $S'(T, E = 0)$ and the cooling $S'(T, E)$ [66].

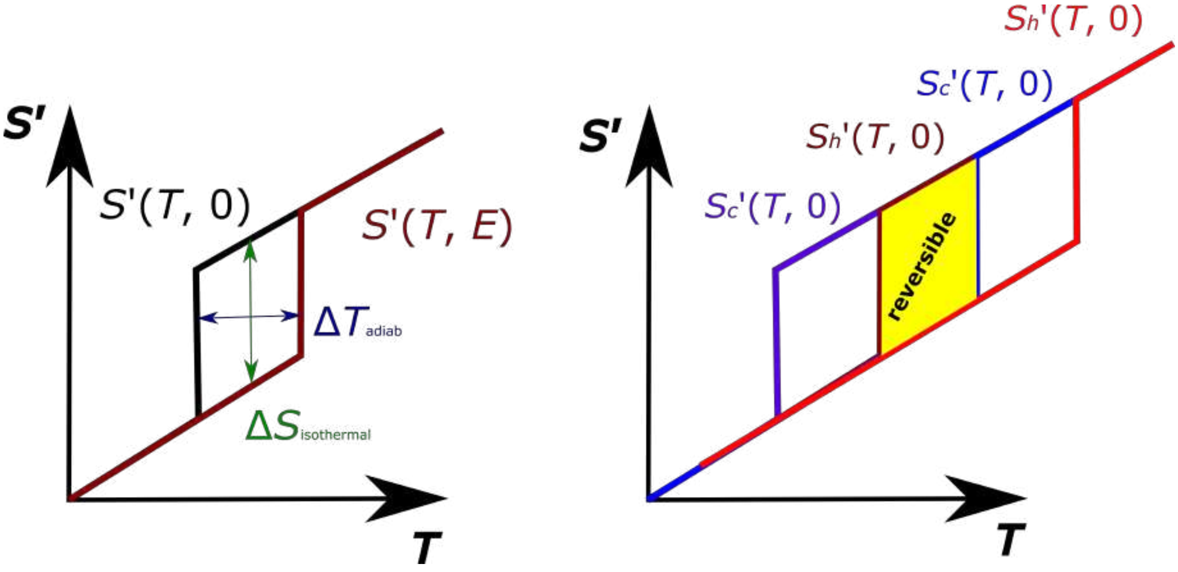

Figure 3.12: ***S*-*T* diagram.**

Isothermal measurements

Isothermal measurements are obtained by applying very slowing an electric field in the sample in order to maintain its temperature constant. An isothermal temperature program was done using the STAR software from Mettler Toledo and the speed of the application of the field is control by the current applied. The current is chosen slow enough for the temperature to be constant or quasi-constant. The heat Q is obtained by integrating the DSC signal $\frac{dQ}{dt}$ presented in Figure 3.13. The isothermal entropy is deduced by dividing the heat to the temperature at which it occurs: $\Delta S_{isothermal} = \frac{Q}{T}$. From the baseline value of specific heat capacity, one can deduce a value of ΔT_{adiab} using the equation: $\Delta T_{adiab} = Q/C_p$.

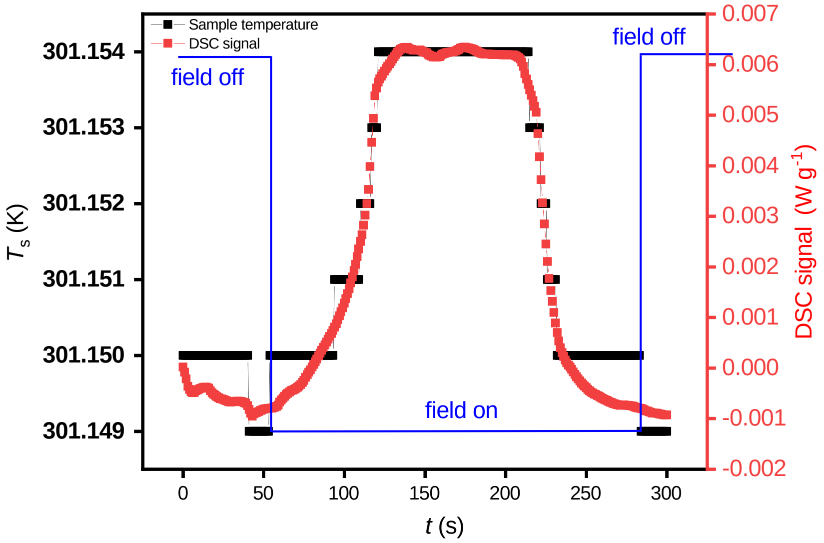

Figure 3.13: **Isothermal heat flow measurements.**

3.3 X-Ray Diffraction (XRD)

X-Ray Diffraction (XRD) is one of the most used techniques to characterize the crystallographic structure of a material. XRD is based on the irradiation of the crystalline sample with incident X-rays. The interaction of the x-rays (electrons) with the crystal atoms leads to a constructive interference observed by applying the following Bragg's law [115–117].

$$2\,d\,sin\theta = n\,\lambda \tag{3.21}$$

With d the spacing between the diffracting planes, θ the incident angle, n the diffraction order integer, and λ the wavelength of the beam.

The diffractometers utilized in this dissertation use copper (Cu) K_{alpha} radiation $\lambda = 1.54\,\mathring{A}$. From a cathode ray tube, a beam of x-rays is generated and bombarded toward the sample. These x-rays passed through the sample and are diffracted by the sample's atoms. Constructive interference occurs when the geometry of the incident x-rays satisfies equation 3.21. The diffracted x-rays are recorded and processed by a detector. Our configuration is such a way that the sample rotates in front of the bombarded x-ray beam at an angle of θ while the detector collects the diffracted x-rays at an angle of 2θ. The corresponding x-ray

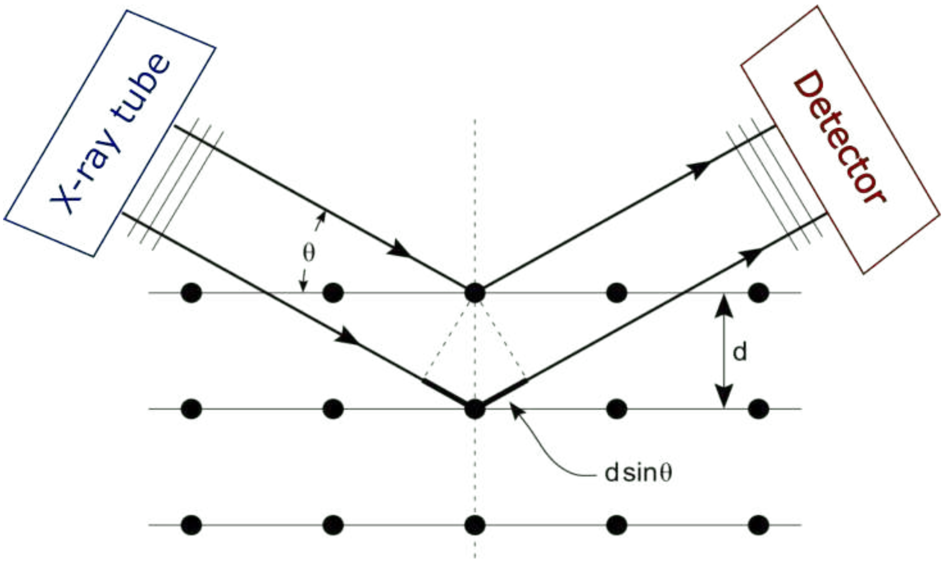

Figure 3.14: **X-Ray Diffraction mechanism.** d is the spacing between the diffracting planes and θ represents the incident angle. This figure was adapted from [117].

signal is converted into counts. When θ matches λ following Bragg's law, a peak appears. The intensity of the peaks observed as a function of 2θ, describes the structure of the material.

In this dissertation, we have used two diffractometers: PANalytical X'Pert Pro and Bruker D8 Discover. The XRD measurements were often done on powdered samples to avoid any preferential orientations.

3.4 Scanning Electron Microscopy (SEM)

A scanning electron microscope is one of the electron microscope techniques used to observe and analyze the surface (or just beneath) of a sample [118, 119]. As described in Figure 3.15a, this is possible by scanning the sample's surface with a focused beam of high-energy electrons. When the incident beam of electrons enters the sample, various signals such as X-rays, backscattered electrons, Auger electrons, secondary electrons, and cathodoluminescence are emitted from the specimen [120, 121]. A secondary electron detector is used to collect the secondary electrons emitted by the specimen. From the secondary electron signal, a SEM image describing the sample surface is formed. In this dissertation, SEM was used to visualize the structure of a multilayer capacitor as shown in Figure 3.15b.

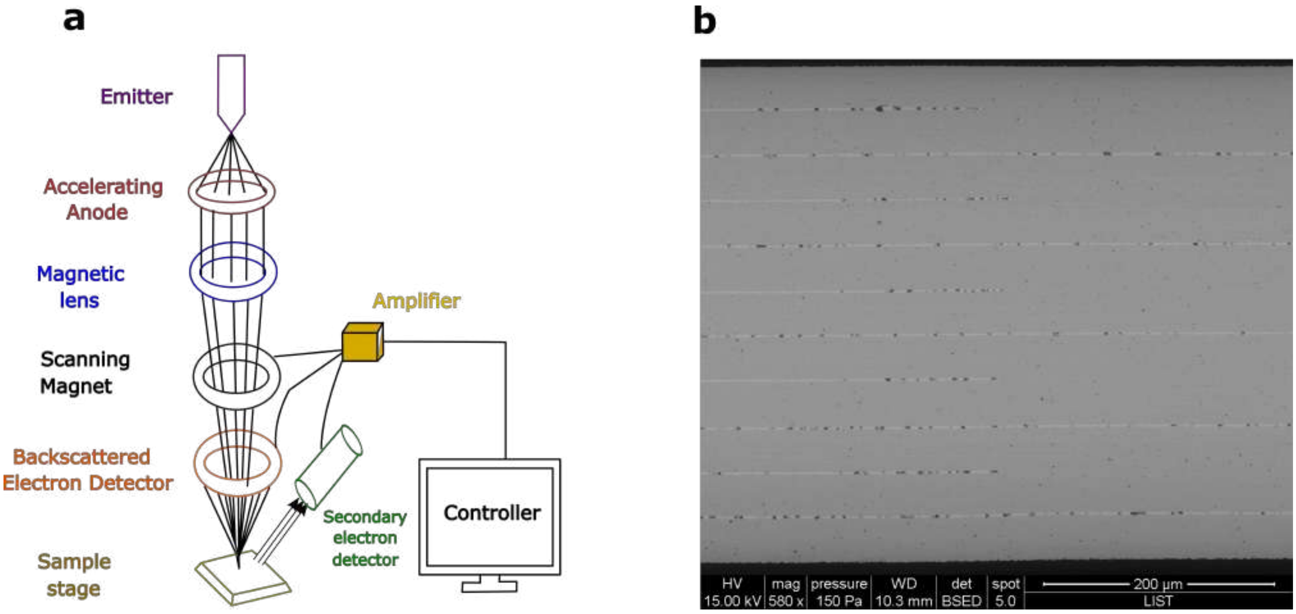

Figure 3.15: **Scanning Electron Microscope a** Basic mechanism of a SEM. This image was adapted from [122]. **b** Example of a SEM image showing the structure of a multilayer capacitor of lead scandium tantalate. From this image the different dimensions (length, width, thickness) of the sample were calculated.

In this dissertation, we have used a Quanta 200 Field Emission Gun Scanning Electron Microscope (FEG SEM) from Philips-FEI. It was used to collect structure images of the PST MLC. The microscope is equipped with a Genesis XM 4i Energy Dispersive Spectrometer (from EDAX) system for chemical analysis. From the backscattered electron detector, pictures of the chemical composition of the observed sample result (composition mode). The contrast of the picture is based on the convention that ”heavier” element areas (high atomic number Z, for example, ZSn=50 compared to ZNa=11) are shown in light grey and low atomic number elements in darker grey.

3.5 Electrical characterization

Electrical measurements were carried out to evaluate the dielectric permittivity and the response in polarization as a function of the electric field. In the following sections, we will describe the principle of each technique and the tools utilized.

3.5.1 Dielectric permittivity

The impedance spectroscopy or dielectric spectroscopy is a tool used to study the dielectric properties and electrical conductivity of a material when subjected to an electrical field at a given frequency. It provides information on the relative permittivity or dielectric constant and dielectric losses of a material as a function of temperature for instance. This will enable us to determine the transition temperature of a material. The dielectric constant ε measures the amount of energy from the external field applied that a material can store and $\tan\delta$ measures how lossy a material is to an electric field.

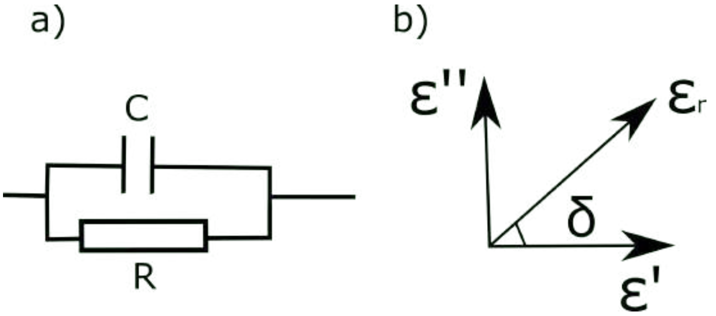

Figure 3.16: **Dielectric constant mechanism a** RC parallel circuit **b** Complex permittivity vector in a complex plane. ε' is the real part, ε'' is the imaginary part and δ is the angle between the sum vector and the real part ε'. The tan δ represents the dielectric losses.

In an RC parallel circuit (Figure 3.16a) made of a capacitor (dielectric material between two metallic plates) and resistance, the relative permittivity ε_r is a complex quantity defined as follows:

$$\varepsilon_r = \varepsilon' - i\,\varepsilon'' \tag{3.22}$$

With i the imaginary unit, ε' the real part which represents the dielectric constant, and ε'' the imaginary part.

From the measurement of the capacitance C, one can obtain the dielectric constant ε'. C is defined as the variation of charge Q to the variation of voltage V.

$$C = \frac{\partial Q}{\partial V}$$

with $Q = A.D$, A the area of the capacitor, and D the electrical displacement. In the case of dielectric materials, $D = \varepsilon_0 E + P = \varepsilon_0 \varepsilon' E$. ε_0 is the vacuum permittivity, P the polarization proportional to $\varepsilon' E$. The electric field E can be written as the ratio of the voltage V to the thickness of the capacitor e.

Therefore the capacitance is written as:

$$C = A\,\varepsilon_0\,\varepsilon'\,\frac{\partial E}{\partial V} = \frac{A\varepsilon_0\varepsilon'}{e} \tag{3.23}$$

Hence the dielectric permittivity is:

$$\varepsilon' = \frac{e}{A\,\varepsilon_0} C \tag{3.24}$$

The dielectric losses tan δ also called loss tangent is defined as the ratio of the imaginary part of the permittivity to its real part. As shown in the Figure 3.16b the angle δ represents the angle made by the vector sum (ε_r) and the real part of the complex permittivity.

$$tan\,\delta = \frac{\varepsilon''}{\varepsilon'} = \frac{1}{RCw} \tag{3.25}$$

where ω is the angular frequency, R the resistance, and C the capacitance.

In this dissertation, we used a Novocontrol Concept 40 to measure the dielectric constant of EC materials. These measurements were carried out as a function of temperature at a frequency of 100 Hz. The temperature was controlled with a cryogenic probe. The dielectric constant measurement performed enables observing transition(s) in our EC materials, thereby deducing the transition temperature.

3.5.2 Polarization – Electric field

The measurements of the ferroelectric hysteresis loop in EC capacitors have been carried out using two methods. The historical Sawyer-Tower circuit and the modern tool aixACCT TF Analyzer 2000. We will describe both techniques in the following.

Sawyer-Tower Circuit

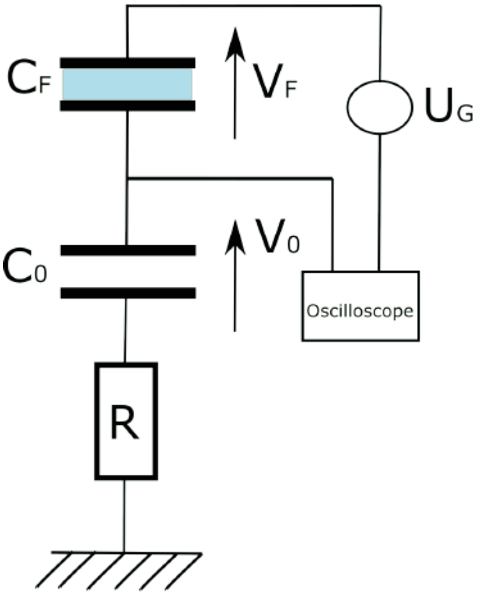

Figure 3.17: **Sawyer-Tower circuit**

Named after his inventors in 1930, the Sawyer-Tower circuit is an electrical circuit that enables the measurement of hysteresis loops of a ferroelectric material [123, 124]. This circuit consists of two capacitors and a resistance mounted in series as shown in Figure 3.17. One of these capacitors is our FE capacitor made of a ferroelectric dielectric material sandwiched with electrodes. The other capacitor is a linear reference capacitor with a well-known capacitance C_0. This capacitance C_0 is chosen much greater than the capacitance

C_F of the FE material so that the voltage applied in the whole circuit is almost equal to the voltage (V_F) across the FE material. In other words,

$$R \ll Z_0 \ll Z_F$$

with Z_0 and Z_F, respectively the impedance of the reference and FE capacitor.

The application of a voltage in the circuit induces polarization switching in the FE material. This polarization P corresponds to the number of charges Q_F per surface A on the FE capacitor. Therefore:

$$P = Q_F/A \tag{3.26}$$

As the charges of both capacitors are identical ($Q_F = Q_0$), one can write $U_F C_F = U_0 C_0$. This implies that:

$$U_0 = \frac{Q_F}{C_0}$$

Therefore, the polarization loops are obtained by measuring the voltage across the reference capacitor as a function of the electric field $E = \frac{U_F}{e}$ with an oscilloscope for instance. e is the thickness of the FE material.

In this dissertation, we used a homemade Sawyer-Tower to measure the change of polarization in bulk ceramic PST at a frequency of 18 Hz.

This technique suffers from the fatigue of the FE material as several cycles are launched to get PE loops. Besides, due to the parasitic capacitances (cables for example), the Sawyer-Tower circuit is less suitable for small capacitances. Hence, modern tools were created such as aixACCT TF Analyzer 2000 which is based on the virtual-ground feedback method.

AixACCT TF Analyzer 2000

In this setup, a triangular bipolar voltage is applied to the sample and a switching current due to the switching of polarization is measured. The corresponding charges are calculated by integrating the switching current over time. Therefore polarization P is obtained using the relation below:

$$P(t) = \frac{1}{A} \int i(t) dt \tag{3.27}$$

With A the surface of the capacitor. This technique offers almost no parasitic capacitances and is much faster than a Sawyer-Tower.

This tool was used to measure PE loops in PST MLC. Tips were used to connect the two terminals of the MLC. Using an amplifier different voltages up to 400 V were applied. The measurements were done at the frequency of 100 Hz and in the temperature range from 283 K to 323 K.

Chapter 4

Giant electrocaloric efficiency of highly ordered lead scandium tantalate

4.1 Motivation

In the late 90s, Lead Scandium Tantalate $\mathrm{PbSc_{1/2}Ta_{1/2}O_3}$ – short form PST was found to be a good candidate for thermal detectors [125] [126] and electrocaloric cooling/heating devices [52]. Its strong pyroelectric response [127] [128] suggests large electrocaloric effect (ECE) and its transition temperature around room temperature makes it interesting for applications [17] [6] [25]. The quest for high performant electrocaloric (EC) materials and EC prototypes has recurred; hence, the increase of publications in the last five years on PST for EC applications. However, its intrinsic or materials efficiency [34] [33] which plays a role in the efficiency of the prototypes [24] remains overlooked. As detailed in Chapter 2, the materials efficiency η_{mat} is the ratio of the EC heat *Q* exchanged by an EC material with its surroundings to the electrical energy used to drive this heat.

In this chapter, η_{mat} of a highly ordered PST, in the shape of bulk ceramic is studied. We will first present in Section 4.2, a background on the perovskite material PST. Secondly, we will study the structural, electrical, and thermal properties of the highly ordered bulk PST in Subsection 4.3.2. Subsequently, the results on the ECE of this material obtained by infrared (IR) imaging and differential scanning calorimetry (DSC) under electric field will be discussed in 4.3.3. We will then show in 4.3.5, the materials efficiency of PST bulk ceramic calculated from the direct characterization of electrical work W_e and EC heat Q. Similarly, we will calculate in 4.3.6, the materials efficiency of the benchmark magnetocaloric (MC) material Gadolinium (Gd) using data collected from the Technical University of Denmark (DTU). Finally, a comparison in terms of energy efficiency of the PST bulk ceramic to Gd will be presented in 4.3.7.

The results shown in this chapter have led to the publication of my first authorship publication: Y. Nouchokgwe, P. Lheritier, C.-H. Hong, A. Torello, R. Faye, W. Jo, C. R. H. Bahl, and E. Defay, “Giant electrocaloric materials energy efficiency in highly ordered lead scandium tantalate”, Nature Communications 12, 3298 (2021). This work was done in collaboration with the School of Materials Science and Engineering from the UNIST (Ulsan national institute of Science and Technology) in South Korea and the Department of Energy Conversion and Storage of DTU in Denmark.

4.2 Lead Scandium Tantalate - PST

Lead scandium tantalate is a ferroelectric (FE) material with a transition temperature T_0 around room temperature, between 295 K and 300 K . It exhibits a first-order displacive transition, from a FE phase at lower temperature to a paraelectric (PE) phase at higher temperature [52, 53, 55, 129–132]. PST has a perovskite structure ABO_3 (Figure 4.1a). The A-site cation is occupied by Lead (Pb^{2+}) ions and the B-site cation is shared between Scandium (Sc^{3+}) and Tantalate (Ta^{5+}) ions. The arrangement between Sc^{3+} and Ta^{5+} defines the B-site ordering of the PST structure [133–136]. An ordered PST has a 1:1 ordering structure where Sc^{3+} and Ta^{5+} alternate in adjacent B-site leading to a double unit cell as shown in Figure 4.1b.

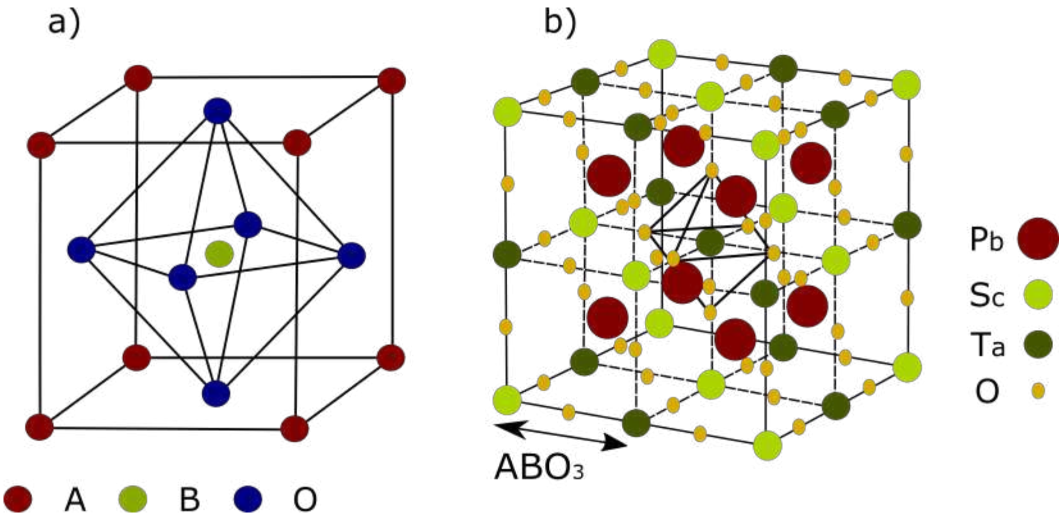

Figure 4.1: **Perovskite structure of $PbSc_{1/2}Ta_{1/2}O_3$. a** A simple cubic perovskite unit cell. **b** Perovskite crystallographic structure of ordered $PbSc_{1/2}Ta_{1/2}O_3$. This image was adapted from [137]. Here, the B-cation is share between two atoms (Sc and Ta) thereby doubling the ABO_3 unit cell. Sc and Ta alternate at the corners of the unit cell.

On the contrary, a random distribution of Sc^{3+} and Ta^{5+} gives a disordered PST [138]. The degree of ordering in PST can be detected in X-Rays Diffraction (XRD) patterns by the presence of superlattice peaks (111) at 19-degree angle [52, 135, 138–140]. It is quantified by the value of the long-range order parameter Ω . In the case of a perfectly ordered PST, Ω = 1 and for a disordered PST, Ω = 0. This parameter can be calculated from the intensities peak of the XRD peaks of the lattice (200) and superlattice (111) using equation (4.1) below.

$$\Omega^2 = \frac{(\frac{I_{111}}{I_{200}})_{exp}}{(\frac{I_{111}}{I_{200}})_{theory,\Omega=1}} \tag{4.1}$$

The CoK_α radiation $(\frac{I_{111}}{I_{200}})_{theory,\Omega=1}$ is equal to 1.4, for perfectly ordered PST [52].

Stenger et *al.* studies [133, 134, 136] have shown that the FE to PE transition observed in PST compounds is strongly correlated with the degree of ordering of the Sc^{3+} and Ta^{5+}. The modification of Ω induces some changes in the electrical (dielectric response)[141–143] and thermal properties (latent heat) [133] of PST. They showed that disordered PST presents relaxor to FE transition, accompanied by a diffuse phase transition (broad transition on a large temperature range). Besides, it was observed that the decrease in the degree of ordering increases the maximum dielectric permittivity and reduces the value of latent heat [55, 133, 139]. The degree of ordering can be improved by increasing the annealing time and temperature. To get high Ω, the PST compounds are annealed at temperatures greater than or equal to 1000 ℃ at different time lengths between 4 and 100 hours [131, 133, 138]. The increase of the degree of order sharpens the peak and a FE to PE transition is observed in ordered PST. This goes along with a diminution of its dielectric constant and an increase of its latent heat.

Oxides lead-based materials are known to be good EC materials i.e they present larger adiabatic temperature change ΔT_{adiab}, larger latent heat Q, or larger isothermal entropy change ΔS than the non-lead EC materials [6, 17]. The ECE of PST has firstly been studied in the late nineties and beginning 2000s by Shebanov and co-authors [52–55]. PST shows a conventional ECE around room temperature. As the ECE is the converse pyroelectric effect, the high pyroelectric coefficient $\frac{\partial P}{\partial T}$ of PST around room temperature [144] makes it interesting for EC cooling applications [145–147] [32, 72, 148].

The ECE in PST results from the field induced first-order transition from PE to FE phase. From Ω = 0 to Ω = 0.85, they showed that the ECE in PST increases with the degree of ordering [55]. At the 25 kV cm^{-1}, they measured broad peaks in ΔT_{adiab} of 0.18 K and 0.5 K in respectively two disordered PST samples of Ω = 0 and Ω = 0.34 [55]. In 2002, they measured a larger ΔT_{adiab} = 2.3 K in an ordered PST (Ω = 0.85) at an electric field as large as 50 kV cm^{-1} [54]. In fact, the transition temperature of PST is shifted towards high temperatures as the degree of order increases [133]. This limits its use in applications to high temperatures. However, Shebanov et *al.* [55], have shown that by doping PST with ions one can shift the transition temperature towards low or high temperatures while keeping a high ECE. Large ECE at low temperature (250 K) is obtained by doping the PST with Sb^{5+}, Co^{3+}, Y^{3+} and, high temperature (310 K) applications are reachable with PST doped Nb and Ti. More than a decade later, the ECE in PST bulk was studied by Crossley et *al.* [129], at the Materials Science department of the University of Cambridge. They measured directly in a PST bulk ceramic (Ω=0.80), a temperature change of 2.2 K at the low electric field of 26 kV cm^{-1}. Lately, the same group has measured a large ΔT_{adiab} of 5.5 K in PST Multi-Layer Capacitors (MLCs) when driven super-critically at 290 kV cm^{-1} [29]. This is so far the largest temperature change reported in a macroscopic EC material. In 2020, two papers [32, 72] were issued simultaneously in *Science*, demonstrating the potential of using PST in the shape of MLCs to build EC devices. Wang et *al.* [72] reported on an EC device of 8 K in temperature span and we showed that an EC prototype built using 128 PST MLCs can reach a giant temperature span of 13 K [32], the highest value obtained up-to-date in an EC device. ECE was also studied in relaxor thin film of disordered (Ω=0.32) PST [59]. Correia et *al.* measured indirectly through Maxwell relations at 774 kV cm^{-1}, an entropy change $|\Delta S|$ = 6.3 J K^{-1} kg^{-1} and $|\Delta T_{adiab}|$ = 6.2 K at 342 K due to the field-induced relaxor to FE phase transition. These values of $|\Delta S|$ and $|\Delta T_{adiab}|$ are larger in thin films thanks to their small thickness which enables the application of higher field than in bulk or MLCs. However, these values remain unconfirmed by direct measurements.

These past and recent works have made PST the EC benchmark material. However, the energy efficiency of this material is overlooked. In other words, the electrical work required to drive EC heat is barely reported. In the following, we will study the materials efficiency of bulk ceramic PST, by measuring its ECE and extracting the electrical work required to drive this effect. This will be done through different thermal and electrical techniques.

4.3 Results

4.3.1 Experimental details

PST - Sample preparation

The bulk ceramic PST sample (PST sample 1) studied here, was fabricated by Dr. C.-H. Hong and Prof. Wook Jo from UNIST.

According to the stoichiometric formula of $\mathrm{Pb(Sc_{1/2}Ta_{1/2})O_3}$, oxide powders of PbO (99.9%), $\mathrm{Sc_2O_3}$ (99.99%) and $\mathrm{Ta_2O_3}$ (99.9%) were mixed. PbO and $\mathrm{Sc_2O_3}$ powders were purchased on Sigma Aldrich. $\mathrm{Ta_2O_3}$ was obtained from Kojundo Chemical. These powders were ball milled for 24 h in ethanol using zirconia grinding media, followed by a calcination at 850 ℃ for 2 h and then crushed and ball-milled again for another 24 h. As a result, disks of 10 mm in diameter were obtained after pelletizing the powder under 180 MPa with the addition of polyvinyl alcohol (PVA) as a binder. Sintering was conducted in a closed crucible with a mixture of $\mathrm{PbZrO_3}$ and PbO as a sacrificial powder at 1300 ℃ for 2 h. Annealing was done at 1000 ℃ for 30 h to get the resulting B-site ordering.

X-Rays Diffraction (XRD) measurements

XRD diffraction (described in Chapter 3) was carried out with PANalytical X'Pert Pro on the powdered PST sample 1 from 15 to 60-degree angle at every 0.02 degree.

Dielectric permittivity measurements

An impedance spectrometer was used to record dielectric measurements of PST sample 1, at 100 Hz on cooling and heating at a heating rate of 0.1 K $\mathrm{min^{-1}}$ in a cryogenic probe. The dielectric losses tan(δ), was calculated by dividing the imaginary part of the dielectric constant by its real part.

Polarisation-Electric (PE) field loops

PE loops were collected on a 0.5 mm-thick bulk PST sample 1 at different temperatures from 288 K to 313 K. The measurements were done using a standard Sawyer-Tower circuit at 20 Hz up to 18 kV cm^{-1}.

Zero-field DSC measurements

The calorimetric measurements under zero electric field were carried on a 25.05 mg PST sample 1 using a commercial Differential Scanning Calorimeter (DSC): DSC 3+ Mettler Toledo (described in Chapter 3), at a heating rate of 10 K min^{-1}.

DSC measurements under an electric field

Heat flow measurements at constant values of electric fields: 0, 4, 8, 11, 14, and 18 kV cm^{-1} were carried out in a customized DSC 3+ from Mettler Toledo (setup described in Chapter 3) at the heating rate of 10 K min^{-1}. These values of electric field correspond to respectively 0, 200, 400, 550, 700, and 900 V in 0.5 mm thick PST sample 1. A thin layer of silver paste (electrodes) was deposited on each face of the 25.05 mg sample. For the application of electric field, both faces were connected to a power supply Keithley 2410 using copper wires.

InfraRed (IR) Imaging measurements

The IR camera X6580sc from FLIR (described in Chapter 3), was used to collect ΔT_{adiab} of a 0.5 mm thick PST sample 1. As shown in Figure 4.2, the sample was completely covered with silver paste on its bottom side and on 0.480 cm^2 of its top side to avoid any short circuit. To get reliable values of temperature change from IR camera, the sample was black painted with *Colorjelt Noir Mat* [104] to obtain emissivity close to 1. The sample was placed on a hot plate in a Linkam cell to control its starting temperature T_s. Measurements were carried out from 283 K to 323 K every 0.5 K around the transition and every 1 K far from the transition. The material was first cooled in the absence of an electric field to 283 K and then heated to the desired temperature where three runs of electric field were applied. Adiabatic temperature change measurements were collected at 11, 14, 18, 22, 40 kV cm^{-1}. These values correspond to 550, 700, 900, 1100, 2000 V in 0.5 mm thick of PST sample 1. For electric fields greater than 22 kV cm^{-1} the samples could break. Via a Keithley 2410, the sample was electrically charged and discharged at a constant current of 0.2 mA to guarantee adiabatic conditions (charging time is less than 0.2 s). An automated system that controls simultaneously the IR Camera, Linkam cell, and Keithley 2410 was done using Python to enable multiple and fast data acquisition. The PST capacitor was charged at constant current rather than at constant voltage, because it is more efficient in terms of energy [24] (explained in Chapter 3).

Figure 4.2: **Structure of bulk PST for IR Camera.** The bulk PST is 0.5 mm thick. The area of the top electrodes seen by the IR Camera is 0.480 cm^2

Gadolinium - Sample preparation

The Gadolinium samples studied were plates of commercial grade Gd bought from China Rare Metal Material CO., Ltd by authors in [149]. They contain 99.5% rare earth metal including 99.94% of Gd. The plates were 25 mm wide, 40 mm long, 0.9 mm thick and 7900 kg m^{-3} dense.

Magnetization measurements

The magnetization characterization was carried out in 0.90 * 4.60 * 2.26 mm^3 Gd plates at DTU by authors in [149]. A LakeShore 7407 VSM (Vibrating Sample Magnetometer) was used to measure isothermal magnetization M as a function of magnetic field. The measurements were taken from 250 K to 310 K, every 1 K around the transition temperature.

M was measured up to the maximum magnetic field of 1.6 T at a ramp rate of 2.5 mT s^{-1}.

DSC measurements under magnetic field

These measurements were done by authors in [149]. Heat flow measurements of 2.04 * 0.89 * 2.78 mm^3 of Gd under different magnetic fields were done using DTU's DSC [150] (described in [149]). The magnetic field was provided with a concentric Halbach cylinder (an adjustable permanent magnetic field source). Data were collected from 250 K to 310 K at a heating rate of 1 K min^{-1} and at different magnetic fields of 0.25, 0.5, 0.75, 1 and 1.3 T. Keeping the same experimental conditions, heat flow measurements on reference samples (copper and titanium) were measured for calculation of C_p. As described in Chapter 3, C_p data were derived in the same temperature range.

MC temperature change

The authors in [149] carried out the MC temperature change in Gadolinium. DTU's home-made instrument based on a pneumatic piston with the magnetic field provided by the same permanent magnet used for DSC characterization under magnetic field, was used to collect ΔT_{adiab} of commercial grade Gd. The pneumatic piston which moves the sample holder every 5 s in and out of the permanent magnet was placed in a freezer to control the temperature. The actual movement time of the piston is smaller than 100 ms. The sample was prepared with two identically sized plates of Gd glued together with a thermocouple placed in between them for temperature recording. The sample was wrapped with isolating foam and placed in the sample holder. ΔT_{adiab} data was collected from 280 K to 310 K at different magnetic fields of 0.25, 0.5, 0.75, 1 and 1.3 T. The measurements can be assumed adiabatic because of the high sweep in temperature and thermal isolation conditions. Changes of less than 3% in the magnetic field produced by the permanent magnet is noticeable as the magnet is cooled in the process.

4.3.2 Characterization of PST bulk ceramic

B-site cation order

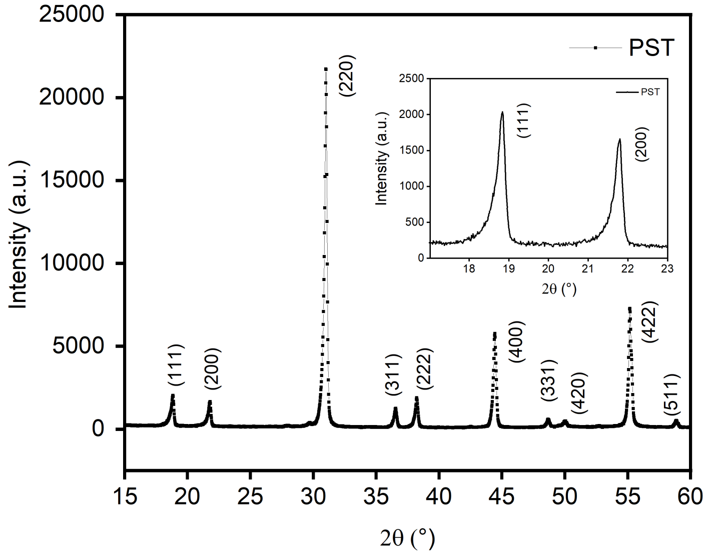

Figure 4.3: **X-Rays Diffraction of bulk PST powerdered.**

XRD measurements (Figure 4.3) were carried out in powdered PST sample 1 to determine its degree of ordering Ω. The PST bulk sample 1 was crashed in powder to avoid any preferential orientations in the XRD measurements. The B-site cation order Ω = 0.98 was obtained. It was calculated from the integrated intensities of the XRD maxima 111 and 200 using equation (4.1).

Dielectic permittivity

Dielectric measurements (Figure 4.4) show a first-order transition with a sharp peak at T_0 = 300 K on heating with a small hysteresis of 3 K. We record dielectric losses of 0.025 in the FE phase, which strongly decreases down to less than 0.01 in the PE phase. This discrepancy in losses is explained by the presence of domain walls in the FE phase, which are absent in the PE phase.

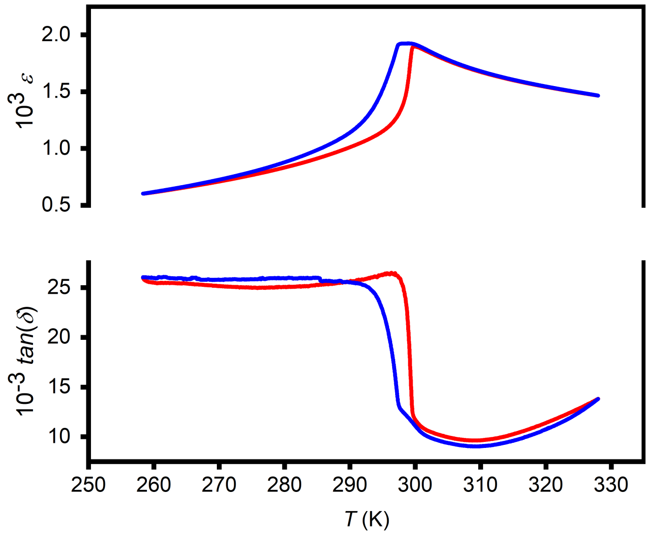

Figure 4.4: **Dielectric measurements of bulk PST.** Blue and red curves denote respectively cooling and heating. The top plot shows the relative permittivity ϵ and the lower plot the loss tangent tan(δ), both as a function of temperature T.

Polarisation versus electric field loops

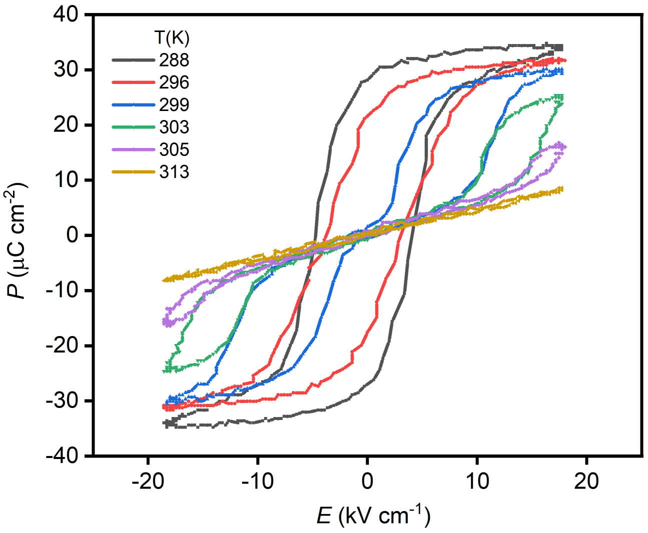

Figure 4.5: **Polarisation versus electric field loops of bulk PST.** PE loops of bulk PST before, around, and after T_0 = 300 K.

PST shows in figure 4.5, a FE loop at 288 K (low temperature) and a PE loop (linear) at 313 K (high temperature). Closed to T_0, between 299 K and 305 K, we observe double loops. These double loops are evidence of a PE to FE field-driven phase transition and should not be considered as antiferroelectric (AFE) loops. They have already been observed in 1953 in the well-known first-order transition material BaTiO$_3$ [151]. The field-induced first-order transition which is manifested by the double hysteresis loops is responsible for the ECE and provides a dominant contribution to this effect [53, 129].

Zero-field calorimetric measurements

The sharp peaks (Figure 4.6a and Figure 4.6b) combined with thermal hysteresis, observed in the zero-field heat flow and specific heat C_p measurements made by DSC (explained in Chapter 3), ascertain the first-order phase transition in PST at T_0 = 300 K. A constant value C_p of 300 J K^{-1} kg^{-1} which corresponds to the background of the zero-field C_p measurements in Figure 4.6b, is measured and in good agreement with the literature [29, 96, 129]. The peak at T_0 is the latent heat Q_0 due to the first-order transition from FE-PE (on heating) or PE-FE (on cooling). The integration of zero-field calorimetric peaks $\frac{dQ}{dT}$ yields Q_0 of 1031 J kg^{-1} on heating and 890 J kg^{-1} on cooling. The peaks of $\frac{dQ}{dT}$ were integrated (trapezoid method) to get the latent heat Q_0 on cooling:

$$Q_{0,c} = \int_{T_{c_1}}^{T_{c_2}} \frac{dQ}{dT}\, dT$$

and on heating:

$$Q_{0,h} = \int_{T_{h_1}}^{T_{h_2}} \frac{dQ}{dT}\, dT$$

T_{c_1} = 300.5 K, T_{c_2} = 288.0 K are respectively chosen above and below the cooling peak. T_{h_1} = 291.5 K and T_{h_2} = 303.3 K have been chosen respectively below and above the heating peak. They are the extreme values for which heat flow $\frac{dQ}{dT}$ is still naught before the latent heat peak starts appearing. From zero-field C_p measurements, we calculate $S'(T)$ the entropy referenced to the entropy at 280 K (S'(280 K) = 0) far away from the transition (described in

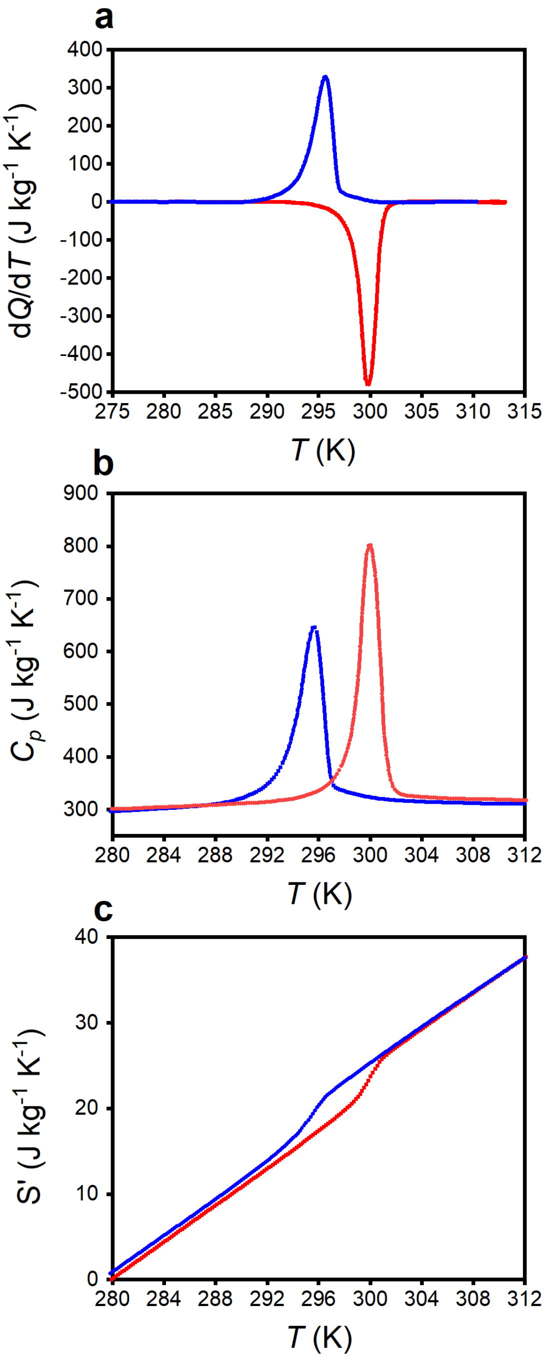

Figure 4.6: **Zero field calorimetric measurements of bulk PST.** Blue and red curves denote respectively cooling and heating in the three plots. **a** Heat flow $\frac{dQ}{dT}$ measurement as function of temperature T. **b** Zero-field specific heat C_p (background value) measurement associated with latent heat Q_0 (integral under the first-order phase transition peak at T_0 = 300 K on heating and 296 K on cooling). **c** $S'(T) = S(T) - S(280\,K)$ represents the entropy $S(T)$ referenced to the entropy at 280 K far from T_0 with $S'(280\,K) = 0$.

Chapter 3). We access a large transition entropy change ΔS_0 = 3.4 J K^{-1} kg^{-1} on heating and ΔS_0 = 3.0 J K^{-1} kg^{-1} on cooling (Figure 4.6c).

4.3.3 Electrocaloric effect of PST bulk ceramic

In this section, we will describe the ECE measured in PST bulk ceramic using an IR Camera and a customize DSC under electric field (as described in Chapter 3).

Isofield measurements

From quasi-direct measurements i.e. isofield measurements of heat flow and specific heat at constant values of electric fields, we determined the isothermal entropy change ΔS induced in PST bulk ceramic due to changes in electric field. These measurements were carried out in PST sample 1.

Isofield measurements in Figure 4.7a show a linear shift (Figure 4.7b) of T_0 towards higher temperatures and thus stabilization of the low-temperature phase (FE phase) due to the electric field. A difference of 10 K between the transition temperature at 0 kV cm^{-1} and the maximum field applied of 18 kV cm^{-1} is measured and gives an estimated value of the temperature range of the ECE. One can notice that there is a slight difference in the heat flow at 0 kV cm^{-1} in Figure 4.7a and Figure 4.6a. In the former, the measurements were carried out on a wired sample attached with silver paste (electrodes) whereas in the latter the measurements were done on a pure PST sample without wires and electrodes. The wires and electrodes induce an inferior thermal contact leading to a slight difference in the peak at zero fields. However, the latent heat Q_0 (integral under the peak $\frac{dQ}{dT}$) is almost the same in Figure 4.6a (1031 J kg^{-1}) and Figure 4.7a (1037 J kg^{-1}). We measure a constant latent heat $\int \frac{dQ}{dT} dT$ (Figure 4.7c) at the transition with the increasing electric field. The integration of the $\frac{\frac{dQ}{dT}}{T}$, gives a constant ΔS_0 (Figure 4.7d) of 3.4 J K^{-1} kg^{-1}. This value is almost constant with the electric field increasing. It corresponds to the entropy change resulting from fully driving the transition.

Figure 4.8a describes the direct measurements of heat capacity under different elec-

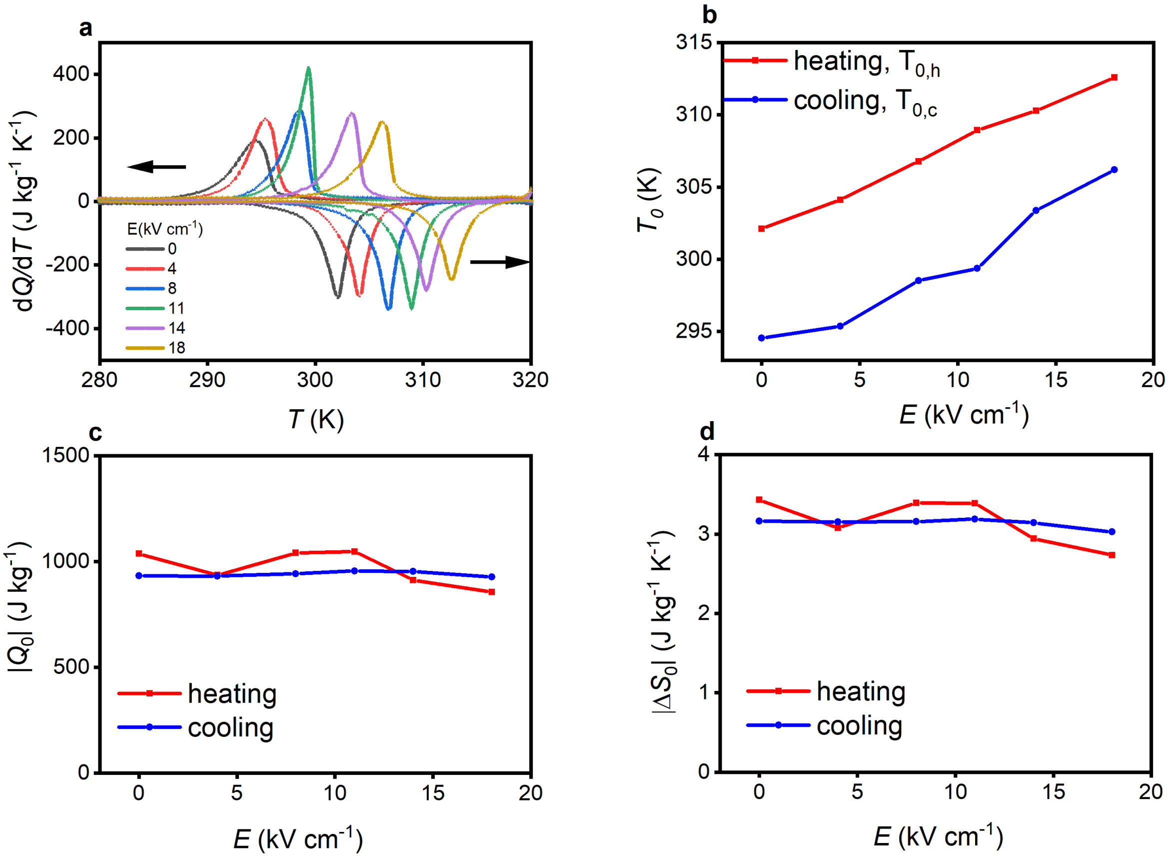

Figure 4.7: **Isofield measurements of bulk PST.** **a** Heat flow measurement as a function of temperature T at constant values of electric fields E on heating and cooling. As the sample was wired with electrodes, we observed a slight difference in the peak at 0 kV cm^{-1} compare to the heat flow measured on pure PST without electrodes and wires (figure 4.6). **b** Transition temperature on heating $T_{0,h}$ and on cooling $T_{0,c}$ as function of electric field E. **c** Latent heat Q_0 (integral under the heat flow peak) as a function of electric field E on heating and cooling. **d** Entropy change at the transition $|\Delta S_0|$ as function of electric field on heating and on cooling.

tric fields. With the accuracy of our set-up (detailed in Chapter 3), we could not deduce any variation of C_p baseline versus electric field. Consequently, C_p equals 300 J K^{-1} kg^{-1} $\pm$ 20 J K^{-1} kg^{-1}, which is in line with literature [129] [131]. The clear influence of electric field is the shift of C_p towards higher temperatures. From isofield heat flow (Figure 4.7a) and specific heat measurements (Figure 4.8a) we built entropy curves S' (detailed in Chapter 3) referenced to 280 K (Figure 4.8b) to determine the isothermal field-driven entropy change $\Delta S = S'(T,E) - S'(T,0)$ versus temperature (Figure 4.8c) and field (Figure 4.8d). As expected, ΔS increases with the electric field. A maximum isothermal entropy change of 3.44 J K^{-1} kg^{-1} on heating and 3.38 J K^{-1} kg^{-1} on cooling is obtained under the electric field of 18 kV cm^{-1}. This value is very similar to ΔS_0 extracted at zero field and proves that the transition can be fully driven with the electric field of 18 kV cm^{-1}. Moreover,these values are in agreement with the transition entropy ΔS_t from the Clausius-Clapeyron equation (2.14). From the linear dependence of transition temperature with the electric field $\frac{dT_0}{dE}$ = 0.59 kV cm^{-1} K (Figure 4.7b) and the change of polarization $\Delta P_0 = \Delta P_r$ = 19.1 μC cm^{-2}, we obtain ΔS_t = 3.55 J K^{-1} kg^{-1} at 18 kV cm^{-1} using the Clausius-Clapeyron equation. These results are higher than previous ECE reported on PST bulk ceramic [129] [131].

Electrocaloric exchangeable heat

We will now collect using an IR camera, direct measurements of adiabatic temperature change ΔT_{adiab} of PST sample 1. From ΔT_{adiab} and C_p (Fig. 3.5.e) we will calculate Q, the EC heat exchanged by PST sample 1 using the equation below:

$$Q = C_p \Delta T_{adiab} \tag{4.2}$$

Reversible and reproducible ΔT_{adiab} measurements were collected on the 0.480 cm^2 area of the top electrodes (Figure 4.2) of PST sample 1 under adiabatic conditions. The adiabaticity of our measurements was controlled by the current applied. To guarantee adiabatic conditions, the charging time of the capacitor must be much faster than the characteristic time of thermal relaxation. The higher is the current applied, the faster the capacitor is charged. Figure 4.9 shows the peak of ΔT_{adiab} as a function of different current applied. For currents smaller than 0.2 mA, ΔT_{adiab} increases with the current. This region is non-adiabatic. However, at current higher or equal to 0.2 mA, ΔT_{adiab} is constant with the increasing current. At 0.2 mA the application/removal time of the field is 0.12 s which is 30 times faster than the thermal relaxation experiences by PST in our measurements. In the following, the current of 0.2 mA will be applied to get adiabatic conditions.

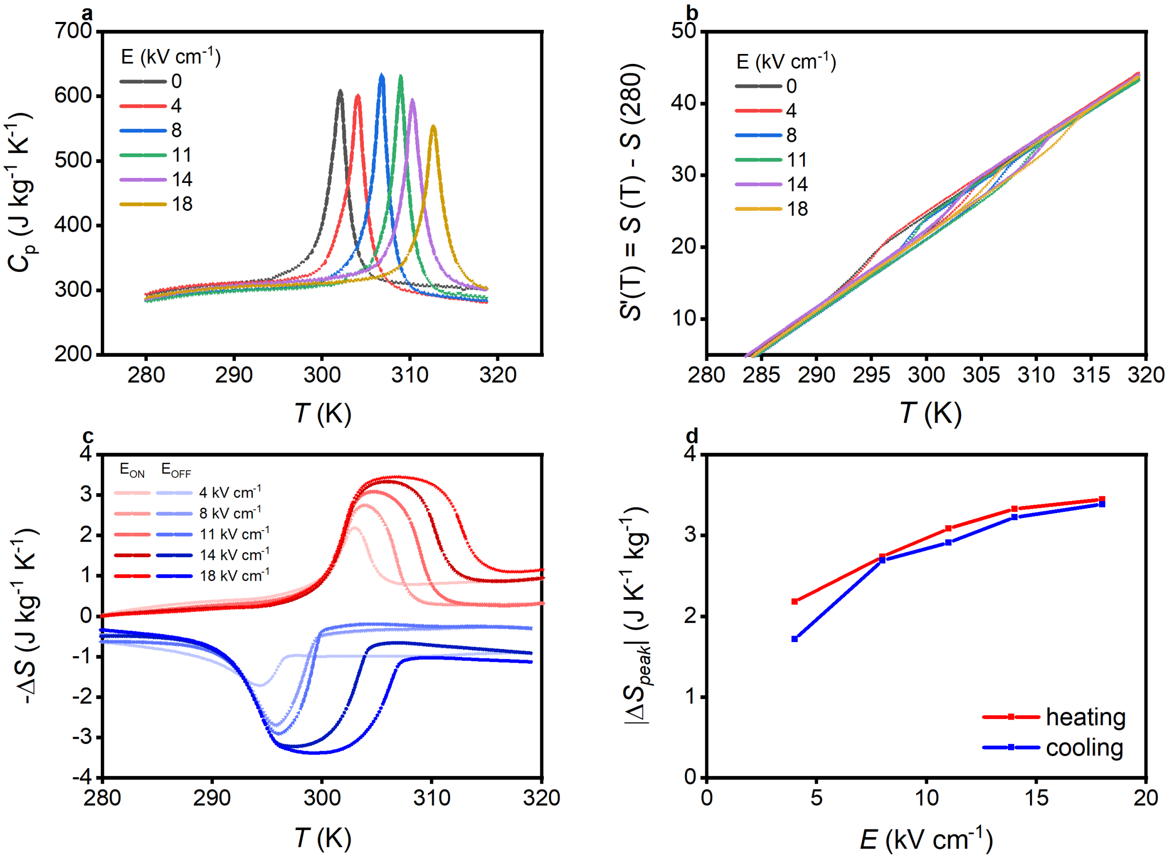

Figure 4.8: **Isothermal entropy change of bulk PST. a** Heat capacity measurements at different electric fields. **b** Entropy curves referenced to the entropy at 280 K, i.e S'(280 K) = 0 K as function of temperature T at different electric fields E. **c** Isothermal entropy change ΔS obtained from isofield and heat capacity measurements (see Chapter 3) at different electric fields, on applying (E_{ON}) and removing (E_{OFF}) field. **d** Peak of isothermal entropy change $|\Delta S_{peak}|$ as function of electric field E, on cooling (blue curves) and heating (red curves).

The IR camera measurements were taken at four electric fields (11, 14, 18, 22 kV cm^{-1}) and from starting temperatures T_s of 283 K to 323 K. As PST shows a conventional EC effect, the positive and negative values result respectively from the application and removal of the electric field. Each value of ΔT_{adiab} at a given T_s and electric field E was collected on three successive cycles (method described in Section 3.1 in Chapter 3) at a constant current of 0.2 mA.

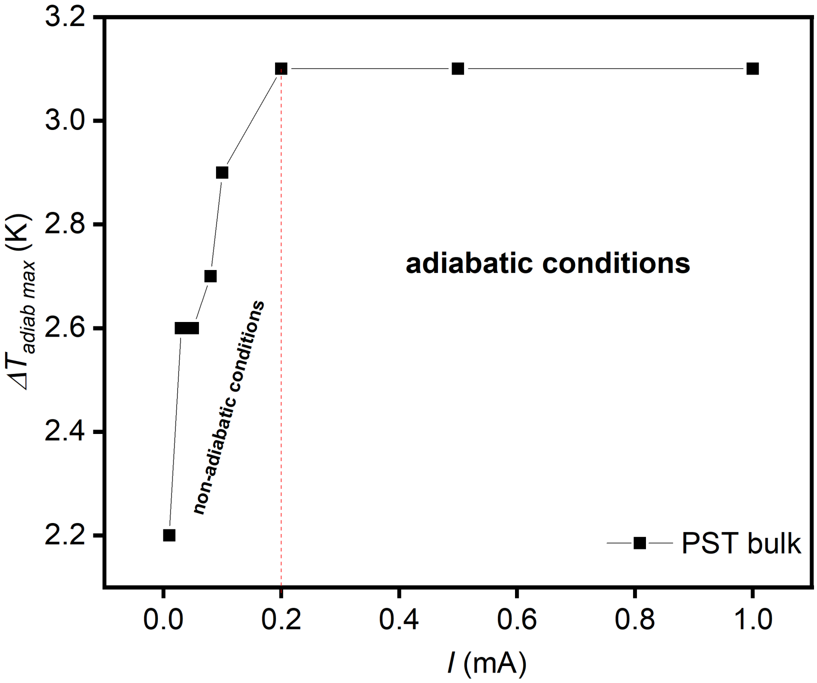

Figure 4.9: **Adiabatic conditions in bulk PST.** ΔT_{adiab} versus applied current I. The measurements were done on PST sample 1 bulk at 22 kV cm^{-1}.

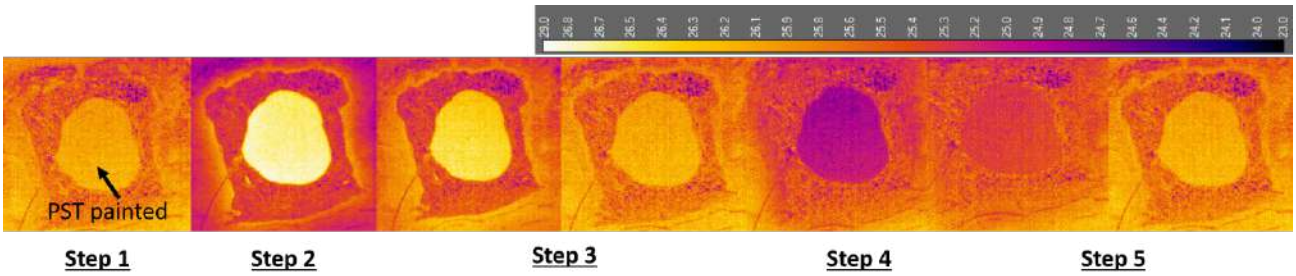

Figure 4.10: **IR images of bulk PST sample 1 during a standard EC characterization sequence.** In step 1 the material is at T_s of 299 K, in step 2, 1100 V are applied and the materials temperature increases. Subsequently, in the two following images the material thermalizes and goes back to T_s (no Joule heating). In step 4, the materials temperature decreases as voltage is removed. Finally, in Step 5 the material thermalizes back to T_s

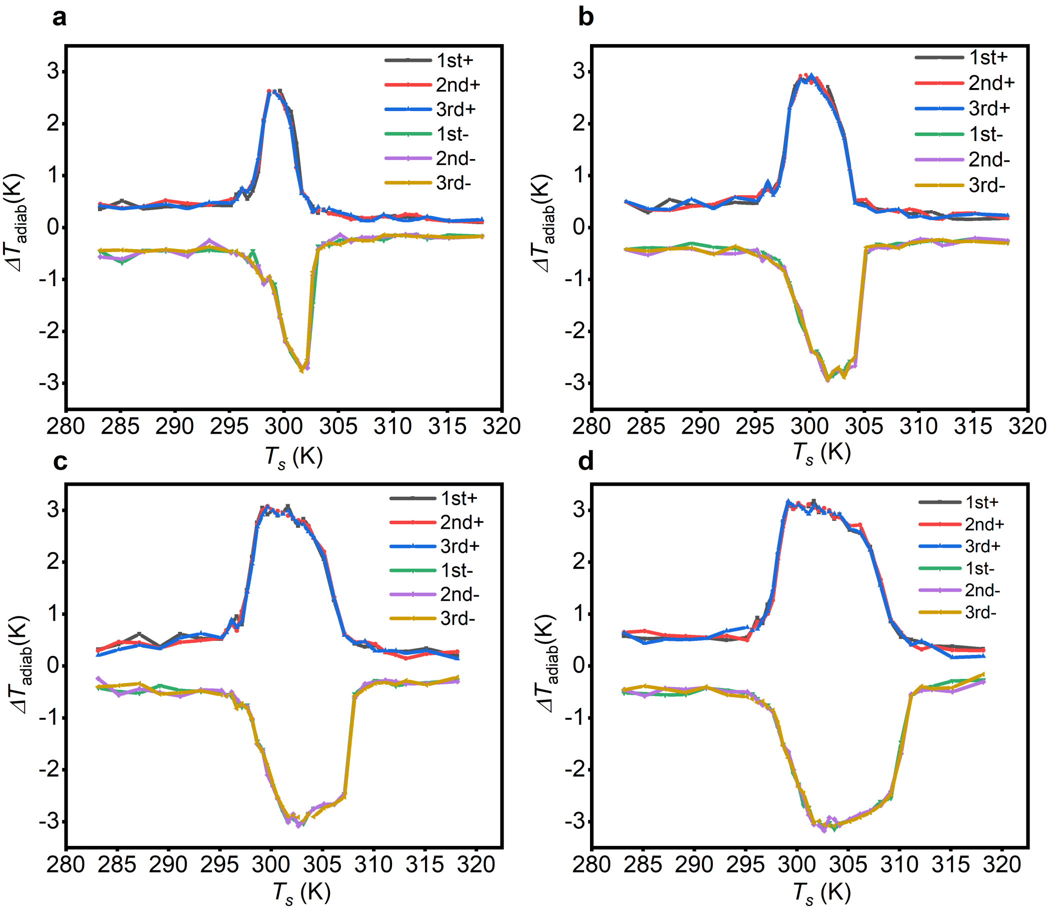

Figure 4.11: **Reproducibility of EC measurements** This figure shows the ΔT_{adiab} measured after of the first, second and third cycle in function of starting temperature T_s at 11 kV cm^{-1} (**a**) 14 kV cm^{-1} (**b**) 18 kV cm^{-1} (**c**) 22 kV cm^{-1} (**d**). In the legend, 1^{st+}, 2^{nd+},3^{rd+} are the ΔT_{adiab} on-field of respectively the first, second and third cycle and, 1^{st-}, 2^{nd-},3^{rd-} are the ΔT_{adiab} off-field of respectively the first, second and third cycle.

As shown in Figure 4.10 these measurements were done without Joule heating as the sample's temperature after thermalization following the application or removal of the electric field is identical in both cases. At the T_s and electric fields studied, we do not observe a decrease in the ΔT_{adiab} after several cycles, thereby showing the reproducibility of our measurements (Figure 4.11).

An average over the three runs is done to extract ΔT_{adiab} of PST bulk sample 1 at a given

T_s and electric field (Figure 4.12a – left y-axis). At the lowest applied field of 11 kV cm^{-1}, we measured a reversible maximum ΔT_{adiab} of 2.6 K at T_0 = 299 K in a temperature range of 2.5 K (Figure 4.12a). This temperature range is calculated as the full width at 80% of the maximum ΔT_{adiab}. By increasing the field, we enlarge the peak towards higher temperatures thereby stabilizing the FE phase. This is in agreement with the isofield measurements in Figure 4.7. ΔT_{adiab} increases up to 3.1 K and the temperature range reaches 8.4 K by doubling the field (22 kV cm^{-1}). Figure 4.12b shows that the temperature range increases linearly with the increasing electric field. Close to its breakdown field, at 40 kV cm^{-1} we measured a higher ΔT_{adiab} of 3.7 K (Figure 4.12c). This temperature change is 60% higher than values (Table 4.1) reported in the literature on less ordered PST [129, 131]. As shown in Figure 4.13, the temperature change increases with the B-site cation ordering. This is in line with Shebanov's studies in the early 2000s.

From Figure 4.12a, it is clear that the corresponding T_s of the maximum point of ΔT_{adiab} field on (red curves) and field off (blue curves) differ. This is explained by the reversibility of the ECE. In fact, by applying an electric field at a given T_s, due to the ECE, the material's temperature increases by $\Delta T_{adiab,on}$ to $T_1 (= T_s + \Delta T_{adiab,on})$. Subsequently, by removing the field at T_1, the material's temperature will decrease by $\Delta T_{adiab,on} = -\Delta T_{adiab,off}$ to $T_2 (= T_1 + \Delta T_{adiab,off})$. Therefore, upon application of the field the maximum ΔT_{adiab} will peak at T_s and upon removal of the field, it will peak at T_1; and the difference between T_s and T_1 corresponds to the maximum value of ΔT_{adiab}.

This mechanism is explained in [152], in which they show that if an EC process is reversible, then $T_s = T_2$ and thereby the relation below must be verified:

$$\Delta T_{adiab,on}(T_s, E) = -\Delta T_{adiab,off}(T_s + \Delta T_{adiab,on}(T_s, E), E) \tag{4.3}$$

with E the applied electric field.

This equation fits well our results as shown in Figure 4.12d. $\Delta T_{adiab,off}$ measured directly

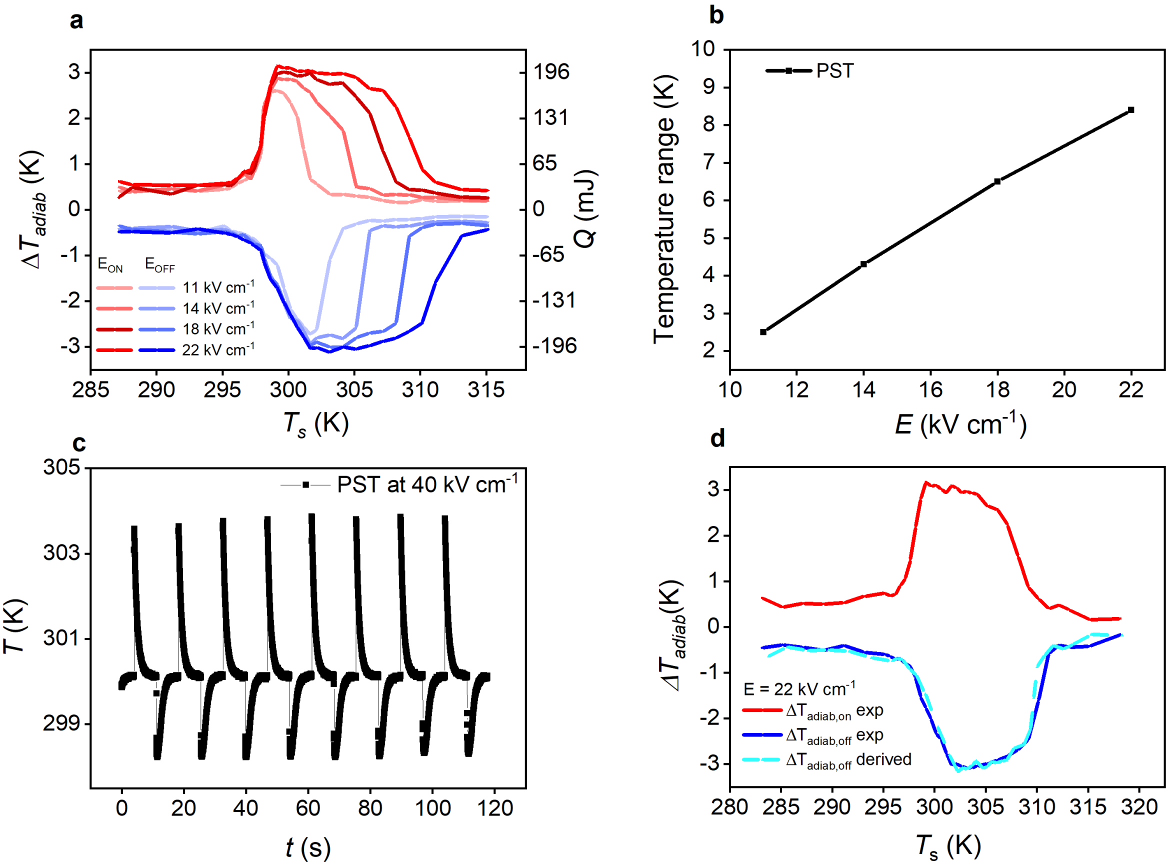

Figure 4.12: **Reversible ECE. a** Direct measurement of adiabatic temperature change ΔT_{adiab} and EC heat Q upon application (red curves) and removal (blue curves) of 11, 14, 18 and 22 kV cm^{-1}. ΔT_{adiab} and Q are shown as a function of T_s. **b** Temperature range (full width at 80% of the maximum ΔT_{adiab}) as a function of electric field. **c** ΔT_{adiab} as a function of time at the electric field of 40 kV cm^{-1} and T_s = 300 K. **d** Reversibility of EC measurements. Here we show ΔT_{adiab} of PST bulk at 22 kV cm^{-1} versus T_s. Red curves and dark blue curves are respectively ΔT_{adiab} due to the ECE when the field is on and off. These two curves are obtained from experimental measurements with an IR camera. The cyan dash curve is the ΔT_{adiab} due to ECE when the field is off and derived from the equation (4.3). $\Delta T_{adiab,off,exp}$ and $\Delta T_{adiab,off,exp,derived}$ coincide well and thereby validate the reversibility of our EC measurements.

is equal to $\Delta T_{adiab,off}$ derived from equation (4.3). This equation could help determine $\Delta T_{adiab,off}$ knowing experimental values of $\Delta T_{adiab,on}$ and vice-versa.

The EC heat Q in Figure 4.12a (right y-axis) was calculated using the equation (4.2) with C_p the constant background value (300 J K^{-1} kg^{-1}) measured with a DSC (Figure 4.6b), and

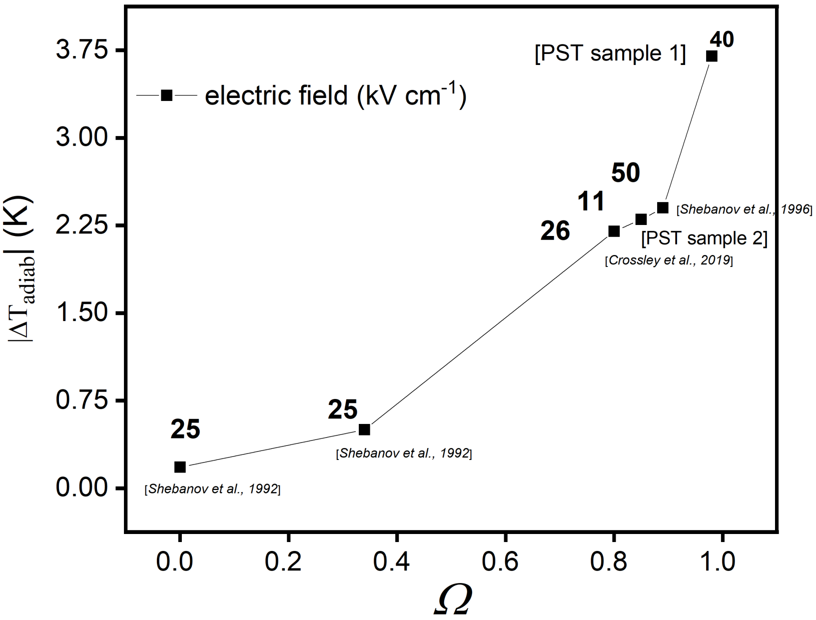

Figure 4.13: **ECE in PST bulk ceramics.** The ΔT_{adiab} values of bulk ceramics PST collected from literature [ref] are compared to our PST samples (PST sample 1, Ω = 0.98 and PST sample 2, Ω =0.89). The number displayed in bold close to each symbol is the field applied in kV cm^{-1} and in brackets are the references. Our PST sample 1 shows the highest ECE measured. The results on PST sample 2 are present in Annex.

ΔT_{adiab} (Figure 4.12a, left y-axis) directly measured with an IR camera. The sample has a density of 9071 kg cm^{-3} and a volume of 0.024 cm^3. As Q is proportional to ΔT_{adiab}, we obtained similar behaviours that are: an increase of heat with the field and the saturation of the ECE with the increasing field. One can also define the EC heat Q as:

$$Q = -T_s \Delta S_{isothermal} \tag{4.4}$$

with $\Delta S_{isothermal}$ the isothermal entropy at constant temperature T_s.

Q can be obtained indirectly by calculating $\Delta S_{isothermal}$ using the Maxwell relations or directly by direct measurements of heat isothermally. Here, we measured Q directly under isothermal conditions in a DSC by applying the electric field very slowly (200 s) in order to maintain the temperature constant throughout the measurement. By integrating with respect

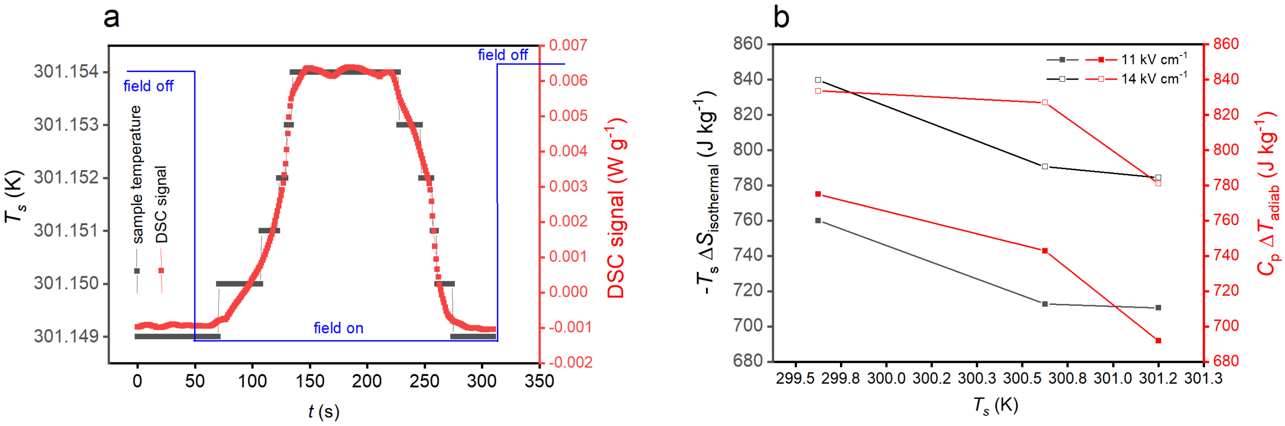

Figure 4.14: **Isothermal heat** Here we justify equation (4.2) as a good approximation for EC heat Q. **a** Isothermal application of electric field (14 kV cm^{-1}) during 200 s. The integral under the peak corresponds to the isothermal heat exchanged $Q = -T_s \Delta S_{isothermal}$. **b** Comparison of $C_p\ \Delta T_{adiab}$ to $-T_s \Delta S_{isothermal}$. ΔT_{adiab} was collected with IR camera (Figure 4.12a). There is a good match between $C_p\ \Delta T_{adiab}$ and $-T_s \Delta S_{isothermal}$.

to time the DSC signal obtain in Figure 4.14a, we obtained the EC heat Q. These measurements were carried out only at the lowest values of electric fields (11 and 14 kV cm^{-1}), which are the most sensitive ones because the transition is not fully driven. In Figure 4.14b, we compared both definitions of heat defined in equation (4.2) and (4.4). The results of Q obtained from both definitions are similar with a slight difference of 5%. This justifies the assumption of using $C_p\ \Delta T_{adiab}$ as a good estimation of Q in PST. Besides, this definition enables fast calculation of Q whereas isothermal measurements of Q can be laborious. Note also that considering the background value of C_p constitutes a lower bound of Q, thereby a lower bound of η_{mat}.

4.3.4 Electrical work

Simultaneously to the ΔT_{adiab} measurements, we used a dedicated setup (described in Chapter 3) to collect the voltage of the PST capacitor at different T_s. As shown in Figure 4.15, the voltage increases almost linearly with time at 288 K (FE phase) and 313 K (PE phase). This indicates no phase transition in the PST capacitor. However, around the transition temperature, between 295 K and 304 K, we observe a change in slope in the voltage-time

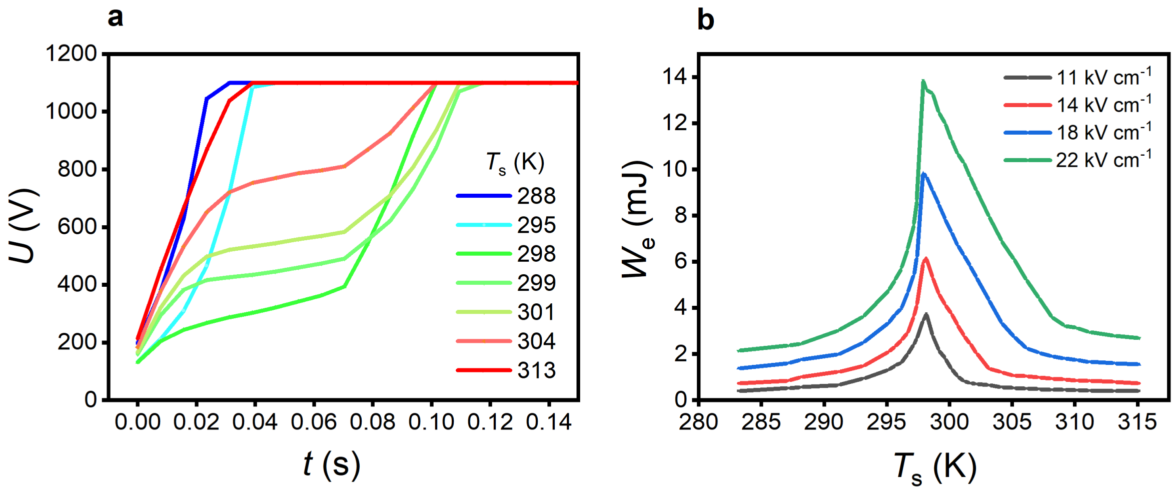

Figure 4.15: **Electrical work of bulk PST. a.** Example of charge in PST capacitor at a maximum voltage of 1100 V (22 kV cm^{-1}) as a function of time t at selected T_s. **b.** Electrical work W_e needed to charge a PST capacitor as a function of T_s at different electric fields E. W_e is obtained from the data of voltage across PST at constant current.

curves. The change in slope corresponds to the field-induced phase transition from PE to FE. From the data of voltage as function of time, we calculate the electrical work energy using the equation (4.5). W_e increases with the electric field and peaks at 297 K at all fields where the PST requires the most energy to be charged (Figure 4.15).

$$W_e = I \int U(t)dt. \tag{4.5}$$

A noteworthy fact is that in our calculation of W_e, we take into account the FE losses, by directly measuring the current needed to charge the PST capacitor. Our direct extraction of W_e is equivalent to using the lower branches of the P(E) loops to calculate W_e indirectly using the equation (4.5) below.

$$W_e = \int EdD \tag{4.6}$$

With D the electrical displacement field which is considered equivalent to P in the case of high dielectric constant materials such as PST.

This integral is illustrated in the P(E) loop at 299 K in Figure 4.16a. It corresponds to the

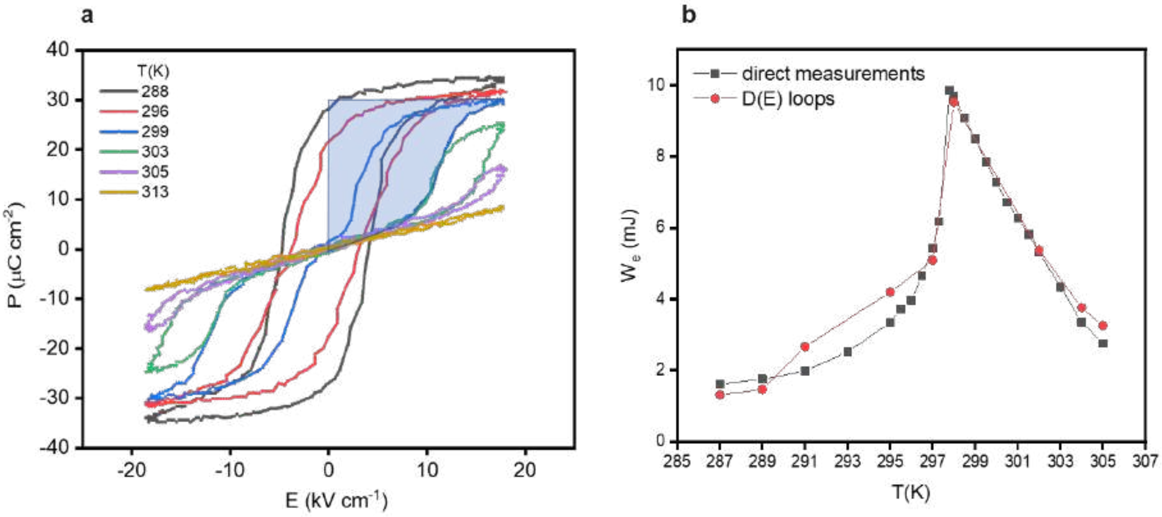

Figure 4.16: **Comparison of direct and indirect calculation of electrical work W_e. a** P(E) loops of bulk PST capacitor at different T_s, from 288 K to 313 K. The blue shaded area is the electrical work ($W_e = \int EdD$) per unit volume to charge the PST capacitor at 299 K up to 18 kV cm^{-1}. This area takes into account the FE hysteresis losses.

shaded area in blue which includes the hysteresis losses and the electrical work needed to fully charge the PST capacitor. We, therefore, compare in Figure 4.16b, both calculations of W_e from unipolar PE loops and direct extraction. At the field of 18 kV cm^{-1}, we obtain similar results of W_e in both methods. Thereby, showing that our calculation of W_e (and η_{mat}) takes into account the FE hysteresis losses.

From both data of Q and W_e, we will determine the materials efficiency η_{mat} of PST sample 1. It is worth it to mention that, compared to Q which shows a saturation with the field, W_e shows sharp peaks. This suggests an optimum in $\eta_{mat} = Q/W_e$.

4.3.5 Materials efficiency of PST bulk ceramic

The EC materials efficiency of bulk PST, $\eta_{mat} = Q/W_e$ was calculated from the data of EC heat Q in Figure 4.12a and W_e in Figure 4.15b. As shown in Figure 4.17, η_{mat} increases with the electric field decreasing. Besides, its temperature range increases with the field. At lower electric fields, η_{mat} shows sharp peaks. At the lowest electric field applied of 11 kV cm^{-1}, we

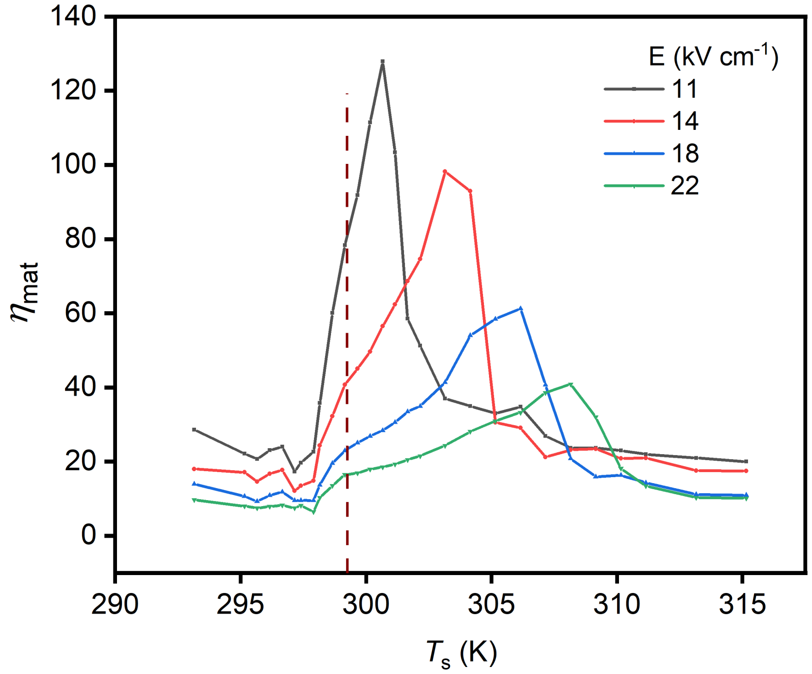

Figure 4.17: **Materials Efficiency of bulk PST.** η_{mat} of bulk PST versus T_s at different electric fields E. The dash line shows the temperature at which PST exchanges the most heat Q. η_{mat} is calculated from data of Q in Fig. 4.12a and W_e in Fig. 4.15b.

measured a maximum value of 128. This value peaks on a temperature span of 2.5 K. η_{mat} decreases down to 40 by doubling the electric field (22 kV cm^{-1}), though on a temperature range of 8.4 K. The peak in η_{mat} is shifted towards high temperatures with the increasing field. The variation observed in η_{mat} is explained by the saturation of Q with the increasing field whereas W_e increases with the field. It is worth it to mention that bulk PST is not the most efficient at the transition temperature (dash line in Figure 4.17).

4.3.6 Materials Efficiency of Gadolinium

From data of C_p, ΔT_{adiab} and magnetization M as a function of internal magnetic field B, we calculated the materials efficiency of a commercial-grade Gadolinium (Gd). These data were collected from Bjork et al. [149] from the Technical University of Denmark. The measurements were carried out at four different magnetic fields: 0.25, 0.5, 0.75, 1, 1.3 Tesla. As expected and observed in Figure 4.18a, Gd shows a second order transition (broader

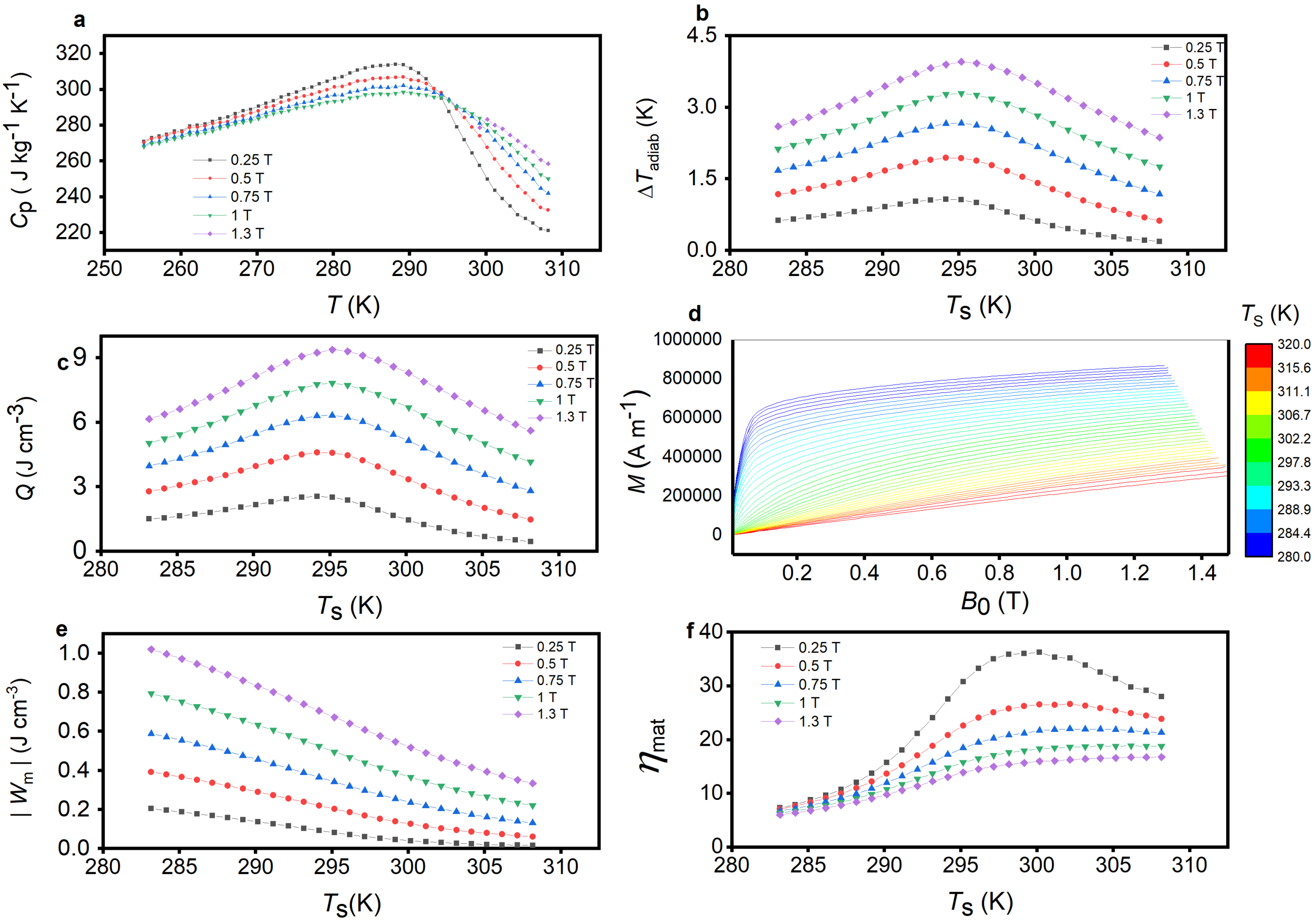

Figure 4.18: **Materials Efficiency of Gd.** Heat Capacity (**a**), ΔT_{adiab} (**b**), and magnetisation M (**d**) of Gd taken from Bjork et al. **c.** Heat exchanged Q of Gd. **e** Mechanical work - W_m. **f** $\eta_{mat} = |Q/W_m|$ of Gd calculated from (**c**) and (**e**).

transition compare to PST). An average C_p of 300 J kg K^{-1} which does not depend on the magnetic field applied was measured. C_p measurements were done using a DSC (see experimental details in Section 4.3.1). Adiabatic temperature change measurements were taken with a homemade instrument at DTU energy described in Section 4.3.1. As shown in Figure 4.18b, at the transition temperature $T_0 = 295.1\,K$, a maximum ΔT_{adiab} of 4 K at 1.3 T was measured. It decreases down to 1 K at the lowest field of 0.25 T. The magnetization M collected at different T_s from 280 K to 320 K, is presented in Figure 4.18d. It was measured using a LakeShore 7407 vibrating sample magnetometer (detailed in Section 4.3.1).

The magnetocaloric heat exchanged by Gd was calculated using equation (4.2), with C_p the constant value of 300 J kg K^{-1}. As shown in Figure 4.18c, Q is proportional to ΔT_{adiab}. The magnetic mechanical work W_m was done to generate the magnetic field $B_0 = \mu_0 H$ by relative motion of the MC material with respect to permanent magnet. W_m (Figure 4.18e) was calculated based on the formalism of Heine [84], already utilized by Moya et al. [34]. W_m is defined as:

$$W_m = -\mu_0 \int M dH \tag{4.7}$$

with μ_0 the permeability of free space and H the internal magnetic field.The minus sign is for the attraction between the permanent magnet and the MC body.

Hence, $\eta_{mat} = |Q/W_m|$ of Gd was calculated. Similarly to PST, the materials efficiency of Gd increases with the decreasing magnetic field. At the lowest field of 0.25 T we measured η_{mat} = 36 which decreases to 17 at 1.3 T.

4.3.7 Comparison of materials efficiency of PST and Gd

We will now compare in terms of energy efficiency PST to Gd the benchmark MC. Even though, they both present respectively a first-order and second-order transition, it is of interest to compare them as they are respectively benchmark materials in their respective caloric family.

In Figure 4.19, we compare for the maximum heat exchanged Q at different fields, the η_{mat} of PST (green bubbles) to Gd (blue bubbles). In both PST and Gd we observe a linear decrease of the efficiency with the increasing Q. However, with different slopes: steeper in PST and flatter in Gd.

At the highest electric field applied of 22 kV cm^{-1} in PST, we measured a η_{mat} = 16 at Q = 8.6 J cm^{-1} and over a temperature range of 8.4 K. The temperature range in Figure 4.19 is given by the size of the bubble. As summarized in Table 4.2, by applying half of the

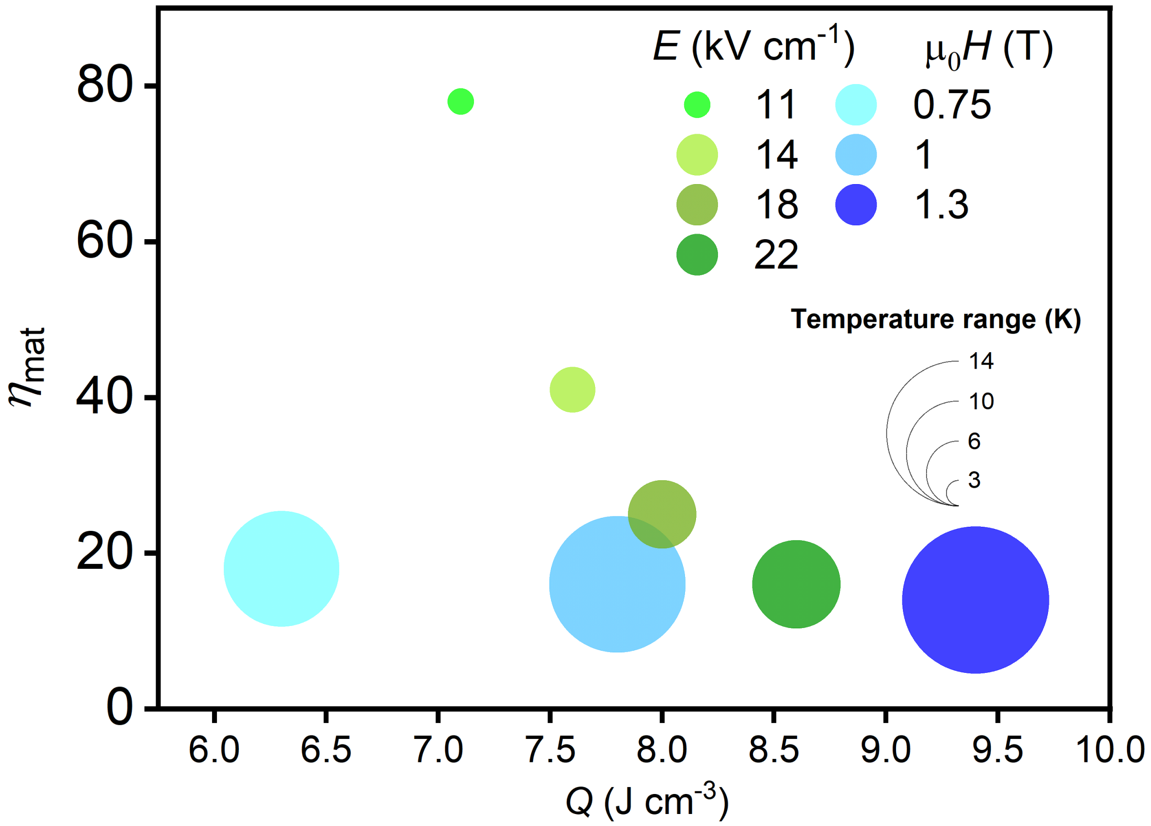

Figure 4.19: **Comparison Materials Efficiency of PST to Gd.** The bubble map represents η_{mat} of PST (green bubbles) and Gd (blue bubbles) as a function of maximum caloric heat Q per cm^3. The values of Q are taken at the material transition temperature. The bubbles' colour yields the field applied. The bubbles' diameter shows the temperature range of the material at a given field.

maximum field (11 kV cm^{-1}), we obtained a lower value of Q though substantial and η_{mat} is multiplied by four, reaching 78. Nevertheless, this four-fold increase of η_{mat} is associated with a three-fold decrease of its temperature range. The large values and abrupt variations in the materials efficiency of highly-ordered PST is due to its strong first-order transition.

It can be seen from Figure 4.19 that Gd exchanges more heat (9.4 J cm^{-1}) than PST because one is able to apply higher variations of magnetic field whereas PST is limited to 22 kV cm^{-1}. η_{mat} in PST decreases from 78 to 20 over the entire range of Q whilst η_{mat} in Gd remains around 20. The large η_{mat} is associated with a small temperature range of 2.5 K. On the contrary Gd presents a large and constant temperature range (between 10 K and 14 K) as is typical of second-order phase transition materials.

4.4 Discussion

Our results show that bulk PST can be extremely energy efficient. This high efficiency in bulk PST is a consequence of its high degree of order Ω which ensures a strong first-order phase transition and thereby larger values of Q and η_{mat}. This work places bulk PST among the best caloric materials in terms of materials efficiency. As shown in Figure 4.20, bulk PST is an order of magnitude more efficient than other EC materials (mainly thin films) reported in [17, 35]. This is without recovering energy which promises even higher efficiency as explained by Defay et al. [24]. The comparison of PST with Gd has shown that the first-order behaviour of PST increases η_{mat} at the expense of working in a narrow temperature range (2.5 K). Instead, Gadolinium has a lower η_{mat} but operates on a larger temperature range ($>$10 K) which can be ascribed to its second-order phase transition.

We suggest two solutions to benefit from the high energy efficiency of bulk PST and overcome its narrow temperature range for future EC cooling devices. One could use PST MLC which has been shown by Nair et al. [29] to exhibit large ΔT_{adiab} (5.5 K) over a temperature range of more than 73 K. Nevertheless, the efficiency of PST MLCs remains overlooked. In fact this will be target in the next chapter in details. Last, but not least, one could utilize PST in a graded PST ceramic which is based on multiple PST with different transition temperatures. It could be assembled in a layered regenerator structure suggested by Olsen in the eighties [153]. Each material of the active regenerator operates close to its respective transition temperature to get a large temperature span in the device. This solution is often used in MC regenerators with for instance La(Fe,Si,Mn)$_{13}$H$_y$ [154], a first-order phase transition MC material. As explained in the Section 4.2 above, PST's transition temperature could be shifted with dopants; towards high temperatures with Sb^{5+}, Y^{3+}, Co^{3+} and towards low temperatures with Nb and Ti [55].

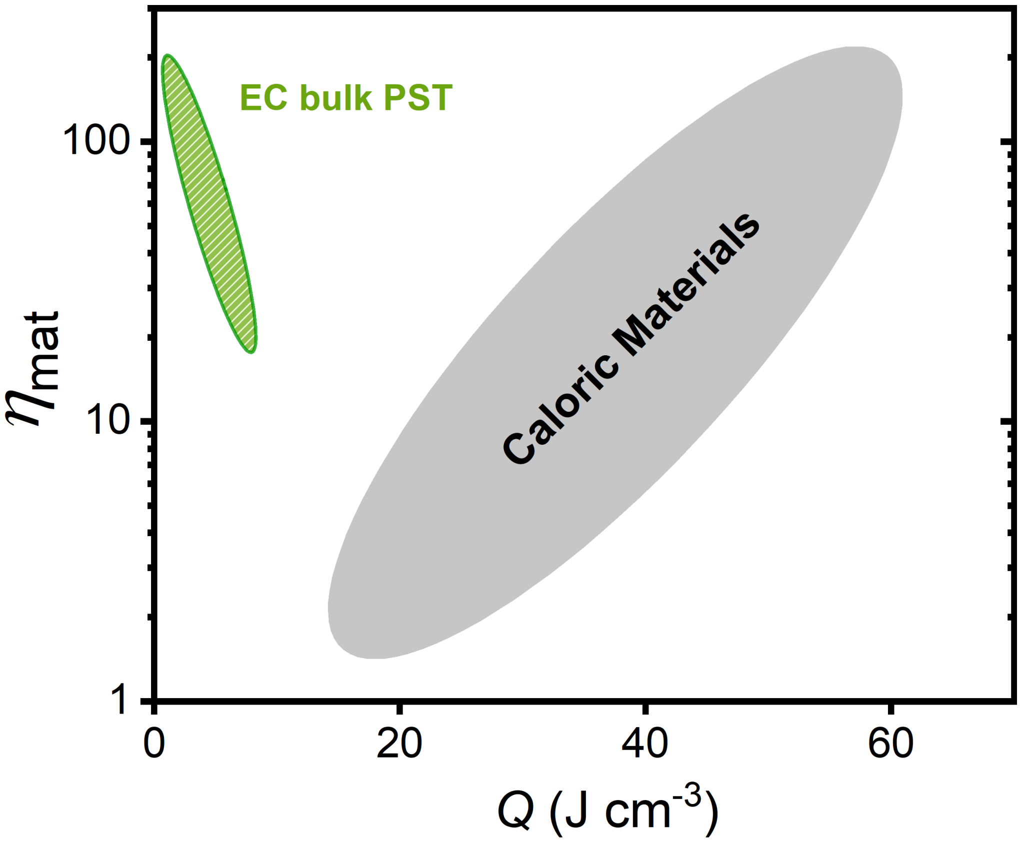

Figure 4.20: **Comparison Materials Efficiency caloric materials.** This energy efficiency map of caloric materials as a function of the heat Q per volume is adapted from Crossley et al. [ref]. The caloric materials include magnetocaloric (MC) under permanent magnet of 2 T, MC under solenoid, elastocaloric (eC) materials, barocaloric (BC), EC (electrically driven) and EC materials using energy recovery. In this map we added the materials efficiency of PST bulk. PST is shown here as being as efficient as the best caloric materials which are magnetocaloric (MC) under permanent magnet 2 T, barocaloric (BC) and EC materials using energy recovery.

Besides being energy efficient in a narrow temperature window, bulk PST suffers from an asymmetry in ΔT_{adiab} measurements and hysteresis losses. It is legitimate to wonder how this material could be used to run a cycle and the impact of its materials efficiency.

Firstly, we experimentally mimicked the working principle of a regenerator on bulk PST sample 1 using a temperature-controlled hot plate stage. The main goal of a regenerator is to build a temperature gradient larger than ΔT_{adiab} by running a specific thermodynamic cycle. To avoid destroying the build-in gradient in a regenerator, the positive ΔT_{adiab} should be triggered at the highest temperature and the negative ΔT_{adiab} at the lowest temperature. Besides both values of ΔT_{adiab} should be of the same magnitude. From ΔT_{adiab} measurements in Figure 4.12a, one can define a temperature window in which the regenerator could operate. At the maximum η_{mat} obtain at 11 kV cm^{-1}, we could simulate experimentally reproducible and reversible regenerators A (yellow line in Figure 4.21c) and B (black line in Figure 4.21c). In Figure 4.21a (resp. Figure 4.21b), PST is first set at 300.5 K (resp. 301 K). The EC positive ΔT_{adiab}=1.7 K (resp. 1.4 K) is then triggered by charging PST. Heat is exchanged and PST goes back to 300.5 K (resp. 301 K). If PST was in a regenerator, a fluid (for instance) would then be displaced and PST temperature would decrease. Here, we suppose that this temperature is 300 K (resp. 299.5 K). This value is chosen in order to obtain a symmetrical position in ΔT_{adiab} = f(T_s) displayed in Figure 4.21c. This EC negative ΔT_{adiab} = -1.7 K (resp. -1.4 K) is then triggered by discharging PST and PST exchanges heat until it reaches 300 K (299.5 K) again. And the cycle carries on as it would in a proper regenerator. The materials efficiency measured here is at least 92 but at a lower heat exchanged Q = 4.63 J cm^{-3}. Other regenerators were built at higher Q by increasing the electric field applied as shown in Figure 4.22. However, the materials efficiency will decrease as the heat saturates and the electrical work increases.

Moreover, we simulate a fluid-based regenerator based on a similar model published in [32] operating at different T_s around room temperature and without any kind of heat losses to the environment. The simulation consists of a finite element method (FEM) 2D representation of an active regenerator made with a single PST plate of 0.2 mm x 4 cm. All the parameters of this model are detailed in [32]. Figure 4.23 shows that a temperature gradient could be reached after several cycles. This study indicates the potential of using bulk PST as a working medium to build a regenerator.

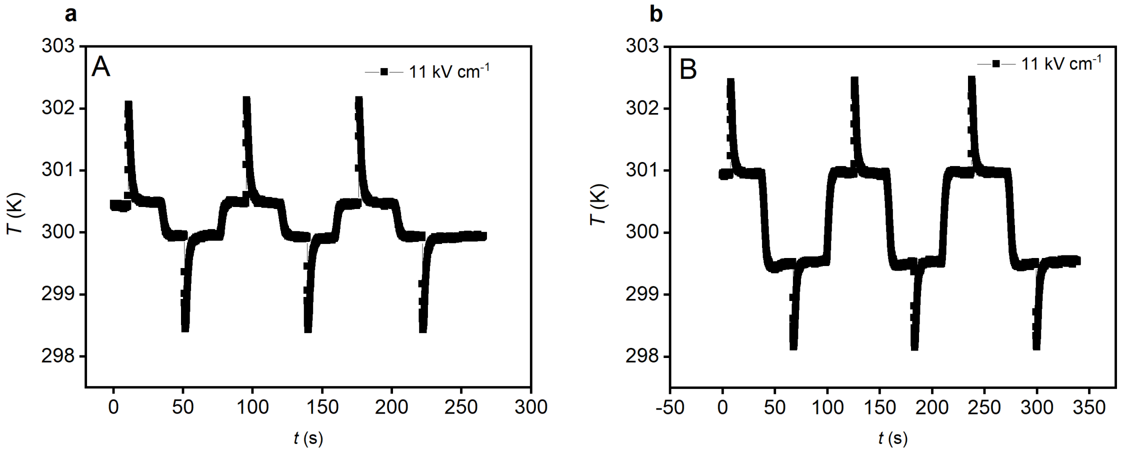

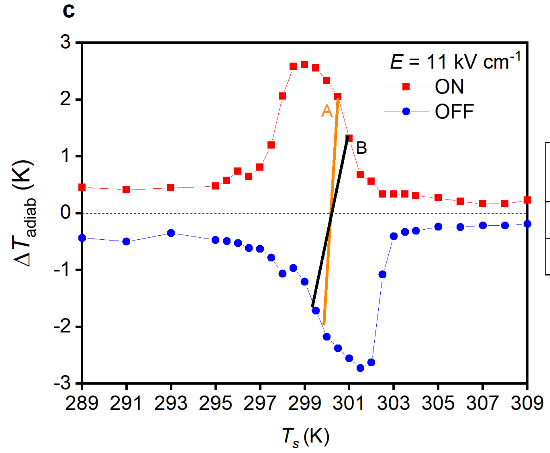

d

Regenerator	Temperature Window (K)	ΔT_{adiab} (K)	Q (J cm^{-3})	η_{mat}
A	[300 - 300.5]	+/- 1.7	4.63	[111 - 128]
B	[299.5 - 301]	+/- 1.4	3.81	[92 - 126]

Figure 4.21: **Potential use of bulk PST in a regenerator.** **a** Regenerator A operating between 300-300.5 K, on a temperature window of 0.5 K. **b** Regenerator B operating on a temperature window of 1.5 K. **c** Adiabatic temperature change of PST bulk at 11 kV cm^{-1}. The orange and black lines represent respectively the regenerators A and B. **d** the table shows for each regenerator, its temperature window, the heat exchanged and the corresponding measured materials efficiency.

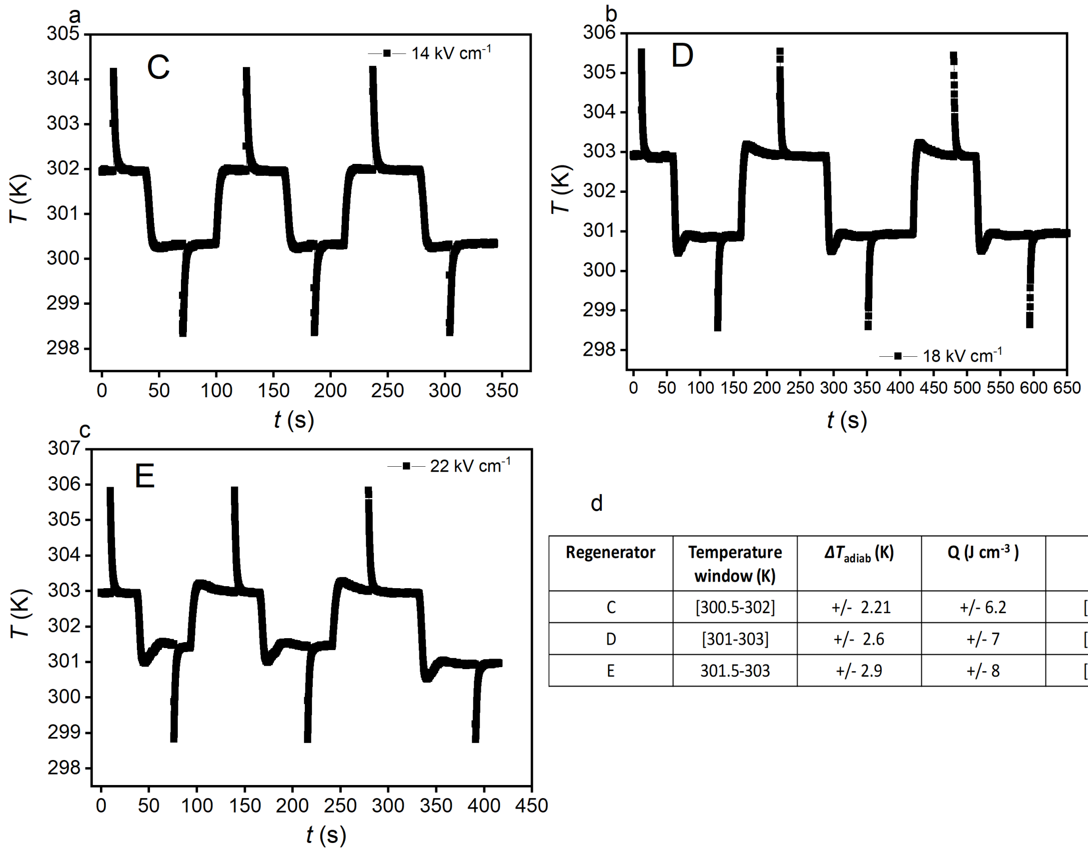

d

Regenerator	**Temperature window (K)**	**$\Delta T_{\mathrm{adiab}}$ (K)**	**Q (J cm^{-3})**	**η_{mat}**
C	[300.5-302]	+/- 2.21	+/- 6.2	[62-75]
D	[301-303]	+/- 2.6	+/- 7	[31-41]
E	301.5-303	+/- 2.9	+/- 8	[19-24]

Figure 4.22: **Potential use of bulk PST in a regenerator at higher Q.** The heat exchanged can be increase by increasing the electric field but this will decrease the materials efficiency as shown in **d**. **a** regenerator C at the electric field of 14 kV cm^{-1} **b** regenerator D at 18 kV cm^{-1} **c** regenerator E at field of 22 kV cm^{-1} **d** for each regenerator, the heat exchanged, materials efficiency and adiabatic temperature change.

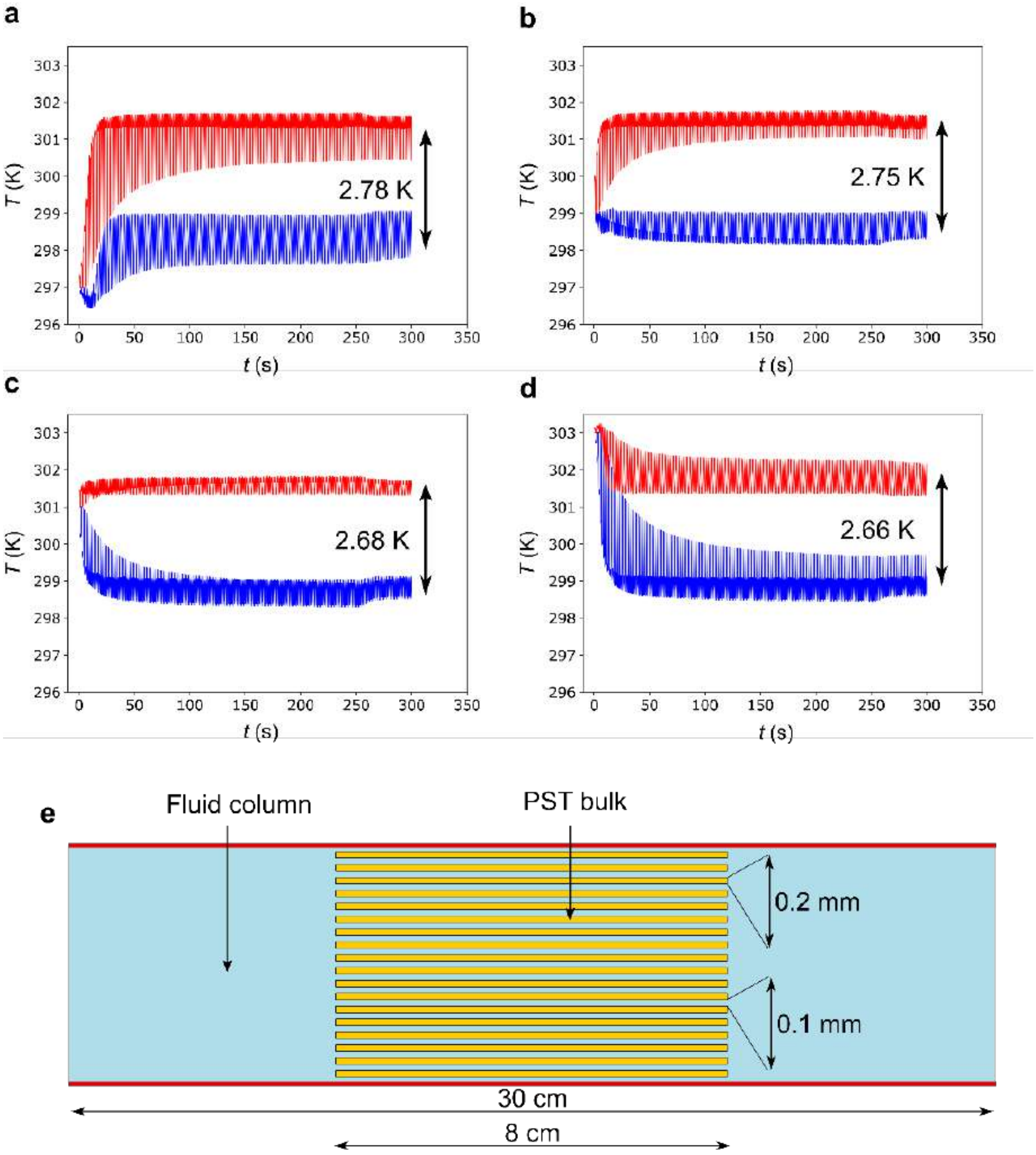

Figure 4.23: **Regenerator Modelling** The time evolution of the hot side (red) and cold side (blue) of an active regenerator based on the EC effect from Supplementary Fig. 20c at starting temperatures **a** 297 K, **b** 299 K, **c** 301 K and **d** 303 K. **e** shows the dimensions of the regenerator simulated. This simulation was done by A. Torello.

Table 4.1: **Adiabatic temperature change of PST bulk ceramics** This table shows the influence of the B-site ordering on the adiabatic temperature change and temperature range of PST bulk ceramics. ΔT_{adiab} were measured directly and the temperature range is defined as the full width at 80% of the maximum ΔT_{adiab}. Data of our PST sample 2 are presented in Appendix. Due to the high B-site ordering of our material (PST sample 1) we obtained the highest ΔT_{adiab} directly measured.

Material	Ω	**T$_0$(K)**	ΔT_{adiab} **(K)**	**Temp. range (K)**	***E*** **(kV cm^{-1})**	**Ref.**
PST sample 1	0.98	300	3.7		40	**this work**
PST sample 1	0.98	300	3.1	8.4	22	**this work**
PST sample 1	0.98	300	2.6	2.5	11	**this work**
PST sample 2	0.89	298	2.4	2.5	11	**this work**
PST	0.85	295	2.3		50	[53]
PST	0.85	295	1.6	7	25	[55]
PST	0.80	295	2.2	14	26	[129]
PST	0.34	263	0.5	19	25	[55]
PST	0	263	0.18	40	25	[55]

Table 4.2: **Comparison of materials efficiency of PST and Gd** In this table we compare the energy efficiency of PST bulk ceramic sample 1 with Gd for the same EC heat exchanged Q (in bold underline and italic).

	Bulk ceramic PST (sample 1)		**Gadolinium**	
Field	11 kV cm^{-1}	22 kV cm^{-1}	1 T	1.3 T
Q (J cm^{-3})	**<u>7.1</u>**	*8.6*	**<u>7</u>**	*9.4*
Temperature range (K)	2.5	8.4	14	14
η_{mat}	78	16	18	14

4.5 Conclusion

In this chapter, we have presented the materials efficiency $\eta_{mat} = \frac{Q}{W_e}$ of highly ordered (Ω = 0.98) bulk PST by direct measurements of the exchangeable EC heat Q and electrical work W_e. Our bulk PST shows near its ferroelectric to paraelectric transition at T_0 = 300 K, a maximum direct ΔT_{adiab} = 3.7 K at the modest electric field of 40 kV cm^{-1}. This is a sixty percent increase compared to values reported in the literature. This improvement is due to the high B-site cation order of our material which induces a strong first-order transition. Besides, we measured from calorimetric measurements an entropy change of 3.4 J kg^{-1} K^{-1} at 22 kV cm^{-1}. A high η_{mat} of 128 was obtained in highly ordered bulk PST, placing it among the most energy-efficient caloric materials. Our comparison of this material to the prototyping MC material Gd shows that PST requires four times less work to exchange the same amount of heat compared to Gd. However, the high efficiency of PST is limited by its small temperature range (2.5 K in PST and more than 10 K in Gd). Hence, highly ordered bulk PST could be considered as a candidate for heat pumps based on layered regenerator. Its high materials efficiency should allow improving the coefficient of performances of future devices.

Chapter 5

Materials efficiency of lead scandium tantalate multilayer capacitors

5.1 Motivation

A Multi-Layer Capacitor (MLC) is an electronic device that comprises film layers of dielectric material electrically connected with interdigitated metallic electrodes [25, 155]. Such a device enables storing a large number of electrical charges in a small volume. This is desirable for high-performance, low-power, or miniatures devices. These electronic components are present in our mobile phones or computers [156, 157]. More than three decades ago, the MLC geometry was suggested for EC purposes as it doesn't suffer from the drawbacks of bulk and thin films [75, 100, 101, 155, 158]. They exhibit breakdown fields larger than bulk and possess more active mass than a single film. Besides, MLCs' inner electrodes facilitate heat exchange between the EC thin layers, making it interesting for cooling applications [32, 72, 148]. Materials scientists, engineers, and chemists have been studying the ECE in MLCs based on doped ferroelectric with larges capacitances which vary with temperature and field. They have made significant improvements such as the fabrication of MLCs based on excellent EC materials which are commonly ferroelectric oxides or polymers [29, 71, 101].

In the previous chapter, we studied the materials efficiency of PbSc$_{1/2}$Ta$_{1/2}$O$_3$ – short form PST- in the shape of bulk ceramic. As a conclusion, we showed that PST bulk is one of the most energy-efficient EC materials. However, its high materials efficiency η_{mat} is limited by its small operating temperature range which can be an issue for building EC cooling devices. To solve this drawback, PST in the form of MLCs was suggested as an alternative solution in order to operate in a large temperature range. Nevertheless, how energy efficient are these PST MLCs? This question remains overlooked in the scientific literature. As a follow-up to the preceding chapter, here, we will investigate the materials efficiency of PST in the form of MLC using the same approach as in the previous chapter. Firstly, we will present a structural, electric, and thermal characterization of this material. Secondly will determine its materials efficiency $\eta_{mat} = Q/W_e$ by directly characterizing its ECE heat exchanged Q and the electrical work W_e required to drive this ECE. Last, a comparison in terms of energy efficiency of PST MLC to PST bulk ceramic and prototypical MC material Gadolinium (Gd) will be presented.

The results shown in this chapter have led to the publication of one of my first-authorship publications: Y. Nouchokgwe, P. Lheritier, T. Usui, A. Torello, A. El Moul, V. Kovacova, T. Granzow, S. Hirose, and E. Defay, "Materials efficiency of electrocaloric lead scandium tantalate multilayer capacitors", Scripta Materiala, 219, 114873 (2022). Besides, my study of the ECE in PST MLCs has been published in one of my co-authorship papers: A. Torello, P. Lheritier, T. Usui, Y. Nouchokgwe, M. Gerard, O. Bouton, S. Hirose, and E. Defay, "Giant temperature span in electrocaloric regenerator", Science, 370, 6512, (2020). In this paper, I characterized the EC modules (PST MLCs) used as working medium to build an EC cooling regenerator. Both publications were done in collaboration with the industrial company Murata Manufacturating in Japan. This company fabricated and provided us with the PST MLCs characterized in this chapter.

5.2 ECE in Multi-Layer Capacitors

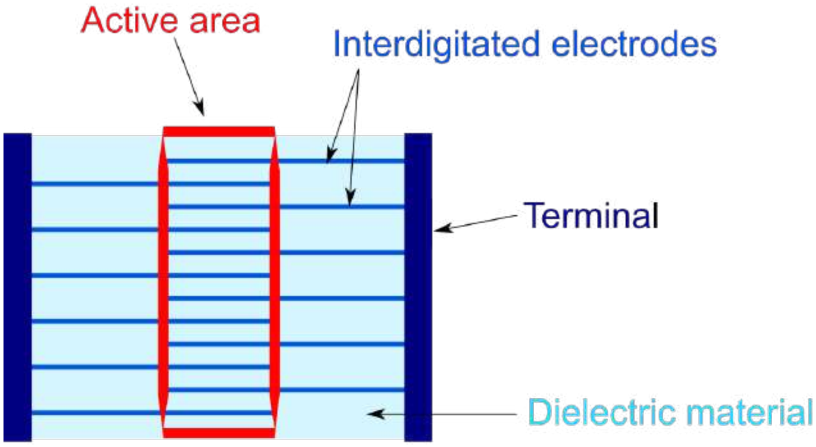

Figure 5.1: **Geometry of a Multi-Layer Capacitor (MLC)** The red rectangle represents the active area of the MLC structure where the layers of interdigitated electrodes overlap. The terminals are the outer electrodes.

MLC is an interesting geometry for EC applications. As described in Figure 5.1 a MLC is a stack of EC dielectric films that are electrically connected in parallel to each other by interdigitated inner electrodes. We distinguish two areas in the structure of a MLC: the active and inactive areas. The active area is described by the red rectangle in Figure 5.1, where the inner layers of electrodes overlap. In this area, the electric field is being applied. Out of this area, the area is considered inactive. Therefore, the ECE is triggered in the active area and it spreads to the inactive area. The two terminals enable reaching the inner electrodes and applying an electric field.

EC materials that exhibit large adiabatic temperature change around room temperature and on a broad temperature are highly desired for EC cooling devices. The MLC geometry has been proven to be an excellent option as one can apply large electric fields [159]. However its fabrication remains a challenge. A few materials such as $BaTiO_3$ (BTO) [75, 100, 101, 160–162], $PbMg_{1/3}Nb_{2/3}O_3$ (PMN) [163, 164], $PbSc_{1/2}Ta_{1/2}O_3$ (PST) [29, 32, 54, 72],

$PbMg_{1/3}Nb_{2/3}O_3$-$PbTiO_3$ (PMN-PT) [158, 165–167] ceramics and polymer poly(vinylidene fluoridetrifluoroethylene) (P(VDF-TrFE)) [71] were used as dielectric material to build MLCs.

The ECE of commercially available MLC based on dielectric $BaTiO_3$ doped and Ni-based electrodes was studied by Kar-Narayan et al.[100]. This MLC comprised 200 layers of 6.5 μm thick of doped $BaTiO_3$ and 2 μm thick of Ni electrodes. The authors measured directly using a thermocouple (Pt-100 thermometer) placed on one of the terminals, a ΔT_{adiab} = 0.5 K around room temperature and at the electric field of 300 kV cm^{-1}. This result agreed well with the indirect measurements done using the Maxwell relations described in Chapter 2 of this dissertation. Three years later [101], the same group, verified these results by measuring the ECE of the same material using two other direct techniques: infrared imaging and scanning thermal microscopy. They measured on one side of the MLC, a slightly higher ΔT_{adiab} of 0.70 K. This discrepancy is explained by the fact that ECE measurements taken on the terminal are reduced by the electrodes thermal mass whereas measurements taken on the side and closer to the EC layers are more accurate. Larger ΔT_{adiab} of 1.8 K at 176 kV cm^{-1} was directly measured in MLCs BTO [162] using a DSC. This MLC was fabricated by tape casting methods by the authors and comprises 180 of 1.4 μm thick of $BaTiO_3$. The highest measured ΔT_{adiab} in BTO MLCs was obtained by Bai et al. [168]. They measured by direct measurements using a calorimeter, a maximum of 7.1 K at 353 K and under the high electric field of 800 kV cm^{-1}. MLCs based on PMN-PT shows the reported value of 2.7 K at 288 kV cm^{-1}.

PST was first suggested in 2002 by Shebanov et al. [54] to be used as active material in a MLC. They stated that their PST MLC had a ΔT_{adiab} of 2.4 K at the electric field of 138 kV cm^{-1} even though no experimental data were shown. It is eighteen years later, after the improvement of the PST MLC fabrication, the increase of its breakdown field, and the enhancement of the B-site cation of PST, that Nair et al.[29] measured in MLC-based PST, the highest value directly measured in a bulky sample. They obtained by IR camera on PST MLC with a B-site ordering of 0.96, a ΔT_{adiab} of 5.5 K around room temperature and when driven supercritically at the strong field of 290 kV cm^{-1}. The supercritical regime is a regime where the entropy change of the material is driven beyond the entropy change induced by temperature[81]. Moreover, a ΔT_{adiab} beyond 3 K on a temperature range of 176 K was measured on PST MLC, making it interesting for EC cooling devices.

MLC-based EC materials have been utilized to build a few EC prototypes [32, 71, 72, 148]. Gu et al.[71] used MLCs based P(VDF-TrFE) with a ΔT_{adiab} = 2.2 K, as a working medium to build an EC regenerator prototype. They obtained a temperature span ΔT_{span} (difference between the hot side and cold side of a cooler) of 5 K. PST MLC was used by Y. Wang et al.[72] to build an EC device with a ΔT_{span} of 5.2 K. The same year, in the same journal volume, we used 128 PST MLCs to build an EC regenerator that could reach the ΔT_{span} of 13 K [32]. This is up-to-date the highest ΔT_{span} measured in an EC cooler. An EC regenerator follows the principle of active regeneration [71, 148, 160, 169, 170] which enables reaching ΔT_{span} larger than the ΔT_{adiab} of the material. Interestingly, the materials efficiency [30, 33, 34] which is the ratio of the heat exchanged by the MLC to the electrical energy required to drive this heat is barely reported. In this work, we will study the intrinsic efficiency of the EC benchmark material PST in the shape of MLC.

5.3 Results

5.3.1 Experimental details

PST MLC - sample preparation

The PST MLCs studied here were fabricated by solid-state reaction and tape casting. These samples were fabricated by T. Usui and S. Hirose from Murata Manufacturing in Japan.

Following the stoichiometric of PST, powders of Pb_3O_4, Sc_2O_3 and Ta_2O_5 were ball milled for 17 hours in distilled water with balls of zirconia. The PST powder was then obtained from the resulting mixture after a 4 hours of drying and calcination at 850 ℃. Subsequently, the PST powder was ball-milled in an organic solvent for 24 hours with a binder. Green sheets of PST of 300 μm-gap doctor blade were made out of the resulting PST powder slurry. The inner electrodes of Pt paste were screen-printed. Following this, the green sheets were stacked, pressed, and cut to obtain green chips. Later, the binder was destroyed by burning it off at 500 ℃ for 4 hours. The MLCs were sintered at 1400 ℃ for 4 hours and later annealed at a temperature smaller than 1000 ℃ for 100-1000 hours with a mixture of Pb_3O_4 and ZrO_2 powders with a Pb:Zr ratio of 1:1. The terminals (outer electrodes) were done with silver paste.

Dielectric permittivity measurements

An impedance spectrometer (Novocontrol) was used to record the dielectric measurements at 100 Hz on cooling and heating at a heating rate of 0.1 K min^{-1} in a cryogenic probe. These measurements were carried out by Torsten Granzow.

Zero-field calorimetric measurements

Heat flux $\frac{dQ}{dT}$ and specific heat measurements C_p were carried out on 18 mg of a PST MLC (cut at its centre) at a heating rate of 5 K min^{-1}. These measurements were done with a commercial Differential Scanning Calorimeter (DSC3 Mettler Toledo) described in Chapter 3. Sapphire was used here as a reference for the calculation of C_p following the method described in Chapter 3.

X-Rays Diffraction (XRD) measurements

XRD diffraction was performed from 15 to 60 degrees angle, every 0.01 degrees on powdered PST MLC using Bruker D8 Discover.

InfraRed (IR) Imaging measurements

A FLIR X6580sc IR camera was used to collect EC temperature change of a PST MLC. The measurements were taken on one of the two surfaces of the PST MLC, at its active area. The sample was black painted with *Colorjet,Noir Mat* to improve the material's emissivity to 1, required for IR camera measurements. Colorjet,Noir Mat [104] is a quick-drying glycerophthalic-type touch-up paints, packaged in aerosols and intended for touch-up marking, decoration and finishing. The starting temperature T_s was controlled with a Linkam cell. More details about EC measurements using IR Camera are given in Chapter 3.

5.3.2 Scanning Electron Microscopy (SEM)

This technique is described in details in Chapter 3 of this dissertation. A Quanta 200 Field Emission Gun Scanning Electron Microscope (FEG SEM) from Philips-FEI was used here to map and collect images of the PST MLC's structure. The microscope is equipped with a Genesis XM 4i Energy Dispersive Spectrometer (from EDAX) system for chemical analysis. From the backscattered electron detector, pictures of the chemical composition of the observed sample result (composition mode). The contrast of the picture is based on the convention that ”heavier” element areas (high atomic number Z, for example, ZSn=50 compared to ZNa=11) are shown in light grey and low atomic number elements in darker grey.

5.3.3 Dedicated setup for work extraction

The PST capacitor was charged at constant current rather than at constant voltage because it is more efficient in terms of energy (more details in Chapter 3). A dedicated setup was used to extract the charge as a function of time and calculate the electric work used to charge the PST capacitor to a given voltage at a constant current.

5.3.4 Characterization of PST MLC

Structural analysis of PST MLC

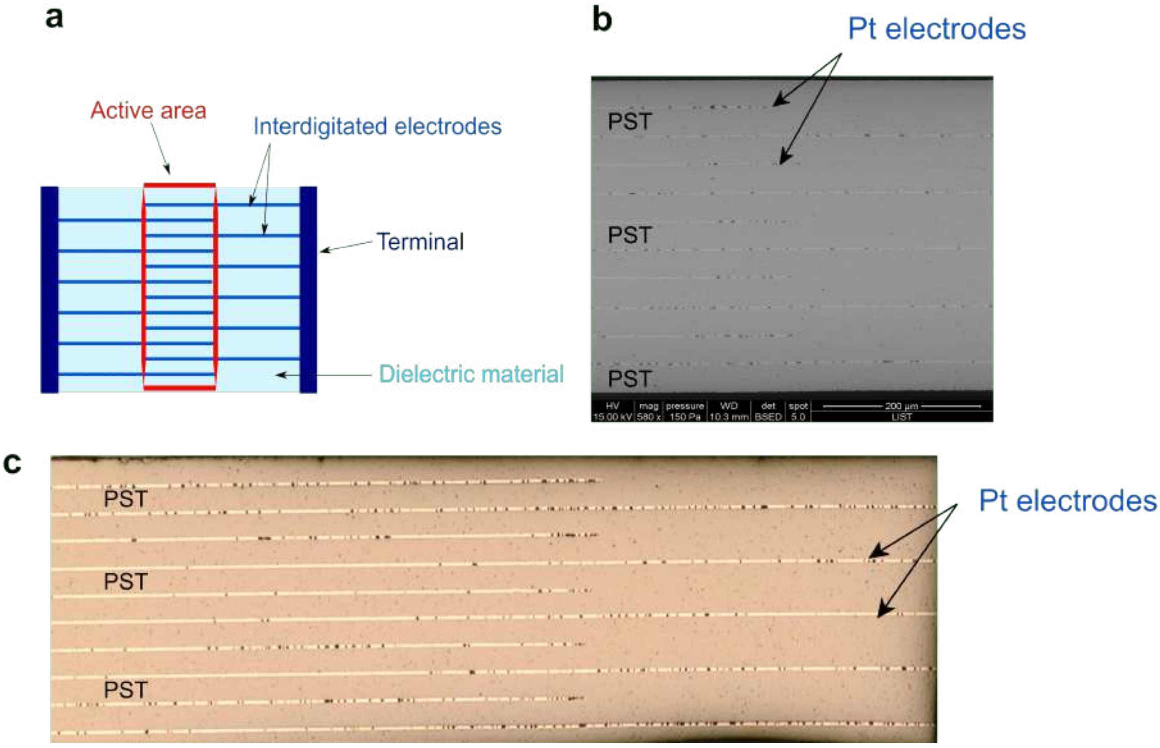

Figure 5.2: **Structure of a PST MLC a** Geometry of a MLC. The red rectangle is the active area where the electrodes overlap. **b** SEM image of a PST MLC. The white lines are the platinum (Pt) electrodes in between layers of PST. **c** Electronic microscope image of a PST MLC.

Utilizing a Scanning Electronic Microscope (SEM), we looked at the structure of the PST MLC studied and measured its dimensions. Figure 5.2 shows the SEM images of a PST MLC. In Figures 5.2b and 5.2c, we can observed the layers of platinum electrodes (white lines) and the layers of PST. We count 11 layers of PST including 9 active layers (layers of PST between two layers of electrodes) and 10 layers of Pt electrodes. We measured a thickness of 0.42 mm (Figure 5.3), a length of 10.1 mm and a width of 7.3 mm.

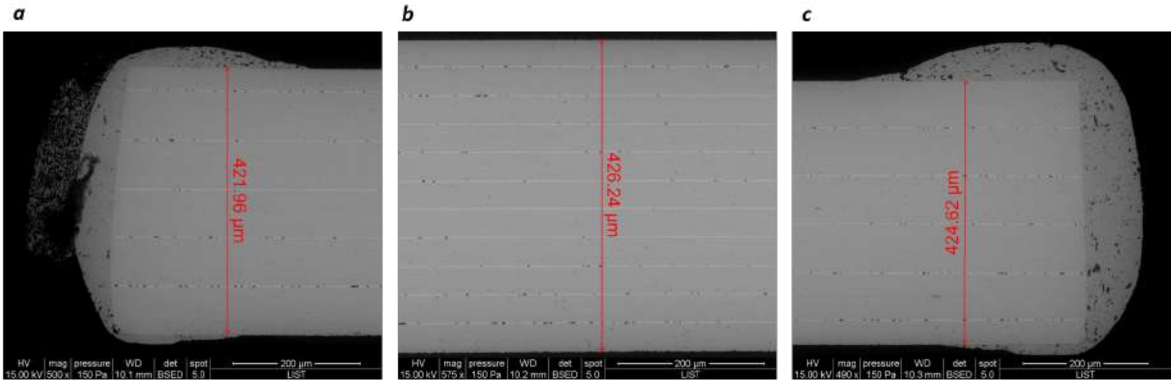

Figure 5.3: **SEM image of the left edge (a), centre (b) and right edge of PST MLC (c).** We measured an average thickness of 0.42 mm.

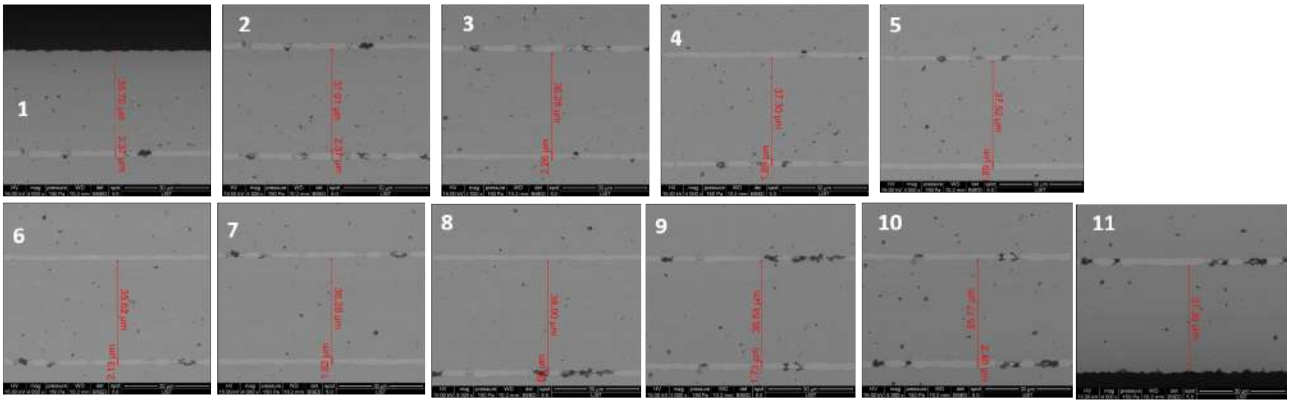

Figure 5.4: **The 11 layers of PST and 10 layers of platinum electrodes of a PST MLC.**

The SEM images in Figure 5.4 show 11 layers of 38.6 ± 0.6 μm thick PST films intercalated with 2.05 ± 0.05 μm thick interdigitated electrodes of platinum. The error bars correspond to the standard deviation measured on three different PST MLCs from the same batch. The active area (red rectangle Figure 5.2a) that corresponds to the overlap between the inner layers of electrodes is 48.7 mm^{-2}. The active volume stands for 54.5% of the total volume of one MLC.

XRD measurements on powdered PST MLC are presented in Figure 5.5. The B-site cation order $\Omega \sim 0.75$ was calculated from the integrated intensities of the (111) and (200) peaks using equation (4.1) [135][52].

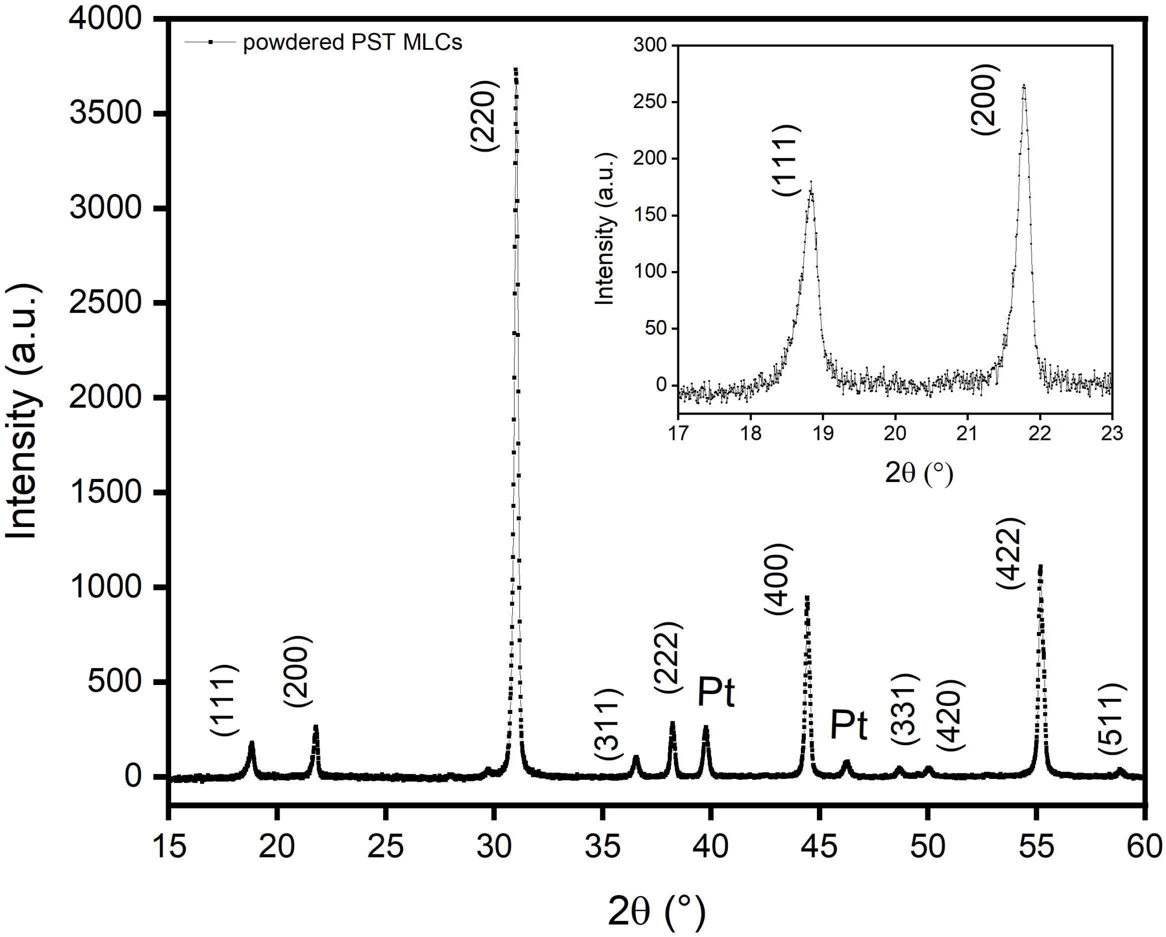

Figure 5.5: **XRD of powdered PST MLCs** X-ray diffraction measurements were carried out on crushed PST MLC. From the intensities of the (111) and (200) peaks (inset image), we calculated the B-site cation ordering Ω of PST MLC using the equation (4.1).

Electrical and thermal characterization of PST MLC

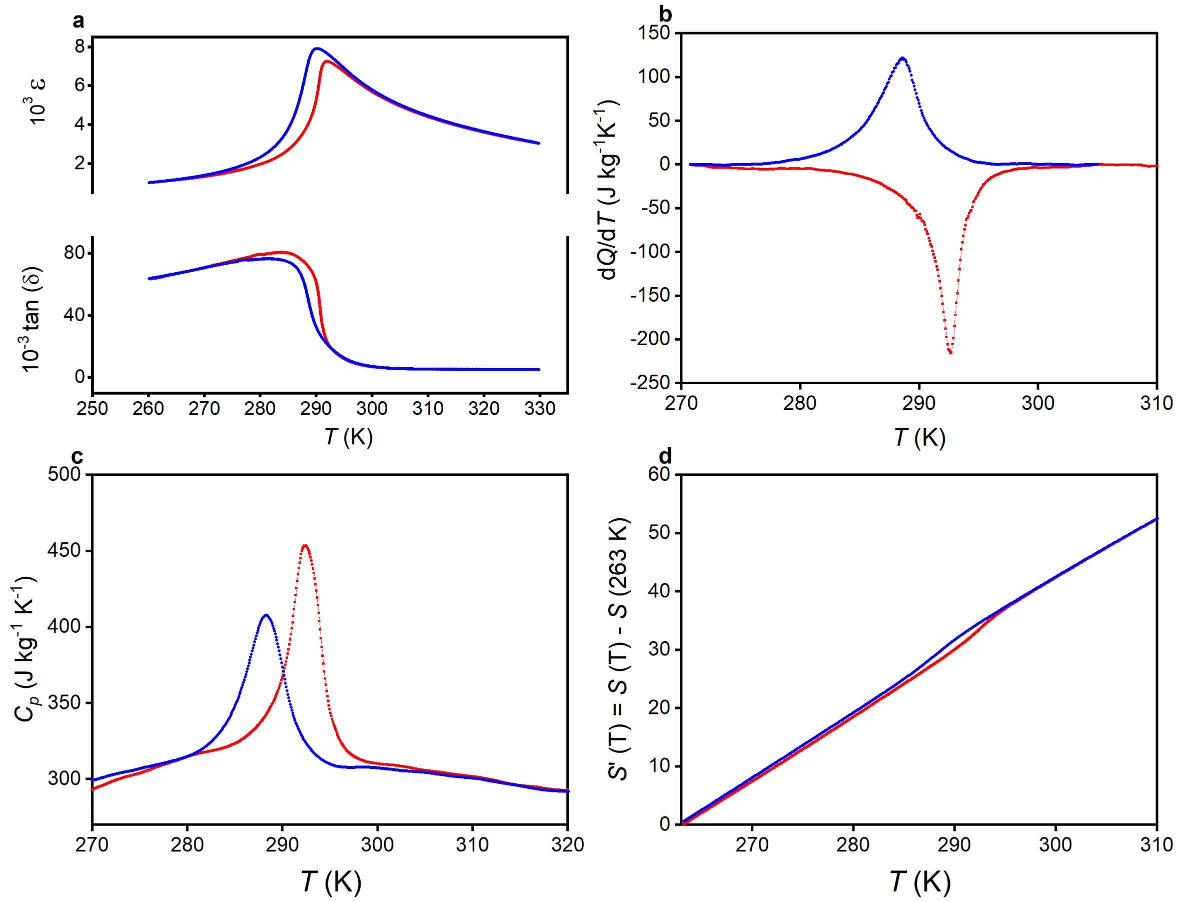

Figure 5.6: **Dielectric and thermal measurements in PST MLC** The blue and red denote respectively the cooling and heating. **a** Dielectric constant (top panel) and losses (bottom panel) as function of temperature *T*. **b** Heat flow measurements at 0 kV cm^{-1}. **c** Zero-field heat capacity measurements. **d** Entropy $S'(T)$ = $S(T)$ - S(263 K) at 0 kV cm^{-1} referenced to the entropy at 263 K. These entropy curves were constructed as explained in Chapter 3.

From the dielectric constant measurements presented in Figure 5.6a, we observe a transition peak at T_0 = 290.2 K on cooling and 292.6 K on heating. The dielectric losses decrease from 0.005 in the paraelectric (PE) phase (high-temperature) to zero in the ferroelectric (FE) phase (low-temperature phase). Calorimetric measurements of heat flow (Figure 5.6b) and specific heat (Figure 5.6c) at zero-field ascertain the first-order behaviour of PST MLC with well-defined latent heat peaks and a thermal hysteresis of 4 K. The heating peak shows a transition from a FE to a PE phase whilst the cooling peak describes a transition from the PE to the FE phase. We obtain a latent heat on heating $Q_{0,h}$ = 640 J kg^{-1} by integration of the heating peak. This value is 45% less than the latent heat (1165 J kg^{-1}) measured by Nair et al. [29] on another PST MLC . This discrepancy is due to the high B-site ordering of their sample (Ω = 0.96) compare to ours (Ω = 0.75). We measured a slightly lower latent heat of cooling $Q_{0,c}$ = 526 J kg^{-1} by integration of the blue peak. The C$_p$ measurement reveals a background value of 300 J kg^{-1} K^{-1} which, is in adequation with similar measurements performed on bulk PST (Chapter 4) [30] and in line with reported values in the literature [29, 96, 129]. We constructed as explained in Chapter 3, the entropy S' referenced to the entropy at 263 K far from the transition. We measured an entropy change of 2.19 J kg^{-1} K^{-1} due to the transition from FE to PE phase triggered by temperature.

5.3.5 Materials efficiency of PST MLC

Using the same approach as in Chapter 4, we will calculate the materials efficiency $\eta_{mat} = Q/W_e$ of PST MLC from measurements of EC heat Q and electrical work W_e.

Electrocaloric effect in PST MLC

As described in Chapter 3 and experimental details above, an IR camera was used to collect ΔT_{adiab} of PST MLC induced by applying and removing an electric field. Electric fields ranging from 13 kV cm^{-1} to 194 kV cm^{-1} were studied here. This corresponds to applying respectively 50 V to 750 V on 38.6 μm thick layer of PST. The EC measurements were carried out under adiabatic conditions. The current of 1 mA was applied to guarantee these conditions. As shown in Figure 5.7, at a current smaller than 1 mA , ΔT_{adiab} keeps on increasing because the charge time is higher than the relaxation time of the PST sample. However, at a current greater or equal to 1 mA, ΔT_{adiab} does change with the increasing current i.e that the charging time of the capacitor (shorter than 0.2 s) is smaller than its relaxation time. Figure 5.8, shows ΔT_{adiab} recorded at the PST MLCs face center (active area) as a function of starting temperature T_s at different electric fields. The reproducibility of these measure-

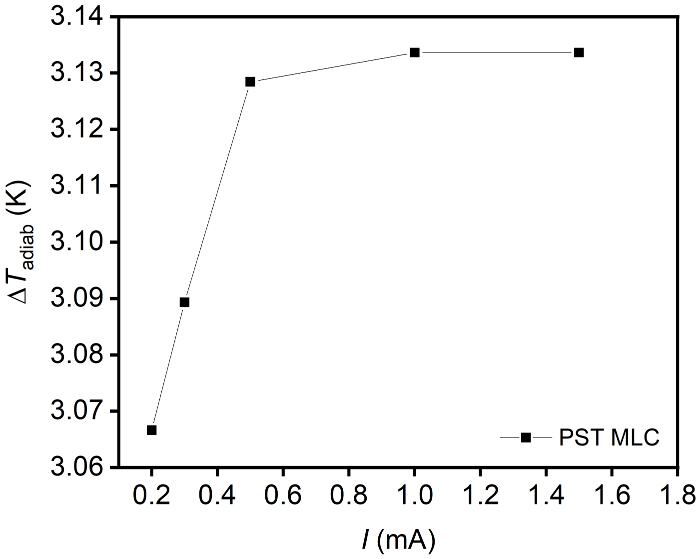

Figure 5.7: **Adiabatic conditions in PST MLC** ΔT_{adiab} versus applied current I. These measurements were done at room temperature on a PST MLC at 118 kV cm^{-1}.

ments was verified upon three successive runs as shown in Figure 5.9. Therefore, ΔT_{adiab} in Figure 5.8 is an average of these runs at any T_s and electric field.

In Figure 5.8, at the lowest electric field applied of 13 kV cm^{-1}, we measured a maximum reversible ΔT_{adiab} = 1.78 K, at T_s = 293 K (close to PST's transition temperature). This temperature change is obtained in a temperature range of 5.5 K. As defined in the previous chapter, this temperature range is the full width at 80% of the maximum ΔT_{adiab}. As observed in Figure 5.8, the ECE in PST MLC is not fully driven at this field as ΔT_{adiab} continues to increase substantially with the increasing electric field. Besides, this increase of ΔT_{adiab} with the field goes along with the increase in the material's temperature range.

From the shift of the maximum value of ΔT_{adiab} towards high temperatures with the increasing electric field, we can deduce a stabilisation of the ferroelectric phase. At the field of 39 kV cm^{-1}, we measured a maximum ΔT_{adiab} of 2.44 K at T_s = 295 K. This change of temperature corresponds to an entropy change ΔS of 2.48 J kg^{-1} K^{-1} estimated using the interconversion relation (5.1). From isothermal entropy change carried out with a DSC and

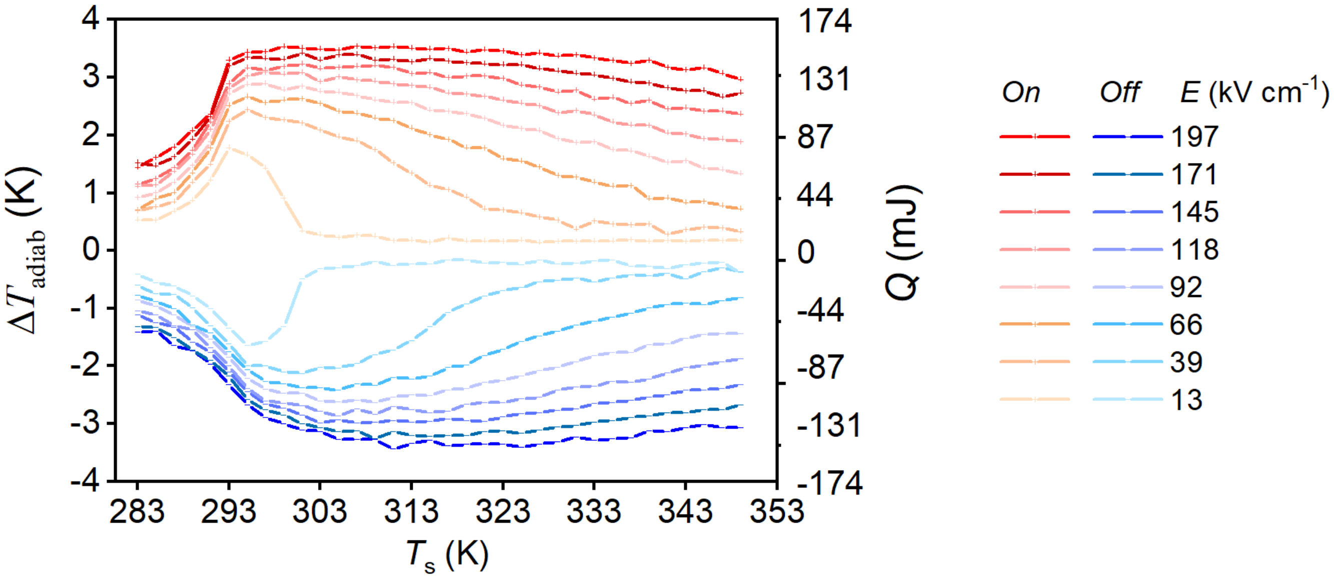

Figure 5.8: **ECE in PST MLC** Adiabatic temperature change ΔT_{adiab} (left y-axis) and exchangeable EC heat Q (right y-axis) as a function of starting temperature T_s at different electric fields E. The orange to red curves corresponds to the temperature change obtained upon application of an electric field. The light to dark blue curves are data of temperature change which result from the removal of an electric field. Q is calculated using the formula in equation (4.2).

adiabatic temperature change with an IR camera, we checked the interconversion relation (5.1) to be correct. For bulk PST ceramic, we obtained similar values of $|C_p\Delta T_{adiab}|$ and $|T_s\Delta S_{isothermal}|$ [30] with C_p = 300 J kg^{-1} K^{-1}.

$$C_p\Delta T_{adiab} = -T_s\Delta S_{isothermal} \tag{5.1}$$

The value of ΔS is very close to ΔS_0 = 2.19 J kg^{-1} K^{-1} measured by DSC when driving the transition completely with temperature. Thereby, with an electric field of 39 kV cm^{-1}, one can fully drive the transition electrically. As shown in Figure 5.10, above this critical field, we define the PST MLCs as being in a supercritical regime where the materials's entropy change is driven beyond the entropy change induced by the change in temperature. At 197 kV cm^{-1}, we reach a maximum ΔT_{adiab} of 3.5 K at around 299 K. The application of higher electric fields expands the temperature range up to 60 K at 197 kV cm^{-1} i.e a MLC

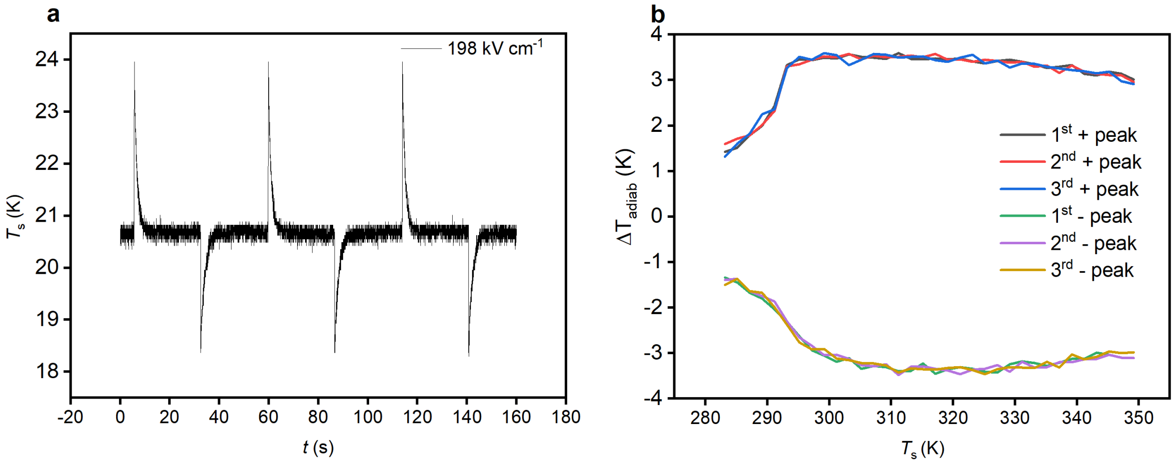

Figure 5.9: **Reproducibility of ECE in PST MLC a** ECE of PST MLC at 198 kV cm^{-1} and T_s = 20.5 ℃ = 293.65 K after three successive runs. From these data collected at different T_s we draw Figure 5.9b. **b** ΔT_{adiab} obtained from first, second and third cycles upon application (positive values) and removal (negative values) of 198 kV cm^{-1}. ΔT_{adiab} under and off field doesn't change after three EC cycle.

shows a temperature change of a least 2.8 K from 292 K to 352 K.

Materials efficiency

As already used in Chapter 4, Q is approximated using equation (4.2), with C_p measured with a DSC (Figure 5.6c). This approximation is extensively used in literature and was verified in our previous work to be a good approximation in the case of PST bulk. The right y-axis in Figure 5.8 shows EC heat exchanged by PST MLC. Q is proportional to ΔT_{adiab}. A PST MLC can exchange at maximum 0.13 J at the highest field applied of 197 kV cm^{-1}.

From voltage U at constant current I, collected as a function of time using a dedicated setup (see chapter 3), we integrated UI versus time to determine W_e (equation 4.5). The curve of U versus time at different temperatures and the curve of W_e versus field are provided in Figure 5.11.

We then deduced from Q and W_e, the materials efficiency of PST MLC presented in

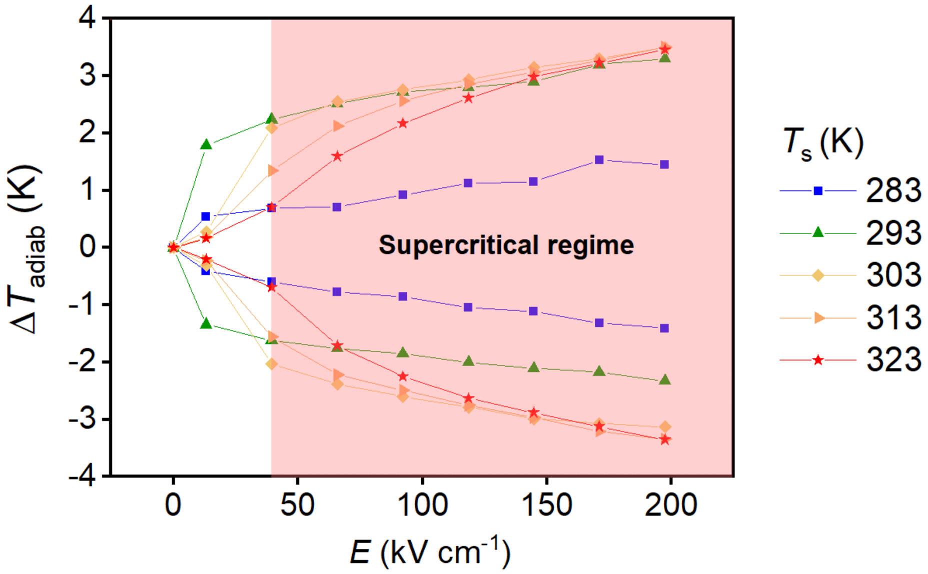

Figure 5.10: **Supercritical region in PST MLC** This figure describes the peak in ΔT_{adiab} as a function of electric field E below (283 K), at (293 K) and beyond (303, 313, 323 K) the transition temperature. The red area represents the supercritical regime.

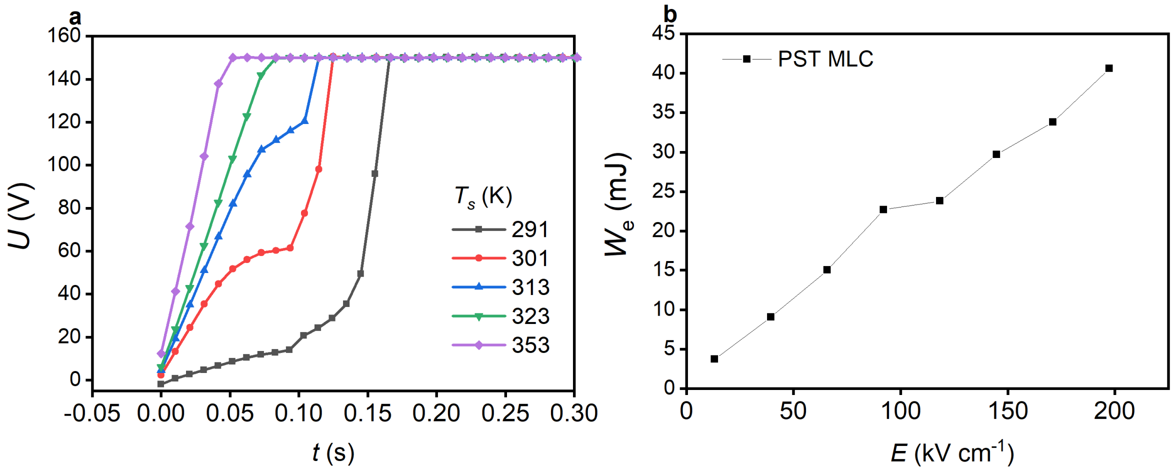

Figure 5.11: **Electrical work of PST MLC. a** Voltage versus time at different starting temperatures Ts. Around the transition temperature (290 K), we observe a difference in slopes in the $U(t)$ curves, showing the change of transition from FE-PE in PST MLC. **b** electrical work as a function of the electric field.

Figure 5.12. η_{mat} increases when the field decreases. The same behaviour was observed in the materials efficiency of PST bulk and Gd. Around the PST MLC's transition temperature,

η_{mat} reaches a maximum value of 25, at the substantial heat exchanged of 4.59 J cm^{-3} under the smallest field of 13 kV cm^{-1}.

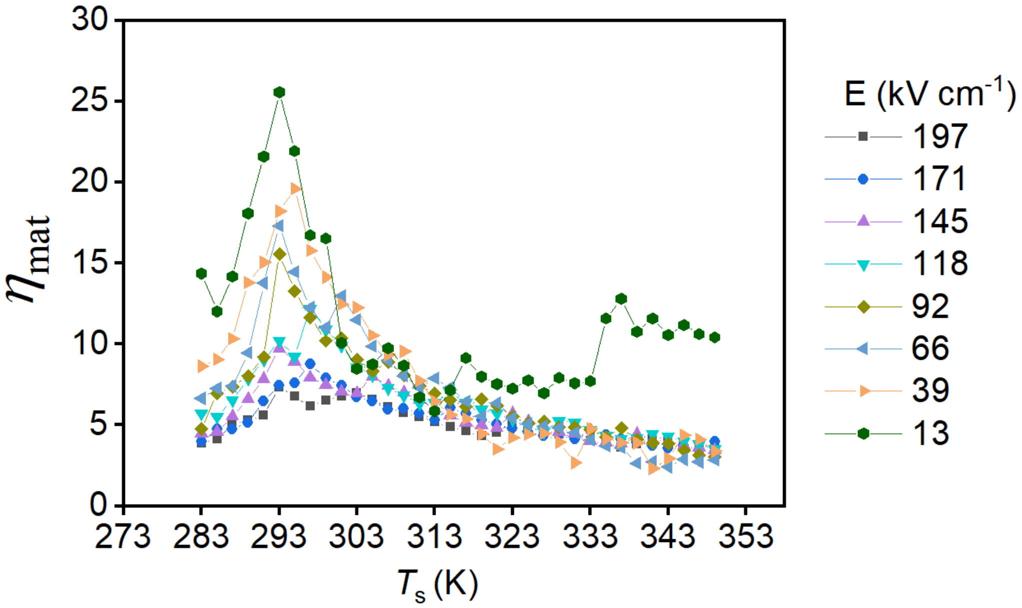

Figure 5.12: **Materials efficiency of PST MLC**

The obvious question to ask ourselves is: how is the materials efficiency of PST MLCs compared to η_{mat} of PST bulk and Gd already studied in the previous Chapter 4? In the next section, we will compare in terms of energy efficiency PST MLC to PST bulk and Gd. Besides, we will conclude with the influence of the shape of the material on its materials efficiency.

5.4 Discussion: Scale law on materials efficiency of PST

The bubble chart in Figure 5.13 compares for the same heat exchanged per volume Q, the materials efficiency of PST bulk, PST MLC to Gd. In other words, we compare the amount of energy (electrical for PST or magnetic for Gd) that the materials studied here, have to pay to exchange the same caloric heat (EC for PST and MC for Gd). In Chapter 4, η_{mat} of PST bulk and Gd was thoroughly studied [30].

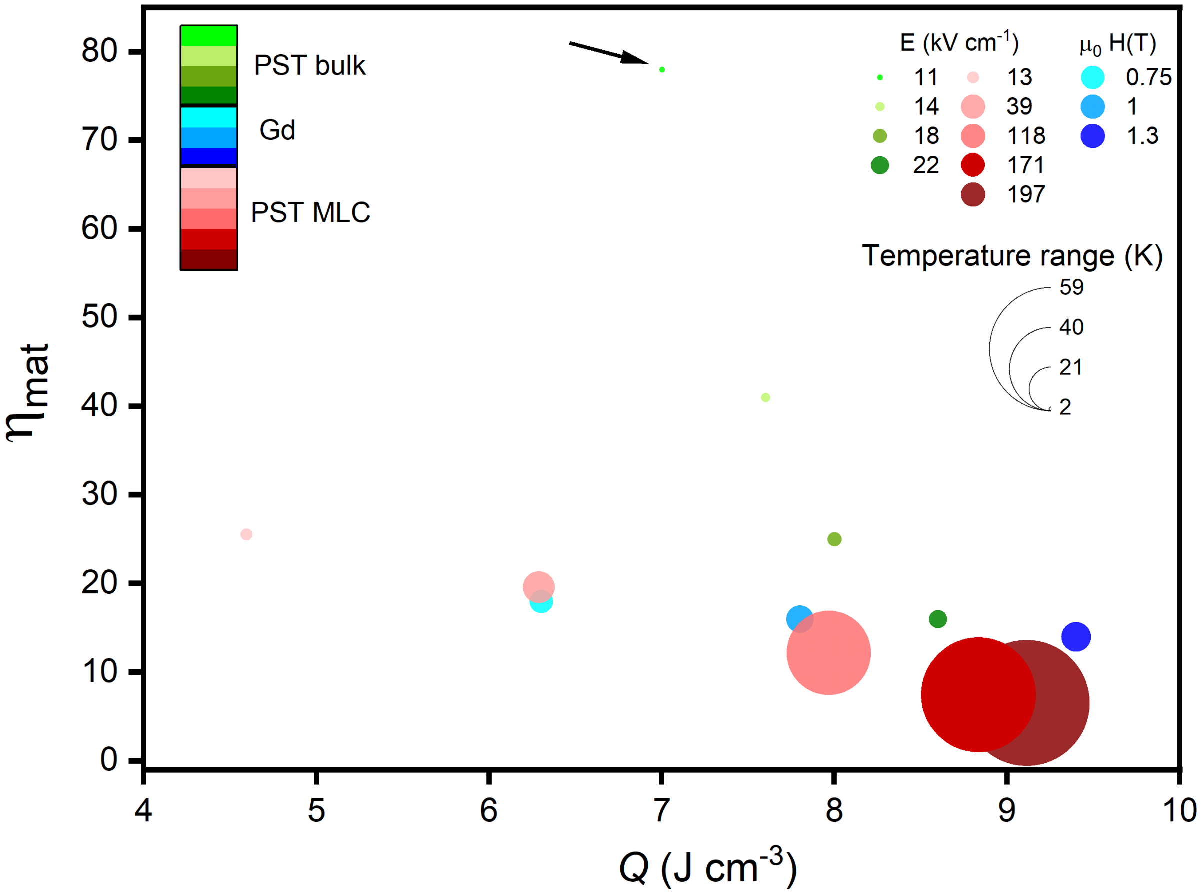

Figure 5.13: **Scale law on material efficiency** The bubble chart compares the materials efficiency of PST MLC, PST bulk and Gd for the same EC heat exchanged by volume Q. The data of η_{mat} of PST MLC (five red bubbles) was included into Figure 4.17 which shows η_{mat} of PST bulk ceramic (green bubbles, the smallest one indicated with an arrow) and Gd (three blue bubbles). The bubble area describes the temperature range defined as the full width at 80% of the maximum ΔT_{adiab}. Each colour represents the field applied (electric field E in PST and magnetic field $\mu_0 H$ in Gd)

From Figure 5.13, we see that the application of high electric fields in PST MLCs permits reaching Q values of 9.1 J cm^{-3} on a temperature range of 60 K however, with an efficiency η_{mat} = 7. Moreover, we observe a linear decrease of η_{mat} with Q. The materials efficiency of PST MLC decreases from 25 (Q = 4.6 J cm^{-3} at 13 kV cm^{-1}) to 7 (Q = 9.1 J cm^{-3} at 194 kV cm^{-1}). A similar linear decrease of η_{mat} is observable for the three materials with the increasing Q, though with different slopes.

η_{mat} of PST bulk is describes in Figure 5.13 by four green bubbles. Its strong first-order transition induces large values of η_{mat} (smaller than 80) which decreases sharply on a narrow temperature range (smaller than 10 K). Contrarily, Gd due to its second-order transition shows a much smaller decrease in η_{mat} (smaller than 20) with Q on a larger temperature range (smaller than 15 K). Finally, the materials efficiency of PST MLC has a slightly steeper slope than Gd with a temperature range considerably larger (smaller than 60 K).

At the same heat exchanged Q = 8.6 J cm^{-3}, PST bulk is as efficient (16) as Gd (14) and slightly more efficient than PST MLC (11). This value of Q corresponds to the highest heat exchanged by PST bulk at 22 kV cm^{-1}. At the lowest Q = 7.1 J cm^{-3} exchanged by PST bulk, it is four times more efficient (78) than both PST MLC (20) and Gd (19). Although PST MLC and PST bulk both present a first-order transition, this transition is rather broad and close to a second-order phase transition in PST MLC. The second-order-like behaviour observe in PST MLC is due to the strong electric fields applied which infers a supercritical regime. This explains the smooth decrease in materials efficiency of PST MLC similar to Gd. Therefore, EC cooling devices should also rely on extrinsic means to enhance further their efficiency compare to magnetocaloric devices [24, 73].

5.5 Conclusion

Following the previous chapter (chapter 4), we studied the materials efficiency of PST in the shape of MultiLayer Capacitor (MLC). We demonstrate that contrarily to bulk, the MLC structure enables reaching large temperature change under large electric fields, and on very large temperature range (higher than 60 K) advantageous for cooling devices. However, the materials efficiency of PST MLC is limited to 25. This is smaller than the values obtained in PST bulk (80). For the same EC heat exchanged, we showed that PST bulk is four times more efficient than PST MLC but on a narrow temperature range (2.5 K in bulk versus 60 K in MLC). This discrepancy in the materials efficiency is due to the steeper and stronger first order transition phase observed in bulk, whereas the supercritical regime used in MLC at very large fields induces a second-order like transition as in Gd. This study shows how the shape of the material influences the materials efficiency of PST. Our work highlights the need of relying on extrinsic energy recovery to improve the efficiency of EC coolers.

Chapter 6

Quantifying the electrocaloric effect in multilayer capacitors using Clausius-Clapeyron equation

6.1 Motivation

Since its first discovery in 1930, different techniques or methods have been utilized to measure the electrocaloric effect (ECE) of electrocaloric (EC) materials in different shapes (bulk, multilayer capacitor (MLC), or thin film). These methods are explained in detail in Chapter 3 of this dissertation. They are divided into four categories: direct, indirect, quasi-direct, and quasi-indirect methods [17, 25]. The main three parameters measured are the adiabatic temperature change ΔT_{adiab}, the isothermal entropy change ΔS or the EC heat exchanged Q. The characterization of EC materials in the form of MLC is usually done:

- **directly** through direct measurements of ΔT_{adiab} using an IR camera [29], a thermometer[100] or a scanning thermal microscope [101].
- **indirectly** by calculating ΔS using Maxwell relations which are based on thermodynamic analysis of ferroelectric PE loops collected isothermally at different temperatures

[29]. ΔT_{adiab} and Q are deduced from each other using the interconversion relation (5.1) $T\Delta S = mC_p\Delta T_{adiab}$.

Calorimeters are the most obvious instrument one could use to measure directly Q in EC materials. However, calorimetric measurements under electric field are challenging and rarely done in the literature [131]. The challenges faced are the application of an electric field in a calorimeter which is not straightforward, the calibration of the sensor, the thermal contact between the sensor and the sample, and Joule heating. Moreover, one of the most important requirements to obtain accurate Differential Scanning Calorimetry (DSC) signal values is to work with samples of small masses i.e approximately smaller than 30 mg. In fact, EC heat Q was measured in 25 mg of PST bulk ceramic using a customized DSC [30]. The results of this study are presented in Chapter 3. This type of measurement is more challenging for a PST MLC as its mass is usually higher than 200 mg, too big to obtain accurate quantitative values of DSC signal.

In this chapter, we suggest an approach to estimate the ECE in $PbSc_{0.5}Ta_{0.5}O_3$ (PST) MLC [81] using a DSC and without worrying about its mass. From infrequent isofield measurements on PST MLC using DSC and isothermal polarisation versus electric field loops at different temperatures, we use the Clausius-Clapeyron method to determine the transition entropy change from fully driving the transition. We obtain using our approach a transition entropy change of 3 J kg^{-1} K^{-1} close to the entropy change of 2.40 J kg^{-1} K^{-1} from driving the transition with temperature. This work was done in collaboration with the industrial company Murata Manufacturing who provided us with the sample investigated here.

The Clausius-Clapeyron method described in details in Chapter 2, is an indirect method that uses the Clausius-Clapeyron equation to determine ΔS_t, the isothermal entropy for fully driving the transition alone [17] [171]. ΔS_t is the change of entropy at the vicinity of the transition from zero to a certain value of electric field E.

$$\Delta S_t = \Delta S\,(0 \rightarrow E)$$

This method fails to work for second-order materials and is only correct for first-order phase transition materials that present a discontinuity in polarization at their transition temperature T_0. The Clausius-Clapeyron method enables obtaining the contribution of the EC effect that stems from the latent heat of the first-order phase transition[172]. This method is nominally equivalent to the Maxwell relations. From the measurements of the jump in polarization ΔP_0 across the transition and inverse of the field dependence of the transition temperature $\frac{dE}{dT_0}$, one can determine ΔS_t using the Clausius-Clapeyron equation below:

$$\Delta S_t = \Delta S\,(0 \rightarrow E) = -\,\Delta P_0\,\frac{dE}{dT_0}\,\frac{1}{\rho} \tag{6.1}$$

with ρ the material's density. The minus sign indicates the diminution of the entropy under the application of an electric field.

In our approach we will measure $\frac{dE}{dT_0}$ from isofield measurements i.e heat flow measurements at a constant electric field while sweeping in temperature. To be able to apply an electric field, these measurements will be done on an entire MLC of approximately 300 mg. The resulting DSC signal is quantitatively incorrect due to the weight of the MLC being too big to measure a good difference in heat flow. However, the position of the transition temperature T_0 is correct as we go slowly enough (5 K min^{-1}) to measure the exact value T_0 of the material.

The change of polarization at the transition $\Delta P_0 = \Delta P_r$ is obtained from $P(E)$ loops of the EC material collected at different temperatures. For a better extraction of ΔP_0, the $P(T)$ curve will be fitted using the Landau theory of phase transitions already utilized by

Nair et *al.* on different PST MLCs [29, 66]. The main idea of this phenomenological theory is to construct the Landau free energy F which, describes the energies of the system in the vicinity of the phase transition [173]. F is expanded as a Taylor expansion of the order parameter (polarization P in the case of ferroelectrics). In the case of first-order transitions, there is a discontinuity at the transition, and the free energy is expanded to the sixth order of the polarization. F is written as follows:

$$F(T,P) = F_0(T) + \alpha_0(T - T_c)P^2 - \frac{\beta}{2}P^4 + \frac{\gamma}{3}P^6 \tag{6.2}$$

with α_0, β, $\gamma \in \mathbb{R}^+$, T the temperature and P the polarization.

At equilibrium:

$$\frac{dF(T,P)}{dP} = 0$$

By derivation of equation (6.2) with respect to P one obtains the equation below:

$$P\left\{\alpha_0(T - T_c) - \beta P^2 + \gamma P^4\right\} = 0 \tag{6.3}$$

Equation (6.3) above has five solutions:

$$P = 0$$

or

$$\alpha_0(T - T_c) - \beta P^2 + \gamma P^4 = 0 \tag{6.4}$$

In equation (6.4), by setting $X = P^2$, we obtain:

$$P^2 = 0\,; \qquad P^2 = \frac{\beta \pm \sqrt{\beta^2 - 4\alpha_0(T - T_c)\gamma}}{2\gamma}$$

The real and stable solutions are:

$$P_{\pm} = \begin{cases} \pm\sqrt{\dfrac{\beta+\sqrt{\beta^2-4\alpha_0(T-T_c)\gamma}}{2\gamma}} & \text{for } T < T_c \\[2em] 0 \quad and \quad \pm\sqrt{\dfrac{\beta+\sqrt{4\alpha_0(T_0-T)\gamma}}{2\gamma}} & \text{for } T_c < T < T_0 \\[2em] 0 & \text{for } T > T_0 \end{cases}$$

As shown in Figure 6.1, T_0 is the transition temperature where the two non zero solutions are unstable (discontinuity in P) and it is expressed as:

$$T_0 = \frac{\beta^2}{4\alpha_0\gamma} + T_c$$

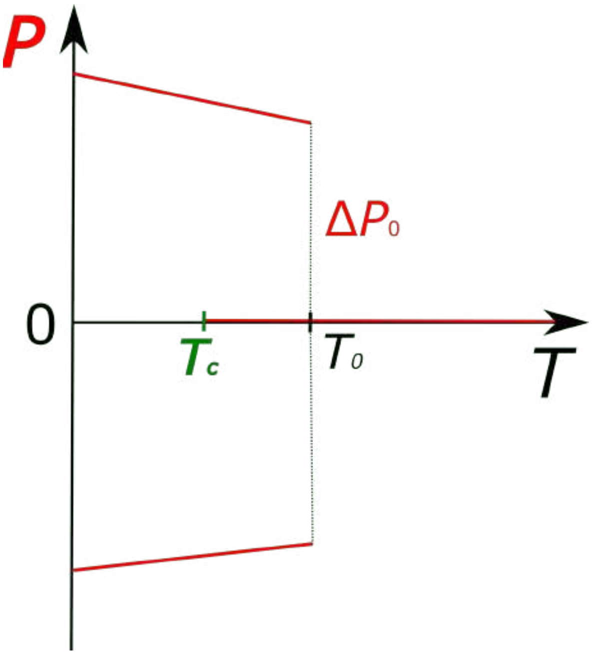

Figure 6.1: **Polarization P versus temperature T of first-order transition material.**

At the transition temperature T_0, the jump in polarization is:

$$\Delta P_0 = \sqrt{\frac{\beta}{2\gamma}} \tag{6.5}$$

The parameters β and γ will be obtained from the fit of the experimental $P(T)$ curve using the function below:

$$P(T) = \sqrt{\frac{\beta + \sqrt{4\alpha_0(T_0 - T)\gamma}}{2\gamma}} \tag{6.6}$$

This equation describes the behaviour of the polarization against temperature before T_0.

6.2 Results

Using the approach described in the section above, we calculated the transition entropy change of the of the first-order transition material, PbSc$_{0.5}$T$_{0.5}$O$_3$ in the shape of a MLC.

6.2.1 Experimental details

PST MLC - sample preparation

The fabrication of the PST MLC sample utilized was fabricated by T. Usui and S. Hirose from Murata Manufacturing in Japan. The details on the fabrication of a PST MLC are presented in Chapter 5 of this dissertation. A density of ρ =8750 kg cm^{-3} was obtained from the PST MLC [29].

Zero-field calorimetric measurements

Heat flux $\frac{dQ}{dT}$ was carried out on 18 mg of a PST MLC (cut at its centre) at a heating rate of 5 K min^{-1}. These measurements were done with a commercial Differential Scanning Calorimeter (DSC3 Mettler Toledo) described in Chapter 3.

DSC measurements under an electric field

Isofield measurements (heat flux measurements at constant electric field) were done on heating and cooling at the heating rate of 5 K min^{-1} using the customized DSC described in Chapter 3 of this dissertation. To be able to apply an electric field, the isofield measurements were carried out on the entire PST MLC of 300 mg. Heat flux $\frac{dQ}{dT}$ were collected versus temperature T.

Polarization - electric field (PE) loops

PE loops were collected using aixACCT TF Analyzer 2000 at the frequency of 10 Hz. The maximum field of 39 kV cm^{-1} was applied at temperatures from 268 K to 323 K.

6.2.2 Case study: PST MLC

PST in the form of MLC presents a first-order phase transition around 292-293 K from a FE phase at low temperature to a PE phase at high temperature. The fabrication, structural and electrical properties, and ECE of this material are presented in Chapter 4 of this dissertation.

Field dependence of the transition temperature in PST MLC

Figure 6.2 shows the heat flow at constant electric fields on an entire PST MLC (mass $\approx$ 300 mg) using a customized DSC (described in Chapter 3). The y-axis, which corresponds to the values of heat flow are not mentioned on the graph as they are quantitatively incorrect due to the weight of the PST sample too big to obtain accurate data of DSC signal. However, the position of the peak (temperature T on x-axis) is correct.

At 0 kV cm^{-1}, we observe a single peak at 292.5 K on heating, which corresponds to the transition from FE to PE. Conversely on cooling, the transition from PE to FE is described by a single peak at 285.5 K. It is worth mentioning that the position of the peaks at 0 kV cm^{-1} on 300 mg PST MLC (Figure 6.2) is similar to those on 18 mg of PST MLC cut at its centre (chapter 4 - Figure 5.6b). Therefore, the heating rate of 5 K min^{-1} is good enough to obtain the right transition temperature in 300 mg - PST MLC.

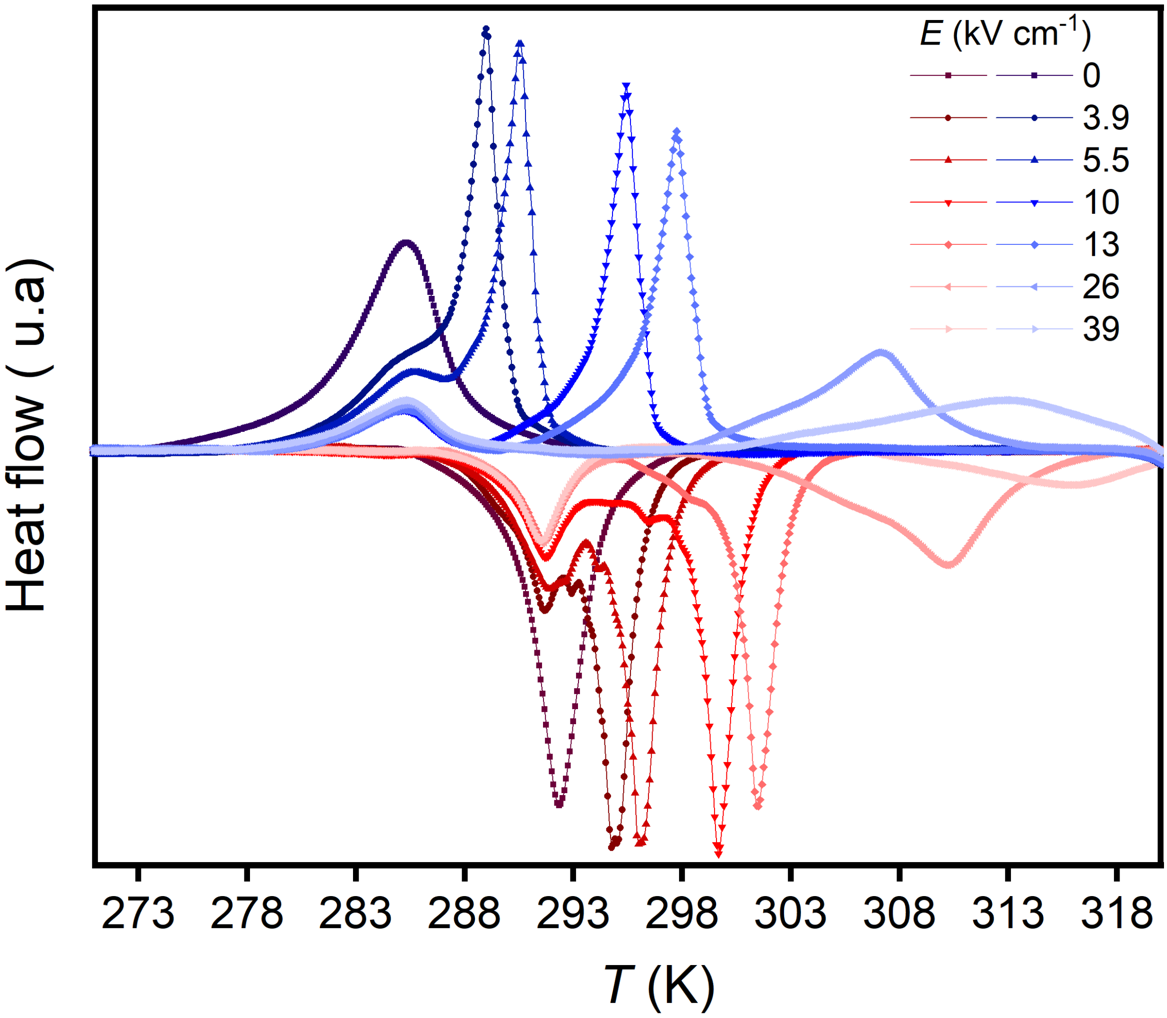

Figure 6.2: **Isofield measurements on PST MLC.** Heat flow measurements at different constant electric fields (0, 3.9, 5.5, 10, 13, 26, 39 kV cm^{-1}) against temperature T. The red and blue data were respectively collected on heating and cooling at 5 K min^{-1}. In order to apply an electric field, these measurements were carried out on an entire PST MLC of $\approx$ 300 mg. The y-axis values are not displayed as they are quantitatively incorrect due to the weight of PST MLC too big for DSC measurements. The position of the peaks in temperature are nonetheless correct.

Under the application of an electric field, it is clear from Figure 6.2 that the single peak observed at 0 kV cm^{-1} splits into two peaks. As shown in Figure 6.3, one of the two peaks remains almost at the same position as the peak at 0 kV cm^{-1} i.e that a part of the MLC

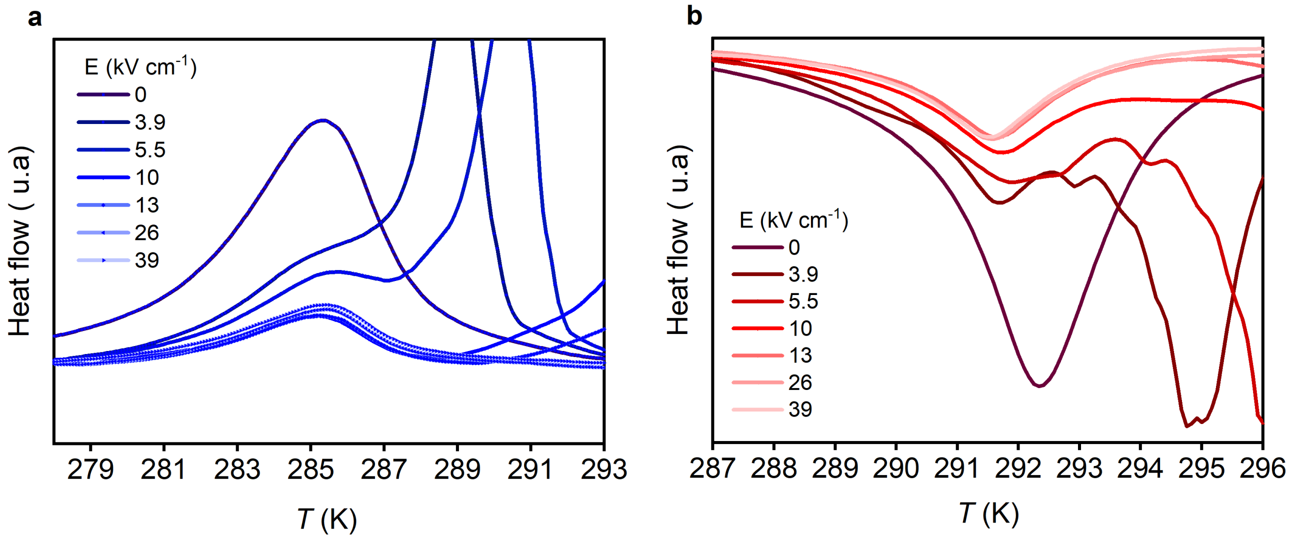

Figure 6.3: **Inactive peak of PST MLC under electric field.** Zoom in of the inactive peak of PST MLC under different electric fields on cooling (**a**) and on heating (**b**).

is insensitive to the electric field. This corresponds to the inactive part of the material (see Figure 5.2). The second peak (active) shifts towards higher temperatures. The shift is a response to the application of an electric field in the active area (where the electrodes overlap) of the MLC (Figure 5.2).Therefore, the electric field stabilizes the low temperature (ferroelectric) phase as also observed in PST bulk ceramic [30]. At values of field greater than 13 kV cm^{-1}, the peak is broader, exhibiting a second-order like behaviour due to the large electric fields applied in PST MLC. The transition peak (active) is completely lost at fields greater than 39 kV cm^{-1}. From Figure 6.4, we obtain an almost linear shift of the transition temperature T_0 with the increasing field. We measure on heating:

$$\frac{dE}{dT_0} = 1.34\, kV\, cm^{-1}\, K^{-1}$$

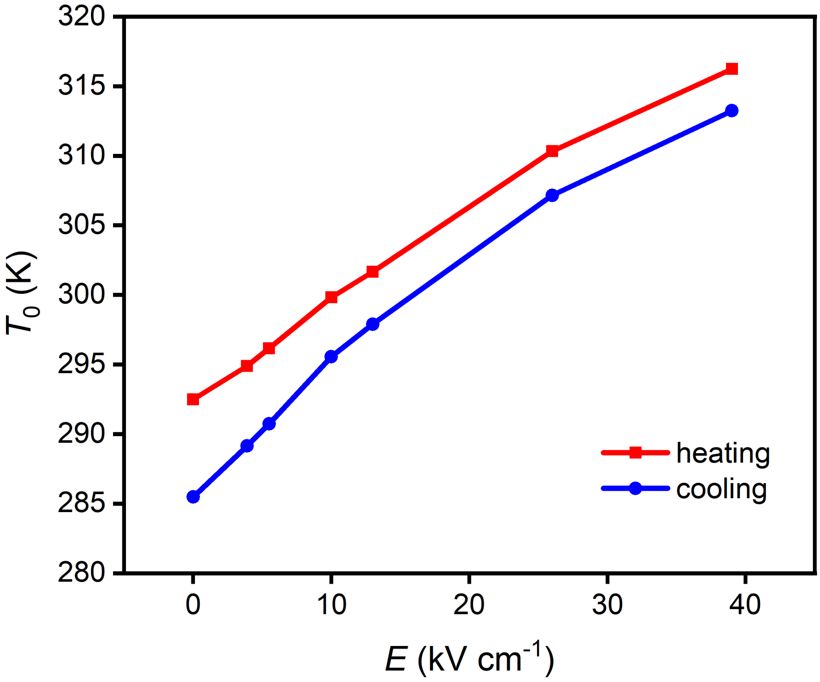

Figure 6.4: **T=f(E) diagram of PST MLC** Temperature versus electric field of PST MLC collected from isofield measurements in Figure 6.2.

Isothermal polarization versus electric field in PST MLC

Figure 6.5b describes the change of polarization versus temperature, collected from P(E) (polarization-electric field) loops at different temperatures (Figure 6.5a). As we can see from Figure 6.5b we observe a jump in polarization at the transition temperature due to the first order transition of PST. This transition is smoother with the increasing electric field and the jump becomes barely visible. The P(T) curve at 0 kV cm^{-1} will be fitted following equation (6.6). From the fitted parameters we deduce the jump in polarization using equation (6.5).

$$\Delta P_0 = 17\,\mu\,cm^{-2}$$

We therefore deduce the entropy change ΔS_t from fully driving the transition:

$$|\Delta S_t| = |-\ \Delta P_0\,\frac{dE}{dT_0}\,\frac{1}{\rho}| = 2.60\,J\,kg^{-1}\,K^{-1}$$

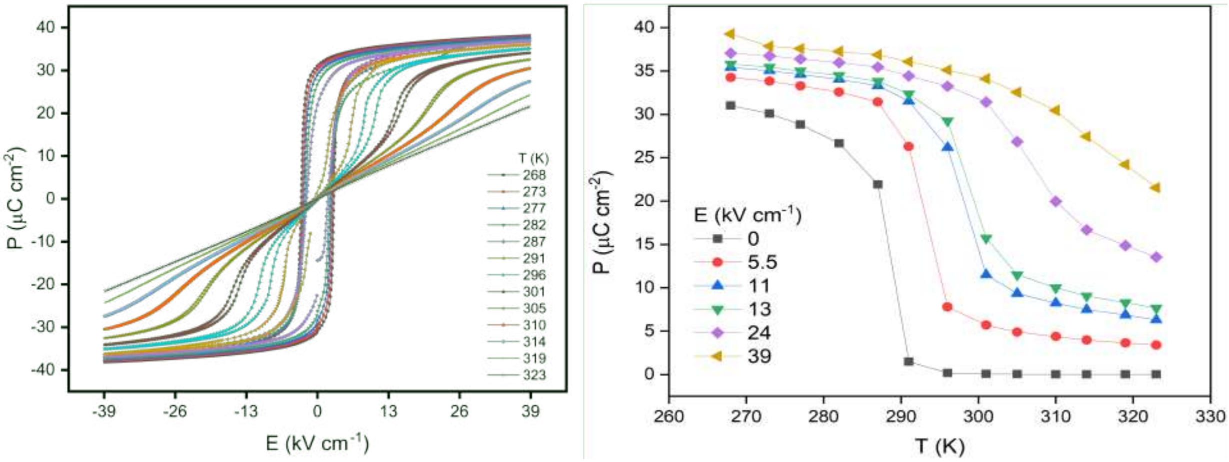

Figure 6.5: **PE loops of PST MLC at different temperatures a** PE loops of PST MLC collected at different temperatures from 266 K to 323 K at the maximum electric field applied of 39 kV cm^{-1}. **b** Remanent polarization as a function of temperature

This value is comparable to the entropy change ΔS_0 obtained by driving the transition with temperature. ΔS_0 is obtained from zero-field calorimetric measurements of 18 mg of PST MLC (cut at its center). In the range of 270 K and 320 K, we measured a latent heat of $Q_{0,h}$ = 698 J kg^{-1} on heating (red peak in Figure 6.6). Hence, the entropy change ΔS_0 due to changes in temperature.

$$\Delta S_0 = \int \frac{dQ}{TdT} dT = 2.40\, J\, kg^{-1}\, K^{-1}$$

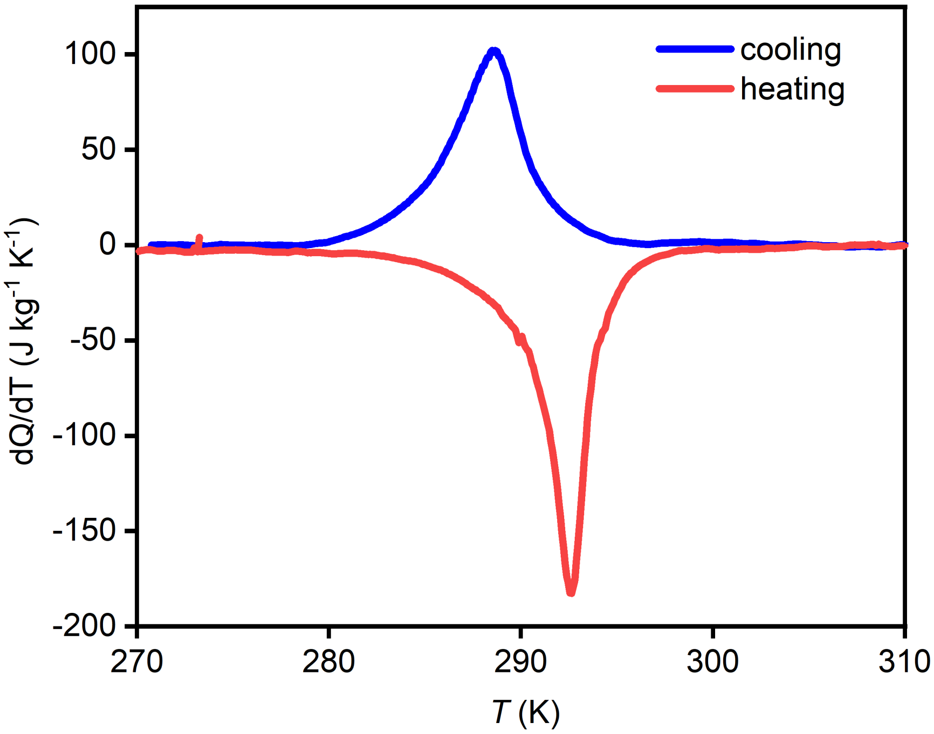

Figure 6.6: **Zero-field calorimetric measurement in PST MLC.** Heat flow measurements on 18 mg of PST MLC cut at its centre. The red and blue curves denotes respectively the heating and cooling.

6.3 Discussion

By using the Clausius-Clapeyron equation we were able to reach similar transition entropy in PST MLC when driven electrically and thermally without electric field. From the change of polarization and the field dependence of the transition temperature in PST MLC we obtained the entropy change by driving completely the transition (latent heat).

Despite the mass (300 mg) of the PST MLC bigger than the mass limit to obtain accurate values of DSC signals, we were able to determine the field dependence of the transition temperature T_0 from isofield measurements carried out with our customized DSC under electric field. This was possible by choosing the right heating rate in order to measure the precise position of the transition peak. At 5 K min^{-1}, heat flow measurements on 18 mg of PST MLC broken at its centre, shows similar peak transition as in 300 mg of entire PST MLC. Therefore, the isofield measurements only possible on the entire PST MLC in which one can apply an electric field, were carried out at 5 K min^{-1}. The application of an electric field in the 18 mg broken PST MLC is impossible as after breaking broken, the electrodes are in contact with each other therefore, creating a short circuit. At large electric fields, the transition peak is lost as the material behaves more like a second-order material. This is also observed in the polarization versus temperature curves where the jump in polarization is barely visible with the increasing field.

Our approach works well to estimate the entropy change at the transition (latent heat) for PST MLC using isofield measurements in a DSC. The difference of 0.2 J kg^{-1} K^{-1} in entropy change could be attributed to errors in fitting.

6.4 Conclusion

As a conclusion, we suggested in this study an approach to determine the ECE in a MLC using the Clausius-Clapeyron equation. From isofield measurements on PST MLC using DSC and polarization versus electric fields loops we show that the entropy change from driving completely the transition (latent heat) is almost similar to the entropy change at the transition driven with temperature. Therefore, our approach could be considered as an alternative to measure the transition entropy in MLC.

Chapter 7

Explaining the negative electrocaloric effect in the antiferroelectric lead zirconate

7.1 Motivation

Alike ferroelectrics (FEs), antiferroelectrics (AFEs) are part of the family of dielectric materials. Firstly defined in 1951 by Kittel [174], AFEs have been less studied than their counterpart FEs discovered for the first time in 1665 in Rochelle salt (sodium potassium tartrate tetrahydrate). AFEs have been mainly attractive due to their high energy storage density [127, 175–178]. They also find applications in pyroelectricity sensors and solid-state cooling devices [179]. Recent studies [62, 180–182] have shown that AFEs could display a negative electrocaloric (NECE). In contrast to the conventional ECE, the NECE or also called *inverse ECE* is described by the decrease of the material's temperature under the application of an electric field and an increase of its temperature after the removal of the field. The combination of the conventional ECE with the NECE could enable working on large temperature ranges and help improve the efficiency of solid-state cooling devices. However, the origin of this NECE in AFEs remains controversial in the literature.

In this chapter, we will study the archetypical AFE Lead Zirconate – short form - $PbZrO_3$. Using calorimetric measurements under electric field carried out by myself at LIST, we will explain the origin of the NECE in bulk ceramic $PbZrO_3$. This work was done in collaboration with the Catalan Institute of Nanoscience and Nanotechnology (ICN2) in Barcelona, which suggested the study and provided the samples for characterization. This work has led to the publication of one of my co-author papers "Pablo Vales-Castro, Romain Faye, Miquel Vellvehi, Youri Nouchokgwe et al., *Origin of negative electrocaloric effect in antiferroelectric* $PbZrO_3$, *Physical Review B*, 103, 054112(2021), https://doi.org/10.1103/PhysRevB.103.054112.

We will first present a background on AFEs and more precisely the material used here $PbZrO_3$. Secondly, we will explain the controversy around the NECE by describing the different origins of this abnormal effect which still remains unclear. Subsequently, we will show our results on the calorimetric measurements under different electric fields in $PbZrO_3$. Finally, based on the later measurements and EC measurements carried out by P. Vales-Castro we will give our explanation of the NECE observed in bulk ceramic $PbZrO_3$.

7.2 Antiferroelectrics

7.2.1 Background

The family of dielectric materials includes FEs, AFEs, relaxor ferroelectrics (RFs), and linear dielectrics (LDs). FEs remain one of the most studied dielectric materials. To better understand AFEs, we will first define FEs. FEs are characterized by: a spontaneous electric polarization i.e a non-zero polarization when the electric field is zero and the reversibility or switching of the spontaneous polarization by applying an external electric field in the opposite direction. Hence, the hysteresis loop observed in FE materials as shown in Figure 7.1a. In these materials, the adjacent dipoles are parallel, and their orientation can be aligned by an external electric field as displayed in Figure 7.1b.

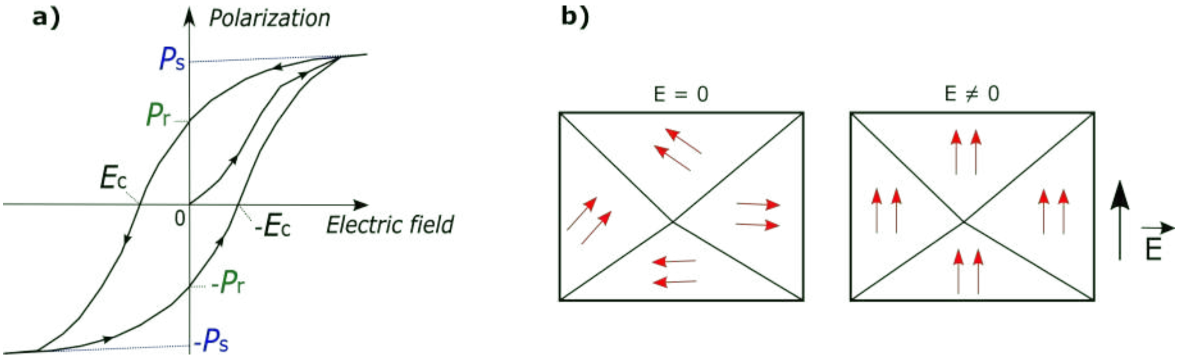

Figure 7.1: **Ferroelectrics.** **a** Hysteresis loop of a FE material. P_s is the saturation polarization, E_c the coercive field (value of the electric field at zero polarization), and P_r the remanent (spontaneous) polarization. **b** FE dipoles in domains in the absence ($E = 0$) and presence ($E \neq 0$) of an electric field.

In contrast, as demonstrated in Figure 7.2b, AFEs possess antiparallel adjacent dipoles (antipolar state) which can be aligned by applying a sufficient electric field (E_{AFE-FE}) leading to a polar state. The electric field induces a phase switching from an AFE phase to a FE phase. The stability of this polar phase until E_{FE-AFE} leads to a hysteresis loop thereby, a double hysteresis when applying the field in the opposite direction (Figure 7.2a). This double hysteresis loop is the feature commonly used to define an AFE material, though it is not sufficient to conclude on antiferroelectricity. The last characteristic to confirm the antiferroelectricity of a material in addition to its antiparallel dipoles and double hysteresis loop is its anomaly in the dielectric permittivity at the AFE to paraelectric (PE) transition temperature [183, 184]. These three features altogether define the antiferroelectricity of a material.

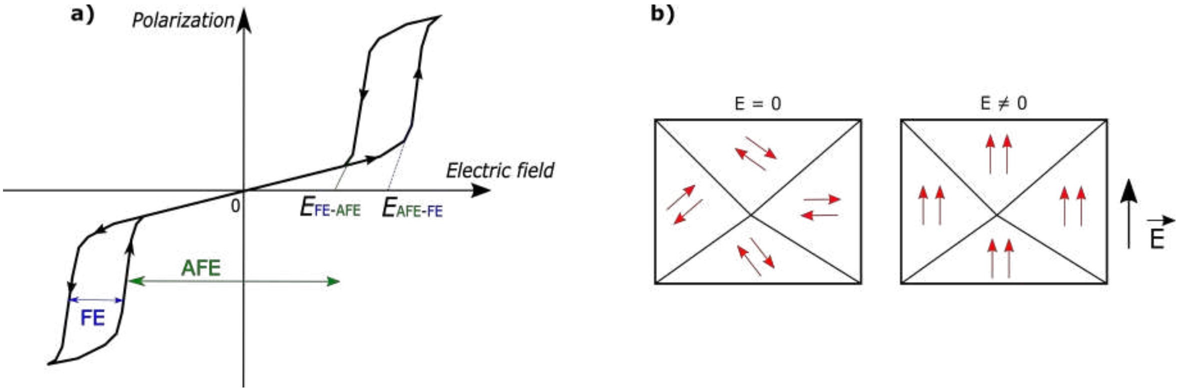

Figure 7.2: **Antiferroelectrics.** **a** Double hysteresis loop of an AFE material **b** AFE dipoles in domains in abscence (E = 0) and presence of an electric field (E $\neq$ 0)

Lead Zirconate - PbZrO$_3$ - short form PZO, is an archetypical and first studied [185] AFE material. It has a perovskite structure (ABO$_3$) and an antiparallel atomic arrangement as shown in Figure 7.3a. PbZrO$_3$ has a transition temperature T_c around 505 K. It transitions from an orthorhombic AFE phase at low temperature to a cubic paraelectric phase at high-temperature [186]. In addition, as shown by Shirane et al. [185] in 1951, PbZrO$_3$ shows a dielectric anomaly at T_c with a double hysteresis loop at the applied field of 20 kV cm^{-1} (Figure 7.3c). This anomaly is described in Figure 7.3b by a jump in the dielectric permittivity around $T_c = 506$ K.

AFEs are good candidates for high-energy storage applications and electrocaloric cooling devices.

Due to their low remanent polarization and high critical field, AFEs display high-energy storage density compared to the other dielectric materials (FEs, relaxor ferroelectric, and

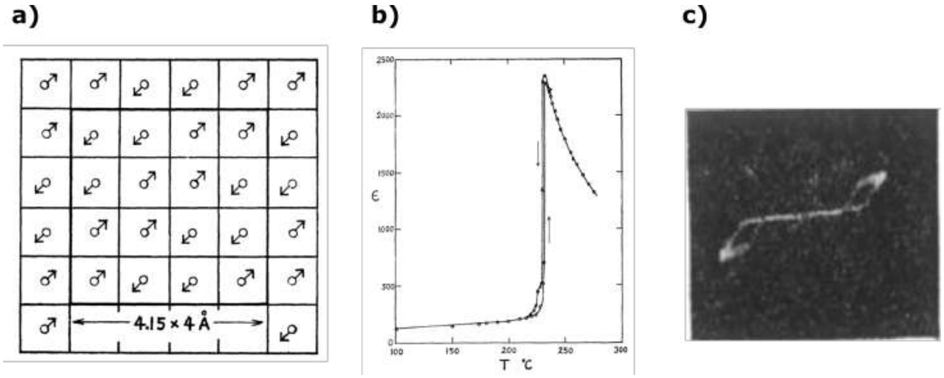

Figure 7.3: **Lead Zirconate - $\mathbf{PbZrO_3}$.** These images were adapted from [185]. **a** Atomic arrangement showing antiparallel dipoles of $PbZrO_3$ in the AFE phase. The arrows show the shift of the lead (Pb) ions. **b** Dielectric constant versus temperature of $PbZrO_3$ and its anomaly at the AFE-PE transition. **c** Double hysteresis loop of $PbZrO_3$ at 501 K under applied field of 20 kV cm^{-1}.

linear) [187]. One can store energy in a dielectric material as the energy used to charge the dielectric can be recovered by discharging the material [184]. The energy stored per unit volume $W_{stored\ energy}$ is defined as the sum of the recoverable energy (shaded in orange in Figure 7.4) and the energy loss [188]. The energy loss corresponds to half of the area in the loop shaded in blue in Figure 7.4. $W_{stored\ energy}$ and $W_{recoverable\ energy}$ are defined as:

$$W_{energy\ stored} = \int_0^{P_{max}} EdP. \tag{7.1}$$

$$W_{energy\ recovered} = -\int_{P_{max}}^{P_r} EdP. \tag{7.2}$$

With E the applied electric field, P the polarization, P_r the remanent polarization and P_{max} the maximum polarization at maximum electric field.

7.2.2 Negative electrocaloric effect in AFEs

As FEs, AFEs also show a high pyroelectric coefficient which is a requisite for large ECE. Contrary to FEs they show a NECE at the AFE to FE transition. As shown in Figure 7.5, NECE means that the AFE material cools down when the electric field is applied and heats

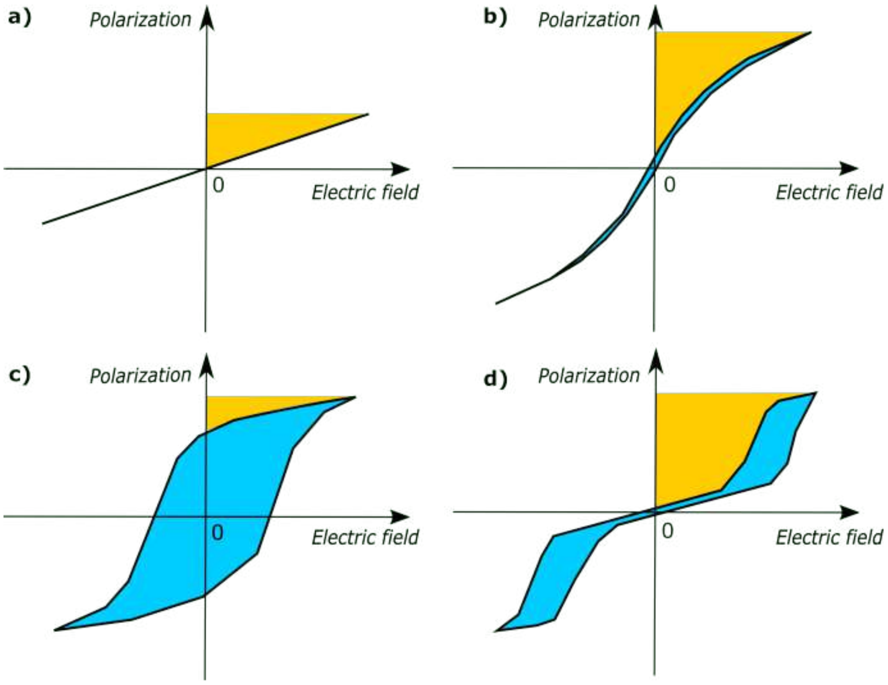

Figure 7.4: **Energy storage in dielectric materials. a** linear dielectric **b** relaxor ferroelectric **c** ferroelectric **d** antiferroelectric. The shaded area in orange represents the energy recovered $W_{energy\ recovered}$ by each dielectric material. $W_{energy\ recovered}$ is larger in AFE compared to its counters dielectrics.The energy loss corresponds to half of the area shaded in blue.

up when the field is withdrawn. This implies a positive slope of $P(T)$ and a positive value of $\frac{\partial P}{\partial T}$. Therefore, a negative ΔT_{adiab} is obtained from the Maxwell relations. It is worth it to mention that NECE could also be observed in FEs that present different FE transitions with different polarization directions [171, 180, 189–192] or in FE materials with polar defects configurations [190, 193]. In this section we are only interested in NECE observed in AFEs and more specifically in bulk ceramic $PbZrO_3$.

Theoretical and experimental measurements done by Pirc et al. [182] have confirmed a maximum NECE of -1.5 K at 80 kV cm^{-1} in the prototypical $PbZrO_3$ ceramics. In 2015, the same group reported on a NECE of nearly -1 K at 40 kV cm^{-1} in Ba-doped $PbZrO_3$ ceramics [194]. Furthermore, in AFE La-doped $PbZrTiO_3$ thin films, Geng et al. [62] have obtained

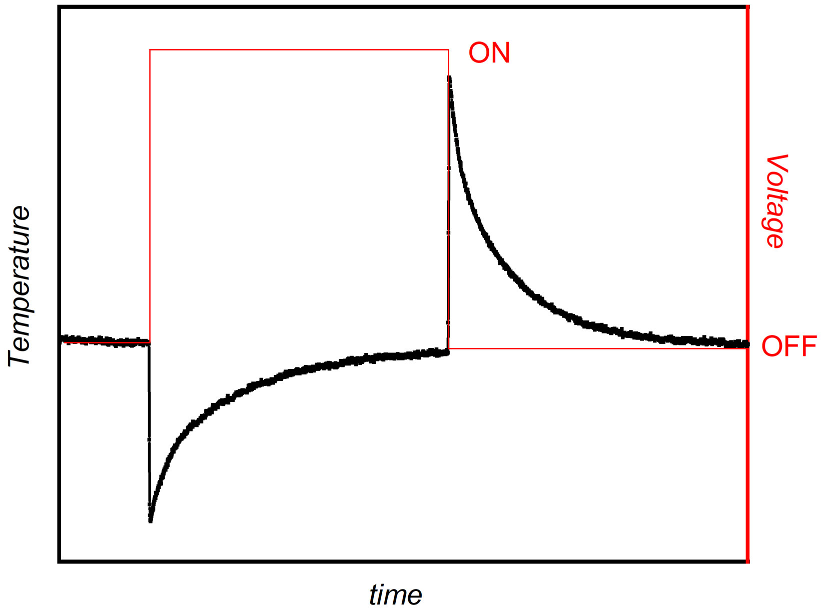

Figure 7.5: **Negative electrocaloric effect** Temperature of a material (y-left axis) as a function of time. The y-right axis in red shows the voltage applied. Here, the material's temperature decreases when the voltage (electric field * thickness) is on and increases when the voltage is off.

a giant NECE of -5 K near room temperature using the indirect method (Maxwell relations). Intriguingly, there is so far in the literature two different explanations for this abnormal effect: the dipole canting model [62, 75] and the latent heat of transformation model [182].

Dipole canting model

In a conventional (positive) ECE, the adiabatic application of an electric field aligns the electrical dipoles of the material, and thus reduces its dipolar entropy $\Delta S_{dipolar}$. This leads to an increase in the phononic contribution $\Delta S_{phononic}$ (vibrational degrees of freedom) thus, the material gets hot. The decrease and increase of respectively $\Delta S_{dipolar}$ and $\Delta S_{phononic}$, satisfy equation (7.3) as the total entropy (ΔS_{tot}) of the system should be zero under adiabatic conditions.

$$\Delta S_{tot} = \Delta S_{phononic} + \Delta S_{dipolar} \tag{7.3}$$

On the contrary, in an inverse ECE, $\Delta S_{dipolar}$ increases as the electric field creates disorder by destabilizing (canting) the dipoles sublattice, antiparallel to the electric field. This will therefore induce a reduction of $\Delta S_{phononic}$ thereby a decrease in the material's temperature. More specifically, at a temperature smaller than T_c, by applying a modest electric field smaller than the AFE-FE transition field (E_{AFE-FE}), the temperature change of the material will decrease as shown in Figure 7.6. At a larger electric field, greater than E_{AFE-FE}, this temperature change will change to a positive effect (green and blue curves in Figure 7.6) as the AFE dipoles are now aligned with the electric field applied.

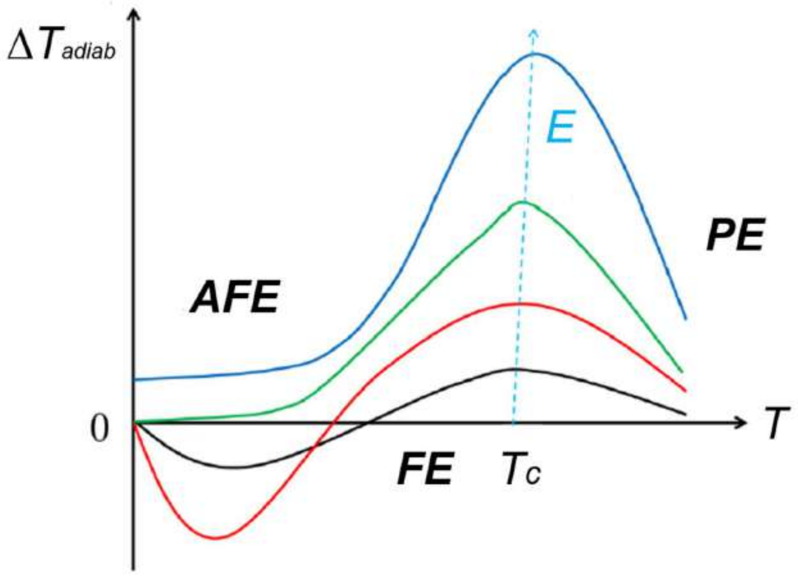

Figure 7.6: **Dipole canting illustration.** This figure was adapted from Liu et al. [75]. It illustrates the NECE of an AFE material based on the dipole canting model. The temperature change ΔT_{adiab} as a function of temperature *T* at increasing electric fields *E*. T_c is the transition temperature.

Latent heat of transformation model

The latent heat of transformation model is based on the fact that the field-induced first-order phase transition (latent heat) between two phases could be responsible for the NECE. The changes in applied voltage (electric field * thickness) induce an intermediate transition described by the appearance of an endothermic peak with a higher entropy than the low-temperature phase. Therefore, ΔS_{tot} in equation (7.3) can be written as:

$$\Delta S_{tot} = \Delta S_{phononic} + \Delta S_{LH} + \Delta S_p = 0 \tag{7.4}$$

with $\Delta S_{dipolar} = \Delta S_{LH} + \Delta S_p$. ΔS_p is the contribution from the smooth variation of polarization with *T* and *E*. ΔS_{LH} is the change of entropy obtained from the first-order transition (latent heat). It stems from the discontinuous jump in polarization.

Contrary to the dipole canting model, in the latent heat of transformation model, the NECE continues to increase above E_{AFE-FE} until the effect saturates.

The main purpose of this work is to determine which of these two reasons is responsible for the NECE measured directly in bulk ceramics $PbZrO_3$.

7.3 Results

7.3.1 Experimental details

Sample preparation

The bulk ceramics of $PbZrO_3$ were fabricated at the Institute of Physics of the University of Silesia in Katowice in Poland. The samples were done following the instructions in [195].

Using 99.95% powdered pure PbO and ZrO from Reachim, ceramics of $PbZrO_3$ were first synthesized at 900 ℃ for 3 h and then pulverized and pressed in discs form of 10 mm diameter. Subsequently, they were annealed for 1 h at 1150 ℃ and pressure of 150 MPa.

The samples obtained, show a low porosity. The discs obtained were polished to a thickness between 100 and 150 μm with a Multi-prep polishing system.

DSC measurements under an electric field

The zero-field measurements and isofield measurements were done using a DSC (as described in Chapter 3) from NETZSCH. The sample used for characterization weighs 6 mg. The measurements were done at the heating rate of 10 K min^{-1} and at different constant electric fields of 0, 2.5, 5, 10 kV cm^{-1}. From the heat flux measurements and after removal of the baseline we obtained $\frac{dQ}{dT}$. The specific heat measurements C_p were done as described in Chapter 3 on the same sample. The silver paste was deposited on both surfaces of the ceramic and connected with copper wires for the application of an electric field using a power source (Keithley 2410). The entropy curves were drawn using the equations described in Chapter 3.

InfraRed (IR) Imaging measurements

The adiabatic temperature change data were collected using the IR cameras FLIR x6580sc and FLIR SC5500. More details on the technique are given in Chapter 3. The starting temperature was controlled with a Linkam cell (described in Chapter 3) and the voltage was applied at the current of 0.1 mA using a power source Keithley 2410. These measurements were carried out by P. Vales-Castro.

7.3.2 Zero-field thermal properties of PbZrO$_3$

The zero-field calorimetric measurements carried out with a DSC in a pure compound PbZrO$_3$ are shown in Figure 7.7. The heat flow and specific heat measurements show the first-order behaviour of ceramic PbZrO$_3$ with sharp peaks on heating and cooling. On heating, we observe one single endothermic peak at the transition temperature of 507 K. This peak (red in Figure 7.7a and 7.7b) corresponds to a transition from the AFE (orthorhombic) phase to a PE (cubic) phase. In contrast to the heating, we note an additional peak on

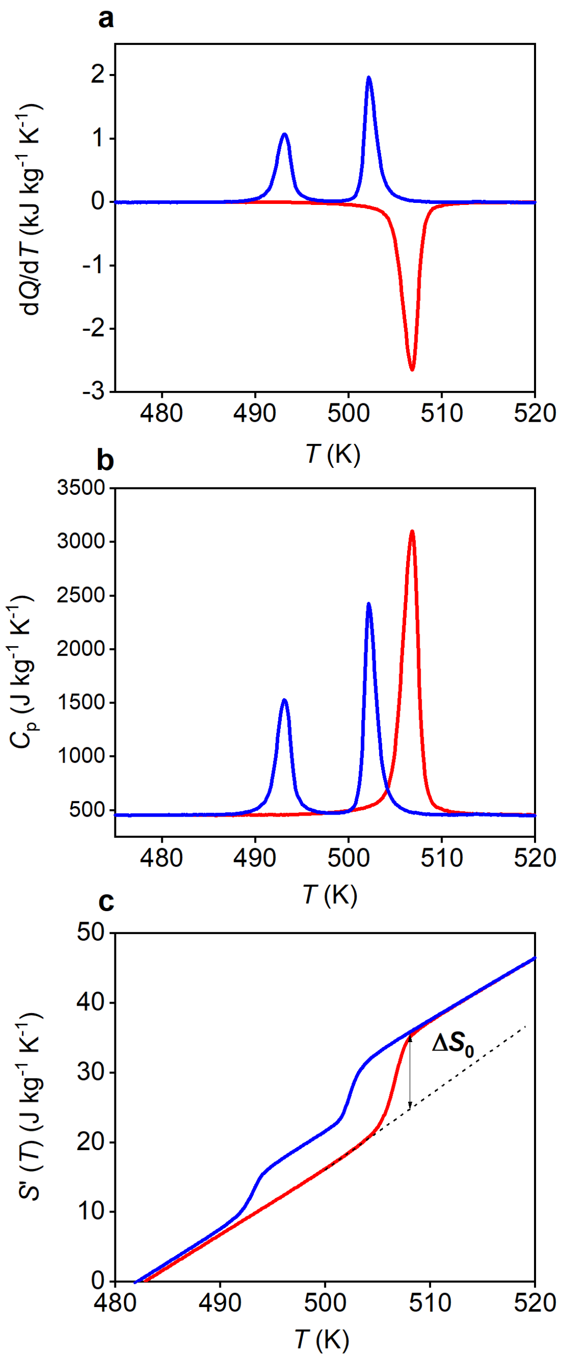

Figure 7.7: **Zero-field measurements in PbZrO$_3$** This figure shows the calorimetric measurements as a function of temperature *T*, done on bulk ceramic PbZrO$_3$ on heating (red curves) and cooling (blue curves) at 0 kV cm^{-1}. **a** Heat flow d*Q*/d*T*. **b** Specific heat C_p. **c** *S*'(*T*) the entropy referenced at 482 K far from the transition. *S*'(*T*) = *S*(*T*) -*S*(482 K) with *S*(482 K) = 0. ΔS_0 is the entropy change at the transition driven thermally.

cooling. This additional peak suggests a stable intermediate phase between the PE and AFE phases. Therefore, the two exothermic peaks (blue in Figure 7.7a and 7.7b) on cooling, describe a transition from PE to FE (rhombohedral) and then to the AFE phase. The PE-FE and FE-AFE respectively peak at 502 K and 493 K. This is consistent with the capacitance measurements carried out by P. Vales-Castro [63] on the same batch of samples. The first-order behaviour of $PbZrO_3$ is accompanied with a thermal hysteresis $\geq$ 5 K. The integration of the red peak in Figure 7.7a yields $Q_{0,h}$ of 6,140 J kg^{-1}. $Q_{0,h}$ is the latent heat, the energy absorbed (endothermic) per unit kilogram of $PbZrO_3$. In the same way, we obtained the energy released per unit kilogram by $PbZrO_3$, by integration of the two peaks on cooling. We access 3,480 J kg^{-1} and 2,330 J kg^{-1} respectively from the PE-FE peak and FE-AFE peak. It is worth it to mention that the sum ($Q_{0,c}$ = 5,810 J kg^{-1}) of the latent heat of both peaks on cooling is almost equal to the latent heat obtained on heating. The C_p measurements in Figure 7.7b shows a constant background value of 457 J kg^{-1} K^{-1}. From the zero-field C_p, we draw in Figure 7.7c, $S'(T)$ the entropy referenced to the entropy at 482 K far from the transition (described in Chapter 3). We achieve a thermally driven entropy change $\Delta S_{0,h}$ = 12.12 J kg^{-1} K^{-1} on heating and $\Delta S_{0,c}$ = 11.65 J kg^{-1} K^{-1} on cooling. The latter corresponds to the sum of entropy change obtained from both peaks on cooling; respectively 6.93 J kg^{-1} K^{-1} (PE-FE) and 4.72 J kg^{-1} K^{-1} (FE-AFE). As shown in Figure 7.7c, the thermally driven entropy change corresponds to the jump in the $S'(T)$ diagram.

7.3.3 Electrocaloric effect in $PbZrO_3$ ceramic

Direct measurements of ECE in bulk ceramic $PbZrO_3$ under application of different electric fields are presented in Figure 7.8. These measurements were carried out by P. Vales-Castro using an IR Camera (see experimental details). In the range of temperatures from 473 K to 493 K i.e in the AFE phase, we observed an increasing NECE with the increasing electric field. At the lowest electric field applied of 10 kV cm^{-1}, we measured a small $\Delta T_{adiab} \leq$ -0.6 K. This value decreases (or increases in absolute value) to -3.6 K at the maximum field applied of 42 kV cm^{-1}. This field is higher than the phase transition field E_{AFE-FE}($\approx$ 35 kV cm^{-1}). In the FE phase between 493 K to 500 K, the NECE changes to zero or weakly

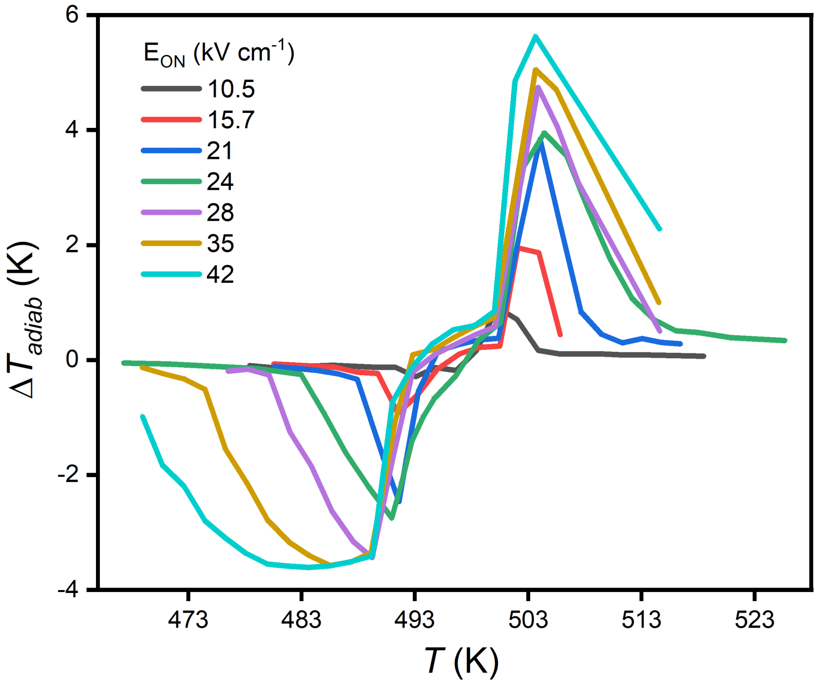

Figure 7.8: **Adiabatic temperature change of PbZrO$_3$.** Direct measurements of ΔT_{adiab} as a function of different starting temperatures T_s under the application of different electric fields E_{ON} (10, 16, 21, 24, 28, 35 and 42 kV cm^{-1}). These measurements were done by P. Vales-Castro.

positive effect. $\Delta T_{adiab} \leq$ 1 K is measured in this temperature range at the maximum field applied. At higher temperatures around T_c, between 500 K to 509 K, we observed a positive ECE which increases with the increasing electric field. The highest value of ΔT_{adiab} = +5.6 K is measured in this temperature range at 42 kV cm^{-1}. Finally, this effect drops to nearly zero or zero above T_c.

7.3.4 Isofield measurements of PbZrO$_3$

Isofield measurements carried out on bulk ceramic PbZrO$_3$ were realized using a customized DSC (see Experimental details). These measurements correspond to the heat flow measured at constant electric fields (0, 2.5, 5, 10 kV cm^{-1}) while sweeping in temperature. The results are presented in Figure 7.9 on heating (Figure 7.9b) and on cooling (Figure 7.9a).

As already observed in Figure 7.7a, our sample shows a single endothermic peak from

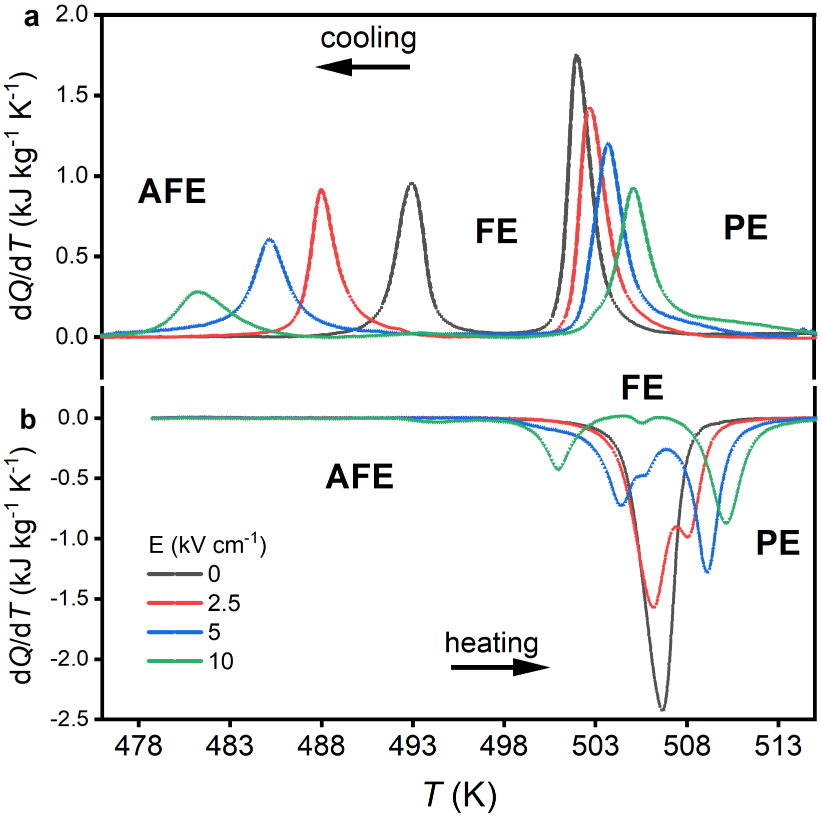

Figure 7.9: **Isofield measurements in $PbZrO_3$ ceramic** Heat flow measurements of bulk ceramic $PbZrO_3$ at different constant electric fields (0, 2.5, 5 and 10 kV cm^{-1}). These measurements were carried out on cooling (**a**) and heating (**b**) using a customized DSC (see experimental details).

AFE-PE on heating with two peaks on cooling. These two peaks describe the presence of an intermediate stable phase (FE) between the PE and the AFE phase. Under the application of the modest electric field of 2.5 kV cm^{-1}, we observe a shoulder on the endothermic peak (red peak in Figure 7.9b). It suggests a splitting of the endothermic peak in two. By increasing the field to the maximum field applied of 10 kV cm^{-1}, it is clear from Figure 7.9b that we separate the single endothermic peak at 0 kV cm^{-1} into two distinct endothermic peaks. Thereby, the field induces an intermediate FE phase between the AFE and PE phases. Moreover, the increase of the electric field shifts the AFE-FE peak to lower temperature and the FE-PE to higher temperature. As a result, the electric field stabilizes the intermediate FE phase (Figure 7.10) which is at higher temperatures than the AFE phase. Similarly, on cooling, the

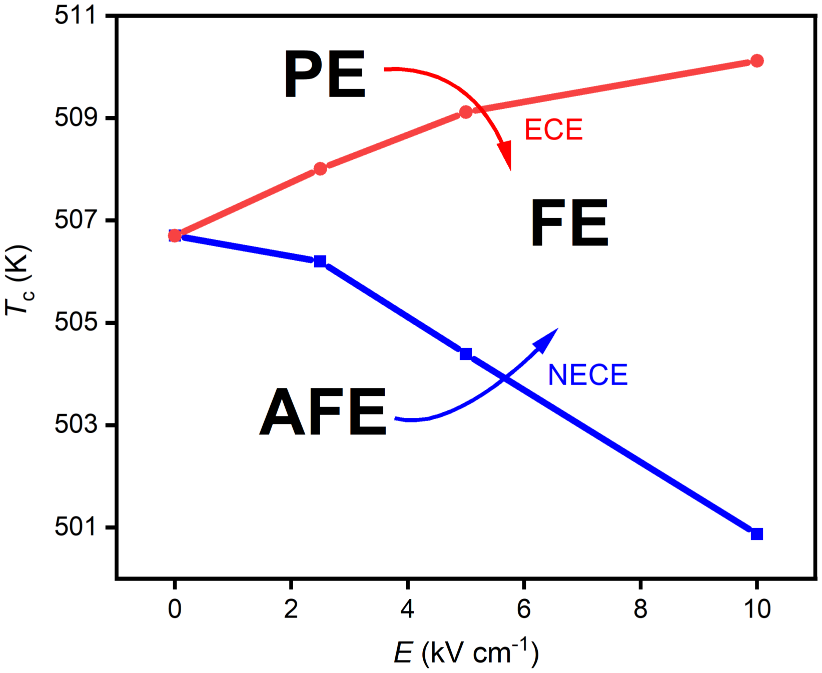

Figure 7.10: **Temperature-Electric field diagram of $PbZrO_3$ ceramic** This *T*-*E* diagram was constructed from DSC measurements on $PbZrO_3$ ceramic. The application of an electric field in the AFE and PE phase, leads respectively to a NECE to the FE phase, and a positive ECE to the FE.

PE-FE and FE-AFE peaks are shifted to respectively higher and lower temperatures with the increasing field. These results are in line with the Dynamic Mechanical Analysis (DMA) measurements carried out by P. Vales-Castro in [63].

7.4 Discussion

From direct adiabatic temperature measurements done with an IR camera, we observed in the AFE phase an increase of the NECE even above the transition electric field of E_{AFE-FE}. Besides, the DSC measurements show that the electric field induces a FE phase between the AFE and the PE phases. These observations, prove that the positive and negative ECE measured in ceramic $PbZrO_3$ are due to the field-induced phase transitions. Furthermore, it is seen from the DSC measurements that the field induces an endothermic AFE-FE peak. In other words, heat is being absorbed by the material leading to cooling under the appli-

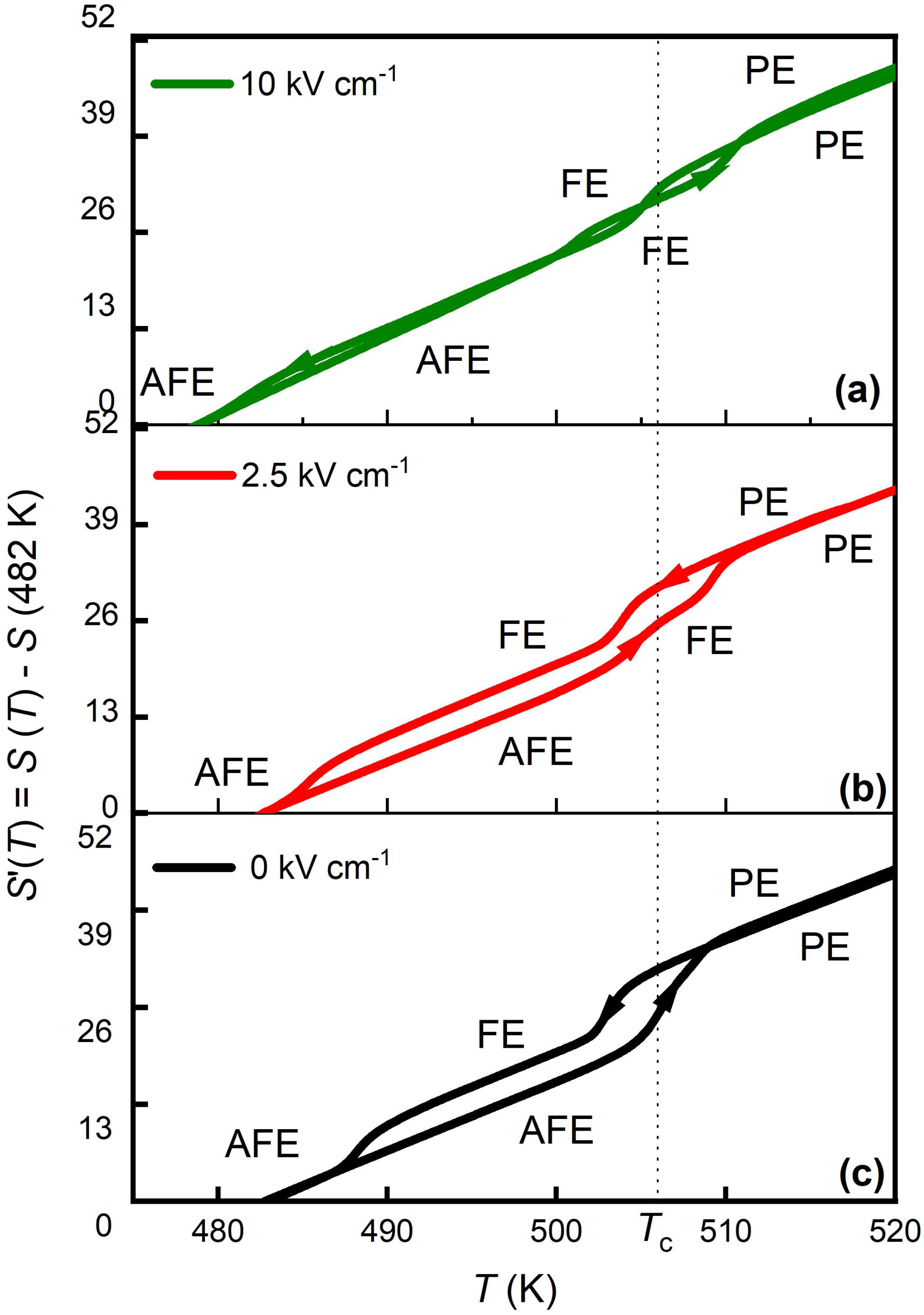

Figure 7.11: **Entropy curves of $PbZrO_3$ ceramic.** $S'(T)$ the entropy referenced at 482 K as a function of temperature T at 0 kV cm^{-1} (**c**), 2. kV cm^{-1} (**b**), 10 kV cm^{-1} (**a**). T_c is the transition temperature which is shifted towards high temperature with increasing electric field

cation of an electric field. Therefore, the AFE-FE peak is then responsible for the NECE of -3.5 K in PbZrO$_3$. These results show that the NECE doesn't arise from the destabilization of the anti-parallel dipoles but rather from the first-order (latent heat) endothermic transition between the AFE (antipolar) and FE (polar) phases induced by changes in the electric field. If the dipole canting, was responsible for the NECE, we would have expected the heat to be released (entropy decreases) or ΔT_{adiab} to turn positive as the anti-parallel dipoles are ordered above the coercive field E_{AFE-FE}. Evidently, this is not the case as shown in our results. The FE phase has a higher entropy (Figure 7.11) than the AFE phase yielding the absorption of heat (endothermic peak from AFE to FE). Contrarily, the positive ECE observed (+5.6 K) at higher temperature (in the PE phase) stems from the PE to FE exothermic (heat is released) peak.

It is worth it to mention that, in La-doped PbZrO$_3$ (PLZT) [196, 197] and Pb$_{0.99}$(Zr, Sn, Ti)$_{0.98}$Nb$_{0.02}$0$_3$ (PNZST) [198] AFEs, the authors measured a positive ECE rather than a NECE as we observed in pure ceramic PbZrO$_3$. This discrepancy is explained by the dopants which affect the position of the FE phase. Contrary to PbZrO$_3$, PLZT and PNZST show a FE phase at low temperature and an AFE at high temperature. Thereby, the field induces an exothermic peak from FE-AFE leading to heating when the field is applied.

7.5 Conclusion

In summary, we have explained the negative electrocaloric effect observed directly in $PbZrO_3$ ceramic. By calorimetric measurements under electric field, we have shown that this NECE is not a consequence of the destabilization of the dipoles (dipoles canting) but rather a result of the field-induced a first-order (latent heat) endothermic transition from an antiferroelectric phase to a ferroelectric phase. Moreover, from the adiabatic temperature change, we have seen that the NECE doesn't disappear or turn positive above the coercive fields. This work gives more insight into the origin of NECE in antiferroelectrics and shows that the magnitude of NECE can keep on increasing above critical fields. This could enable working on a large temperature range by combining large NECE with conventional ECE. However, different ways such as doping have to be found to shift the material transition close to room temperature.

Chapter 8

Conclusions and future perspectives

The main goal of this dissertation has been to study the intrinsic efficiency of EC materials as it plays a role in the efficiency of the device. The figure of merit ”materials efficiency” η_{mat} defined as the ratio of the electrocaloric (EC) heat to the electrical work required to drive this heat, has been used for this purpose. As explained in the Introduction, the main goal of this dissertation was to answer the following research questions: **How energy efficient are our best EC materials? How much electrical work is required to drive EC heat in an EC material? How does the shape of material influences its materials efficiency?** To answer these questions we have studied the materials efficiency of the benchmark first-order transition material: lead scandium tantalate (PST), in the shape of bulk ceramic and multilayer capacitors. In this section, we will summarize the results obtained in this dissertation and we will discuss potential outlooks.

In Chapter 4, we firstly investigated the electrocaloric effect of highly ordered bulk ceramic PST. Secondly, we extracted the electrical work required to drive these EC effects and finally calculated its materials efficiency. The ECE in bulk PST was measured directly using an infrared camera. A differential scanning calorimeter under an electrical field was also utilized to describe and quantity the ECE in bulk PST ceramic. Near the material's ferroelectric to paraelectric transition at T_0 = 300 K, we measured a maximum direct ΔT_{adiab} = 3.7 K at the modest electric field of 40 kV cm^{-1} with an entropy change of 3.4 J kg^{-1} K^{-1} at

22 kV cm^{-1}. PST bulk can reach efficiency values as high as 128. This is as efficient as the best caloric materials. We observed a strong decrease of η_{mat} with the increasing electric field. For the same heat exchanged in PST and prototypical Gadolinium, we showed that PST requires four times less work than Gd. Nevertheless, due to its strong first-order transition, PST's high efficiency is limited to a narrow temperature range (2.5 K) which could be a handicap for cooling devices. Following the results presented in Chapter 4, in Chapter 5 we studied the efficiency of PST in the shape of multilayer capacitors. This structure offers large temperature change ($\Delta T_{adiab} =$ 3.5 K) under large electric fields (197 kV cm^{-1}), and on very large temperature range (higher than 60 K) advantageous for cooling devices. The materials efficiency of PST MLC is limited to 25. This is four times less compared to PST bulk and as efficient as Gadolinium for the same heat exchanged. We showed that even though PST MLC and PST bulk are first-order transition materials, the strong electric fields applied in PST MLC induce a second-order-like behavior which, explains the smooth decrease in the efficiency of PST MLC.

Our study on the materials efficiency of PST in different shapes has shown the pros on cons of the material's shape on its efficiency. In general, our work shows that PST is not only an EC performant material but also a very efficient material comparable to the best caloric materials (magnetocaloric materials driven with a permanent magnet). PST bulk suffers from its small temperature, therefore, can be used in layered regenerator in which PST bulk of different transitions (through doping) are assembled. This could help to benefit from the high intrinsic efficiency of PST bulk and expand its temperature range for cooling devices. PST MLC requires a large electric field inducing low efficiency. Caloric materials in general are attractive because of their potential high efficiency. This work could serve as a tool to consider the intrinsic efficiency of caloric materials in order to improve the efficiency of devices. The direct open question one can ask himself for further investigations is: how comparable is the efficiency of thin films to bulk and MLC? Ceramics materials have been mainly studied in this work. One could wonder how energy efficient are non-ceramic materials such as polymers that offer high electrocaloric effect as reported in the literature [64].

Moreover, the efficiency of plastic crystals [199] that show entropy changes comparable to that of the fluorinated gases used currently in our cooling systems, could be investigated. One crucial question that need to be answered is: What is the impact of the materials efficiency on the overall efficiency of a cooling device ? How comparable is the efficiency of a first-order transition MC material such as LaFeCoSi to a first-order transition EC material like PST ?

In Chapter 6, we quantified the entropy change from driving the transition in PST MLC. This entropy change was calculated from direct measurements of the field dependence of the transition temperature obtained from differential scanning calorimetry under an electric field, and from the polarization change at the materials' transition temperature. The results obtained are in adequation with reported values. Our approach which combines, isofield measurement under DSC, isothermal polarization versus electric field measurements and Landau theory could help deduce the transition entropy of caloric materials in general.

Chapter 7 stems from a collaboration with Gustau Catalan's group in Spain. We studied the negative electrocaloric effect in $PbZrO_3$ (short form PZO) ceramic. From calorimetric measurements under electric field and direct IR camera measurements of ΔT_{adiab}, we have shown that the NECE in pure ceramic PZO is not a consequence of the destabilization of the dipoles (dipoles canting) as claimed in the literature but rather a result of the field-induced a first-order (latent heat) endothermic transition from an antiferroelectric phase to a ferroelectric phase. Moreover, from the adiabatic temperature change, we have seen that the NECE doesn't disappear or turn positive above the coercive fields. This work gives more insight into the origin of NECE in antiferroelectrics and shows that the magnitude of NECE can keep on increasing above critical fields. Moreover, it could enable working on a large temperature range by combining large NECE with conventional ECE.

PhD Output

List of Publications

Articles in peer-reviewed journals

As first author:

1. Y. Nouchokgwe, P. Lheritier, C.-H. Hong, A. Torello, R. Faye, W. Jo, C. R. H. Bahl, and E. Defay, “Giant electrocaloric materials energy efficiency in highly ordered lead scandium tantalate”,*Nature Communications* 12, 3298, **2021**.
2. Y. Nouchokgwe, P. Lheritier, T. Usui, A. Torello, A. El Moul, V. Kovacova, T. Granzow, S. Hirose, and E. Defay, “Materials efficiency of electrocaloric lead scandium tantalate multilayer capacitors”, *Scripta Materiala*, 219, 114873, **2022**.

As co-author:

1. P. Vales-Castro, R. Faye, M. Vellvehi, Y. Nouchokgwe et al., ”Origin of negative electrocaloric effect in antiferroelectric $PbZrO_3$”, *Physical Review B*, 103, 054112, **2021**.
2. P. Lheritier, A. Torelló, T. Usui, Y. Nouchokgwe, A. Aravindhan, J. Li, U. Prah, V. Kovacova, O. Bouton, S. Hirose, E. Defay, ”Large harvested energy with non-linear pyroelectric modules”, *Nature*, **2022**.
3. A. Torello, P. Lheritier, T. Usui, Y. Nouchokgwe, M. Gerard, O. Bouton, S. Hirose, and E. Defay, “Giant temperature span in electrocaloric regenerator”, *Science*, 370, 6512,

2020.

4. P. Lhéritier, Y. Nouchokgwe, V. Kovacova, C.-H. Hong, À. Torelló, W. Jo, E. Defay, *J. Eur. Ceram. Soc.*, 41, **2021**.

Submitted:

1. A. Aravindhan, P. Lheritier, A. Torello, U. Prah, Y. Nouchokgwe, A. El Moul, X. Chevalier, F. Domingues Dos Santos, E. Defay, V. Kovacova, ”Direct measurement of electrocaloric effect in P(VDF-TrFE-CFE) film using infrared imaging”, **2022**.

Conferences

Oral Presentations:

1. Youri Nouchokgwe,Alvar Torello, Pierre Lhéritier, Régis Vaudemont, Olivier Bouton, Chang-Hyo Hong, Wook Jo, Tomoyasu Usui, Sakyo Hirose, Emmanuel Defay, ”Direct measurements of electrocaloric efficiency”, *EMRS 2019 Fall Meeting*, **15–19 April 2019**, Warsaw, Poland.
2. Youri Nouchokgwe, Pierre Lheritier, C.H. Hong, Alvar Torello, Romain Faye, Jo Wook, C.R.H. Bahl, Emmanuel Defay, ”Giant electrocaloric materials energy efficiency in highly ordered lead scandium tantalate”, *THERMAG IX, 9th IIR International Conference on Caloric Cooling and Applications of Caloric Materials*, **JUNE 7-11, 2021**, Maryland, USA (virtual).
3. Youri Nouchokgwe, Pierre Lheritier, Alvar Torello, Veronika Kovacova, Emmanuel Defay, ”An energy efficient electrocaloric material”, *MASSENA YSC 2021*, **JUNE 24-25, 2021**, Diekrich, Luxembourg.
4. Youri Nouchokgwe, Pierre Lheritier, Tomoyasu Usui, Alvar Torelló Massana, Uros Prah, Veronika Kovacova, Sakyo Hirose, Emmanuel Defay, ”Electrocaloric Entropy Change

in Lead Scandium Tantalate Multilayer Capacitors Using a Differential Scanning Calorimeter and Clausius-Clapeyron Equation”, *IEE ISAF 2022*, **JUNE 27 - JULY 1st, 2022**, Tours, France.

5. Youri Nouchokgwe, Pierre Lheritier, Tomoyasu Usui, Alvar Torelló Massana, Uros Prah, Veronika Kovacova, Sakyo Hirose, Emmanuel Defay, ”Comparison of materials efficiency in electrocaloric and magnetocaloric materials”, *EUROTHERM 2021 Caloric Heating and Cooling Conference*, **JUNE 13 - JULY 15, 2021**, Twente, Netherlands (virtual).

Summer Schools

1. International School of Oxide Electronics (ISOE) **2019, JUNE 25 – JULY 5th**, Cargèse, France.

Teaching

1. ”Thermodynamics Lab classes”, University of Luxembourg (Campus Limpertsberg),winter semester 2018/2019.

Awards

1. **Best pitch Award** at *IEE ISAF 2022* - ”An energy efficient and green refrigerant” - Youri Nouchokgwe.
2. **Best student pre-recorded presentation** at *THERMAG 9th IIR International Conference on Caloric Cooling and Applications of Caloric Materials* — ”Giant electrocaloric materials energy efficiency in highly ordered lead scandium tantalate” —Youri Dilan, Nouchokgwe Kamgue, et al.
3. **Outstanding Scientific Achievement Award** from FNR (Fonds National de la Recherche)

4. **Favourite video - 2022 Nature Awards - Science In Shorts**

   https://www.youtube.com/watch?v=MVOpQ0abxQ8

Bibliography

[1] J. L. Dupont, P. Domanski, P. Lebrun, and F. Ziegler, “The role of refrigeration in the global economy (2019), 38th note on refrigeration technologies (international institute of refrigeration,” Phys. Rev. (2009).

[2] A. Mota-Babiloni, J. Navarro-Esbrí, Á. Barragán-Cervera, F. Molés, B. Peris, and G. Verdú, “Commercial refrigeration – an overview of current status”, International Journal of Refrigeration **57**, 186–196 (2015).

[3] K. Gschneidner and V. Pecharsky, “Thirty years of near room temperature magnetic cooling: where we are today and future prospects”, International Journal of Refrigeration **31**, 945–961 (2008).

[4] O. Gutfleisch, M. A. Willard, E. Brück, C. H. Chen, S. G. Sankar, and J. P. Liu, “Magnetic materials and devices for the 21st century: stronger, lighter, and more energy efficient”, Advanced Materials **23**, 821–842 (2011).

[5] M. Braun, H. Altan, and S. Beck, “Using regression analysis to predict the future energy consumption of a supermarket in the uk”, Applied Energy **130**, 305–313 (2014).

[6] A. Barman, S. Kar-Narayan, and D. Mukherjee, “Caloric Effects in Perovskite Oxides”, Advanced Materials Interfaces **6**, 1–31 (2019).

[7] O. Sari and M. Balli, “From conventional to magnetic refrigerator technology”, International Journal of Refrigeration **37**, `10.1016/j.ijrefrig.2013.09.027` (2013).

[8] H. H. M. M. Sattar R. Saidur, “Performance investigation of domestic refrigerator using pure hydrocarbons and blends of hydrocarbons as refrigerants”, Proc. World Academy of Science, Engineering and Technology, **23**, 223 (2007).

[9] D. Wang, Y. Li, D. Li, Y. Xia, and J. Zhang, “A review on adsorption refrigeration technology and adsorption deterioration in physical adsorption systems”, Renewable and Sustainable Energy Reviews **14**, 344–353 (2010).

[10] G. Maidment, *Clean cold and the global goals*.

[11] B. German Federal Ministry for the Environment Nature Conservation and N. Safety, *Green cooling initiative*, `http://www.green-cooling-initiative.org/`.

[12] IPCC, *Le sixième rapport d’évaluation*, `https://www.ipcc.ch/languages-2/francais/`.

[13] Jelt, *How your fridge is heating up the planet*, `https://www.bbc.com/future/article/20201204-climate-change-how-chemicals-in-your-fridge-warm-the-planet#:~:text=This%5C%20is%5C%20because%5C%20HFCs%5C%20and,effect%5C%20that%5C%20warms%5C%20the%5C%20planet.`.

[14] S. K. Fischer, J. Tomlinson, and P. J. Hughes, *Energy and global warming impacts of not-in-kind and next generation cfc and hcfc alternatives* (AFEAS, 1994).

[15] J. Shi, D. Han, Z. Li, L. Yang, S.-G. Lu, Z. Zhong, J. Chen, Q. Zhang, and X. Qian, “Electrocaloric cooling materials and devices for zero-global-warming-potential, high-efficiency refrigeration”, Joule **3**, 1200–1225 (2019).

[16] S. Qian, D. Nasuta, A. Rhoads, Y. Wang, Y. Geng, Y. Hwang, R. Radermacher, and I. Takeuchi, “Not-in-kind cooling technologies: a quantitative comparison of refrigerants and system performance”, International Journal of Refrigeration **62**, 177–192 (2016).

[17] X. Moya, S. Kar-Narayan, and N. D. Mathur, *Caloric materials near ferroic phase transitions*, 2014.

[18] A. Kitanovski, J. Tušek, U. Tomc, U. Plaznik, M. Ožbolt, and A. Poredoš, “Alternative caloric energy conversions”, in *Magnetocaloric energy conversion: from theory to applications* (Springer International Publishing, Cham, 2015), pp. 395–450.

[19] H. Hou, S. Qian, and I. Takeuchi, “Materials, physics and systems for multicaloric cooling”, Nature Reviews Materials, `10.1038/s41578-022-00428-x` (2022).

[20] E. Stern-Taulats, T. Castán, L. Mañosa, A. Planes, N. D. Mathur, and X. Moya, “Multicaloric materials and effects”, MRS Bulletin **43**, 295–299 (2018).

[21] S.-W. Cheong and M. Mostovoy, “Multiferroics: a magnetic twist for ferroelectricity”, Nature Materials **6**, 13–20 (2007).

[22] M. M. Vopson, “The induced magnetic and electric fields’ paradox leading to multicaloric effects in multiferroics”, Solid State Communications **231-232**, 14–16 (2016).

[23] Z. Kutnjak, B. Rožič, and R. Pirc, “Electrocaloric effect: theory, measurements, and applications”, in *Wiley encyclopedia of electrical and electronics engineering* (John Wiley Sons, Ltd, 2015), pp. 1–19.

[24] E. Defay, R. Faye, G. Despesse, H. Strozyk, D. Sette, S. Crossley, X. Moya, and N. D. Mathur, “Enhanced electrocaloric efficiency via energy recovery”, Nature Communications **9**, `10.1038/s41467-018-04027-9` (2018).

[25] X. Moya and N. D. Mathur, “Caloric materials for cooling and heating”, Science **370**, 797–803 (2020).

[26] S. Fähler, “Caloric effects in ferroic materials: new concepts for cooling”, Energy Technology **6**, 1394–1396 (2018).

[27] L. Mañosa, A. Planes, and M. Acet, “Advanced materials for solid-state refrigeration”, J. Mater. Chem. A **1**, 4925–4936 (2013).

[28] A. S. Mischenko, Q. Zhang, J. F. Scott, R. W. Whatmore, and N. D. Mathur, “Giant Electrocaloric Effect in Thin-Film $PbZr_{0.95}Ti_{0.05}O_3$”, Science **311**, 1270–1271 (2006).

[29] B. P. Nair, “Electrocaloric applications based on multilayer capacitors of $PbSc_{0.5}Ta_{0.5}O_3$”, (2020).

[30] Y. Nouchokgwe, P. Lheritier, C.-H. Hong, A. Torelló, R. Faye, W. Jo, C. R. H. Bahl, and E. Defay, “Giant electrocaloric materials energy efficiency in highly ordered lead scandium tantalate”, Nature Communications **12**, 3298 (2021).

[31] V. Kovacova, S. Glinsek, S. Girod, and E. Defay, "High electrocaloric effect in lead scandium tantalate thin films with interdigitated electrodes", Sensors **22**, `10.3390/s22114049` (2022).

[32] A. Torelló, P. Lheritier, T. Usui, Y. Nouchokgwe, M. Gérard, O. Bouton, S. Hirose, and E. Defay, "Giant temperature span in electrocaloric regenerator", Science **370**, 125–129 (2020).

[33] E. Defay, S. Crossley, S. Kar-Narayan, X. Moya, and N. D. Mathur, "The electrocaloric efficiency of ceramic and polymer films", Advanced Materials **25**, 3337–3342 (2013).

[34] X. Moya, E. Defay, V. Heine, and N. D. Mathur, "Too cool to work", Nature Physics **11**, 202–205 (2015).

[35] S. Crossley, N. D. Mathur, and X. Moya, "New developments in caloric materials for cooling applications", AIP Advances **5**, `10.1063/1.4922871` (2015).

[36] L. D. Griffith, Y. Mudryk, J. Slaughter, and V. K. Pecharsky, "Material-based figure of merit for caloric materials", Journal of Applied Physics **123**, 034902 (2018).

[37] J. A. Gough, "Material-based figure of merit for caloric materials", Mem. Lit. Phil. Soc. Manchester **1**, 288–295 (1805).

[38] A. Smith, "Who discovered the magnetocaloric effect?", The European Physical Journal H **38**, 507–517 (2013).

[39] E. Warburg, "Magnetische untersuchungen", Annalen der Physik **249**, 141–164 (1881).

[40] A. P. Pierre Weiss, "Le phénomène magnétocalorique", J. Phys. Theor. Appl. **7**, 103–109 (1917).

[41] P. Kobeko and J. Kurtschatov, "Magnetische untersuchungen", Zeit. Phys. **66**, 291–205 (19030).

[42] G. G. Wiseman and J. K. Kuebler, "Electrocaloric effect in ferroelectric rochelle salt", Phys. Rev. **131**, 2023–2027 (1963).

[43] B. WUL, "Barium titanate: a new ferro-electric", Nature **157**, 808–808 (1946).

[44] A. Kikuchi and E. Sawaguchi, “Electrocaloric effect in $SrTiO_3$”, Journal of the Physical Society of Japan **19**, 1497–1498 (1964).

[45] A. I. Karchevskii, “Electrocaloric effect in polycrystalline barium titanate”, Phys. Solid State **3**, 2249–2254 (1962).

[46] P. D. Thacher, “Electrocaloric effects in some ferroelectric and antiferroelectric Pb(Zr, Ti)O_3 compounds”, Journal of Applied Physics **39**, 1996–2002 (1968).

[47] B. A. Tuttle and D. A. Payne, “The effects of microstructure on the electrocaloric properties of Pb(Zr,Sn,Ti)O_3 ceramics”, Ferroelectrics **37**, 603–606 (1981).

[48] L. Shebanov, P. Kapostinsh, E. K. Birks, and Y. A. Zvirgzds, “Some peculiarities in the rearrangement of the crystal-structure and electrocaloric effect of single lead magnoniobate crystals in the region of a diffused phase-transition”, Kristallografiya **31**, 317–320 (1986).

[49] R. B. Olsen, W. F. Butler, D. A. Payne, B. A. Tuttle, and P. C. Held, “Observation of a polarocaloric (electrocaloric) effect of 2 °c in lead zirconate modified with Sn^{4+} and ti^{4+}”, Phys. Rev. Lett. **45**, 1436–1438 (1980).

[50] E. Birks, L. Shebanov, and A. Sternberg, “Electrocaloric effect in PLZT ceramics”, Ferroelectrics **69**, 125–129 (1986).

[51] W. N. Lawless, “Specific heat and electrocaloric properties of $KTaO_3$ at low temperatures”, Phys. Rev. B **16**, 433–439 (1977).

[52] L. A. Shebanov, E. Birks, and K. J. Borman, “X-ray studies of electrocaloric lead- scandium tantalate ordered solid solutions”, Ferroelectrics **90**, 165–172 (1989).

[53] L. Shebanovs, A. Sternberg, W. N. Lawless, and K. Borman, “Isomorphous ion substitutions and order-disorder phenomena in highly electrocaloric lead-scandium tantalate solid solutions”, Ferroelectrics **184**, 239–242 (1996).

[54] L. Shebanovs, K. Borman, W. N. Lawless, and A. Kalvane, “Electrocaloric effect in some perovskite ferroelectric ceramics and multilayer capacitors”, **273**, 137–142 (2002).

[55] L. Shebanov and K. Borman, “On lead-scandium tantalate solid solutions with high electrocalcric effect”, Ferroelectrics **127**, 143–148 (1992).

[56] B. Neese, B. Chu, S.-G. Lu, Y. Wang, E. Furman, and Q. M. Zhang, “Large electrocaloric effect in ferroelectric polymers near room temperature”, Science **321**, 821–823 (2008).

[57] S. G. Lu, B. Rožič, Q. M. Zhang, Z. Kutnjak, X. Li, E. Furman, L. J. Gorny, M. Lin, B. Malič, M. Kosec, R. Blinc, and R. Pirc, “Organic and inorganic relaxor ferroelectrics with giant electrocaloric effect”, Applied Physics Letters **97**, 162904 (2010).

[58] T. M. Correia, J. S. Young, R. W. Whatmore, J. F. Scott, N. D. Mathur, and Q. Zhang, “Investigation of the electrocaloric effect in a $PbMg_{2/3}Nb_{1/3}O_3$-$PbTiO_3$ relaxor thin film”, Applied Physics Letters **95**, 182904 (2009).

[59] T. M. Correia, S. Kar-Narayan, J. S. Young, J. F. Scott, N. D. Mathur, R. W. Whatmore, and Q. Zhang, “PST thin films for electrocaloric coolers”, Journal of Physics D: Applied Physics **44**, `10.1088/0022-3727/44/16/165407` (2011).

[60] X.-S. Qian, S.-G. Lu, X. Li, H. Gu, L.-C. Chien, and Q. Zhang, “Large electrocaloric effect in a dielectric liquid possessing a large dielectric anisotropy near the isotropic–nematic transition”, Advanced Functional Materials **23**, 2894–2898 (2013).

[61] M. Trcek, M. Lavric, G. Cordoyiannis, B. Zalar, B. Rozic, S. Kralj, V. Tzitzios, G. Nounesisand, and Z. Kutnjak, “Electrocaloric and elastocaloric effects in soft materials”, Phil. Trans. R. Soc. A **374**, 20150301 (2016).

[62] W. Geng, Y. Liu, X. Meng, L. Bellaiche, J. F. Scott, B. Dkhil, and A. Jiang, “Giant negative electrocaloric effect in antiferroelectric la-doped Pb(ZrTi)O_3 thin films near room temperature”, Advanced Materials **27**, 3165–3169 (2015).

[63] P. Vales-Castro, R. Faye, M. Vellvehi, Y. Nouchokgwe, X. Perpiñà, J. M. Caicedo, X. Jordà, K. Roleder, D. Kajewski, A. Perez-Tomas, E. Defay, and G. Catalan, “Origin of large negative electrocaloric effect in antiferroelectric $\mathrm{PbZrO_3}$”, Phys. Rev. B **103**, 054112 (2021).

[64]X. Qian, D. Han, L. Zheng, J. Chen, M. Tyagi, Q. Li, F. Du, S. Zheng, X. Huang, S. Zhang, J. Shi, H. Huang, X. Shi, J. Chen, H. Qin, J. Bernholc, X. Chen, L.-Q. Chen, L. Hong, and Q. M. Zhang, “High-entropy polymer produces a giant electrocaloric effect at low fields”, Nature **600**, 664–669 (2021).

[65]X. Moya and N. D. Mathur, “Double bond with a licence to chill”, Joule **6**, 289–290 (2022).

[66]B. P. Nair, “Electrocaloric applications based on multilayer capacitors of PbSc$_{0.5}$Ta$_{0.5}$O$_3$”, PhD thesis (2020).

[67]A. Torelló and E. Defay, “Electrocaloric coolers: a review”, Advanced Electronic Materials **8**, 2101031 (2022).

[68]Y. Meng, J. Pu, and Q. Pei, “Electrocaloric cooling over high device temperature span”, Joule **5**, 780–793 (2021).

[69]K. Nielsen, J. Tusek, K. Engelbrecht, S. Schopfer, A. Kitanovski, C. Bahl, A. Smith, N. Pryds, and A. Poredos, “Review on numerical modeling of active magnetic regenerators for room temperature applications”, International Journal of Refrigeration **34**, 603–616 (2011).

[70]B. Yu, M. Liu, P. W. Egolf, and A. Kitanovski, “A review of magnetic refrigerator and heat pump prototypes built before the year 2010”, International Journal of Refrigeration **33**, 1029–1060 (2010).

[71]H. Gu, X. Qian, X. Li, B. Craven, W. Zhu, A. Cheng, S. C. Yao, and Q. M. Zhang, “A chip scale electrocaloric effect based cooling device”, Applied Physics Letters **102**, `10.1063/1.4799283` (2013).

[72]Y. Wang, Z. Zhang, T. Usui, M. Benedict, S. Hirose, J. Lee, J. Kalb, and D. Schwartz, “A high-performance solid-state electrocaloric cooling system”, Science **370**, 129–133 (2020).

[73]Y. Meng, Z. Zhang, H. Wu, R. Wu, J. Wu, H. Wang, and Q. Pei, “A cascade electrocaloric cooling device for large temperature lift”, Nature Energy **5**, 996–1002 (2020).

[74]X. Moya and N. D. Mathur, “It’s not about the mass”, Nature Energy **5**, 941–942 (2020).

[75]Y. Liu, J. F. Scott, and B. Dkhil, “Direct and indirect measurements on electrocaloric effect: recent developments and perspectives”, Applied Physics Reviews **3**, 031102 (2016).

[76]A. Giguère, M. Foldeaki, B. Ravi Gopal, R. Chahine, T. K. Bose, A. Frydman, and J. A. Barclay, “Direct measurement of the “giant” adiabatic temperature change in $\mathrm{Gd_5Si_2Ge_2}$”, Phys. Rev. Lett. **83**, 2262–2265 (1999).

[77]J. R. Sun, F. X. Hu, and B. G. Shen, “Comment on “direct measurement of the ‘giant’ adiabatic temperature change in $\mathrm{Gd_5Si_2Ge_2}$””, Phys. Rev. Lett. **85**, 4191–4191 (2000).

[78]M. Földeàki, R. Chahine, T. K. Bose, and J. A. Barclay, “Földeàki et al. reply:” Phys. Rev. Lett. **85**, 4192–4192 (2000).

[79]A. Planes, T. Castán, and A. Saxena, “Thermodynamics of multicaloric effects in multiferroics”, Philosophical Magazine **94**, 1893–1908 (2014).

[80]J. Li, “Barocaloric effects in the vicinity of first-order phase transitions”, PhD thesis (Queen Mary University of London, 2021).

[81]Y. Nouchokgwe, P. Lheritier, T. Usui, A. Torello, A. E. Moul, V. Kovacova, T. Granzow, S. Hirose, and E. Defay, “Materials efficiency of electrocaloric lead scandium tantalate multilayer capacitors”, Scripta Materialia **219**, 114873 (2022).

[82]T. Hess, L. M. Maier, N. Bachmann, P. Corhan, O. Schäfer-Welsen, J. Wöllenstein, and K. Bartholomé, “Thermal hysteresis and its impact on the efficiency of first-order caloric materials”, Journal of Applied Physics **127**, 075103 (2020).

[83]C. Basceri, S. K. Streiffer, A. I. Kingon, and R. Waser, “The dielectric response as a function of temperature and film thickness of fiber-textured (Ba,Sr)$\mathrm{TiO_3}$ thin films grown by chemical vapor deposition”, Journal of Applied Physics **82**, 2497–2504 (1997).

[84]V. Heine, “The thermodynamics of bodies in static electromagnetic fields”, Mathematical Proceedings of the Cambridge Philosophical Society **52**, 546–552 (1956).

[85]K. Zhang, G. Kang, and Q. Sun, “High fatigue life and cooling efficiency of niti shape memory alloy under cyclic compression”, Scripta Materialia **159**, 62–67 (2019).

[86] J. Chen, K. Zhang, Q. Kan, H. Yin, and Q. Sun, “Ultra-high fatigue life of niti cylinders for compression-based elastocaloric cooling”, Applied Physics Letters **115**, 093902 (2019).

[87] J. Cui, Y. Wu, J. Muehlbauer, Y. Hwang, R. Radermacher, S. Fackler, M. Wuttig, and I. Takeuchi, “Demonstration of high efficiency elastocaloric cooling with large ΔT using NiTi wires”, Applied Physics Letters **101**, 73904 (2012).

[88] S. Qian, Y. Geng, Y. Wang, J. Ling, Y. Hwang, R. Radermacher, I. Takeuchi, and J. Cui, “A review of elastocaloric cooling: materials, cycles and system integrations”, International Journal of Refrigeration **64**, 1–19 (2016).

[89] H. Hou, E. Simsek, T. Ma, N. S. Johnson, S. Qian, C. Cissé, D. Stasak, N. A. Hasan, L. Zhou, Y. Hwang, R. Radermacher, V. I. Levitas, M. J. Kramer, M. A. Zaeem, A. P. Stebner, R. T. Ott, J. Cui, and I. Takeuchi, “Fatigue-resistant high-performance elastocaloric materials made by additive manufacturing”, Science **366**, 1116–1121 (2019).

[90] S. Qian, J. Ling, Y. Hwang, R. Radermacher, and I. Takeuchi, “Thermodynamics cycle analysis and numerical modeling of thermoelastic cooling systems”, International Journal of Refrigeration **56**, 65–80 (2015).

[91] S. Qian, Y. Geng, Y. Wang, T. E. Pillsbury, Y. Hada, Y. Yamaguchi, K. Fujimoto, Y. Hwang, R. Radermacher, J. Cui, Y. Yuki, K. Toyotake, and I. Takeuchi, “Elastocaloric effect in cualzn and cualmn shape memory alloys under compression”, Philosophical Transactions of the Royal Society A: Mathematical, Physical and Engineering Sciences **374**, 20150309 (2016).

[92] Y. Liu, B. Dkhil, and E. Defay, “Spatially Resolved Imaging of Electrocaloric Effect and the Resultant Heat Flux in Multilayer Capacitors”, ACS Energy Letters **1**, 521–528 (2016).

[93] J. Tušek, K. Engelbrecht, D. Eriksen, S. Dall’Olio, J. Tušek, and N. Pryds, “A regenerative elastocaloric heat pump”, Nature Energy **1**, 16134 (2016).

[94] J. Tušek, K. Engelbrecht, L. Mañosa, E. Vives, and N. Pryds, “Understanding the Thermodynamic Properties of the Elastocaloric Effect Through Experimentation and Modelling”, Shape Memory and Superelasticity **2**, 317–329 (2016).

[95] Y. Hirayama, R. Iguchi, X.-F. Miao, K. Hono, and K.-i. Uchida, “High-throughput direct measurement of magnetocaloric effect based on lock-in thermography technique”, Applied Physics Letters **111**, 163901 (2017).

[96] P. Lhéritier, Y. Nouchokgwe, V. Kovacova, C. H. Hong, À. Torelló, W. Jo, and E. Defay, “Measuring lead scandium tantalate phase transition entropy by infrared camera”, Journal of the European Ceramic Society **41**, 7000–7004 (2021).

[97] M. Sanlialp, C. Molin, V. V. Shvartsman, S. Gebhardt, and D. C. Lupascu, “Modified differential scanning calorimeter for direct electrocaloric measurements”, IEEE Transactions on Ultrasonics, Ferroelectrics, and Frequency Control **63**, 1690–1696 (2016).

[98] X. Moya, E. Stern-Taulats, S. Crossley, D. González-Alonso, S. Kar-Narayan, A. Planes, L. Mañosa, and N. D. Mathur, “Giant Electrocaloric Strength in Single-Crystal $BaTiO_3$”, Advanced Materials **25**, 1360–1365 (2013).

[99] J. Hagberg, A. Uusimäki, and H. Jantunen, “Electrocaloric characteristics in reactive sintered $0.87Pb(Mg_{13}Nb_{23})O_3$–$0.13PbTiO_3$”, Applied Physics Letters **92**, 132909 (2008).

[100] S. Kar-Narayan and N. D. Mathur, “Direct and indirect electrocaloric measurements using multilayer capacitors”, Journal of Physics D: Applied Physics **43**, `10.1088/0022-3727/43/3/032002` (2010).

[101] S. Kar-Narayan, S. Crossley, X. Moya, V. Kovacova, J. Abergel, A. Bontempi, N. Baier, E. Defay, and N. D. Mathur, “Direct electrocaloric measurements of a multilayer capacitor using scanning thermal microscopy and infra-red imaging”, Applied Physics Letters **102**, 32903 (2013).

[102] D. B. Short, “Thermal imaging in the science classroom”, School Science Review **94**, 75–78 (2012).

[103] A. Charogiannis, I. Zadrazil, and C. N. Markides, “Thermographic particle velocimetry (TPV) for simultaneous interfacial temperature and velocity measurements”, International Journal of Heat and Mass Transfer **97**, 589–595 (2016).

[104] Jelt, *Colorjelt noir mat*, `https://www.itwpc.com/produits/colorjelt-noir-mat`.

[105] G. T. Armstrong, “The calorimeter and its influence on the development of chemistry”, Journal of Chemical Education **41**, 297 (1964).

[106] I. Wadsö, “Chapter 3 - Calorimetric Techniques”, in *Thermal and energetic studies of cellular biological systems*, edited by A. M. James (Butterworth-Heinemann, 1987), pp. 34–67.

[107] E. F. Mueller and F. D. Rossini, “The Calory and the Joule in Thermodynamics and Thermochemistry”, American Journal of Physics **12**, 1–7 (1944).

[108] J. J.P, Philosophical Magazine **23**, 263, 347, 435 (1843).

[109] G. W. H. Höhne, W. F. Hemminger, and H.-J. Flammersheim, *Differential Scanning Calorimetry* (Springer Berlin Heidelberg, Berlin, Heidelberg, 2003).

[110] Y. Z. Zhan, Y. Du, and Y. H. Zhuang, “CHAPTER FOUR - DETERMINATION OF PHASE DIAGRAMS USING EQUILIBRATED ALLOYS”, in *Methods for phase diagram determination*, edited by J.-C. Zhao (Elsevier Science Ltd, Oxford, 2007), pp. 108–150.

[111] W. Brostow, S. H. Goodman, and J. Wahrmund, “8 - Epoxies”, in *Handbook of thermoset plastics (third edition)*, edited by H. Dodiuk and S. H. Goodman, Third Edition (William Andrew Publishing, Boston, 2014), pp. 191–252.

[112] L. Mañosa, M. Bou, C. Calles, and A. Cirera, “Low-cost differential scanning calorimeter”, American Journal of Physics **64**, 283–287 (1996).

[113] J. Marcos, F. Casanova, X. Batlle, A. Labarta, A. Planes, and L. Mañosa, “A high-sensitivity differential scanning calorimeter with magnetic field for magnetostructural transitions”, Review of Scientific Instruments **74**, 4768–4771 (2003).

[114] B. Wunderlich, “CHAPTER 5 - CALORIMETRY”, in *Thermal analysis*, edited by B. Wunderlich (Academic Press, 1990), pp. 219–310.

[115] A. A. Bunaciu, E. gabriela Udriştioiu, and H. Y. Aboul-Enein, “X-Ray Diffraction: Instrumentation and Applications”, Critical Reviews in Analytical Chemistry **45**, 289–299 (2015).

[116] C. G. Pope, “X-Ray Diffraction and the Bragg Equation”, Journal of Chemical Education **74**, 129 (1997).

[117] W. H. Bragg and W. L. Bragg, *X rays and crystal structure* (London: G, 1918).

[118] K. Vernon-Parry, "Scanning electron microscopy: an introduction", III-Vs Review **13**, 40–44 (2000).

[119] E. Ruska, "The development of the electron microscope and of electron microscopy", Rev. Mod. Phys. **59**, 627–638 (1987).

[120] W. Zhou, R. Apkarian, Z. L. Wang, and D. Joy, "Fundamentals of scanning electron microscopy (sem)", in *Scanning microscopy for nanotechnology* (Springer, 2006), pp. 1–40.

[121] D. McMullan, "Scanning electron microscopy 1928–1965", Scanning **17**, 175–185 (1995).

[122] S. Sharma, S. Jaiswal, B. Duffy, and A. K. Jaiswal, "Nanostructured Materials for Food Applications: Spectroscopy, Microscopy and Physical Properties", Bioengineering **6**, `10.3390/bioengineering6010026` (2019).

[123] R. Andika, L. O. Husein Zilullah Toresano, M. Hikam, B. Soegijono, and A. Sudarmaji, "The Electrical Hysteresis Loop and Polarization Value of BaZr$_x$Ti$_{1-x}$O$_3$ Multilayer Films Material at Different Annealing Temperature (x = 0.1 and 0.08) based on Sawyer Tower Circuit", in (2014).

[124] C. Das, A. Shahee, N. Lalla, and T. Shripathi, "A simple and low cost Sawyer-Tower ferroelectric loop tracer with variable frequency and compensation circuit", Proceedings of the 54th DAE Solid State Physics Symposium (2009), 439– (2009).

[125] N. M. Shorrocks, R. W. Whatmore, and P. C. Osbond, "Lead scandium tantalate for thermal detector applications", Ferroelectrics **106**, 387–392 (1990).

[126] R. W. Whatmore, "Pyroelectric ceramics and devices for thermal infra-red detection and imaging", Ferroelectrics **118**, 241–259 (1991).

[127] N. Shorrocks, A. Patel, and R. Whatmore, "Pyl11: Pyroelectric properties of thin film lead scandium tantalate", Ferroelectrics **133**, 35–40 (1992).

[128] R. Watton and M. A. Todd, "Induced pyroelectricity in sputtered lead scandium tantalate films and their merit for IR detector arrays", Ferroelectrics **118**, 279–295 (1991).

[129] S. Crossley, B. Nair, R. W. Whatmore, X. Moya, and N. D. Mathur, “Electrocaloric Cooling Cycles in Lead Scandium Tantalate with True Regeneration via Field Variation”, Physical Review X **9**, `10.1103/PhysRevX.9.041002` (2019).

[130] S. Crossley, “Electrocaloric materials and devices”, PhD thesis (2013).

[131] E. Stern, “Giant caloric effects in the vicinity of first-order giant caloric effects in the vicinity of first-order phase transition”, PhD thesis (2017).

[132] S. Crossley, R. W. Whatmore, N. D. Mathur, and X. Moya, “Quasi-indirect measurement of electrocaloric temperature change in $PbSc_{0.5}Ta_{0.5}O_3$ via comparison of adiabatic and isothermal electrical polarization data”, APL Materials **9**, `10.1063/5.0037809` (2021).

[133] F. Stenger C. G.F.and Scholten and A. J. Burggraaf, “Ordering and diffuse phase transitions in $Pb(Sc_{0.5}Ta_{0.5})O_3$ ceramics”, Solid State Communications **32** (1979).

[134] C. G. Stenger and A. J. Burggraaf, “Order–disorder reactions in the ferroelectric perovskites $Pb(Sc_{1/2}Nb_{1/2})O_3$ and $Pb(Sc_{1/2}Ta_{1/2})O_3$. II. Relation between ordering and properties”, physica status solidi (a) **61**, 653–664 (1980).

[135] H.-C. .-. Wang and W. A. Schulze, “Order-Disorder Phenomenon in Lead Scandium Tantalate”, Journal of the American Ceramic Society **73**, 1228–1234 (1990).

[136] C. Stenger and A. Burggraaf, “Order–disorder reactions in the ferroelectric perovskites $Pb(Sc_{1/2}Nb_{1/2})O_3$ and $Pb(Sc_{1/2}Ta_{1/2})O_3$: i. kinetics of the ordering process”, English, Physica status solidi A **61**, 275–285 (1980).

[137] S. G. Francis, *Structure, properties and preparation of perovskite-type compounds:international series of monographs in solid state physics*, Vol. 5 (Elsevier, 2013).

[138] J. R. Giniewicz, A. S. Bhalla, and L. E. Cross, “Variable structural ordering in lead scandium tantalate-lead titanate materials”, Ferroelectrics **211**, 281–297 (1998).

[139] N. Setter and L. E. Cross, “The contribution of structural disorder to diffuse phase transitions in ferroelectrics”, JOURNAL OF MATERIALS SCIENCE **15**, 2478–2482 (1980).

[140] L. E. Cross, “Relaxor ferroelectrics”, Ferroelectrics **76**, 241–267 (1987).

[141] K. Brinkman, Y. Wang, D. Su, A. Tagantsev, P. Muralt, and N. Setter, “The Impact of chemical ordering on the dielectric properties of lead scandium tantalate Pb(Sc$_{1/2}$Ta$_{1/2}$)O$_3$ thin films”, Journal of Applied Physics **102**, `10.1063/1.2770834` (2007).

[142] N. Setter and L. E. Cross, “The role of B-site cation disorder in diffuse phase transition behavior of perovskite ferroelectrics”, Journal of Applied Physics **51**, 4356–4360 (1980).

[143] A. Sternberg, L. Shebanovs, E. Birks, and M. Ozolinsh, “Structure Ordering Effects in Lead Containing Ceramic Perovskites”, **32**, 981–984 (1998).

[144] T. Correia and Q. Zhang, *Electrocaloric materials - New Generations of Coolers*, Vol. 41 (2014), pp. 229–240.

[145] Y. V. Sinyavsky, N. D. Pashkov, Y. M. Gorovoy, G. E. Lugansky, and L. Shebanov, “The Optical Ferroelectric Ceramic As Working Body For Electrocaloric Refrigeration”, Ferroelectrics **90**, 213–217 (1989).

[146] Y. V. Sinyavsky and V. M. Brodyansky, “Experimental testing of electrocaloric cooling with transparent ferroelectric ceramic as a working body”, Ferroelectrics **131**, 321–325 (1992).

[147] Y. V. Sinyavsky, “Electrocaloric Refrigerators : a Promising”, Chemical and Petroleum Engineering **31**, 5–12 (1995).

[148] D. Sette, A. Asseman, M. Gérard, H. Strozyk, R. Faye, and E. Defay, “Electrocaloric cooler combining ceramic multi-layer capacitors and fluid”, APL Materials **4**, `10.1063/1.4961954` (2016).

[149] R. Bjørk, C. R. Bahl, and M. Katter, “Magnetocaloric properties of LaFe$_{13-x-y}$Co$_x$Si$_y$ and commercial grade Gd”, Journal of Magnetism and Magnetic Materials **322**, 3882–3888 (2010).

[150] S. Jeppesen, S. Linderoth, N. Pryds, L. T. Kuhn, and J. B. Jensen, “Indirect measurement of the magnetocaloric effect using a novel differential scanning calorimeter with magnetic field”, Review of Scientific Instruments **79**, 083901 (2008).

[151] W. J. Merz, “Double hysteresis loop of BaTiO$_3$ at the curie point”, Phys. Rev. **91**, 513–517 (1953).

[152] K. K. Nielsen, C. R. H. Bahl, and A. Smith, “Constraints on the adiabatic temperature change in magnetocaloric materials”, Phys. Rev. B **81**, 054423 (2010).

[153] R. B. Olsen, “Ferroelectric Conversion of Heat to Electrical EnergyA Demonstration”, Journal of Energy **6**, 91–95 (1982).

[154] K. Navickaitė, H. N. Bez, T. Lei, A. Barcza, H. Vieyra, C. R. H. Bahl, and K. Engelbrecht, “Experimental and numerical comparison of multi-layered La(Fe,Si,Mn)$_{13}$H$_y$ active magnetic regenerators”, International Journal of Refrigeration **86**, 322–330 (2018).

[155] X. Moya, E. Defay, N. D. Mathur, and S. Hirose, “Electrocaloric effects in multilayer capacitors for cooling applications”, MRS Bulletin **43**, 291–294 (2018).

[156] K. Hong, T. H. Lee, J. M. Suh, S.-H. Yoon, and H. W. Jang, “Perspectives and challenges in multilayer ceramic capacitors for next generation electronics”, J. Mater. Chem. C **7**, 9782–9802 (2019).

[157] M.-J. Pan and C. A. Randall, “A brief introduction to ceramic capacitors”, IEEE Electrical Insulation Magazine **26**, 44–50 (2010).

[158] S. Hirose, T. Usui, S. Crossley, B. Nair, A. Ando, X. Moya, and N. D. Mathur, “Progress on electrocaloric multilayer ceramic capacitor development”, APL Materials **4**, 64105 (2016).

[159] S. Kar-Narayan and N. D. Mathur, “Predicted cooling powers for multilayer capacitors based on various electrocaloric and electrode materials”, Applied Physics Letters **95**, 242903 (2009).

[160] T. Zhang, X.-S. Qian, H. Gu, Y. Hou, and Q. M. Zhang, “An electrocaloric refrigerator with direct solid to solid regeneration”, Applied Physics Letters **110**, 243503 (2017).

[161] R. Faye, H. Strozyk, B. Dkhil, and E. Defay, “Large heat flux in electrocaloric multilayer capacitors”, Journal of Physics D: Applied Physics **50**, 464002 (2017).

[162] Y. Bai, G. Zheng, and S. Shi, “Direct measurement of giant electrocaloric effect in BaTiO$_3$ multilayer thick film structure beyond theoretical prediction”, Applied Physics Letters **96**, 192902 (2010).

[163] L. Fulanović, J. Koruza, N. Novak, F. Weyland, B. Malič, and V. Bobnar, "Fatigue-less electrocaloric effect in relaxor Pb($Mg_{1/3}$$Nb_{2/3}$)$O_3$ multilayer elements", Journal of the European Ceramic Society **37**, 5105–5108 (2017).

[164] R. Faye, T. Usui, A. Torello, B. Dkhil, X. Moya, N. D. Mathur, S. Hirose, and E. Defay, "Heat flow in electrocaloric multilayer capacitors", Journal of Alloys and Compounds **834**, `10.1016/j.jallcom.2020.155042` (2020).

[165] L. Fulanović, S. Drnovšek, H. Uršič, M. Vrabelj, D. Kuščer, K. Makarovič, V. Bobnar, Z. Kutnjak, and B. Malič, "Multilayer 0.9Pb($Mg_{1/3}$$Nb_{2/3}$)$O_3$–0.1Pb$TiO_3$ elements for electrocaloric cooling", Journal of the European Ceramic Society **37**, 599–603 (2017).

[166] P. Blumenthal, C. Molin, S. Gebhardt, and A. Raatz, "Active electrocaloric demonstrator for direct comparison of PMN-PT bulk and multilayer samples", Ferroelectrics **497**, 1–8 (2016).

[167] T. Usui, S. Hirose, A. Ando, S. Crossley, B. Nair, X. Moya, and N. D. Mathur, "Effect of inactive volume on thermocouple measurements of electrocaloric temperature change in multilayer capacitors of 0.9Pb($Mg_{1/3}$$Nb_{2/3}$)$O_3$-0.1Pb$TiO_3$", Journal of Physics D: Applied Physics **50**, 424002 (2017).

[168] Y. Bai, G.-P. Zheng, K. Ding, L. Qiao, S.-Q. Shi, and D. Guo, "The giant electrocaloric effect and high effective cooling power near room temperature for BaTiO_3 thick film", Journal of Applied Physics **110**, 94103 (2011).

[169] U. Plaznik, A. Kitanovski, B. Rožič, B. Malič, H. Uršič, S. Drnovšek, J. Cilenšek, M. Vrabelj, A. Poredoš, and Z. Kutnjak, "Bulk relaxor ferroelectric ceramics as a working body for an electrocaloric cooling device", Applied Physics Letters **106**, 43903 (2015).

[170] P. Blumenthal, C. Molin, S. Gebhardt, and A. Raatz, "Active electrocaloric demonstrator for direct comparison of PMN-PT bulk and multilayer samples", Ferroelectrics **497**, 1–8 (2016).

[171] M. Marathe, D. Renggli, M. Sanlialp, M. O. Karabasov, V. V. Shvartsman, D. C. Lupascu, A. Grünebohm, and C. Ederer, "Electrocaloric effect in $\mathrm{BaTiO_3}$ at all three ferroelectric transitions: anisotropy and inverse caloric effects", Phys. Rev. B **96**, 014102 (2017).

[172]M. Marathe, A. Grünebohm, T. Nishimatsu, P. Entel, and C. Ederer, "First-principles-based calculation of the electrocaloric effect in $\mathrm{BaTiO_3}$: a comparison of direct and indirect methods", Phys. Rev. B **93**, 054110 (2016).

[173]L. Landau and E. Lifshitz, *Course of theoretical physics*, 3rd ed. (Elsevier, Butterworth Heinemann, 1980).

[174]C. Kittel, "Theory of antiferromagnetic resonance", Phys. Rev. **82**, 565–565 (1951).

[175]X. Hao, J. Zhou, and S. An, "Effects of PbO Content on the Dielectric Properties and Energy Storage Performance of $(Pb_{0.97}La_{0.02})(Zr_{0.97}Ti_{0.03})O_3$ Antiferroelectric Thin Films", Journal of the American Ceramic Society **94**, 1647–1650 (2011).

[176]I. Burn and D. M. Smyth, "Energy storage in ceramic dielectrics", Journal of Materials Science **7**, 339–343 (1972).

[177]H. Pan, Y. Zeng, Y. Shen, Y.-H. Lin, and C.-W. Nan, "Thickness-dependent dielectric and energy storage properties of $(Pb_{0.96}La_{0.04})(Zr_{0.98}Ti_{0.02})O_3$ antiferroelectric thin films", Journal of Applied Physics **119**, 124106 (2016).

[178]J. Yi, L. Zhang, B. Xie, and S. Jiang, "The influence of temperature induced phase transition on the energy storage density of anti-ferroelectric ceramics", Journal of Applied Physics **118**, 124107 (2015).

[179]X. Hao, J. Zhai, L. B. Kong, and Z. Xu, "A comprehensive review on the progress of lead zirconate-based antiferroelectric materials", Progress in Materials Science **63**, 1–57 (2014).

[180]F. L. Goupil, A. Berenov, A.-K. Axelsson, M. Valant, and N. M. Alford, "Direct and indirect electrocaloric measurements on $\langle 001\rangle$-$PbMg_{1/3}Nb_{2/3}O_3$-$30PbTiO_3$ single crystals", Journal of Applied Physics **111**, 124109 (2012).

[181]Y. Bai, G.-P. Zheng, and S.-Q. Shi, "Abnormal electrocaloric effect of $Na_{0.5}Bi_{0.5}TiO_3$–$BaTiO_3$ lead-free ferroelectric ceramics above room temperature", Materials Research Bulletin **46**, 1866–1869 (2011).

[182]R. Pirc, B. Rožič, J. Koruza, B. Malič, and Z. Kutnjak, “Negative electrocaloric effect in antiferroelectric $\mathrm{PbZrO_3}$”, EPL (Europhysics Letters) **107**, 17002 (2014).

[183]P. Tolédano and M. Guennou, “Theory of antiferroelectric phase transitions”, Phys. Rev. B **94**, 014107 (2016).

[184]C. Milesi-Brault, “Old and new antiferroelectrics: experimental studies of phase transition in model materials”, PhD thesis (2021).

[185]G. Shirane, E. Sawaguchi, and Y. Takagi, “Dielectric properties of lead zirconate”, Phys. Rev. **84**, 476–481 (1951).

[186]H. Liu and B. Dkhil, “A brief review on the model antiferroelectric $\mathrm{PbZrO_3}$ perovskite-like material”, **226**, 163–170 (2011).

[187]Z. Liu, T. Lu, J. Ye, G. Wang, X. Dong, R. Withers, and Y. Liu, “Antiferroelectrics for Energy Storage Applications: a Review”, Advanced Materials Technologies **3**, 1800111 (2018).

[188]B. Fan, F. Liu, G. Yang, H. Li, G. Zhang, S. Jiang, and Q. Wang, “Dielectric materials for high-temperature capacitors”, IET Nanodielectrics **1**, 32–40 (2018).

[189]J. Peräntie, J. Hagberg, A. Uusimäki, and H. Jantunen, “Electric-field-induced dielectric and temperature changes in a $<011>$-oriented $\mathrm{Pb(Mg_{1/3}Nb_{2/3})O_3}$-$\mathrm{PbTiO_3}$ single crystal”, Phys. Rev. B **82**, 134119 (2010).

[190]A. Grünebohm and T. Nishimatsu, “Influence of defects on ferroelectric and electrocaloric properties of $\mathrm{BaTiO_3}$”, Phys. Rev. B **93**, 134101 (2016).

[191]I. Ponomareva and S. Lisenkov, “Bridging the macroscopic and atomistic descriptions of the electrocaloric effect”, Phys. Rev. Lett. **108**, 167604 (2012).

[192]M. Marathe, C. Ederer, and A. Grünebohm, “The impact of hysteresis on the electrocaloric effect at first-order phase transitions”, physica status solidi (b) **255**, 1700308 (2018).

[193]A. Grünebohm, Y.-B. Ma, M. Marathe, B.-X. Xu, K. Albe, C. Kalcher, K.-C. Meyer, V. V. Shvartsman, D. C. Lupascu, and C. Ederer, “Origins of the inverse electrocaloric effect”, Energy Technology **6**, 1491–1511 (2018).

[194] R. Pirc, B. Rožič, J. Koruza, G. Cordoyiannis, B. Malič, and Z. Kutnjak, “Anomalous dielectric and thermal properties of ba-doped PbZrO_3 ceramics”, en, J. Phys. Condens. Matter **27**, 455902 (2015).

[195] K. Roleder and K. Wojcik, “The electrostrictive effect and ferroelectric properties in pbzro3”, Ferroelectrics **61**, 293–298 (1984).

[196] B. Lu, P. Li, Z. Tang, Y. Yao, X. Gao, W. Kleemann, and S.-G. Lu, “Large Electrocaloric Effect in Relaxor Ferroelectric and Antiferroelectric Lanthanum Doped Lead Zirconate Titanate Ceramics”, Scientific Reports **7**, 45335 (2017).

[197] A. Peláiz-Barranco, J. Wang, and T. Yang, “Direct and indirect analysis of the electrocaloric effect for lanthanum-modified lead zirconate titanate antiferroelectric ceramics”, Ceramics International **42**, 229–233 (2016).

[198] N. Novak, F. Weyland, S. Patel, H. Guo, X. Tan, J. Rödel, and J. Koruza, “Interplay of conventional with inverse electrocaloric response in $(\mathrm{Pb},\mathrm{Nb})(\mathrm{Zr},\mathrm{Sn},\mathrm{Ti})\mathrm{O}_3$ antiferroelectric materials”, Phys. Rev. B **97**, 094113 (2018).

[199] P. Lloveras, A. Aznar, M. Barrio, P. Negrier, C. Popescu, A. Planes, L. Mañosa, E. Stern-Taulats, A. Avramenko, N. D. Mathur, X. Moya, and J.-L. Tamarit, “Colossal barocaloric effects near room temperature in plastic crystals of neopentylglycol”, Nature Communications **10**, 1803 (2019).